AD-A098 265 SRI INTERNATIONAL MENLO PARK CA MOLECULAR PHYSICS LAB F/G 20/9
PROPERTIES OF THE EXCITED STATES OF MOLECULAR IONS.(U)
APR 81 P C COSBY, J T MOSELEY, J R PETERSON DAAG29-77-C-0037
UNCLASSIFIED SRI-MP-81-72 ARO-15069.8-P NL

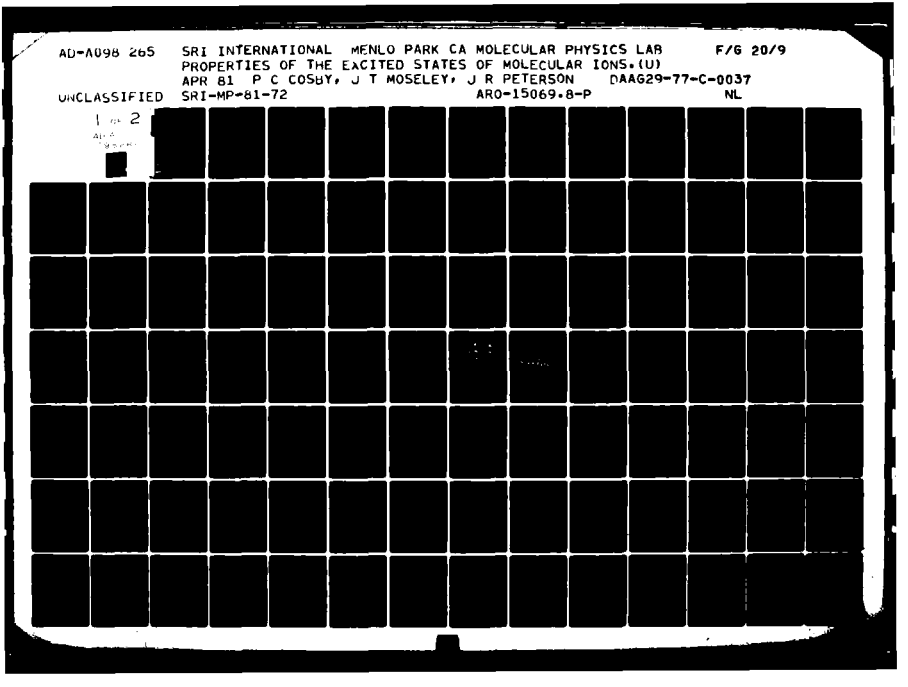

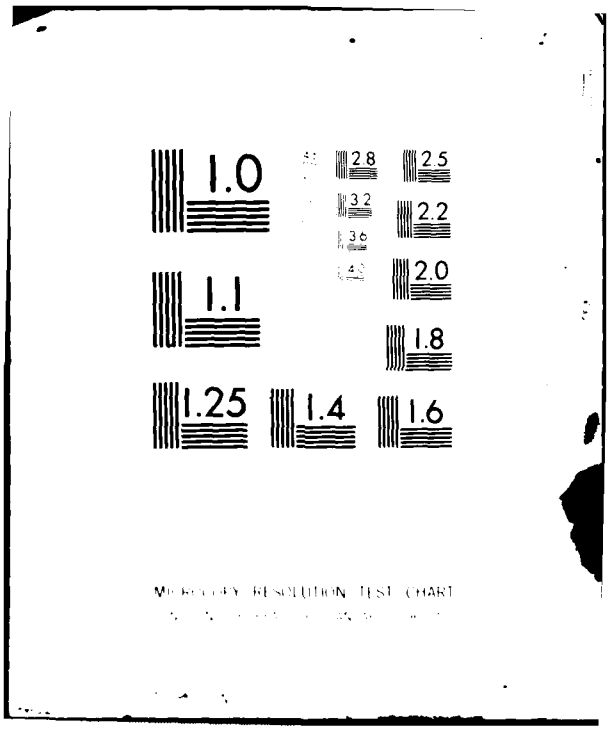
1.0
2.8
2.5
3.2
2.2
3.6
4.0
2.0
1.1
1.8
1.25
1.4
1.6
MICROCOPY RESOLUTION TEST CHART

PROPERTIES OF THE EXCITED STATES OF MOLECULAR IONS

FINAL REPORT
MP 81-72

13 April 1981

Philip C. Cosby, Project Leader
John T. Moseley and James R. Peterson,
Project Supervisors
G. P. Smith, R. V. Hodges, L. C. Lee,
and H. P. Helm

Prepared for:

U. S. ARMY RESEARCH OFFICE
P.O. Box 12211
Research Triangle Park, North Carolina 27709

Contract DAAG29-77-C-0037

SRI Project PYU 6772

Molecular Physics Laboratory
SRI International
Menlo Park, California 94025

Approved for Public Release;
Distribution Umlimited

SRI International
333 Ravenswood Avenue
Menlo Park, California 94025
(415) 326-6200
Cable: SRI INTL MPK
TWX: 910-373-1246

(18) ARO (19) 13067.8-P (14) SRI-MP-81-72

SECURITY CLASSIFICATION OF THIS PAGE (When Data Entered)

REPORT DOCUMENTATION PAGE		READ INSTRUCTIONS BEFORE COMPLETING FORM
1. REPORT NUMBER MP 81-72	2. GOVT ACCESSION NO. AD-A098265	3. RECIPIENT'S CATALOG NUMBER
4. TITLE (and Subtitle) PROPERTIES OF THE EXCITED STATES OF MOLECULAR IONS		5. TYPE OF REPORT & PERIOD COVERED Final 1 Oct 77 - 15 Sept 80
		6. PERFORMING ORG. REPORT NUMBER
7. AUTHOR(s) P. C. Cosby, H. Helm J. T. Moseley, R. V. Hodges J. R. Peterson, L. C. Lee G. P. Smith		8. CONTRACT OR GRANT NUMBER(s) DAAG29-77-C-0037
9. PERFORMING ORGANIZATION NAME AND ADDRESS Molecular Physics Laboratory SRI International Menlo Park, CA 94025		10. PROGRAM ELEMENT, PROJECT, TASK AREA & WORK UNIT NUMBERS 12) 13.7 1
11. CONTROLLING OFFICE NAME AND ADDRESS U.S. Army Research Office P. O. Box 12211 Research Triangle Park, NC 27709		12. REPORT DATE 13 Apr 81 13. NUMBER OF PAGES 125
14. MONITORING AGENCY NAME & ADDRESS (if different from Controlling Office) (10) Philip C. Cosby John T. Moseley James R. Peterson H. H. Helm L. C. Lee		15. SECURITY CLASS. (of this report) Unclassified 15a. DECLASSIFICATION/DOWNGRADING SCHEDULE

16. DISTRIBUTION STATEMENT (of this Report)

Approved for public release; distribution unlimited.

17. DISTRIBUTION STATEMENT (of the abstract entered in Block 20, if different from Report)

NA

18. SUPPLEMENTARY NOTES

The views, opinions, and/or findings contained in this report are those of the author and should not be construed as an official Department of the Army position, policy, or decision, unless so designated by other documentation.

19. KEY WORDS (Continue on reverse side if necessary and identify by block number)

Molecular Ions, Excited States, Photodissociation, Photofragment Spectroscopy.
$O_2^+(a^4\Pi_u)$, $O_2^+(b^4\Sigma_g^-)$, $O_2^+(f^4\Pi_g)$, $NO^+(b'^3\Sigma^-)$, $NO^+(2^3\Pi)$, NO_3^-, $OONO^-$, $NO_3^-\cdot H_2O$, CO_3^-

20. ABSTRACT (Continue on reverse side if necessary and identify by block number)

The techniques of photodissociation-spectroscopy and photofragment spectroscopy were developed and applied to characterize the excited states of a number of important molecular ions that occur in both natural and laboratory discharges and plasmas. → next page

(see reverse)

DD FORM 1 JAN 73 1473 EDITION OF 1 NOV 65 IS OBSOLETE

SECURITY CLASSIFICATION OF THIS PAGE (When Data Entered)

Dissociative excited states in O_2^{+} and NO^{+} were identified, together with their predissociation mechanisms, using photofragment spectroscopy techniques. In O_2^{+}, transitions from $\underline{a}^4\Pi_u$ to $\underline{b}^4\Sigma^-$ and $\underline{f}^4\Pi_g$ showed five distinct dissociation processes. This work yielded an order of magnitude improvement in resolution over conventional spectroscopic techniques, measurements of predissociation lifetimes, and several new observations of molecular dynamics and properties.

In NO^{+} a complicated band system was found to consist of transitions from $\underline{b}'\ ^3\Sigma^-$ to predissociated levels of the previously unobserved $2^3\Pi$ state. Perturbations in both the $2^3\Pi$ and the $b'^3\Sigma^-$ states were observed. These studies will have a major impact on current knowledge of NO^{+} excited states.

The structure of the $OONO^-$ isomer of NO_3^- was confirmed, and the probable mechanism for its stabilization in atmospheric reactions was identified as due to clustering with H_2O, which preserves its structure and prevents conversion to NO_3^-.

The possibility that previous observations of CO_3^- photodissociation in a drift tube can be attributed to excited ions was investigated. The results showed that the drift tube CO_3^- ions are in the ground state, but were not able to resolve the discrepancy in the CO_3^- bond dissociation energy.

THE VIEWS, OPINIONS, AND/OR FINDINGS CONTAINED IN THIS REPORT ARE THOSE OF THE AUTHOR AND SHOULD NOT BE CONSTRUED AS AN OFFICIAL DEPARTMENT OF THE ARMY POSITION, POLICY, OR DECISION, UNLESS SO DESIGNATED BY OTHER DOCUMENTATION.

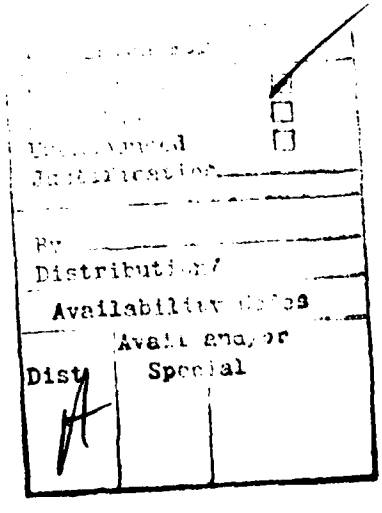

CONTENTS

I INTRODUCITON

Molecular ions are present in a wide range of gaseous media including the earth's atmosphere and other planetary atmospheres, interstellar space, gas discharges, and lasers, MHD power generators, explosives and combustion, rocket exhaust plumes, ballistic missile reactor wakes, switches, and in the environment of proposed particle beam weapons systems. Knowledge of the characteristics and reactions of these ions is required for developing diagnostic methods to determine the conditions that prevail in these media and for developing theoretical models of the media.

The objective of this research was to identify the excited states of relevent molecular ions and study their structure and decay processes. During this three-year program, we have developed two unique experimental approaches that use photodissociation as a sensitive probe of molecular ion excited states: total photodissociation cross sections measured in a drift tube mass spectrometer and partial photodissociation cross sections measured in a laser-fast-ion-beam photofragment spectrometer. Each of these approaches, summarized in Section II, offers distinct advantages to the study of molecular ion excited states.

Using these techniques, we have investigated the excited states of several important positive and negative ions: $O_2^+(\underline{a}^4\Pi_u)$, $O_2^+(\underline{b}^4\Sigma_g^-)$, $O_2^+(\underline{f}^4\Pi_g)$, $NO^+(\underline{b}'^3\Sigma^-)$, $NO^+(2^3\Pi)$, NO_3^-, $NO_3^- \cdot H_2O$, and CO_3^-. These studies have resulted in seven publications in The Journal of Chemical Physics. The most important results of this work are summarized in Section III. Detailed descriptions of the work are given in Appendices A through G.

II EXPERIMENTAL APPROACH

The high reactivity of molecular ions and the very low densities with which they can be produced preclude direct application of the traditional spectroscopic techniques developed for neutral species to the study of molecular ion excited states. Consequently, current information on the structure and internal energy states of molecular ions is extremely limited. We have found that photodissociation can be used as a particularly sensitive probe to obtain detailed information on molecular ion energy levels. This information is analogous to, and even surpasses, that obtained for neutral molecules using absorption spectroscopy.

Here, a laser is used to pump the molecular ion from specific vibrational, rotational, and fine structure levels in a bound electronic state to levels in an excited state of the ion that lie in energy above its dissociation limit. If these levels are predissociated (as is generally the case), the absorption of photons can be detected with high efficiency by either the loss of the parent molecular ion or the appearance of the fragment ion. These two methods of detecting the photoabsorption form the basis for the two experimental techniques used in this research program.

A. Drift-Tube Mass Spectrometer

The drift-tube mass spectrometer is shown schematically in Figure 1. Positive or negative ions are formed in the ion source by electron impact or attachment in a relatively high pressure (0.05-1.0 torr) of neutral gas. The ion swarm then drifts within a weak, homogeneous electric field at a fraction of the ions' random, thermal velocities. The high pressure drift region is terminated by a small exit aperture subtended by a quadrupole mass spectrometer. Just before arriving at the aperture, the ion swarm is intersected by a tunable laser beam.

Absorption by an ion species into a dissociating state is detected by a reduction in the current at the mass of that species detected by the mass spectrometer or by the increase in the ion current at the mass of the photofragments as the laser is tuned in wavelength. By adjustment of the drift

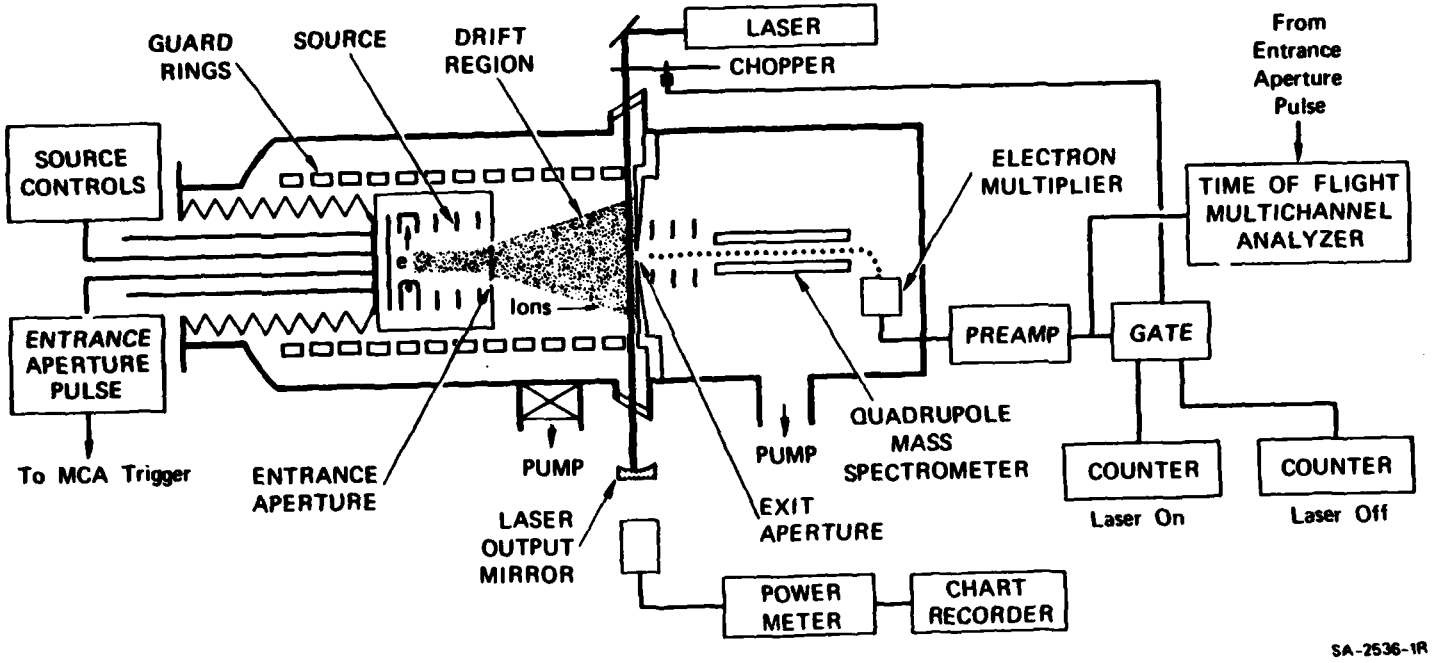

FIGURE 1 *DRIFT-TUBE MASS SPECTROMETER PHOTODISSOCIATION APPARATUS*

distance between the ion source and the laser, the gas pressure, and the gas composition, complex molecular ions can be produced by ion-molecule reactions. In general, these ions will be formed in an unknown distribution of internal energy states. However, by varying the number of thermal collisions encountered by the ion between the time of its formation and its arrival at the laser, we can study the photodissociation of the relaxed ion. Hence the photoabsorption reflects the structure of the dissociating state.

This ability to produce relaxed ions is crucial for the measurement of physically meaningful photodissociation cross sections. However, this technique suffers three limitations. First, only the relative locations of the ground and excited states can be determined; hence only an upper limit can be established for such an important ion property as the bond dissociation energy. Second, transient species cannot be studied because of the large ion-molecule reaction rates in the high pressure drift region, and third, the photoabsorptions are Doppler-broadened by the thermal motion of the ions. The following technique aviods these limitations.

B. Laser-Fast-Ion-Beam Photofragment Spectrometer

The laser-fast-ion-beam photofragment spectrometer is shown schematically in Figure 2. The ions are produced in an electron impact or discharge type ion source, extracted to form a beam, and accelerated under collision-free conditions to several thousand electron volts of energy. The desired mass species is selected by a magnetic sector, collimated to 2 mrad angular divergence, and bent by 90° into the photon interaction region by a two-dimensional electrostatic quadrupole field. In this region the ions are intersected by a laser beam directed either perpendicular to the ion beam or coaxial to it. The fragment ions produced by photodissociation are bent out of this region by a second quadrupole field into a hemispherical electrostatic energy analyzer where they are detected.

There are two basic methods for observing the photodissociation process. One is to irradiate the ion beam with a fixed laser wavelength and scan the electrostatic energy analyzer. The resulting kinetic energy spectrum of the photofragment ions identifies the locations of both the absorbing and dissociating ion states relative to the molecule's dissociation limit (rather than only relative to each other) as well as the mass of the fragment ions.

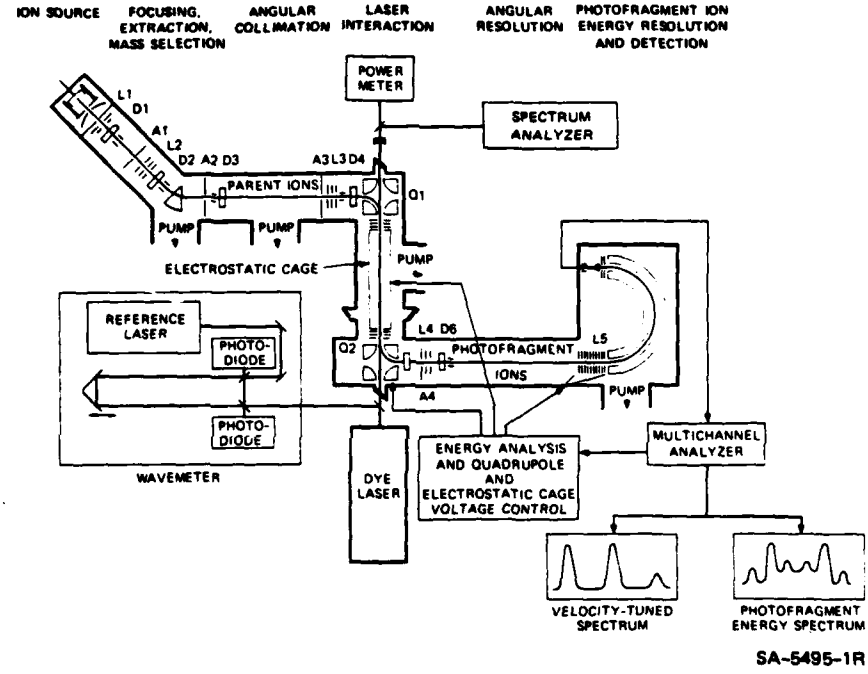

FIGURE 2 SRI LASER-ION COAXIAL BEAMS PHOTOFRAGMENT SPECTROMETER

The laser is shown in the coaxial configuration.

The second method is to fix the energy analyzer to observe only those photofragments produced with a given energy relative to the dissociation limit and scan the wavelength of the laser. This gives the absorption spectrum of the ion for transitions that terminate in the selected predissociating[4] levels of the upper electronic state.

As mentioned above, the laser can be directed either perpendicular to the ion beam or coaxial with it. In the perpendicular configuration, the polarization of the laser can be varied relative to the ion beam velocity vector. Thus the angular distribution of the photofragments can be determined, which identifies the symmetries of the molecular states involved in the optical absorption. In the coaxial configuration, the orientation of the laser polarization and the ion beam velocity are fixed. However, this arrangement allows a much larger ion-laser interaction volume, thus improving the photofragment sensitivity. A second, crucial advantage of the coaxial configuration is that it allows a very narrow Doppler width for the absorption of photons.

Although the kinetic energy spread of the ions produced in the source is large (~ 1 eV) compared with that of a room temperature gas, the magnitude of this energy spread (in the laboratory system) remains unchanged as the ion beam is accelerated to several thousand electron volts. This results in the well-known kinematic compression in the ion beam velocity spread and permits Doppler widths equivalent to those of a gas at a temperature of 1 K or less for absorptions in the coaxial laser ion beam configuration. The predissociation lifetimes of discrete vibrational, rotational, and fine-structure levels can thus be measured directly from homogeneously broadened absorption linewidths for transitions into the level.

III SUMMARY OF RESULTS

A. Photofragment Spectroscopy of O_2^+

The $\underline{a}^4\Pi_u$ state of O_2^+ is metastable with respect to radiative decay to the $\underline{X}^2\Pi_g$ ground state. As such, this state plays an important role in a variety of ion-molecule reactions in both naturally occurring and laboratory processes involving the ionization of oxygen. In addition to its practical applications, the ease with which we can form an intense O_2^+ ion beam containing a significant (~ 30%) fraction of ions in this state has made it the prototype system in our program for the development of high resolution techniques for photofragment spectroscopy.

We have thus far observed, at readily accessible visible wavelengths, transitions from the $\underline{a}^4\Pi_u$ state into both the $\underline{b}^4\Sigma_g^-$ and $\underline{f}^4\Pi_g$ states. These transitions result in five distinct dissociation processes: predissociation of $b^4\Sigma_g^-$(v=3,4,5) by spin-orbit coupling to the $\underline{f}^4\Pi_g$ and to the $\underline{d}^4\Sigma_g^+$ states, direct dissociation following transitions to the repulsive wall of the $\underline{f}^4\Pi_g$ state, and predissociation of quasi-bound levels of the $\underline{f}^4\Pi_g$ state by spin-orbit coupling to the $\underline{a}^6\Sigma_g^+$ state and by quantum-mechanical tunneling through the $\underline{f}$ state potential barrier.

These studies have resulted in an order of magnitude improvement in spectral resolution over conventional absorption or emission techniques, direct measurement of predissociation lifetimes from absorption line profiles and development of their use in identification of predissociation mechanisms, direct measurement of bond dissociation energies for both ionic and neutral states, the first observation of a $^4\Pi - {}^4\Pi$ electronic transition, the first observation of bound levels in the $\underline{f}^4\Pi_g$ state, the first measurements of anisotropy parameters for fully resolved quantum states, and the first observation of partitioning of dissociation products among atomic fine-structure levels.

A complete description of this research is given in Appendices A through D. Appendix A discusses the initial identification of the predissociating v=3,4,5 levels of the $\underline{b}^3\Sigma_g^-$ state. The predissociation lifetime measurements of these levels are discussed in Appendix B, together with their predis-

sociation mechanisms. Appendix C presents the angular distribution measurements for the fully resolved levels and the precise measurement of bond dissociation energies for the $\underline{a}^4\Pi_u$ and $\underline{b}^3\Sigma_g^-$ states of O_2^+ and the ground state of O_2. Appendix D reports the predissociation of two quasi-bound vibrational levels in the $\underline{f}^4\Pi_g$ state, analysis of the predissociation mechanisms, and the observation of partitioning among $O(^3P_{2,1,0})$ fine-structure levels in the dissociation.

B. Photofragment Spectroscopy of NO^+

The NO^+ ion is the crucial constituent in the ionosphere and in N_2/O_2 discharges and plasmas. Yet the information on the excited states of this ion is notoriously deficient, even though ionization produces 30% to 40% of the ion population in long-lived metastable states. We have made a preliminary survey of NO^+ photodissociation in the 6600-5650 Å wavelength range and found more than 40 NO^+ absorption bands that produce O^+ photofragments with center-of-mass kinetic energies (W) between 0 and 900 meV and N^+ photofragments with W in the range of 0 to 600 meV. A detailed study was made of the band system that produced O^+ fragments with W between 698 and 925 meV. This study is discussed in Appendix E.

We found that the band system was composed of transitions from $\underline{b}'^3\Sigma^-(v=8,9,10)$ to 20 predissociated levels of the previously unobserved $2^3\Pi(v=0\text{-}19)$ state. The rotational population of $\underline{b}'^3\Sigma^-(v=9)$ was found to be perturbed by $\underline{A}^1\Pi(v=3)$. In addition, the $2^3\Pi$ state was found to be homogeneously perturbed at $v \geq 3$. High resolution spectra of the absorption bands disclosed a predissociation lifetime of $\tau \geq 1.6$ ns for the lower vibrational levels in the $2^3\Pi$ state. The predissociation of this state is likely caused by spin-orbit coupling to the $\underline{\alpha}^5\Sigma^+$ state. Because of the perturbations that occur in both the upper and lower states, the complex rotational structure, although fully resolved, cannot yet be assigned. However, future analysis of the numerous other predissociation band systems will likely provide the additional information necessary for a full characterization of the $2^3\Pi$ state.

The present investigation will have a major impact on current knowledge of NO^+ excited states. It probes for the first time the states lying in the region of the lowest NO^+ dissociation limits. Although two extensive *ab initio* calculations of the NO^+ excited states have been made, neither

accurately describes the electronic states in this region. Yet it is precisely this region that dominates a theoretical description of $N^+ + O$ or $O^+ + N$ collisions.

C. The Peroxy Isomer of NO_3^-

A peroxy isomer of the NO_3^- ion ($OONO^-$) had been postulated on the basis of reaction rate measurements. Those measurements also found that the isomer was rapidly converted to normal (C_{3v} symmetry) NO_3^- by reaction with NO. We have observed photodissociation of the isomeric NO_3^- ion into $O_2^- + NO$, thus confirming its peroxy structure. We have further found that $OONO^-$ is rapidly hydrated and that its peroxy structure is preserved in the hydrate. Moreover, we find that hydration of $OONO^-$ effectively stabilizes it against conversion into NO_3^- by reaction with NO.

These observations suggest the importance of considering the chemistry and photochemistry of the peroxy ion and its hydrates in modeling the ionosphere. A detailed discussion of this research is given in Appendix F.

D. Photodissociation of CO_3^-

Several years ago it was discovered in our laboratory that CO_3^- photodissociates into $O^- + CO_2$ with a highly structured cross section at visible wavelengths. The longest wavelength at which photodissociation could be observed implied an upper limit of < 1.85 eV. for the bond dissociation energy of CO_3^-. This value, however, conflicted with the lower limit of > 2.27 eV established for the dissociation energy of this ion by ion-molecule reaction studies. Consequently, we undertook an extensive series of tests to determine whether the observed photodissociation could have arisen from a long-lived excited state of the CO_3^- ion that was not collisionally quenched in the initial drift tube studies. This work is reported in Appendix G.

In summary, we found that the absorbing state in the photodissociation process was the ground electronic state of the ion. We also found that the lifetime of the state populated by the absorption was approximately 0.5 μs. We eliminated the possibility that collisional dissociation of this long-lived state, populated at energies below the thermodynamic limit, could produce the low apparent threshold for photodissociation. None of these findings was able to resolve the discrepancy in the CO_3^- bond dissociation energy.

IV LIST OF PUBLICATIONS

The research conducted under contract DAAG29-77-C-0037 has resulted in the following publications.

1. M. Tadjeddine, R. Abouaf, P. C. Cosby, B. A. Huber, and J. T. Moseley, "Predissociation photofragment spectroscopy of O_2^+ quartet states," J. Chem. Phys. 69, 710 (1978).

2. J. T. Moseley, P. C. Cosby, J. B. Ozenne, and J. Durup, "Predissociation lifetimes of the rotational and fine structure levels of $O_2^+(b\,^4\Sigma_g^-, v=3,4,5)$," J. Chem. Phys. 70, 1474 (1979).

3. C. Pernot, J. Durup, J. B. Ozenne, J. A. Beswick, P. C. Cosby, and J. T. Moseley, "Angular distributions and separation energies of predissociation photofragments of $O_2^+(b\,^4\Sigma_g^-, v'=4,N',F')$," J. Chem. Phys. 71, 2387 (1979).

4. H. Helm, P. C. Cosby, and D. L. Huestis, "Laser predissociation spectroscopy of the $f\,^4\Pi_g$ state of O_2^+," J. Chem. Phys. 73, 2629 (1980).

5. P. C. Cosby and H. Helm, "Laser photofragment spectroscopy of NO^+ I. Predissociation of the $2\,^3\Pi$ state," J. Chem. Phys. (submitted for publication).

6. G. P. Smith, L. C. Lee, and P. C. Cosby, "Photodissociation and photodetachment of molecular negative ions VIII. Nitrogen oxides and hydrates, 3500-8250 Å," J. Chem. Phys. 71, 4464 (1979).

7. G. P. Smith, L. C. Lee, and J. T. Moseley, "Photodissociation and photodetachment of molecular negative ions VII. Ions formed in $CO_2/O_2/H_2O$ mixtures, 3500-5300 Å," J. Chem. Phys. 71, 4034 (1979).

V LIST OF PERSONNEL

The following Molecular Physics Laboratory personnel have participated in the research described in this report with partial support from contract DAAG29-77-C-0037:

John T. Moseley
Philip C. Cosby
James R. Peterson
Joseph A. Dallarosa
Gregory P. Smith
Ronald V. Hodges
Long C. Lee
Hanspeter Helm.

The following visiting personnel, listed with their home institutions, have contributed to the research described in this report:

Mireille Tadjeddine Université de Paris - Sud, France
Robert Abouaf Université de Paris - Sud, France
Jean-Bernard Ozenne Université de Paris - Sud, France
Jean Durup Université de Paris - Sud, France
J. Alberto Beswick Université de Paris - Sud, France
Christiane Pernot Université de Paris - Sud, France
Bernd A. Huber Ruhruniversität, West Germany.

APPENDIX A

Predissociation photofragment spectroscopy of O_2^+ quartet states[a)]

M. Tadjeddine[b)] and R. Abouaf[c)]

Laboratoire de Collisions Atomiques et Moléculaires, Université de Paris-Sud, 91405 Orsay, France

P. C. Cosby, B. A. Huber,[d)] and J. T. Moseley

Molecular Physics Laboratory, SRI International, Menlo Park, California 94025
(Received 20 March 1978)

The technique of predissociation photofragment spectroscopy is applied to a study of the photodissociation of O_2^+, primarily in the 5730 to 5870 Å wavelength region. The major part of this predissociation is shown to be due to the transition $b\,^4\Sigma_g^- \rightarrow a\,^4\Pi_u$, with predissociation of levels $N' = 9$–23 of a ($v' = 4$) and $N' = 7$–15 of a ($v' = 5$) observed. The $N' = 9$ level of a ($v' = 4$) is shown to be 1.1 ± 1.1 meV above the $O(^3P_2) + O^+(^4S^o)$ dissociation limit, providing, in conjunction with other previously measured spectroscopic quantities, improved dissociation energies for the $O_2^+(a\,^4\Pi_u)$ and ($b\,^4\Sigma_g^-$) states, as well as for the previously reported $O_2(X\,^3\Sigma_g^-)$. The lifetimes of the $N' = 9$–15 levels are shown to be $(70 \pm 15) \times 10^{-11}$ sec for the F_1' and F_2' components, and $(42 \pm 8) \times 10^{-11}$ sec for the F_3' and F_4' components, with the lifetimes of the F_1' and F_2' components at least 1.5 times greater than the lifetimes of the F_3' and F_4' components.

I. INTRODUCTION

The first-negative band system of O_2^+, the transitions between the $b\,^4\Sigma_g^-$ and the metastable $a\,^4\Pi_u$ states, has been known and studied[1–3] for many years. It is a rare example of an easily observable transition between states of such high multiplicity. Due to the prevalence of this band system in many ionization processes in oxygen[4] and to the chemical reactivity[5] of the resulting $a\,^4\Pi_u$ state, it is desirable to have more detailed knowledge of these quartet states. Such knowledge will assist in the understanding of the many naturally occurring and laboratory environments where ionized oxygen is important, and will also increase the theoretical understanding of quartet states.

During the past two years, several new experimental techniques have been applied to the study of quartet states of O_2^+. The four potential curves most relevant to these investigations are shown in Fig. 1. Laser photofragment spectroscopy demonstrated[6] that the $a\,^4\Pi_u$ state can be photodissociated at visible wavelengths by transitions to the $f\,^4\Pi_g$ state (transition I in Fig. 1). This was the first experimental observation of the f state, and its location was shown to be approximately as had been recently calculated by Beebe, Thulstrup, and Andersen.[7] Observation of the photofragment current near the $O^+(^4S^o) + O(^3P_2)$ threshold as a function of laser wavelength revealed structure[6] apparently characteristic of the rotational and fine structure levels of the $a\,^4\Pi_u$ state. The dissociation was tentatively identified as occurring via rotationally predissociated levels of the f state (transition III in Fig. 1).

Next, Carrington, Roberts, and Sarre showed[8] that the $v = 4$ level of the $b\,^4\Sigma_g^-$ state was predissociated for rotational levels $N' = 9$ or greater (transition II in Fig. 1, followed by dissociation). They used coaxial laser and ion beams and the Doppler effect to scan the absorption wavelength in the vicinity of the 4965 Å line of an argon ion laser, and observed well-resolved rotational transitions in the (4 – 1) vibrational band of the first-negative system. By taking advantage of the velocity narrowing[10–12] in a fast ion beam, a resolution of better than 0.01 cm^{-1} was obtained, and lifetimes in the range of a nanosecond determined for several of the predissociated levels. In the more recent work,[9] the predissociation has been tentatively assigned to a coupling with the $^4\Sigma_g^-$ state, which crosses the b state near its intersection with the f state (see Fig. 1).

Guyon *et al.*, using a synchrotron radiation photon source and the technique of threshold photoelectron–photoion coincidence spectroscopy, observed[13] the predissociation of both the $b\,^4\Sigma_g^-$ state and the higher lying $c\,^4\Sigma_u^-$ state. They concluded that the $v' = 4$, 5, and 6 levels of the b state are predissociated to the extent of $\geq 70\%$, and they estimated the lifetimes of the predissociated levels to be ≤ 50 nsec. On the other hand, Erman and Larsson[14] observed the first-negative emis-

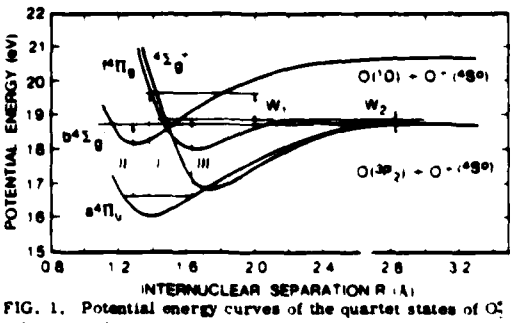

FIG. 1. Potential energy curves of the quartet states of O_2^+ relevant to the present study.

a)Research supported by the U. S. Army Office of Scientific Research, and the National Science Foundation under Grant No. CHE 77-00428.

b)International Fellow at SRI International, March and April, 1977.

c)International Fellow at SRI International, 1976–77 academic year.

d)Permanent address: Ruhruniversität, Institut für Experimental Physik II, Bochum, West Germany.

 0021-9606/78/6902-0710$01.00

sion induced by electron impact, and found lifetimes which increased smoothly from 1.35 μsec for $v' = 0$ to 2 μsec for $v' = 7$.

A detailed analysis[15] of the O_2^+ first-negative system was recently completed by Albritton, Schmeltekopf, Harrop, Zare, and Czarny. This analysis included the best experimental data available for transitions including vibrational levels 0 through 6 of the a state and 0 through 3 of the b state. The resulting molecular constants can be used, via a short extrapolation, in the assignment of the observed predissociated levels, or conversely, measurements on these levels, if of sufficient accuracy, could be used to further improve the molecular constants.

The work reported here is essentially an extension of that reported in Ref. 8, but was performed on a new apparatus of much higher resolution and sensitivity. 24 branches of the (4, 4) vibrational band of first-negative system have been resolved for the first time, and assigned using the abovementioned molecular constants. Transitions of the (5, 5), (4, 5), and (4, 3) bands were also observed. Further, a direct measurement of the dissociation energy of a number of the predissociated levels has been made, and observations are made on the lifetimes of these levels.

II. EXPERIMENTAL PROCEDURES

The experiments were performed using a new laser–ion coaxial beams spectrometer[12,16] which has been described in detail elsewhere. The O_2^+ ions are formed in a hollow-cathode discharge source, accelerated to 3 keV, mass selected by a 45° sector magnet, collimated to 2 mrad and bent through 90° into the laser interaction region using a specially designed[17] quadrupole deflection system. Tunable lasers can be made either coaxial or crossed with the ion beam. Following the laser interaction region, photofragment O^+ ions are bent through 90° and directed into an energy analysis system with an angular resolution of 2 mrad. This system,[12] consisting of a decelerating lens and hemispherical energy analyzer, had a resolution of 3000 with respect to the laboratory beam energies in the present experiments. Ions which pass through the energy analyzer are detected by a continuous-dynode electron multiplier and counted in a multichannel analyzer.

Two cw jet-stream tunable dye lasers were used, one crossed and one coaxial with the ion beam, pumped by argon and krypton ion lasers. The polarization of the laser crossed with the ion beam was always parallel to the beam direction. This laser was arranged so that the ion beam passed through the laser cavity, in order to enhance the photofragment current. The polarization of the laser coaxial with the ion beam was necessarily always perpendicular to the beam direction. Proper account was taken of the approximately 2.6 Å Doppler shift with coaxial beams, and in order to have only one Doppler component, the extracavity laser beam was used. Each laser had a line width of about 0.2 Å. The wavelength was measured in air using a monochromator with a resolution of 30 000 (approximately 0.2 Å at 5800 Å), and corrected to the vacuum wavelength.

The primary experimental data were scans of the laser wavelength from 5750 to 5870 Å, covering all of the expected (4, 4) and (5, 5) transitions while observing the photofragment current for fragment ions corresponding to total separation energies W centered at 0, 12, 25, 50, and 100 meV. Spectra at $W = 0$ were also obtained for the (4, 5) transition (6090 to 6210 Å) and for the (4, 3) transition (5430 to 5550 Å). Such scans are designated predissociation spectra. At selected fixed wavelengths, photofragment energy spectra were obtained by scanning the energy analyzer. Finally, a few spectra were obtained using a single-mode laser coaxial with the ion beam to demonstrate the very high resolution that can be obtained using this technique, and to obtain estimates of the lifetimes of the dissociated levels for comparison with the recent work[9] of Carrington, Roberts, and Sarre.

III. EXPERIMENTAL RESULTS

A. Identification of the transition

The predissociation spectrum obtained for $W = 0$ with crossed beams is shown in Fig. 2. The $W = 0$ spectrum obtained for coaxial beams is essentially identical, since the angular acceptance of the apparatus is such that there is no angular discrimination for photofragment ions whose energy is less than 12 meV. The resolution of the peaks in this spectrum is seen to be about 0.2 Å, and the uncertainty in the absolute wavelength scale is also about 0.2 Å. From the width and spacing of the peaks it is clear that rotational structure is resolved.

The first task is to identify the optical transition resulting in the predissociated levels. Previous work[9,13] suggests that the first-negative (4, 4) transitions are responsible, but rotationally-resolved spectra have not been previously obtained, and there exist at least two other types of transitions[8] which could result in a highly structured cross section near $W = 0$.

The wavelengths for the transitions expected for the first-negative (4, 4) band can be calculated using the work of Albritton *et al.*[15] Because of its high multiplicity, the structure of this band is quite complex. Figure 3 shows schematically the expected transitions, along with the relevant quantum numbers and their designations. The lower $a\,{}^4\Pi_u$ state is split by the spin–orbit interaction into four sublevels denoted ${}^4\Pi_\Omega$. In the order of increasing energy, these sublevels are ${}^4\Pi_{5/2}(\Sigma'' = 3/2)$, ${}^4\Pi_{3/2}(\Sigma'' = 1/2)$, ${}^4\Pi_{1/2}(\Sigma'' = -1/2)$ and ${}^4\Pi_{-1/2}(\Sigma'' = -3/2)$ where $\Omega = \Lambda + \Sigma$, and Λ and Σ are the projections of the orbital and spin angular momenta, respectively, on the internuclear axis. The total angular momentum quantum number in this Hund's case (a) limit is J''. Although each J'' level is Λ doubled, only negative parity levels are present, since ${}^{16}O_2^+$ is a homonuclear molecule whose nuclei have zero nuclear spin. In the upper $b\,{}^4\Sigma_g^-$ state each N' rotational level consists of four closely-spaced spin components $F_1'(J' = N' + 3/2)$, $F_2'(J' = N' + 1/2)$, $F_3'(J' = N' - 1/2)$, and $F_4'(J' = N' - 3/2)$,

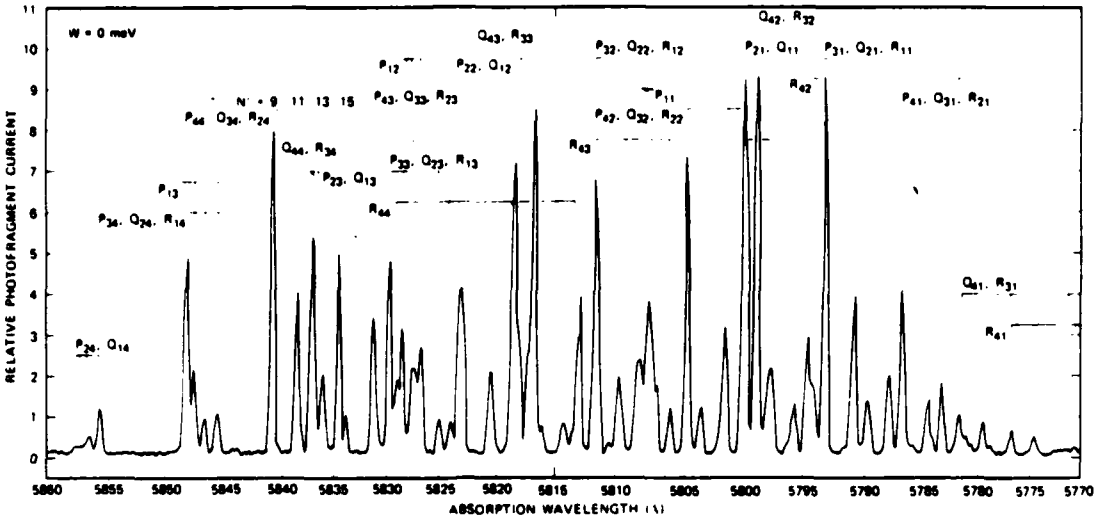

FIG. 2. Predissociation photofragment spectrum for O_2^+ obtained for separation energy $W = 0$ from 5770 to 5860 Å. The noted transition wavelengths are for the $O_2^+(b, v' = 4 - a, v'' = 4)$ band, calculated as discussed in the text.

where J' is the total angular momentum quantum number and N' is the nuclear rotation quantum number. Due to the nuclear spin statistics, only odd-valued N' levels, which have positive parity, are present. For this $^4\Sigma_g^-$ state, treated as Hund's case (b), Ω is not a good quantum number. For simplicity in designating transitions between these two states, a quantum number F_1'' may be associated[15] with the $^4\Pi_{5/2}$ designation of the a state, F_2'' with $^4\Pi_{3/2}$, F_3'' with $^4\Pi_{1/2}$, and F_4'' with $^4\Pi_{-1/2}$. This, of course, would be the Hund's case (a) designation for this state. Transitions between the b and a states can then be uniquely designated by P, Q, or R, depending on whether ΔJ is -1, 0, or $+1$ subscripted by $F'F''$. For example, the transition to the far left of Fig. 3, P_{34}, corresponds to $\Delta J = -1$, $F' = 2$ and $F'' = 4$.

It can be seen from Fig. 3 that in principle 48 transitions can be observed which obey the selection rule

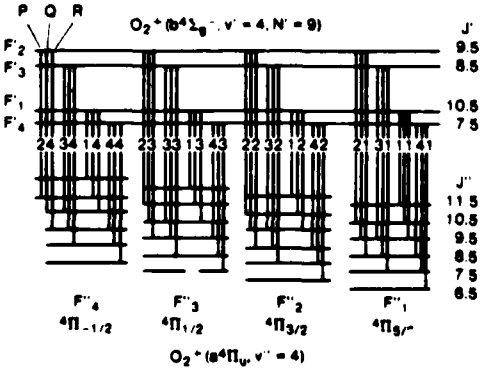

FIG. 3. Transitions which can occur to the $(b\,^4\Sigma_g^-, v' = 4, N' = 9)$ levels of O_2^+ from $(a\,^4\Pi_u, v'' = 4)$ levels.

$\Delta J = 0, \pm 1$, and terminate in a given N' level of the b state. However, with the present resolution of 0.2 Å, only 24 branches can be resolved, 16 of these consisting of blends of two or three of the transitions of Fig. 3. Even in the highest-resolution optical spectroscopy only 40 branches can be resolved. Table I shows the pure branches and the branches that can be resolved in the present work, as well as the branches that have been resolved by high-resolution optical spectroscopy for the lower vibrational levels of the b state.

In order to calculate the expected transition wavelengths for comparison with the data of Fig. 2, the $G(v, J)$ energies of the a and b states must be determined. The molecular constants of the $v'' = 4$ and 5 levels of the a state are well known (see Table VIII, in Ref. 15); the constants for the $v' = 4$ and 5 levels of the b state were determined using the Dunham coefficients from Table IX of Ref. 15. The $G(v, J)$ energies were then computed by diagonalization of the Hamiltonian whose matrix elements are defined in Tables II and III of Ref. 15. All molecular constants used for the interpretation of the (4, 4) and (5, 5) bands are given in Table

TABLE I. The unblended branches, blended [ ] branches observed in this work, and the high-resolution blended ( ) branches (Ref. 15) of the $O_2^+(b\,^4\Sigma_g^- - a\,^4\Pi_u)$ band system.

$^4\Sigma - {}^4\Pi_{-1/2}$	$^4\Sigma - {}^4\Pi_{1/2}$	$^4\Sigma - {}^4\Pi_{3/2}$	$^4\Sigma - {}^4\Pi_{5/2}$
P_{14}	P_{13}	P_{12}	P_{11}
$[P_{24}\ Q_{14}]$	$[P_{23}\ Q_{13}]$	$[P_{22}\ Q_{12}]$	$[P_{21}\ Q_{11}]$
$[(Q_{24}\ P_{34})R_{14}]$	$[(Q_{23}\ P_{33})R_{13}]$	$[(Q_{22}\ P_{32})R_{12}]$	$[(Q_{21}\ P_{31})R_{11}]$
$[(R_{24}\ Q_{34})P_{44}]$	$[(R_{23}\ Q_{33})P_{43}]$	$[(R_{22}\ Q_{32})P_{42}]$	$[(R_{21}\ Q_{31})P_{41}]$
$[R_{34}\ Q_{44}]$	$[R_{33}\ Q_{43}]$	$[R_{32}\ Q_{42}]$	$[R_{31}\ Q_{41}]$
R_{44}	R_{43}	R_{42}	R_{41}

TABLE II. Molecular constants used for the interpretation of the spectra. All units are cm^{-1}.

$b\,^4\Sigma_g^-$[a]	v'	T'[c]	B'	$D'(10^{-6})$	$\gamma'(10^{-4})$	ϵ'			
	5	22138.4	1.163443	6.6657	−10.84	0.1450			
	4	21112.40	1.186547	6.5583	−9.6	0.1450			
$a\,^4\Pi_u$[b]	v''	T''[c]	A''	B''	$D''(10^{-6})$	ϵ''	$q''(10^{-4})$	$p''(10^{-3})$	γ''
	5	4866.798	−47.635	1.01930	5.25	0.640	−1	3.1	0.189
	4	3935.283	−47.777	1.03491	5.39	0.633	2	6.0	0.188

[a]The molecular constants of the $b\,^4\Sigma_g^-$ state have been deduced from the Dunham coefficients [Table IX in Ref. 15].
[b]From Table VIII in Ref. 15.
[c]The origin is the energy of the $v''=0$ vibrational level of the $a\,^4\Pi_u$ state.

II. The energies here are referenced to the $v''=0$ level of the $a\,^4\Pi_u$ state, as defined by Albritton *et al.*[15] Determination of these energies relative to the $O(^3P_2)+O^-(^4S^0)$ dissociation limit (and hence to the ground state of O_2) will be discussed later.

The results of these calculations for the (4, 4) band, rotational levels $N'=9$, 11, 13, and 15, are shown in the upper part of Fig. 2. Comparison with Table I shows that the branches expected to be resolved are indeed resolved. Clear evidence is seen in Fig. 2 for 22 of the possible 24 branches; there is some indication of the R_{41}, but no indication of the P_{14}, which is at about 5865 Å, is shown there. Both of these transitions, however, have been clearly observed using longer counting times. All of the observed structure can be explained *by the indicated transitions.*

Characteristically, the peak corresponding to $N'=9$ is the most intense for each branch. This is not due primarily to population differences or vibrational line strengths but to the energy resolution function of the apparatus. With the energy resolution set nominally at $W=0$, the analyzer will discriminate more and more strongly against the higher rotational levels. We shall discuss this point in more detail in a following section.

B. Dissociation energies of the N' levels

Before attempting to understand in detail the dependence of the predissociation spectra on photofragment kinetic energy, it is important to establish the dissociation energies $W_d(N', {}^3P_2)$ of the various N' levels with respect to the $O(^3P_2)+O^-(^4S^0)$ dissociation limit. These dissociation energies can be calculated from the cycle[18]

$$W_d(N', {}^3P_2)+IP_1(O\,{}^3P_2)+D_0(O_2X) = E(O_2^+b)+E(O_2^+b, v'=4, N'), \quad (1)$$

where $E(O_2^+b, v'=4, N')$ is the energy of the designated level above the $v'=0$, $N'=0$ level of the b state. For $N'=9$, this energy has been calculated to be 4552.1 ± 0.5 cm^{-1} using the molecular constants of Table II. The other quantities in Eq. (1) have well-established values and uncertainties: the first ionization potential of $O(^3P)$, $IP_1(O\,{}^3P_2)$, is[19] 109 837.02 ± 0.06 cm^{-1}, $D_0(O_2X)$ is[20] 41 260 ± 15 cm^{-1}, and the energy of the $v=0$, $N=0$ level of the b state above the $v=0$, $N=0$ level of $O_2(X\,{}^3\Sigma_g^-)$, $E(O_2^+b)$, is[21] 146 556 ± 2 cm^{-1}. This yields $W_d(9, {}^3P_2)=1.4^{+0.8}_{-1.4}$ meV, where the lower limit of zero is set by the fact that photofragments that arise from the $N'=9$ level are observed.

It is possible to obtain a better value for $W_d(9, {}^3P_2)$ directly by measurement of the photofragment kinetic energy. Figure 4(a) shows such an energy spectrum obtained for the (P_{34}, Q_{24}, R_{14}) transition at 5848 Å. The half-width at half-maximum of this peak corresponds to 2.2 meV separation energy, indicating that $W_d(9, {}^3P_2) \leq 2.2$ meV. Thirteen separate measurements were made on various peaks corresponding to $N'=9$, establishing 2.2 meV as a firm upper limit on $W_d(9, {}^3P_2)$. Thus the value 1.1 ± 1.1 meV is adopted for $W_d(9, {}^3P_2)$. This allows calculation of the W_d values for the other N' levels, and upper limits for these W_d values can also

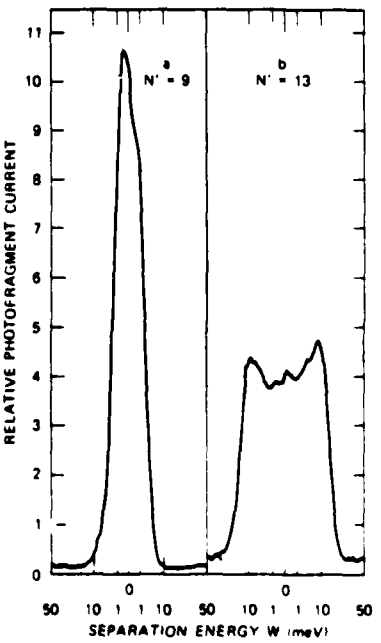

FIG. 4. Photofragment kinetic energy spectra for the (P_{34}, Q_{24}, R_{14}) transitions terminating in the $N'=9$ level of the b state (a), and in the $N'=13$ level (b).

TABLE III. Rotational N' levels of the $O_2^+(b\,^4\Sigma_g^-, v'=4)$ with their kinetic energies of separation W calculated with respect to the $O(^3P_{2,1,0})$ dissociation limits, and the experimentally determined upper limits with respect to the $O(^3P_2)$ limit.

	Calculated[$W_e(9, {}^3P_2) = 1.1$ meV]			Measured Upper Limits
N'	$O(^3P_2)$	$O(^3P_1)$	$O(^3P_0)$	(meV)
9	1.1[a]			2.2
11	7.2[a]			8.7
13	14.6[a,b]			16.7
15	23.1[b,c]	3.1[a]		24.5
17	32.8[c]	12.8[b]	4.8[a,e]	35.7
19	43.6[c,d]	23.6[c]	15.6[b,e]	48.3
21	55.7[d]	35.7[c]	27.6[c,e]	58.2
23	68.8[d]	48.8[d]	40.8[c,e]	73.4
25	83.1	63.1[d,e]	55.1[d,e]	

[a]Observed in the $W = 0$ spectrum.
[b]Observed in the $W = 12$ meV spectrum.
[c]Observed in the $W = 25$ meV spectrum.
[d]Observed in the $W = 50$ meV spectrum.
[e]Observation not firmly established.

be measured experimentally. Table III gives measured limits and calculated values for the N' levels 9 through 25, with respect to the possible $^3P_{2,1,0}$ dissociation limits.

It has been pointed out[18] that this direct measurement of $W_e(9, {}^3P_2)$ allows a better determination of the dissociation energies for the $O_2(X\,^3\Sigma_g^-)$, $O_2^+(a\,^4\Pi_u)$ and $O_2^+(b\,^4\Sigma_g^-)$ states. The determination of the dissociation energy $D(O_2 X\,^3\Sigma_g^-)$ has been discussed in detail,[18] and the value shown to be 41262 ± 10 cm^{-1}. In an analogous way, the dissociation energy for the lowest existing level of the a state can be shown to be $D(O_2^+ a\,^4\Pi_u, v = 0, J = 2\frac{1}{2}, \Omega = \frac{1}{2}) = 21276 \pm 10$ cm^{-1}, and of the b state to be $D(O_2^+ b\,^4\Sigma_g^-, v = 0, N = 0) = 20411 \pm 10$ cm^{-1}.

C. Dependence of the spectra on photofragment energy

In order to understand the dependence of the predissociation spectra on photofragment energy, it is necessary to discuss the collection efficiency of the apparatus as a function of energy and angular distributions. Figure 5 shows a velocity diagram of dissociating ions for two values W_1 and W_2 of the separation energy. The apparatus acceptance angle α for photofragment ions is 2 mrad, the parent ion beam energy is typically 3000 eV, and W, for the work reported here, is on the range 0–100 meV. Thus the maximum angle in the center-of-mass frame which is subtended by the detection system is given to an excellent approximation by

$$\varphi = \sin^{-1}(\alpha\sqrt{T_0/W}). \tag{2}$$

As has already been mentioned, there is no angular discrimination for photofragment ions whose separation energy W is less than 12 meV. Ions of higher energy will be recorded if they are ejected into a cone whose ap x half-angle decreases with energy. For ions of 100 meV, this angle is 20.3° in the center-of-mass frame.

The effect of the energy resolution window can also be seen in Fig. 5. With an analyzer resolution width in the center-of-mass, ΔW_c, photofragments of energy W_1 will be detected if the ions are ejected into the portion of the sphere indicated by the solid arc A_1B_1; photofragments of energy W_2 will be detected only if they are ejected into that portion indicated by A_2A_2' and B_2B_2'.

With the analyzer centered at $W = 0$ (in this homonuclear diatomic case, to pass ions of energy $\frac{1}{2}T_0$), the maximum energy photofragment which can be detected corresponds to $T = \frac{1}{2}(T_0 + \Delta T)$, where ΔT is the energy resolution, assumed here for simplicity to be a step function. Although the energy analyzer resolution is about 1 eV, the ion beam has an energy width of about 2.5 eV for the discharge source used here, thus the overall energy resolution will be limited to 2.5 eV. From the expression[22] relating the observed laboratory photofragment energy T to the separation energy W,

$$T = \tfrac{1}{2}(T_0 + W) + \sqrt{WT_0}, \tag{3}$$

it can be shown that the energy resolution ΔW for center-of-mass energies is

$$\Delta W = \Delta T^2/4T_0 \;(W \le \Delta T^2/4T_0);$$
$$\Delta W = 2\Delta T(W/T_0)^{1/2} \;(W > \Delta T^2/4T_0). \tag{4}$$

Although the center-of-mass energy resolution at $W = 0$ implied by these equations is 0.5 meV for $\Delta T = 2.5$ eV, photofragments ejected at higher energy but perpendicular to the beam direction can be detected until they are cut off by the angular collimation at 12 meV. Figure 6 shows a calculated collection factor function, for $\alpha = 2$ mrad, $W = 0$, and $\Delta T = 2.5$ eV, taking into account as well the fact that the angular distributions of the photofragments will be different[23] when the laser is polarized parallel (crossed beams) or perpendicular (coaxial beams) to the ion flight direction. This collection efficiency is certainly not precisely correct, particularly in that the sharp cut-off at 12 meV would be smoothed out and extended to higher energy if a more realistic energy resolution function such as a Gaussian were used. However, it does show quite well the observed behavior, as can be seen from the experimental points taken from the heights of the peaks in the spec-

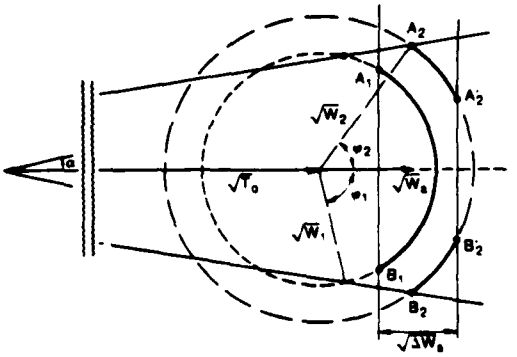

FIG. 5. Velocity diagram of dissociating ions for two values W_1 and W_2 of the separation energy.

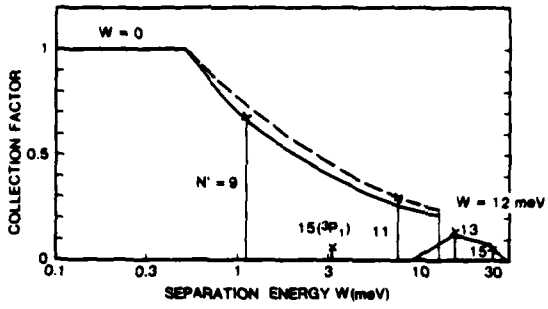

FIG. 6. Calculated collection efficiency functions for separation energies $W = 0$ and $W = 12$ meV. The dashed curve was calculated for parallel laser polarization; the solid curve for perpendicular polarizaiton. The separation energies for the $N' = 9$–15 levels are all with respect to the $^3P_2$ dissociation limit, except for the $N' = 15$ level indicated $^3P_1$. The data points (x) show the observed relative peak heights in the $W = 0$ spectrum, normalized for the $N' = 9$ peak to the solid curve.

trum corresponding to $N' = 9$, 11, 13, and 15. The $N' = 9$ peaks were normalized to the solid curve, then the other peak heights were multiplied by the same normalization factor. The peak heights were not corrected to account for different rotational line strengths nor for the (unknown) population distribution in the $a\,^4\Pi_u$ state.

The placement of the $N' = 15$ data point in Fig. 6 at 23.1 meV, corresponding to dissociation to the $O(^3P_2)$ limit, is not necessarily correct, since ions from this rotational level can also dissociate to the $^3P_1$ limit with $W = 3.1$ meV. Recall that Table III shows the rotational energy levels $N' = 9$ through 21 compared to the three $O(^3P_{2,1,0})$ dissociation limits. We might expect a simply statistical branching ratio, which for $N' = 15$ would imply that 3/8 of the intensity would appear in the $^3P_1$ channel, 5/8 in $^3P_2$. If this were true, then in the $W = 0$ spectrum the $N' = 15$ peak should probably be more intense than the $N' = 13$ peak, which can dissociate only to the $^3P_2$ limit. Future work will be directed toward the determination of a more precise collection efficiency function, as well as to the determination of the branching ratios to the three dissociation limits.

As the energy analyzer is adjusted to higher energy, the width of the collection efficiency function will increase [see Eq. (4)], and the total collection efficiency will decrease due to the decreasing angular collection efficiency [see Eq. (2)]. The collection efficiency function calculated for $W_A = 12$ meV is also shown in Fig. 6. This calculation shows that we should see photofragments with kinetic energies between 9 and 27 meV. In fact, the real range may be slightly broader. We thus expect that in a spectrum obtained at 12 meV the major peaks will correspond to dissociation of the $N' = 13$ and 15 levels (see Table III), with the further possibility of observing $N' = 17$ levels dissociating to the $^3P_1$ limit and $N' = 19$ levels to the $^3P_0$. Figure 7 shows a portion of the $W = 12$ spectrum for the (4, 4) band, with calculated transitions indicated at the top of the figure. Clearly, the observed spectrum is well explained by dissociations from $N' = 13$, 15, and 17 levels. Three very small peaks, labeled *a*, *d* and *f*, do not correspond to any transition terminating in $N' = 13$, 15, 17, or 19.

In a similar manner, a spectrum obtained for a nominal $W = 25$ meV should yield photofragments between 21 and 41 meV, yielding possible N' levels 15, 17, and probably 19 to $^3P_2$, 19 and 21 to $^3P_1$, and 21 to $^3P_0$. In fact, peaks are observed corresponding to all of these N' levels, as is shown in Fig. 8. Again, small peaks are observed which do not correlate with any of the predicted transitions. They are labeled a–e in the figure. The peaks a and d are in the same locations as the peaks so labeled in the $W = 12$ meV spectrum. The peak labeled *f* in that spectrum also appears here, but may be accounted for by a P_{21}, Q_{11} ($N' = 21$, $^3P_0$) transition.

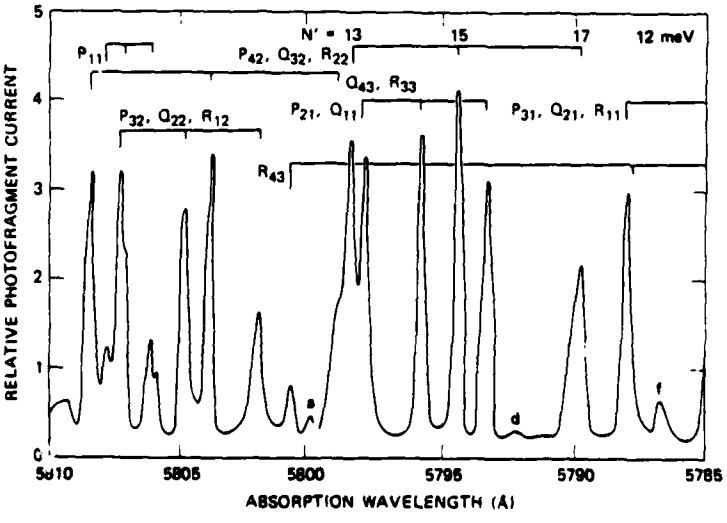

FIG. 7. A portion of the O_2^+ $(b, v' = 4 - a, v'' = 4)$ band obtained with the energy analyzer set for $W = 12$ meV.

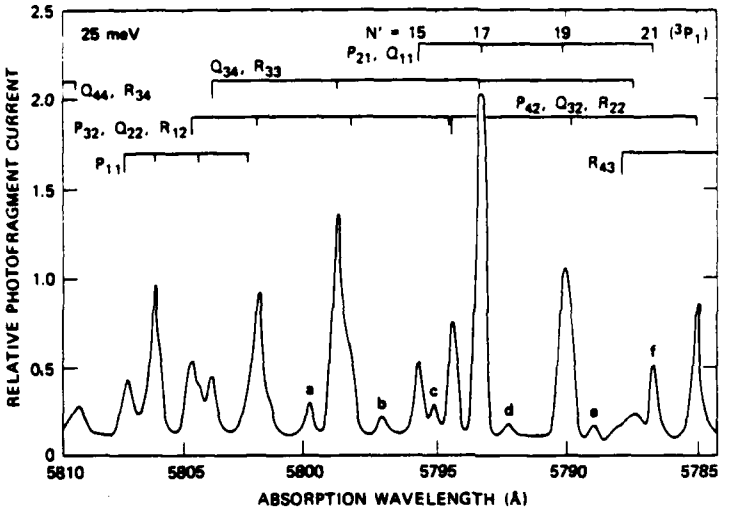

FIG. 8. A portion of the O_2^+ ($b, v' = 4 \leftarrow a, v'' = 4$) band obtained for $W = 25$ meV.

Figure 9 shows a $W = 50$ meV spectrum, which should yield photofragments between 45 and 67 meV. This would allow N' levels 19, 21, and probably 23 to $^3P_2$, 23 and 25 to $^3P_1$, and 25 to $^3P_0$. Again, peaks are observed corresponding to all of these N' levels, with the possible exception of $N' = 25$, which is inconclusive. All of the peaks labeled a–f in the previous spectra are seen to correspond reasonably well with transitions indicated here, with the exception of peak e. Apparently the apparatus can detect a small fraction of the photofragments with separation energies as large as 55 meV when adjusted for a nominal W of 12 meV. Obviously, the efficiency for transmission of these higher energy photofragments is much lower then for photofragments in the expected 9–27 meV range.

D. Lifetimes of the predissociated levels

We have previously demonstrated[12] the capability of our apparatus to obtain much higher resolution than that of the spectra in Figs. 2 and 7–9, using a single-mode laser coaxial with the ion beam. Rather than fine tuning the laser by conventional techniques, the absorption wavelength is tuned by varying the ion beam velocity.[9–12] A spectrum obtained in this way is shown in Fig. 10, where the three components of the peak labeled P_{44}, Q_{34}, R_{24} ($N' = 9$) of Fig. 2 are resolved. Thus the lines normally blended[15] in even high-resolution optical spectroscopy (see Table I) are easily resolved. Measurement of the absolute transition energies to a higher accuracy than the optical data (0.03 cm^{-1}) is difficult,

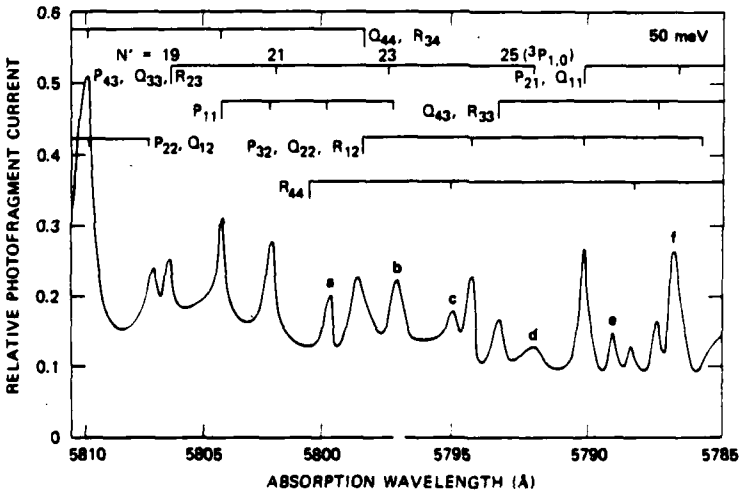

FIG. 9. A portion of the O_2^+ ($b, v' = 4 \leftarrow a, v'' = 4$) band obtained for $W = 50$ meV.

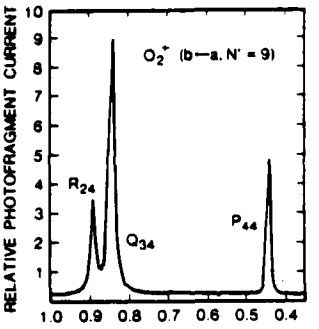

FIG. 10. Velocity-tuned spectrum obtained with a single mode laser coaxial with the ion beam. The three components of the peak labeled P_{44}, Q_{34}, R_{24} ($N' = 9$) of Fig. 2 are resolved.

but in principle possible. The locations of the transitions relative to each other can be measured to about 0.003 cm^{-1}. The relative intensities of the lines can also be measured and compared with calculations.[24] It is thus possible to do a very high resolution study of the predissociated levels of $O_2^+(b\ ^4\Sigma_g^-)$ and better determine the molecular constants for this state as well as learn more about the predissociation process. Such a detailed study is currently underway.

One feature of these high-resolution results is relatively easy to interpret. The widths of the peaks in spectra such as Fig. 10 yield information on the lifetimes of the predissociated levels, assuming the linewidth is not dominated by the Doppler width of the ions in the beam or by the effects of angular divergence of the beam. For an ion beam energy spread of 2.5 eV, the Doppler width is 120 MHz and for our apparatus the angular divergence adds about 20 MHz to the width. In the spectrum, the R_{24} and Q_{34} peaks are about 460 MHz wide, while the P_{44} peak is about 300 MHz wide, clearly demonstrating that the linewidths are not dominated by the instrumental width. Measurements on a number of transitions corresponding to $N' = 9$, 11, 13, and 15 yield linewidths between 450 and 480 MHz for the dissociation of F_2' and F_3' levels, and between 250 and 350 MHz for F_1' and F_4' levels. No strong dependence on N' is observed. After an approximate correction for the instrumental width, we obtain lifetimes of $(70 \pm 15) \times 10^{-11}$ sec for the F_1' and F_4' levels, and $(42 \pm 8) \times 10^{-11}$ sec for the F_2' and F_3' levels. The ratio of these lifetimes was consistently 1.5 or greater. These lifetimes are in excellent agreement with those obtained by Carrington, Roberts, and Sarre[9(b)] for the same dissociating levels by observing the (4, 1) band in an experiment very similar to the one reported here. They are also consistent with the upper limit of 50 nsec by Guyon *et al.*[13] The much longer lifetimes (1.35 to 2 μsec) obtained by Erman and Larsson[14] do not seem to apply to these predissociated levels, although such a lifetime would be very reasonable for the nonpredissociated levels ($N' < 9$). Predissociation lifetime measurements are needed on the $v' = 5$, 6, and 7 levels for further comparison with Ermann and Larsson's measurements.

E. The (5,5) band

Figure 11 shows a part of the spectrum obtained for $W = 100$ meV. From the model of the apparatus collection efficiency, photofragments with energies between 92 and 120 meV should be observable in this spectrum. In this energy range, photofragments can be produced from two bands:

$$O_2^+(a, v'' = 4) - O_2^+(b, v' = 4, N'),\ 27 \le N' \le 31,$$

or

$$O_2^+(a, v'' = 5) - O_2^+(b, v' = 5, N'),\ 3 \le N' \le 13.$$

Two arguments favor the (5, 5) band. First, a reasonable rotational temperature would not result in significant population of the J'' levels which can undergo transitions to the $N' = 27$ to 31 levels. At 300° the most

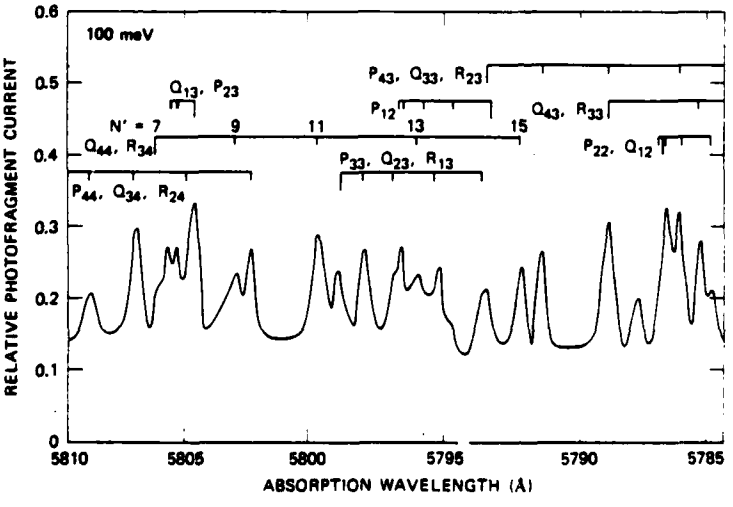

FIG. 11. A portion of the O_2^+ $(b, v' = 5 - a, v'' = 5)$ band obtained for $W = 100$ meV.

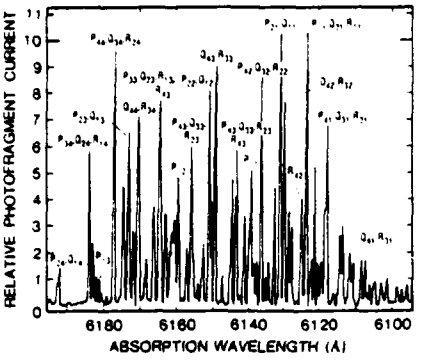

FIG. 12. Predissociation photofragment spectrum for O_2^+ obtained for $W = 0$ from 6195 to 6095 Å. The noted transitions are for $O_2^+(b, v' = 4 - a, v'' = 5, N' = 9)$, calculated as discussed in the text.

probable J'' is 11. More definitively, the calculated transitions for the (4, 4) band do not agree well with the observed peaks, while those for the (5, 5) band do agree. Calculations of the (5, 5) transitions are shown on Fig. 11. To explain all of the observed peaks, it is necessary to consider also the $N' = 15$ level of this band, but we have already seen that the apparatus detects photofragments with slightly higher energy than predicted by the model. The $N' = 3$ and 5 levels were not calculated, but do not appear to be necessary to explain the observed structure. The corresponding rotational levels of the a state would not be expected to be strongly populated.

F. Other bands

In addition to the (4, 4) band, which has been discussed in detail, and the (5, 5) band (Fig. 11), which has been more briefly considered, the (4, 3) and (4, 5) bands were also observed for $W = 0$. The (4, 5) band, with the peaks corresponding to $N' = 9$ identified, is shown in Fig. 12. This figure and Fig. 2 are very similar, as expected, and the same branches are observed. Similar results were obtained for the (4, 3) band. As previously discussed, Carrington *et al.*[9] have studied this predissociation in the (4, 1) band.

IV. CONCLUSIONS

The predissociation of O_2^+ observed in the 5750 to 5870 Å region is due primarily to the (4, 4) and (5, 5) bands of the first-negative system $b\,^4\Sigma_g^- - a\,^4\Pi_u$. The predissociation in the 6090 to 6210 Å region is similarly due to the (4, 5) and probably (5, 6) bands of this same electronic transitions, and that in the 5430 to 5550 Å region to the (4, 3) and probably (5, 4). Thus the earlier identification[8] of this predissociation with the transition $f\,^4\Pi_g - a\,^4\Pi_u$ was incorrect. In this same wavelength range the direct dissociation via the f state is also significant.

Measurement of the kinetic energy of photofragments from the $(v' = 4, N' = 9)$ level located the rotational and vibrational levels of the $b\,^4\Sigma_g^-$ state with respect to the $O(^3P_2) + O^+(^4S^0)$ dissociation limit to higher accuracy than previous optical spectroscopy results, leading to improved dissociation energies for this state, the $a\,^4\Pi_u$, and, as previously reported,[18] $O_2(X\,^3\Sigma_g^-)$.

A single mode laser and velocity tuning were used to resolve the fine structure components of some of the observed transitions in the (4, 4) band. From the widths of these peaks, lifetimes of $(70 \pm 15) \times 10^{-11}$ sec were determined for the F_1' and F_4' components, and of $(42 \pm 8) \times 10^{-11}$ sec for the F_2' and F_3', with the lifetimes of the F_1' and F_4' components at least 1.5 times greater than the lifetimes of the F_2' and F_3' components.

ACKNOWLEDGMENTS

The authors gratefully acknowledge valuable discussions with D. L. Albritton, Jean Durup, J. R. Peterson, and Joëlle Rostas, and the assistance of Jean-Bernard Ozenne in obtaining the velocity tuned spectra.

[1] Y. Tanaka and T. Takamine, Sci. Pap. Inst. Phys. Chem. Res. Tokyo 39, 437 (1942).
[2] T. E. Nevin, Philos. Trans. R. Soc. London Ser. A 237, 471 (1938); Proc. R. Soc. London, Ser. A 174, 371 (1940); T. E. Nevin and T. Murphy, Proc. R. Ir. Acad. Sect. A 46, 169 (1941).
[3] S. Weniger, J. Phys. Radium 23, 225 (1962).
[4] P. H. Krupenie, J. Phys Chem. Ref. Data 1, 423 (1972).
[5] W. Lindinger, D. L. Albritton, M. McFarland, F. L. Fehsenfeld, A. L. Schmeltekopf, and E. E. Ferguson, J. Chem. Phys. 62, 4101 (1975).
[6] A. Tabché-Fouhaillé, J. Durup, J. T. Moseley, J.-B. Ozenne, C. Pernot, and M. Tadjeddine, Chem. Phys. 17, 81 (1976).
[7] N. H. F. Beebe, E. W. Thulstrup, and A. Andersen, J. Chem. Phys. 64, 2080 (1976).
[8] J. T. Moseley, M. Tadjeddine, J. Durup, J.-B. Ozenne, C. Pernot, and A. Tabché-Fouhaillé, Phys. Rev. Lett. 37, 891 (1976).
[9] A. Carrington, P. G. Roberts, and P. J. Sarre, Mol. Phys. 34, 291 (1977); Mol. Phys. (submitted).
[10] S. L. Kaufman, Opt. Commun. 17, 309 (1976).
[11] W. H. Wing, G. A. Ruff, W. E. Lamb, Jr., and J. J. Spezeski, Phys. Rev. Lett. 36, 1488 (1976).
[12] B. A. Huber, T. M. Miller, P. C. Cosby, H. D. Zeman, R. L. Leon, J. T. Moseley, and J. R. Peterson, Rev. Sci. Instrum. 48, 1306 (1977).
[13] P. M. Guyon, T. Baer, L. F. A. Ferreira, I. Nenner, A. Tabché-Fouhaillé, R. Botter, and T. R. Govers, J. Phys. B (submitted for publication).
[14] P. Erman and M. Larsson, Physica Scripta (in press).
[15] D. L. Albritton, A. L. Schmeltekopf, W. J. Harrop, R. N. Zare, and J. Czarny, J. Mol. Spectrosc. 67, 157 (1977).
[16] J. T. Moseley, R. P. Saxon, B. A. Huber, P. C. Cosby, R. Abouaf, and M. Tadjeddine, J. Chem. Phys. 67, 1659 (1977).
[17] H. D. Zeman, Rev. Sci. Instrum. 48, 1079 (1977).
[18] D. L. Albritton, J. T. Moseley, P. C. Cosby, and M. Tadjeddine, J. Mol. Spec. 70, 326 (1978).
[19] C. E. Moore, "Selected Tables of Atomic Spectra, Atomic Energy Levels and Multiplet Tables, VI," Natl. NSROS-NBS 3, Sec. 7, U. S. Govern nent Printing Office, Washington, D. C. (1976).
[20] P. Brix and G. Herzberg, Can. J. Phys. 32, 110 (1954).
[21] K. Yoshino and Y. Tanaka, J. Chem. Phys. 48, 4859 (1968).

[32]J.-B. Ozenne, J. Durup, R. W. Odom, C. Pernot, A. Tabché-Fouhaillé, and M. Tadjeddine, Chem. Phys. 16, 17 (1976), and references therein; N. P. F. B. van Asselt, J. G. Mass, and J. Los, Chem. Phys. 11, 253 (1975), and references therein.

[33]R. N. Zare and D. R. Herschback, Proc. IEEE 51, 173 (1963); R. N. Zare, Ph. D. thesis, Harvard University (1964); Mol. Photochem. 4, 1 (1972).

[34]A. M. Lambert, J. P. Goure, and D. L. Albritton, Can. J. Phys. 55, 1842 (1977).

APPENDIX B

Predissociation lifetimes of the rotational and fine structure levels of $O_2^+(b\,^4\Sigma_g^-, v=3,4,5)$

J. T. Moseley and P. C. Cosby

Molecular Physics Laboratory, SRI International, Menlo Park, California 94025

J.-B. Ozenne[a] and J. Durup

Laboratoire des Collisions Atomiques et Moleculaires, [b]
Universite de Paris-Sud, 91405 Orsay, France
(Received 30 August 1978)

A fast ion beam coaxial with a single mode laser has been used to measure the absorption linewidths of predissociated levels of $O_2^+(b\,^4\Sigma_g^-, v=3,4,5)$ by detection of the O^+ photofragments. Tuning of the absorption wavelength was accomplished by a combination of intracavity etalons and variation of the ion beam velocity (Doppler tuning). Lifetimes were determined for the b state fine structure levels of rotational levels $N=31$ and 33 of $^{16}O_2^+(v=3)$, $N=9$–25 of $^{16}O_2^+(v=4)$, $N=14$–27 of $^{16}{}^{18}O_2^+(v=4)$, and $N=5$–7 of $^{16}O_2^+(v=5)$. The lifetimes vary from 0.06 to 4 nsec. Variation with all relevant quantum numbers and with isotopic composition is discussed.

I. INTRODUCTION

Photodissociations in the lowest-lying quartet system of O_2^+ have been the subject of substantial recent study since the demonstration that the metastable $a\,^4\Pi_u$ state could be photodissociated by transitions to the repulsive part of the $f\,^4\Pi_g$ state,[1] and that a highly structured predissociation could also be observed.[2] The four potential curves relevant to these photodissociations are shown in Fig. 1. The direct dissociation to the $f\,^4\Pi_g$ state is indicated by transition I in this figure. Carrington, Roberts, and Sarre[3] identified the predissociation as due to transitions *from* the $a\,^4\Pi_u$ state to the $v=4$ level *of* $b\,^4\Sigma_g^-$, where rotational levels $N'=9$ or greater are predissociated. These transitions are indicated by II in Fig. 1. The first observation that O_2^+ could be photodissociated at visible wavelengths was made by Vestal, Mauclaire, and Futrell,[4] although this work did not include an identification of the states involved.

Tadjeddine, Abouaf, Cosby, Huber, and Moseley[5] made a detailed investigation of the (4, 4) band of transition II, and a less detailed study of the (5, 5), (4, 5) and (4, 3) bands, all at 0.2 Å resolution. This resolution was sufficient to resolve 24 of the possible 48 branches in each of these bands, and to confirm the identifications[3,6] of the predissociated levels. Direct measurement of the photofragment kinetic energies also allowed improved determination of the $O_2^+(a\,^4\Pi_u)$, $O_2^+(b\,^4\Sigma_g^-)$, and $O_2(X\,^3\Sigma_g^-)^7$ bond energies.

Investigations into the lifetimes of the predissociated levels quickly followed. Guyon *et al.*,[6] using a synchrotron radiation photon source to photoionize O_2, observed the predissociation of both the $b\,^4\Sigma_g^-$ and the higher-lying $c\,^4\Sigma_g^-$ state, and set an upper limit on the lifetimes of the predissociated levels of 50 nsec. On the other hand, Erman and Larson[8] observed the first negative emission $O_2^+(a-b)$ induced by electron impact on O_2, and found lifetimes which increased smoothly from 1.35 μsec for $v'=0$ to 2 μsec for $v'=7$. However, a recent re-evaluation of the data (private communication) showed that all observed emissions corresponded to vibrational levels $v'=0$–3.

In a recent work,[9] Carrington, Roberts, and Sarre were able to measure the linewidths for 13 levels of $v'=4$, using a technique similar to that to be described in detail here. They obtained lifetimes of the F_1' and F_4' levels of about 0.6 nsec, and of the F_3' levels of about 0.4 nsec, and suggested that the major contribution to the predissociation was made by the $^4\Sigma_g^+$ state. Tadjeddine *et al.*,[5] in work preliminary to that reported here, obtained lifetimes of (0.70 ± 0.15) nsec for F_1' and F_4' levels, and of (0.42 ± 0.08) nsec for F_2' and F_3' levels. However, in neither of these works were a sufficient number of transitions studied to allow a more detailed investigation of the variation of the lifetimes with the various quantum numbers involved, nor were the lifetimes of the $v=5$ levels or of isotopic O_2^+ studied.

The purpose of the work reported here is to provide a much more extensive data set upon which a detailed study of this predissociation can be based. To this end, over 1000 transitions have been studied, involving vibrational levels 3, 4, and 5, rotational levels between 5 and 33, and both normal and isotopic O_2^+. A first attempt at interpretation of the results is also made, which is in some cases definitive while in others only qualitative or suggestive.

II. EXPERIMENTAL PROCEDURES

The apparatus used to obtain the data reported here has been described in detail elsewhere,[10] as has its application to the normal photofragment spectroscopy of Ar_2^+[11] and Kr_2^+,[12] and to the predissociation photofragment spectroscopy of O_2^+.[5] The specific type of experiment reported here is discussed in Ref. 10, Sec. III. A, and in Ref. 5, Sec. III. D.

Briefly, a single-mode tunable dye laser, pumped by an Ar or Kr ion laser, is made coaxial with a fast beam

[a] International Fellow at SRI International, 1977–78 academic year.

[b] Associated with the Centre National de la Recherche Scientifique.

 0021-9606/79/031474-08$01.00

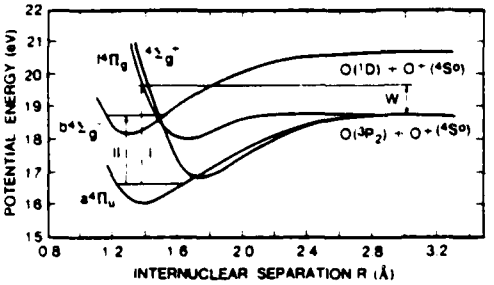

FIG. 1. The lowest-lying quartet potential curves of O_2^+.

of O_2^+ over an interaction length of about 30 cm. The O_2^+ is formed in a hollow cathode discharge source, accelerated to 3600 eV, and collimated to 2 mrad before being bent into the interaction region. In this region, the beams are surrounded by an electrostatic cage which can accelerate or decelerate the ion beam, thus using the Doppler shift to tune the absorption wavelength in the ion center-of-mass frame. If an absorption occurs which results in a photodissociation, the O^+ photofragment can be detected after passing through an energy analyzer.

The ability to obtain linewidths that are substantially more narrow than a Doppler-broadened line at room temperature arises from the narrowing of the velocity distribution in an ion beam when it is accelerated. This effect has been discussed[13] and exploited[2,3,5,14–16] by a number of researchers in the past three years. The velocity narrowing arises very simply from the fact that a population of ions with an energy spread ΔE which is extracted from an ion source and accelerated to an energy E maintains this energy spread ΔE; however, since $E = \frac{1}{2}mv^2$, the velocity spread at an energy $E \gg \Delta E$ is substantially reduced from its value before acceleration. In fact, an ion beam with a 1 eV energy spread has at 3 keV laboratory energy a velocity spread corresponding to less than 1 °K.

The experimental data are obtained in the following way: A beam of O_2^+ ions is established at an energy of 3600 eV. The single-mode laser is tuned by tilting its etalons until its Doppler-shifted frequency is in the vicinity of one of the absorptions already studied in detail[5] at lower resolution (0.2 Å). The velocity of the beam is then scanned by varying the potential on the electrostatic cage. As the absorption wavelength is Doppler tuned into resonance with a transition, photofragment ions appear at the energy analyzer. If the energy analyzer is set to pass ions of the energy of these photofragments, counts are observed at the detector.

A typical scan is shown in Fig. 2. Such a scan, which covers about 0.5 cm^{-1}, required a variation in the ion beam energy of approximately 500 eV. The kinetic energy (and hence absorption wavelength) scan is controlled by a multichannel scaler, and thus each channel of the scaler corresponds to a specific absorption wavelength. The wave number listed at the center of Fig. 2 is that of the single-mode laser beam. The abscissa of Fig. 2 gives the Doppler shift from that value due to the ion velocity. The absolute value of the wavelength was determined[17] using a digital wavemeter interferometer[18] to an accuracy of 0.003 cm^{-1}.

The designations of the peaks give the values of the relevant quantum numbers, except for vibrational level, which was $v' = 4$ here. These quantum numbers will be defined in the following section. The identification of the peaks was made using calculations based on the O_2^+ molecular constants of Albritton, Schmeltekopf, Harrop, Zare, and Czarny,[19] as previously described.[5] A detailed description of this identification, the determination of precise transition energies (±0.003 cm^{-1}) for the (4, 4), (4, 5), and (5, 5) bands of O_2^+, and the improvement in the Hamiltonian description of the $a\,^4\Pi_u$ and $b\,^4\Sigma_g^-$ states have been submitted for publication.[17]

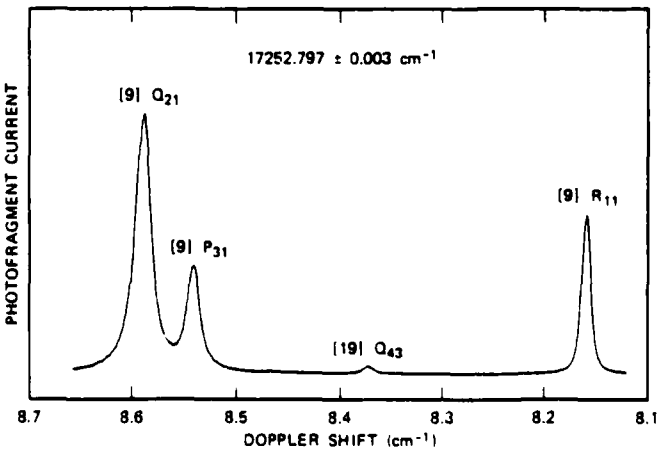

FIG. 2. Typical wavelength (velocity) scan for the band $O_2^+(a\,^4\Pi_u, v'' = 4) \rightarrow O_2^+(b\,^4\Sigma_g^-, v' = 4) \rightarrow O^+ + O$.

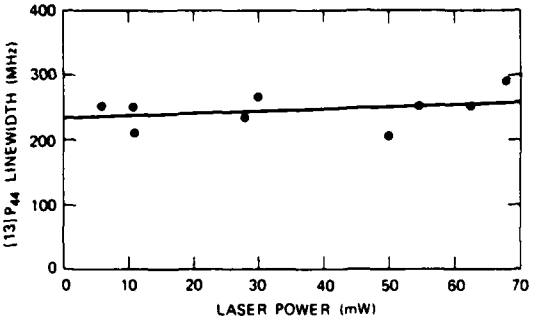

FIG. 3. Dependence on laser power of the observed linewidth for the $[13]P_{44}$ transition.

The fact that the peaks in Fig. 2 have different widths indicates that the linewidths are not dominated by the apparatus-induced Doppler width, but contain information about the natural lifetime of the levels. The Doppler contribution to the linewidths arises from three sources; the velocity spread in the ion beam, the angular divergence between the ion beam and laser in the interaction region, and the jitter of the single-mode laser. These contributions can be calculated from measured experimental parameters.

Another factor which can lead to broadening of the peaks, but is neither Doppler nor Lorentzian in character, is saturation of a transition, and power broadening. Carrington, Roberts, and Sarre observed[9] broadening at laser powers around 1 W, and obtained the lines used to determine lifetimes at laser powers low enough that this broadening was stated to be eliminated. We have investigated this broadening in two ways.

The most obvious type of investigation is to measure the width of a line resulting from a given transition as a function of laser power. Such a measurement for the $[13]P_{44}$ line is shown in Fig. 3. The solid line is a least-squares fit to these points. The power dependence for this line is seen to be very small, and data obtained at laser powers below 20 mW should yield good linewidths for this transition.

The $[13]P_{44}$ line has a relative line strength of 4.5, as calculated for us by D. L. Albritton. Line strengths for the transitions used in this research varied from about 0.1 to 40. Clearly, the stronger lines will be susceptible to saturation at lower laser powers. An alternative way to investigate this effect is to access a given predissociated level with transitions of varying strength, using fixed laser power. An example of such an investigation for a laser power of (15 ± 5) mW is given in Fig. 4. The triangles are linewidths measured for the $(v'=4,\ N'=14,\ F_1')$ level of the b state of $^{16,18}O_2^+$ accessed by a large number of transitions of widely varying strength. The circles are linewidths measured similarly for the $(v'=4,\ N'=9, F_1')$ level of the b state. The solid and dashed lines are least-squares fits to these points, respectively.

Clearly, there is a weak dependence on transition strength. The average of the linewidths measured for the $N'=14$ level is 223 MHz, while the least-squares fit extrapolates to 213 MHz at zero line strength. Similarly, the average for the $N'=9$ level is 297 MHz, while the extrapolated value is 287 MHz. This effect was noted for other levels where sufficient data were taken to justify such an analysis, and the extrapolated values were $(4 \pm 2)\%$ lower than the simple averages. Thus, for other levels where sufficient data did not exist to make a least squares fit, the average values were simply reduced by 4%.

The contribution due to the velocity spread in the beam can be written

$$\frac{\Delta\nu}{\nu} = \frac{2\Delta v}{c} = 2.317\times10^{-5}\,\frac{\Delta E}{\sqrt{mE}}\ , \qquad (1)$$

where $\Delta\nu$ is the Doppler linewidth for a line at frequency ν due to a velocity spread Δv caused by an energy spread ΔE. The ion beam energy spread can be determined by direct measurement with the energy analyzer. Since the analyzer has a resolution of 0.3%[10] of the transmitted ion energy, a most accurate value will be obtained by measuring the energy distribution of the ions over a range of energies, and extrapolating the full widths at half-maximum to zero transmission energy. Such a procedure, for the ion beam transmission energy varied from 83 to 883 eV, yields (1.55 ± 0.20) eV for the ion beam energy spread. Thus, $\Delta\nu$ for a 3600 eV beam and $\nu = 17\,200$ cm^{-1} has the value 0.0018 cm^{-1}, or 54 MHz.

The effect of the angular divergence, equivalent to the fact that the ion and laser beams are not necessarily precisely coaxial, can be similarly calculated using

$$\frac{\Delta\nu}{\nu} = \frac{\Delta v(\theta)}{c} = \frac{v\theta^2}{2c} = 2.317\times10^{-5}\,\theta^2\sqrt{E/m}\ , \qquad (2)$$

where θ is the angle between the ion and laser beams. For the geometry of the interaction region, θ has a maximum value of 1.3×10^{-2} rad, and is probably substantially smaller than this. Thus, $\Delta\nu$ from this broadening is at most 0.0005 cm^{-1}, or 15 MHz.

The jitter in the single-mode laser can be observed directly using a spectrum analyzer. During the time

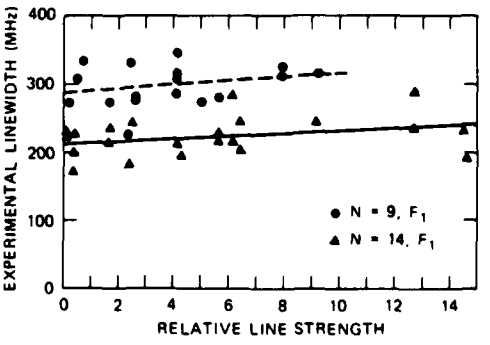

FIG. 4. Dependence on transition strength of the observed linewidths of the F_1 levels for $N=9$ ($^{16}O_2^+$) and for $N=14$ ($^{16,18}O_2^+$).

required to make a wavelength scan, about 1 min, the jitter was typically ±25 MHz.

The total apparatus-induced Doppler width obtained by simply adding these three contributions is 119 MHz; taking the square root of the sum of the squares yields 75 MHz. Thus, a Doppler width of 100 ± 20 MHz is appropriate for analysis of these linewidths.

A confirmation of this value for the Doppler width was given by a peak observed near 17 234 cm^{-1}. This peak, which arises from rotational level $N' = 31$ of the (3, 3) band, has a average width of 118 MHz, and in one measurement the observed width was 100 MHz. Observation of linewidths as small as 100 MHz sets this value as an upper limit on the apparatus-induced Doppler width. The analysis presented above shows that this width is surely not much less than 100 MHz.

It should be pointed out that it would not be overly difficult to substantially decrease this Doppler width. Actively stabilized dye lasers routinely attain linewidths of 10 MHz or less for extended periods. Reducing the ion beam energy spread to 0.5 eV, a value typical of electron impact sources, would reduce the velocity spread contribution to 18 MHz. Thus, Doppler widths in the range of 25 MHz should be attainable with reasonable effort, and lifetimes as long as 10 nsec should be measurable. The Doppler width of 100 MHz was sufficient in the present research, but a smaller Doppler width would have improved the precision of the measurements, particularly for the $v' = 3$ levels.

The observed lines are assumed to have a Voigt line shape, which is a convolution of Doppler and Lorentzian profiles. Numerical analysis of Voigt line shapes has been extensively studied.[20] The Lorentzian linewidth can be conveniently obtained from a Voigt profile when the width of the Doppler contribution is known by using the tabulated results of the Voigt line shapes given by Watson and Yin.[21] This was the procedure followed here.

TABLE I. Lifetimes, in units of 10^{-12} sec, of the rotational and fine structure levels of the fourth vibrational level of the $b\,^4\Sigma_g^-$ state of $^{16}O_2^+$.

N	F_1	F_2	F_3	F_4
9	635 ± 43	385 ± 27	413 ± 34	712 ± 52
11	656 ± 90	375 ± 40	405 ± 46	724 ± 120
13	702 ± 59	356 ± 29	392 ± 33	814 ± 75
15	696 ± 87	351 ± 31	334	694 ± 95
17	744	337	305	835
19	782	318	336	767
21	748	364	···	721
23	667	···	···	···
25	627	···	···	···
Ref. [a]	673 ± 65	364 ± 28	403 ± 31	···

[a] These values are for the $[9|R_{11}$, $[9|Q_{21}$, and $[9|P_{31}$ reference lines mentioned in the text.

III. RESULTS

Each line measured in this research is due to a transition which has several quantum numbers associated with it. The purpose of this research is to investigate the dependence of the lifetimes on those quantum numbers which apply to the dissociating state. From this point on in this paper, the transition which accessed the dissociating level is irrelevant, and all quantum numbers discussed refer to the dissociating state. Thus, symbols will no longer be primed. For each vibrational level v studied, dissociations are observed from a number of rotational levels N. Each rotational level is, for this quartet state, split into four fine structure levels F_1 to F_4. For $^{16}O_2^+$, the symmetry rules dictate that only odd-valued N levels are present, while for $^{16,18}O_2^+$, all N values are present. Further, the location of levels of the same quantum numbers will be different for normal and isotopic O_2^+. Thus, a predissociating level is uniquely identified by the specification of v, N, F_i, and isotopic composition.

Each predissociating level can, however, be accessed by transitions from a large number of lower levels. In the designation of the peaks of Fig. 2, the letter Q or (P, R) designates $\Delta J = 0$ or ∓1, the first subscript i designates F_i for the upper $^4\Sigma_g^-$ state, and the second subscript j designates the fine structure level[5] $^4\Pi_{(7/2)-j}$ of the lower $^4\Pi_u$ state. The value in brackets is N of the upper state. The vibrational level must be determined from a statement of the band, e.g., (4, 5) designates $v = 4$ for the upper state, $v = 5$ for the lower. The isotopic composition must be separately stated. A more detailed description of the structure of these O_2^+ first negative bands may be found in Refs. 5 and 19.

Table I gives the lifetimes for the rotational and fine structure levels for $v = 4$ of the b state for normal O_2^+. These lifetimes were obtained using both the (4, 4) and (4, 5) bands. For the $N = 9$–15 levels, a sufficiently large number of transitions to each fine structure level was observed, typically more than 20, to warrant calculation of the standard deviation of these observations. In addition, a set of reference lines for the (4, 4) band $[9|R_{11}$, $[9|Q_{21}$, and $[9|P_{31}$ were used throughout the research, with over 50 observations made on each, as a check on the wavelength and ion beam energy calibration. The lifetimes obtained from these lines are listed separately in Table I.

Table II gives the lifetimes for the rotational and fine structure levels of $v = 4$ for $^{16,18}O_2^+$. Again, the lifetimes were obtained using both the (4, 4) and (4, 5) bands, and standard deviations are given where a sufficiently large number of measurements were made on a level to warrant it.

Table III gives the lifetimes for the rotational and fine structure levels of $v = 5$ for $^{16}O_2^+$. These lifetimes were obtained using the (5, 5) band, and the total investigation included only 45 lines. Thus, standard deviations are not given for any of the lifetimes. However, the data are quite consistent, and show less scatter than do the much more extensive investigations of the $v = 4$ levels. This is due to the fact that the linewidths are much

TABLE II. Lifetimes, in units of 10^{-12} sec, of the rotational and fine structure levels of the fourth vibrational level of the $b\,^4\Sigma_g^-$ state of $^{16,18}O_2^+$.

N	F_1	F_2	F_3	F_4
14	956 ± 160	580 ± 43	562 ± 52	1135 ± 143
15	915 ± 71	480	459	871 ± 90
16	923 ± 110	534	575	1019 ± 135
17	912 ± 107	464	575	728
18	877 ± 115	481	484	835
19	882 ± 110	498	584	979
20	814	464	491	877
21	1030	···	···	877
22	902	···	···	877
23	800	···	···	815
24	800	···	···	···
25	912	···	···	···
26	814	···	···	···
27	800	···	···	···

broader (1000 to 2000 MHz) and thus the experimental broadenings are much less significant. In fact, the correction to the Voigt linewidth for a 100 MHz Doppler contribution at 1500 MHz is only about 5 MHz.

Table IV gives the lifetimes observed for the $N=31$ and 33 levels of $v=3$. The uncertainty in the lifetime of the single F_1 level studied is high, since the observed average linewidth of 118 MHz is very close to the instrumental Doppler width. The uncertainties in the F_2 and F_3 values are $\pm 500\times10^{-12}$ sec. Measurement of the kinetic energy spectrum of photofragments dissociating from these levels established[17] that $N=31$ is the lowest rotational level of $v=3$ that is predissociated.

IV. INTERPRETATION OF RESULTS

The results presented in the preceding section are in agreement with, and substantially extend, the previous results of Carrington *et al.*,[9] and of Tadjeddine *et al.*[5] These results also generally substantiate the conclusions of Carrington *et al.*, which are summarized below. The only predissociations which have reasonable Franck–Condon factors are $b\,^4\Sigma_g^- - f\,^4\Pi_g$ and $b\,^4\Sigma_g^- - {}^4\Sigma_g^+$. The linewidth for predissociation by $f\,^4\Pi_g$ should be independent of the fine structure if due to rotational coupling, while it should be larger for F_1 and F_4 than for F_2 and F_3 by a factor 1.5 if due to spin–orbit coupling. The linewidth for predissociation by $^4\Sigma_g^+$, which can occur only by spin–orbit coupling, should be larger for F_2 and F_3 than for F_1 and F_4 by a factor 2.5, which is in better agreement with their data, where the ratio of linewidths was observed to be about 1.7, favoring F_2 and F_3. Thus, Carrington *et al.* concluded "It seems, therefore, that the major contribution to predissociation is made by the $^4\Sigma_g^+$ state in the energy region covered by our study."

TABLE III. Lifetimes, in units of 10^{-12} sec, of the rotational and fine structure levels of the fifth vibrational level of the $b\,^4\Sigma_g^-$ state of $^{16}O_2^+$.

N	F_1	F_2	F_3	F_4
5	97	66	81	137
7	114	···	92	143
9	109	···	77	125
11	···	51	···	128
13	113	···	···	135
15	132	···	···	117
17	···	67	···	117

TABLE IV. Lifetimes, in units of 10^{-12} sec, of the rotational and fine structure levels of the third vibrational level of the $b\,^4\Sigma_g^-$ state of $^{16}O_2^+$.

N	F_1	F_2	F_3	F_4
31	~4000	1740	1980	···
33	···	1560	1590	···

In following sections, implications of the more extensive results of the present research will be discussed.

A. Lack of variation of the lifetimes with N

Tables I–III clearly demonstrate that there is no substantial change in the lifetimes with N. For example, from Table I, the lifetime is constant to within about 10% over the range of N from 9 to 25. Pure rotational coupling, for which the lifetimes would be inversely proportional to $N(N+1)$, would yield a change by more than a factor of 7 over this range. Thus, rotational coupling can contribute at most a few percent to the observed predissociation, and the primary predissociation mechanism must be spin–orbit coupling.

B. Ratio of lifetimes $\bar{\tau}(F_1, F_4)/\bar{\tau}(F_2, F_3)$

It has been previously observed[5,9] that the mean lifetimes for the F_1 and F_4 levels $\bar{\tau}(F_1, F_4)$ are substantially larger than the mean lifetimes for the F_2 and F_3 levels $\bar{\tau}(F_2, F_3)$ by a factor of about 1.7. The ratios of these lifetimes observed here are listed in Table V. With the exception of the $N=17$ and 19 levels of $v=4$ of normal O_2^+, all of these ratios lie on the range 1.80 ± 0.23. The $v=4$ data for normal O_2^+ show a consistent increase with increasing N, but it is not certain that this is statistically significant. Taking into account the standard deviations of the $N=9$ lifetimes of Table I, one obtains an uncertainty of ±0.25 in this ratio of 1.69. On the other hand, the ratios for isotopic O_2^+ are remarkably consistent over the range $N=14$–20, with a value of 1.74 ± 0.16, and show no apparent trend. It is thus not clear that there is any significant variation in this lifetime ratio with N, v, or isotopic composition, and the ratio 1.8 ± 0.2 will be used for this discussion.

This value of 1.8 is very much higher than the value of about 0.67 expected[9] for predissociation by the $f\,^4\Pi_g$, and much closer to, but still significantly lower than,

TABLE V. Ratios of the lifetimes $\bar{\tau}(F_1, F_2)/\bar{\tau}(F_2, F_3)$ for the $b\,^4\Sigma_g^-$ state of O_2^+.

v	Isotope	N	$\bar{\tau}(F_1, F_2)/\bar{\tau}(F_2, F_3)$
4	16, 16	9	1.69
		11	1.84
		13	2.03
		15	2.03
		17	2.46
		19	2.37
4	16, 18	14	1.83
		15	1.90
		16	1.81
		17	1.58
		18	1.77
		19	1.72
		20	1.77
5	16, 16	5	1.59

the value of about 2.5 expected[9] for predissociation by the $^4\Sigma_g^-$. Carrington *et al.*[9] listed the rates of this predissociation for the various F components; the relative rates k are

$$k(F_1) \propto \frac{3(2N+5)}{2N+3},$$

$$k(F_2) \propto \frac{14N+27}{2N+3}, \tag{3}$$

$$k(F_3) \propto \frac{14N-13}{2N-1},$$

and

$$k(F_4) \propto \frac{3(2N-3)}{2N-1}.$$

Thus, the $\bar{\tau}(F_1, F_2)/\bar{\tau}(F_2, F_3)$ ratio should be within the range 2.33 to 2.35 for N between 9 and 25.

Derivation of expressions (3) from well-established formulas[22] required only the following assumptions: (i) *description of the* $b\,^4\Sigma_g^-$ *state as a pure Hund's case b*; (ii) additivity of the predissociation rates for the transitions from F_2 to F_1 and F_3 or from F_3 to F_2 and F_4. Assumption (ii) is equivalent to also describing the predissociating $^4\Sigma_g^-$ state as a pure Hund's case b. Assumption (i) was verified by making use of the molecular constants derived by Albritton *et al.*[19] It turns out that, in the range of rotational quantum numbers present in our spectra, an "F_3" level for example includes in its wave function a maximum contribution $0.011|F_1\rangle$ (i.e., $J = N + \frac{3}{2}$) contaminating its major $|F_3\rangle$ character (i.e., $J = N - \frac{1}{2}$); the same holds for the other levels. Thus, the description of the $b\,^4\Sigma_g^-$ state as a pure Hund's case b alters the ratio by at most 8×10^{-4}. A similar result is likely to hold for assumption (ii).

The only remaining explanation for the difference between the experimental value of 1.8 ± 0.2 and the values of 0.67 and 2.34 corresponding to dissociation by the $f\,^4\Pi_g$ and $^4\Sigma_g^-$ states, respectively, appears to be that both states are participating in the predissociation of $b\,^4\Sigma_g^-$. A branching ratio of $(78 \pm 10)\%$ dissociation by the $^4\Sigma_g^-$ state to $(22 \pm 10)\%$ dissociation by the $f\,^4\Pi_g$ state would explain the observed ratio $\bar{\tau}(F_1, F_2)/\bar{\tau}(F_2, F_3)$.

It should be noted that such a contribution of the $f\,^4\Pi_g$ state to the predissociation of the ($v = 4$, $N = 9$) level of $b\,^4\Sigma_g^-$ precludes the existence of a significant bump in the $f\,^4\Pi_g$ potential. This level of the b state has been shown[7] to lie no more than 2.2 meV above the $O(^3P) + O^+(^4S^0)$ dissociation limit. The *ab initio* calculations of Beebe, Thulstrup, and Andersen[23] (which did not include spin–orbit coupling) predicted a bump of about 50 meV in this potential curve.

Both the potential curves of the $^4\Sigma_g^-$ and of the $f\,^4\Pi_g$ states cross that of the $b\,^4\Sigma_g^-$ state, according to Beebe *et al.*'s calculations.[23] Thus, large Franck–Condon factors must exist for the predissociation of some vibrational levels of the $b\,^4\Sigma_g^-$ state into each of the predissociation channels. In contrast, electronic factors are comparatively unfavored since both predissociations are forbidden for the dominant electronic configurations of the relevant states at short internuclear distances. More precisely, the dominant configuration of the $b\,^4\Sigma_g^-$ state

$$(1\sigma_g)^2(1\sigma_u)^2(2\sigma_g)^2(2\sigma_u)^2(3\sigma_g)(1\pi_u)^4(1\pi_g)^2,\ ^{4,2}\Sigma_g^-,\ ^2\Delta_g,\ ^2\Sigma_g^+ \tag{4}$$

has no $^4\Sigma_g^+$ term, and therefore cannot be predissociated by any state of $^4\Sigma_g^+$ symmetry, since the $^4\Sigma^- - ^4\Sigma^+$ spin–orbit coupling requires that both states belong to a same electronic configuration including a $\pi\pi^*$ electron pair or vacancy pair. Only two minor configurations of the $b\,^4\Sigma_g^-$ state, namely,[24]

$$(1\sigma_g)^2(1\sigma_u)^2(2\sigma_g)^2(2\sigma_u)^2(1\pi_u)^3(1\pi_g)^3(3\sigma_u),\ ^{4,2,2}(\Delta_g, \Sigma_g^-, \Sigma_g^+) \tag{5}$$

and

$$(1\sigma_g)^2(1\sigma_u)^2(2\sigma_u)^2(3\sigma_g)^2(1\pi_u)^3(1\pi_g)(3\sigma_u),\ ^{4,2,2}(\Delta_g, \Sigma_g^-, \Sigma_g^+), \tag{6}$$

obey this requirement, and thus their $^4\Sigma_g^-$ component can be predissociated by the companion $^4\Sigma_g^+$ component. However, configuration (6) is the dominant contribution[24] to the $^4\Sigma_g^+$ state of interest to us, i.e., to the one connected with the lowest $O^+ + O$ states. This should explain the reasonably fast rate of the $b\,^4\Sigma_g^- - {}^4\Sigma_g^+$ predissociation.

Again, only a minor configuration of the $b\,^4\Sigma_g^-$ state

$$(1\sigma_g)^2(1\sigma_u)^2(2\sigma_g)^2(2\sigma_u)^2(3\sigma_g)(1\pi_u)^2(1\pi_g)^4 \tag{7}$$

is connected with the dominant configuration of the $f\,^4\Pi_g$ state[1]

$$(1\sigma_g)^2(1\sigma_u)^2(2\sigma_g)^2(2\sigma_u)^2(3\sigma_g)^2(1\pi_u)^2(1\pi_g)^3, \tag{8}$$

whereas the dominant configuration of the $b\,^4\Sigma_g^-$ state, configuration (4), is connected with a minor configuration of the $f\,^4\Pi_g$ state

$$(1\sigma_g)^2(1\sigma_u)^2(2\sigma_g)^2(2\sigma_u)^2(3\sigma_g)(1\pi_u)^4(1\pi_g)(4\sigma_g). \tag{9}$$

Terms (7) ($^4\Sigma_g^-$) and (8) ($f\,^4\Pi_g$) as well as terms (4) ($b\ ^{-}$) and (9) ($^4\Pi_g$) are connected both by spin–orbit coupling and by rotational coupling. It is interesting to compare the strengths of these two couplings. The total predissociation rates of the various F components of a $^4\Sigma_g^-$ state into a $^4\Pi_g$ state have been given by Carrington *et al.*[9] (see also Ref. 22, pp. 263–265). They are proportional to

$$k(F_1) \propto \frac{3(4N+5)}{4(2N+3)}\xi^2 + \sqrt{9/2}\,N\xi\eta + N(N+1)\eta^2 ,$$

$$k(F_2) \propto \frac{8N+9}{4(2N+3)}\xi^2 - \sqrt{1/2}\,(N-3)\xi\eta + N(N+1)\eta^2 , \quad (10)$$

$$k(F_3) \propto \frac{8N-1}{4(2N-1)}\xi^2 + \sqrt{1/2}\,(N+4)\xi\eta + N(N+1)\eta^2 ,$$

and

$$k(F_4) \propto \frac{3(4N-1)}{4(2N-1)}\xi^2 + \sqrt{9/2}\,(N+1)\xi\eta + N(N+1)\eta^2 ,$$

where the spin–orbit coupling is determined from the matrix element[22]

$$\xi = \langle {}^4\Sigma_g^- | \sum a_i l_{iz} | {}^4\Pi_g \rangle \quad (11)$$

and the rotational coupling from the matrix element[22]

$$\eta = \langle {}^4\Sigma_g^- | B L_y | {}^4\Pi_g \rangle . \quad (12)$$

Let us consider configurations (7) and (8). Expressions (11) and (12) become

$$\xi = a_g \langle 1\pi_g | l_z | 3\sigma_g \rangle \langle v | \chi \rangle \quad (13)$$

and

$$\eta = \frac{\hbar^2}{2\mu} \langle 1\pi_g | l_y | 3\sigma_g \rangle \langle v | \frac{1}{r^2} | \chi \rangle , \quad (14)$$

respectively, where $|v\rangle$ and $|\chi\rangle$ are the vibrational wave functions of the initial and final states, respectively, and r is the internuclear distance.

By taking $a_g = 191\ \mathrm{cm}^{-1}$ for O_2^+, and approximating $\langle v | 1/r^2 | \chi \rangle$ as $[1/(\bar{r})^2]\langle v | \chi \rangle$, where $\bar{r}$ is the internuclear distance at the potential curve crossing (1.5 Å),[25] we find

$$\frac{\eta}{\xi} = \frac{\hbar^2}{2\mu(\bar{r})^2} = 4.89 \times 10^{-3} . \quad (15)$$

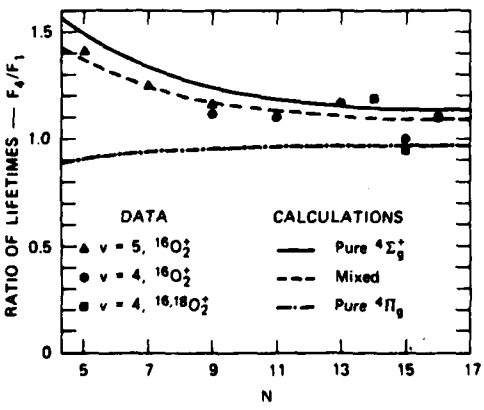

FIG. 5. Dependence of the ratio of lifetimes $\tau(F_4)/\tau(F_1)$ on rotational quantum number N. Data for $v=5$, $^{16}O_2^+$ (▲); for $v=4$, $^{16}O_2^+$ (●); and for $v=4$, $^{16,18}O_2^+$ (■) are included. The smooth curves are calculations for a pure $^4\Sigma_g^-$ dissociation (——), a pure $^4\Pi_g$ (– · – · –) and a mixed 0.78 $^4\Sigma_g^-$/0.22 $^4\Pi_g$ (– – –) as discussed in the text.

Thus, clearly, in Eq. (10) the contribution of rotational predissociation is essentially the cross term. It produces an increase in the rate of predissociation through $f\,{}^4\Pi_g$ of 10% of the F_1 and F_4 levels when N rises from 9 to 25. The effect for the F_2 and F_3 levels is about a factor of 2 smaller. Similar results can be obtained for the case of $b\,{}^4\Sigma_g^- - f\,{}^4\Pi_g$ predissociation through configurations (4) and (9). In this case, the matrix elements (13) and (14) would involve the $4\sigma_g$ orbital in place of $3\sigma_g$.

The preceding analysis shows that the branching ratio for predissociation through $^4\Sigma_g^+$ and $f\,{}^4\Pi_g$ of about 78/22 implies that the total predissociation width should increase by at most a few percent when N increases from 9 to 25. This is in agreement with the results described earlier in this section.

C. Ratios of lifetimes $\tau(F_4)/\tau(F_1)$ and $\tau(F_3)/\tau(F_2)$

Tables I–III show that the lifetimes for the F_1 and F_4 levels, and for the F_2 and F_3 levels, which are nearly equal, consistently have the order $\tau(F_1) < \tau(F_4)$ and $\tau(F_2) < \tau(F_3)$. The expected lifetime ratios can be calculated from expressions (3) and (10) for a pure $^4\Sigma_g^+$ predissociation, or for a mixed predissociation through this and the $f\,{}^4\Pi_g$ state, in the ratio 78/22. Figure 5 presents these calculations and the observed lifetimes for the F_4/F_1 lifetime ratio. The $v=4$ and 5 and the isotopic data are all included on this figure. The results clearly support the interpretation of a primarily $^4\Sigma_g^+$ dissociation. All of the data, however, support the conclusion that $^4\Pi_g$ is participating in the dissociation to a nonnegligible extent.

A similar plot could be made of the F_3/F_2 lifetime ratios. However, it would not be as definitive, since the predicted ratio varies much less over this range of N (only from 1.08 to 1.02), and the data are of poorer quality. However, these lifetime ratios are consistent with the above interpretation.

Now that the general location of the $^4\Sigma_g^+$ state has been clearly evidenced, it is convenient to assign it a conventional letter. We propose the designation $d\,{}^4\Sigma_g^+$ for this state.

D. Lifetime differences for $v = 3$, 4, and 5 levels, and for normal and isotopic O_2^+

The strong similarities of the various ratios of lifetimes for the fine structure levels, independent of v, N, or isotopic composition, shows that the predissociation process is basically the same for $v=4$ and 5, and for normal and isotopic O_2^+. Those differences in lifetimes $\tau[^{16}O_2^+(v=3)] > \tau[^{16,18}O_2^+(v=4)] > \tau[^{18}O_2^+(v=4)] > \tau[^{16}O_2^+(v=5)]$ can be explained by the vibrational overlap integrals for the predissociation. All results are consistent with the classical description of predissociation with curve crossing, provided it is assumed that the crossing takes place at an energy which is closer to the $v=5$ than to the $v=4$ level of the $b\,{}^4\Sigma_g^-$ state of the $^{16}O_2^+$ normal isotope. The crossing may be above or below level $v=5$. Thus, the predissociation rate will be lower for $v=4$ than for $v=5$ in $^{16}O_2^+$, still lower for $^{16}O^{18}O^+$, $v=4$,

whose energy is slightly under that of the normal isotope, and still lower for $^{16}O_2^+$, $v=3$. The influence of quantum number N is of minor importance here, since the crossing point energy is raised with increasing N in the same way as the effective potential curves are. A study of higher vibrational levels could more precisely locate the curve crossing.

ACKNOWLEDGMENTS

The research at SRI was supported by the U.S. Army Research Office and by the National Science Foundation under Grant No. CHE77-00428. JBO wishes to acknowledge an NSF–CNRS Exchange Fellowship. We have benefited from useful discussions with R. N. Zare, D. L. Albritton, A.-L. Roche, and H. Lefebvre-Brion.

[1]A. Tabché-Fouhaillé, J. Durup, J. T. Moseley, J.-B. Ozenne, C. Pernot, and M. Tadjeddine, Chem. Phys. 17, 81 (1976).
[2]J. T. Moseley, M. Tadjeddine, J. Durup, J.-B. Ozenne, C. Pernot, and A. Tabché-Fouhaillé, Phys. Rev. Lett. 37, 891 (1976).
[3]A. Carrington, P. G. Roberts, and P. J. Sarre, Mol. Phys. 34, 291 (1977).
[4]M. Vestal, G. Mauclaire, and J. H. Futnell, 23rd Annual Conference on Mass Spectrometry, Houston, Texas (1975); M. L. Vestal and G. H. Mauclaire, J. Chem. Phys. 67, 3767 (1977).
[5]M. Tadjeddine, R. Abouaf, P. C. Cosby, B. A. Huber, and J. T. Moseley, J. Chem. Phys. 69, 710 (1978).
[6]P. M. Guyon, T. Baer, L. F. A. Ferreira, I. Nenner, A. Tabché-Fouhaillé, R. Botter, and T. R. Govers, J. Phys. B 11, L141 (1978).
[7]D. L. Albritton, J. T. Moseley, P. C. Cosby, and M. Tadjeddine, J. Mol. Spectrosc. 70, 326 (1978).
[8]P. Erman and M. Larsson, Phys. Scr. (in press), and private communication.
[9]A. Carrington, P. G. Roberts, and P. J. Sarre, Mol. Phys. 36, 1523 (1978).
[10]B. A. Huber, T. M. Miller, P. C. Cosby, H. D. Zeman, R. L. Leon, J. T. Moseley, and J. R. Peterson, Rev. Sci. Instrum. 48, 1306 (1977).
[11]J. T. Moseley, R. P. Saxon, B. A. Huber, P. C. Cosby, R. Abouaf, and M. Tadjeddine, J. Chem. Phys. 67, 1659 (1977).
[12]R. Abouaf, B. A. Huber, P. C. Cosby, R. P. Saxon, and J. T. Moseley, J. Chem. Phys. 68, 2406 (1978).
[13]S. L. Kaufman, Opt. Commun. 17, 309 (1976).
[14]W. H. Wing, G. A. Ruff, W. E. Lamb, Jr., and J. J. Spezeski, Phys. Rev. Lett. 36, 1488 (1976).
[15]M. Dufay, M. Carre, M. L. Gaillard, G. Neunier, H. Winter, and A. Zgainski, Phys. Rev. Lett. 37, 1678 (1976).
[16]A. Carrington and P. J. Sarre, Mol. Phys. 33, 1495 (1977).
[17]P. C. Cosby, J.-B. Ozenne, J. T. Moseley, and D. L. Albritton, J. Mol. Spectrosc. (submitted for publication).
[18]F. V. Kowalski, R. T. Hawkins, and A. L. Schalow, J. Opt. Soc. Am. 66, 965 (1976).
[19]D. L. Albritton, A. L. Schmeltekopf, W. J. Harrop, R. N. Zare, and J. Czarny, J. Mol. Spectrosc. 67, 157 (1977).
[20]B. H. Armstrong and R. W. Nicholls, *Emission, Absorption and Transfer of Radiation in Heated Atmospheres* (Pergamon, Oxford, 1972).
[21]J. K. G. Watson and P. K. L. Lin, "The Effects of Refraction and Dispersion on High-Altitude Measurements of Atmospheric Gases. II. Calculations with the Voigt Line Shape," Final Report on Project 3460, Ohio State University Research Foundation (1975).
[22]I. Kovacs, *Rotational Structure in the Spectra of Diatomic Molecules* (Hilger, London, 1969), pp. 243–245.
[23]N. H. F. Beebe, E. W. Thulstrup, and A. Andersen, J. Chem. Phys. 64, 2080 (1976).
[24]A.-L. Roche, Université de Paris-Sud, Orsay (private communication).
[25]E. Ishiguro and M. Kobori, J. Phys. Soc. Jpn. 22, 263 (1967).

APPENDIX C

Angular distributions and separation energies of predissociation photofragments of O_2^+ ($b\,^4\Sigma_g^-$, $v'=4$, N', F')

C. Pernot, J. Durup, and J.-B. Ozenne[a)]

Laboratoire des Collisions Atomiques et Moléculaires,[b)] Université de Paris-Sud, 91405 Orsay, France

J. A. Beswick

Laboratoire de Photophysique Moléculaire du C.N.R.S., Université de Paris-Sud, 91405 Orsay, France

P. C. Cosby and J. T. Moseley

Molecular Physics Laboratory, SRI International, Menlo Park, California 94025
(Received 19 April 1979; accepted 13 June 1979)

Kinetic energy distributions have been measured for O^+ photofragments resulting from transitions O_2^+ ($a\,^4\Pi_u$, v'', J'', Ω'')$\rightarrow O_2^+$ ($b\,^2\Sigma_g^-, v'=4, N', F'$)$\rightarrow O^+(^4S^0) + O(^3P)$, where for the first time in the study of photodissociation *all* relevant quantum numbers involved are specified. Both $^{16,16}O_2^+$ and $^{16,18}O_2^+$ were studied. The measurements were made using a laser-ion coaxial-beams photofragment spectrometer, a single-mode laser, and velocity tuning of the absorption wavelength. Experimental values of the anisotropy parameter β, which describes the angular distributions of the photofragments, were obtained by fitting the experimental energy distributions with calculated distributions, obtained from a Monte Carlo computer simulation of ion trajectories in the apparatus. Values of β were thus determined with an uncertainty of ± 0.05 or less. They are compared with theoretical values of β obtained by a generalization to Hund's case (b) of the theory previously developed by R. N. Zare. In a similar manner, values of the kinetic energy of separation of the photofragments in the center-of-mass system, W, are determined with an accuracy, in the most favorable case, of ± 0.14 meV. The experimental W values are used, along with other spectroscopic data, to improve the bond dissociation energy values of the ground $X\,^2\Sigma_g^-$ state of O_2, and of the a and b states of O_2^+. It is shown that for $W < 50$ meV the dissociation strongly favors the $O(^3P_2)$ channel over $^3P_1$ and $^3P_0$. This result is compared with several possible limiting-case models of the long-range couplings involved in the dissociation process, and it is concluded that the dissociation proceeds in a completely adiabatic way. Finally, further possible refinements of the present work are discussed.

I. INTRODUCTION

The angular distributions of photofragments from photodissociation processes have been studied for a number of neutral molecules[1] and for a few ions.[2] While the ground and dissociative electronic states were usually identified in these studies, in each case a distribution of energy levels was involved in the dissociative process. The angular distribution of photofragments represents in general a weighted sum of squared angular parts of the nuclear wave functions of the involved molecular states. Contributions from different initial states, in particular the various M_J components of a $|J, M_J\rangle$ level, will add their intensities, whereas contributions of different final (dissociating) states arising from a same initial state and feeding a same set of states of the fragments will add their amplitudes and can give rise to interference effects. In order to understand in detail the dissociative process, it is of interest to study the angular distribution of photofragments from a predissociation since a given transition with all relevant quantum numbers specified can be optically selected. We report here such a study, where angular distributions as well as the separation energies between the predissociated levels and the dissociation limit are obtained from photofragment kinetic energy spectra.

Four states are involved in the photopredissociation process: (i) the initial (ground or metastable) state, (ii) the predissociated (upper) state, (iii) the predissociating state as defined at short internuclear distances, where it is coupled with the predissociated state and possibly also radiatively coupled with the initial state, and (iv) the predissociating state at infinitely large internuclear distances. The observed angular distribution of course pertains to the last state. It will depend on the couplings between the various kinds of angular momenta all along the process.

The general theory of the angular distribution of photodissociation and photopredissociation fragments was initially worked out by Zare[3,4] and further developed by Bersohn, Jonah, and co-workers[5] and by Mukamel and Jortner.[6] The theory was applied by Zare in particular to the photodissociation of diatomic molecules in Hund's cases (a) or (c). This treatment will be generalized in the present paper and applied in pa. 'icular to Hund's case (b).

The experimental method used here is a direct extension of laser photofragment spectroscopy of molecular ions to very high optical resolution.[7-10] It was first shown by Schopman, Barua, and Los[11] that a high resolution could be achieved in the measurement of the momenta of predissociation fragments from fast molecular

---

[a)] International Fellow at SRI International, 1977–1978 academic year.

[b)] Associated to the Centre National de la Recherche Scientifique.

 0021-9606/79/182387-12$01.00

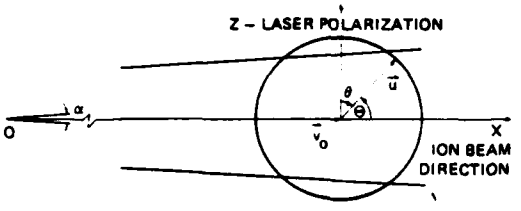

FIG. 1. Schematic of the dissociation kinematics, showing the relevant angles and the effect of angular discrimination. The initial beam velocity is v_0, u is the c.m. velocity of the charged photofragment, and α is the angular aperture of the apparatus.

ions, due to the amplification of the center-of-mass (c. m.) separation energies when measured in the laboratory frame.[12] As in previous work, the fact that this resolution of the c. m. kinetic energy of the photofragments is highest for a dissociation near threshold[6,13,14] was utilized.

With the aid of the velocity diagram shown in Fig. 1, it can be seen that the angular distributions of photopredissociation fragments can be determined from measurement of their kinetic energy distributions. If a given energy level in the upper state is selected by the optical transition, a *unique* value of the total photofragment energy W and therefore of the c. m. speed of the charged fragment $|u|$ will occur provided the predissociated level is close enough to threshold for being connected with only one pair of states of the fragments, usually their ground states. Thus, the end point of the velocity of the charged fragment (to be detected) will be somewhere on a sphere as indicated in Fig. 1. Momentum or energy analyzers aligned to view photofragments along the incident beam direction measure only the ion velocity component v_z along this direction. This component is given by

$$v_z = v_0 + |\mathbf{u}| \cos\Theta \,, \tag{1}$$

where Θ is the angle of ejection of the charged fragment, in the c. m. frame, with respect to the velocity vector of the diatomic ion (x axis). Thus, if the angular discrimination in the apparatus is properly taken into account, and v_0 and u are known, the measurement of kinetic energy distributions of the photofragments in the laboratory can be used to determine their angular distributions in the c. m. frame.

The O_2^+ ion was the obvious first candidate for such a study. Its photofragment spectroscopy[15] and the observation of its predissociation[13] were first performed in Orsay. Predissociation studies in Southampton by Carrington, Roberts, and Sarre[7] at very high optical resolution led them to the identification of a number of predissociated levels, of the main predissociation channel, and to lifetime measurements. Full identification of the transitions involved was achieved by the SRI group at very high optical resolution and high photofragment kinetic energy resolution with a determination of the lifetimes, for both $^{16}O_2^+$ and $^{16,18}O_2^+$.[8,9,16,17]

The predissociation process studied here is the transition labeled II in Fig. 2. The optical transition takes place from the metastable $a\,^4\Pi_u$ state to the $b\,^4\Sigma_g^-$ state,[7-9] whose radiative lifetime (1.35–1.68 μs)[18] is much longer than the predissociation lifetimes observed. The main predissociation channel is through the $^4\Sigma_g^+$ state.[7,9] A minor predissociation channel, through the $f\,^4\Pi_g$ state, was proposed[9] to account for (22 ± 10)% of the predissociation of levels $b\,^4\Sigma_g^-$, $v' = 4$, 5. The $b\,^4\Sigma_g^- - {}^4\Sigma_g^+$ predissociation is allowed only by spin–orbit coupling. The $b\,^4\Sigma_g^- - f\,^4\Pi_g$ predissociation takes place predominantly by spin–orbit coupling, with a contribution from rotational coupling of no more than a few percent.[9] The potential curves of the $^4\Sigma_g^+$ and $f\,^4\Pi_g$ states are known only from the *ab initio* calculations of Beebe *et al.*[19]; the $f\,^4\Pi_g$ state was observed in photofragment spectroscopy experiments.[15] A full discussion of the transitions involved here can be found in Refs. 8, 9, and 20.

II. EXPERIMENTAL RESULTS

The experimental data were obtained using the apparatus at SRI, which is described in detail in earlier papers.[8,9,12,16] Briefly, a single-mode tunable dye laser, pumped by an Ar or Kr ion laser, is made coaxial with a fast beam of O_2^+ over an interaction length of about 30 cm. The O_2^+ ions are formed in a hollow-cathode discharge source, accelerated to 3600 eV, and collimated to 2 mrad before being bent into the interaction region.

Then the beam passes through an electrostatic cage allowing the ions to be accelerated or decelerated, thus permitting velocity tuning of the effective wavelength in order to bring it into coincidence with any particular line of the absorption spectrum, here O_2^+ ($a\,^4\Pi_u - b\,^4\Sigma_g^-$). Further, apertures are used to obtain angular resolution of the photofragment ions after the interaction region. The fragment ions finally are decelerated to a few hundred eV, energy analyzed with an electrostatic analyzer, and counted. Two typical kinetic energy spectra obtained in this way are shown in Fig. 3.

Throughout this paper, we shall describe each line of the absorption spectrum by the following notation: the rotational quantum number N'' of the upper state, followed by the ΔJ (P for $\Delta J = -1$, Q for $\Delta J = 0$, R for $\Delta J = +1$), a first subscript indicating F' (i. e., 1, 2, 3, and 4 for $J' - N' = 3/2$, $1/2$, $-1/2$, and $-3/2$, respectively), a second subscript denoting Ω'' (conventionally,

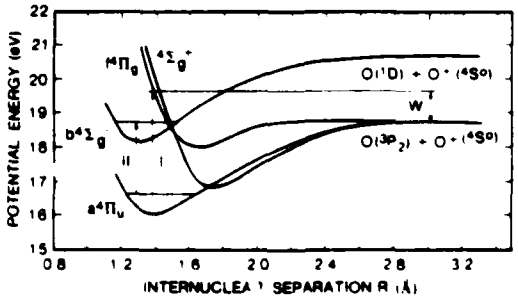

FIG. 2. The lowest-lying quartet potential curves of O_2^+ taken from Refs. 8 and 9

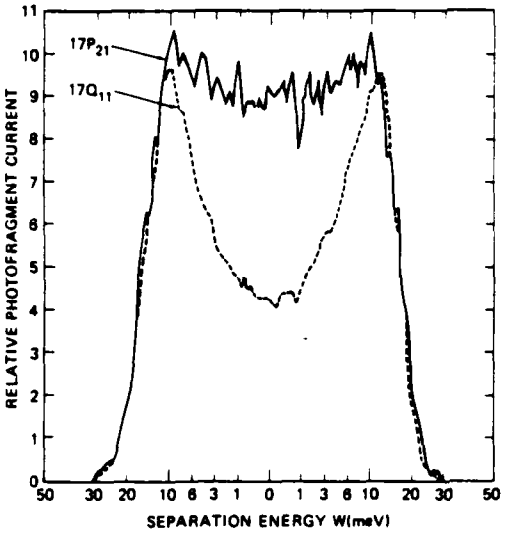

FIG. 3. Kinetic energy spectra of photofragments from two transitions of $^{16,18}O_2^+(a\,^4\Pi_u,\ v''=4 \rightarrow b\,^4\Sigma_g^-,\ v'=4)$. The horizontal and the vertical scales are the same in both spectra. Solid line, 17 P_{21} ($\Delta J=-1$); broken line, 17 Q_{11} ($\Delta J=0$).

1, 2, 3, and 4 for $\Omega''=5/2$, 3/2, 1/2, and $-1/2$, respectively). Thus, a 17 P_{21} line means $N'=17$, $\Delta J=-1$, $J'-N'=1/2$ (and therefore $J''=17.5$, $J'=18.5$), $\Omega''=5/2$. The solid line spectrum in Fig. 3 corresponds to this transition. The broken line corresponds to 17 Q_{11}.

In previous measurements of photofragment angular distributions,[1,2] the distribution has been controlled by the symmetries of the two electronic states involved, and by the lifetime of the predissociated state. For the transitions represented in Fig. 3, the electronic states are identical and the lifetimes of both predissociated levels are sufficiently long[3] that the difference between them cannot affect the angular distribution. In fact, the angular distributions observed here arise not from semiclassical considerations of the orientation of the transition dipole moment or of the amount of rotation the molecule undergoes after absorption of a photon, but from a purely quantum mechanical effect. The main difference in the spectra in Fig. 3 arises from the difference in ΔJ values. This comes from the fact that ΔJ controls the set of M_J's appearing in the upper state, account being taken of the selection rule $\Delta M_J=0$, with the laser polarization direction as the axis of quantization. This will be quantitatively shown in Sec. III. The largest difference in energy (and hence angular) distributions is between a P and a Q line, as seen in Fig. 3 and Table I. Kinetic energy spectra corresponding to P and R lines with the same upper states are similar to each other but distinguishably different. Spectra differing only by the values of F' or Ω'' are indistinguishable in shape. This will appear more clearly from the experimental results and the discussion in Sec. III.

Since, for the coaxial-beams arrangement used here, the laser polarization is necessarily perpendicular to the ion beam direction, it thus appears that the $\Delta J=0$ transition leads to an angular distribution peaked perpendicular to the laser polarization (i.e., along the beam direction), while $\Delta J=\pm 1$ leads to a different distribution. This quantitative result was predicted by Durup,[21] based on Zare's theory.[3,4] A major purpose of the present paper is to extract the angular distributions from such kinetic energy spectra, and compare the results with theoretical calculations applied to the specific type of dissociation studied here.

A second piece of information clearly contained in spectra such as shown in Fig. 3 is the energy of the dissociating level with respect to the dissociation limit. Advantage has already been taken of this fact, using data where the P, Q, and R components were not resolved, to obtain improved bond dissociation energies for O_2 ($X\,^3\Sigma_g^-$),[14] and O_2^+ ($a\,^4\Pi_u$) and ($b\,^4\Sigma_g^-$),[8] with an uncertainty of ± 10 cm^{-1}. The higher-resolution data presented here will allow a further improvement in the energies of the dissociating levels and in the bond dissociation energies.

In order to take into account the geometry and angular discrimination of the apparatus, a computer program for Monte Carlo calculation of the ion trajectories was developed. This program prepared earlier for another experimental setup,[22,23] samples in a quasirandom way the incident ion trajectories, the location of photon absorption, and the properly weighted direction of ejection of the fragments. After the appropriate geometric constants describing the apparatus are put into the program, the only input data are the total photofragment separation energy W and the anisotropy parameter β. The value of β, as is well known, is the only physical parameter occurring in the angular distribution $I(\theta)$ of photofragments from initially randomly oriented molecules

$$I(\theta)=\frac{1}{4\pi}\left[1+\beta P_2(\cos\theta)\right], \tag{2}$$

where θ is the angle between the laser polarization and the direction of ejection of the fragments in the c. m. frame, and $P_2(\cos\theta)=\frac{1}{2}(3\cos^2\theta-1)$ is the second Legendre polynomial. As β varies from -1 to 2, the angular distribution varies from $\sin^2\theta$ through isotropic ($\beta=0$) to $\cos^2\theta$.

In order to determine experimental values of β and W, their values were varied in the computer program until an acceptable fit was obtained with an experimental spectrum. This procedure is neither as inconclusive nor as time consuming as it might first appear, for the following reasons: First, the value of W can be obtained in a first approximation to a good accuracy directly from the half-width at half-maximum of the kinetic energy distribution. The fitting then improves this accuracy by up to an order of magnitude. Second, the theoretical value of β (see Sec. III) may be used for choosing the range of values of β to explore. Finally, the effects of W and β on the spectrum are nearly independent, W controlling the width and β the shape, particularly near $W=0$. Thus, it is possible with only a few computer runs to fit the spectra to within the statistical noise,

TABLE I. Experimental and calculated values of W and β for most of the $O_2^+(a\,^4\Pi_u - b\,^4\Sigma_g^-)$ transitions studied in this work. In all cases, $v''=4$ and $v'=4$.

					W (meV)		β	
Isotope	N'	F'	Ω''	ΔJ	Exptl.	Calc.[a]	Exptl.[b]	Calc.
	14	1	5/2	0	1.52 ± 0.07	(1.52)	−0.95 ± 0.05	−0.979
	14	2	5/2	−1	1.51 ± 0.06	1.58	0.45 ± 0.05	0.440
	14	3	−1/2	+1	1.68 ± 0.04	1.57	0.55 ± 0.05	0.554
	14	4	−1/2	0	1.47 ± 0.05	1.52	···	−0.970
	15	1	5/2	0	5.60 ± 0.13	5.69	−0.975 ± 0.025	−0.982
	15	2	5/2	−1	5.76 ± 0.06	5.75	0.45 ± 0.05	0.444
	15	4	1/2	+1	5.70 ± 0.14	5.69	0.55 ± 0.05	0.544
16,18	15	4	1/2	0	5.40 ± 0.10	5.69	−0.975 ± 0.025	−0.975
	16	1	5/2	0	10.31 ± 0.14	10.14	···	−0.984
	16	2	5/2	−1	10.40 ± 0.09	10.19	0.45 ± 0.05	0.448
	17	1	5/2	0	14.87 ± 0.16	14.86	−0.975 ± 0.025	−0.985
	17	2	5/2	−1	15.42 ± 0.12	14.91	0.45 ± 0.05	0.451
	18	1	5/2	0	20.86 ± 0.23	19.85	−0.975 ± 0.025	−0.987
	18	2	5/2	−1	20.40 ± 0.17	19.91	···	0.454
	19	1	5/2	0	24.98 ± 0.17	25.12	−0.975 ± 0.025	−0.988
	20	4	1/2	0	31.32 ± 0.13	30.67	−0.95 ± 0.05	−0.985
	9	1	5/2	+1	1.77 ± 0.01	1.763	0.55 ± 0.05	0.551
	9	2	5/2	−1	1.74 ± 0.07	1.817	0.40 ± 0.05	0.403
	9	3	5/2	−1	1.77 ± 0.03	1.811	···	0.416
	9	3	3/2	+1	1.77 ± 0.03	1.811	0.60 ± 0.05	0.582
16, 16	9	4	3/2	0	1.86 ± 0.11	(1.76)	···	−0.923
	11	1	5/2	0	7.59 ± 0.34	7.933	−0.95 ± 0.05	−0.969
	11	2	5/2	−1	7.64 ± 0.34	7.986	···	0.422
	13	1	5/2	0	13.55 ± 0.72	15.275	···	−0.976
	13	2	5/2	−1	14.70 ± 0.60	15.329	0.45 ± 0.05	0.435

[a] For each isotope, we extracted from experiment the energy of the *lowest* predissociated level of ($b\,^4\Sigma_g^-$, $v''=4$), namely, 14 F_1' for $^{16}O^{18}O^+$ and 9 F_1' for $^{16,16}O_2^+$ as described in the text. This set of values was then averaged, yielding the values in parentheses in column 6. All other theoretical W's are from Albritton, using the former as reference values.

[b] The missing β values correspond to spectra which either did not present a good enough forward–backward symmetry or could not be corrected for the background of collisional dissociation due to the residual gas. In both these cases, the W values could however be extracted by using computed spectra with the theoretical β values.

and to obtain values of β and W, as well as uncertainties in these values.

The accuracy of the experimental determination of β can be estimated from Fig. 4, where the computed spectra for $W=20.86$ meV and $\beta=-0.9$ and -1.0 are compared with the experimental spectrum for the 18 Q_{11} transition. It is seen that β can be determined from this kinetic energy distribution to within ±0.025. The spectrum computed for the theoretical value $\beta=-0.987$ is in close agreement with the experimental spectrum. Variation of β over the range shown in Fig. 4 does not significantly affect the widths of the computed spectra. Thus, the determination of W will be nearly independent of that of β.

Figure 5 shows the sensitivity of the determination of W. Here spectra are computed for two values of W which differ by 0.21 meV and the theoretical value of $\beta=0.440$. All three spectra are aligned on the left-hand side in order to obtain maximum sensitivity to the misalignment on the right. It is clear that this spectrum can be fit much closer than the interval between the two values of W shown. Such bracketing led to the value W

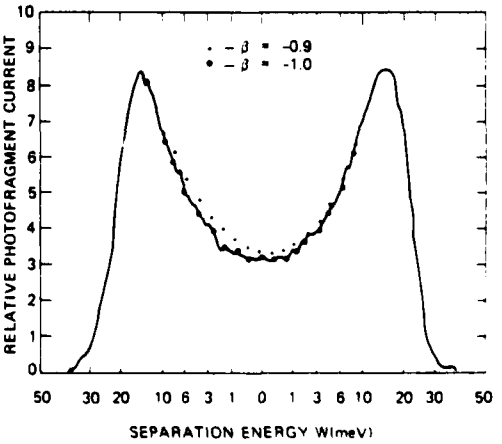

FIG. 4. Comparison of an experimental kinetic energy spectrum, line 18 Q_{11}, with computed spectra with β values bracketing the true one, and $W=20.86$ meV. Solid line, experimental data; +, computed with $\beta=-0.9$; ●, computed with $\beta=-1.0$.

$= (1.51 \pm 0.06)$ meV. Since the kinetic energy resolution is highest near $W = 0$, the absolute uncertainty in W will be smallest for levels nearest threshold. These are $N' = 9$ for $^{16,16}O_2^+$ and $N' = 14$ for $^{16,18}O_2^+$. Since the *relative* positions of the various levels are now well known from spectroscopy,[16] the *absolute* position of the higher levels in the $b\,^4\Sigma_g^-$ state can be obtained from these threshold levels to higher accuracy using the spectroscopic results than by measurement of the photofragment kinetic energies. Therefore, the main effort was to determine the separation energies W of photofragments for the $N' = 9$ (in normal O_2^+) and $N' = 14$ (in isotopic O_2^+) levels to as high an accuracy as possible.

Table I gives the values of β and W determine using the above-described fitting procedure, together with calculated relative values of W, normalized as will be discussed below, and calculated absolute values of β, which will also be discussed in the following section. The uncertainties in the experimental data refer only to the uncertainty in the fit. Other experimental uncertainties will be discussed here.

For a homonuclear diatomic, a photofragment will appear at $\theta = 0°$ or 180° in the laboratory with an energy E given by[12]

$$E = \tfrac{1}{2}(E_0 + W) \pm (WE_0)^{1/2}\,, \tag{3}$$

where E_0 is the parent ion energy. Thus, the uncertainty in W depends on the uncertainty in E_0 and E. For $W \ll E_0$, which practically speaking is always the case, this dependence can be expressed as

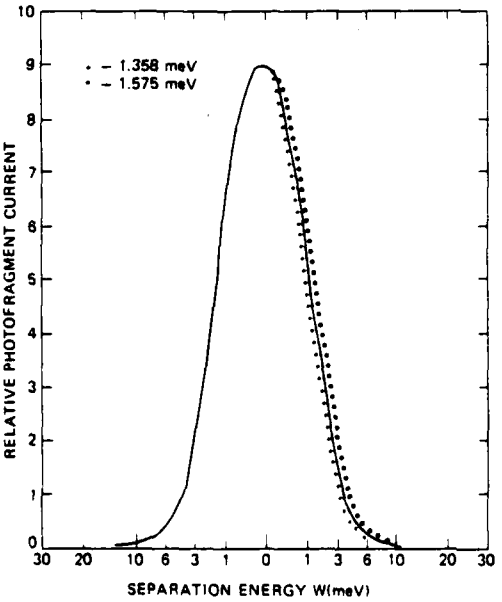

FIG. 5. Comparison of an experimental kinetic energy spectrum, line 14 P_{21}, with computed spectra with W values bracketing the experimental one, and $\beta = 0.440$. Solid line, experimental data; +, computed with $W = 1.358$ meV; •, computed with $W = 1.575$ meV.

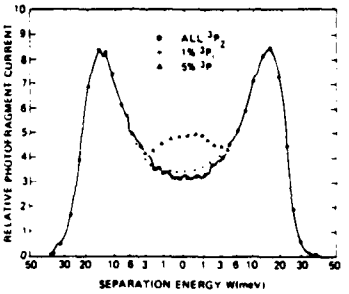

FIG. 6. Comparison of an experimental energy spectrum, line 18 Q_{11}, with spectra computed with the theoretical β values (~ 0.987), the best W value (20.86 meV), and various relative contributions from the $O^+(^4S^0) + O(^3P_1)$ second dissociation channel with respect to the main contribution due to the $O^+(^4S^0) + O(^3P_2)$ dissociation channel [the third dissociation channel $O(^3P_0)$ is not energetically allowed]. Full line, experimental data; •, computed with $^3P_2$ only; +, computed with 99% $^3P_2$, 1% $^3P_1$; ▲, computed with 95% $^3P_2$, 5% $^3P_1$.

$$\Delta W = 2\Delta E(W/E_0)^{1/2}\,. \tag{4}$$

The properties of the beam deceleration and energy analysis system allow a resolution in ΔE of 0.05 eV, as demonstrated by spectra such as Figs. 3–6 (when plotted versus laboratory energy E rather than W). Thus, for W near 2 meV, a ΔW of about 0.07 meV should be resolvable. This is consistent with the observations in Table I. The absolute kinetic energy of the ion beam E_0 was established to within ± 1.5 eV,[16] leading to an uncertainty in W at 2 meV of only 0.04%, since the uncertainties in E and E_0 are related, and tend to cancel in the calculation of W. Thus, this source of uncertainty is negligible.

All of the above discussion assumes that both the ion beam and the energy analyzer are properly aligned with the x axis. The 2 mrad angular resolution of the apparatus assures that this alignment is reasonably good, but misalignment within this angle can occur. However, inspection of Fig. 1 shows that a misalignment, i.e., observation of the photofragments along a line other than the x axis, will lead to an asymmetry both in the height of the peaks on either side of $W = 0$ and in the W value at the peak half-maximum. The asymmetry in W is small unless the misalignment is large enough to cause a substantial asymmetry in the peak heights and a significant decrease in the photofragment count rate. Adjustment of the apparatus for symmetric peaks and maximum count rate leads to reproducible W values near 2 meV of ± 0.1 meV. This reproducibility decreases with increasing W, as does the resolution in W. Therefore, W values for peaks at higher W will be more uncertain than for those at low W.

The experimental results of Table I can be used to check the uncertainty and the internal consistency of the W values in two ways. First consider the set of four $N' = 14$ levels for isotopic O_2^+. These levels lie very close in energy, and the highly accurate spectroscopic values[24] for the energy differences can be used to adjust them so that all four measurements refer to the lowest

level F_1'. The set of four values then is (1.52 ± 0.07), (1.45 ± 0.06), (1.63 ± 0.04), and (1.47 ± 0.05) meV. The average value is then 1.52 meV; the maximum range of values is [1.39, 1.67] meV, or 1.53 ± 0.14 meV. It is thus certainly reasonable to choose 1.52 meV as the absolute value of the F_1' level, and to normalize all of the calculated relative values to this value. The uncertainty in the *absolute* values of all the calculated levels is now the same as the uncertainty in the F_1' level, which will be assigned below.

A second test is now available: comparison of the measured W values with the now normalized calculated values, or, effectively, a comparison between the differences in energy levels for experimental and calculated values. For isotopic O_2^+, the standard deviation between the experimental and normalized calculated values is 0.05 meV when only $N' = 14$ and 15 levels are considered, 0.06 meV when levels up to $N' = 17$ are included, and 0.1 meV when all measurements are included.

All the evidence thus points to an uncertainty in the absolute value of the energy of the $(N' = 14, F_1')$ level of the O_2^+ b state with respect to the $O(^3P_2) + O^+(^4S^0)$ limit about ± 0.1 meV. We choose the largest uncertainty derived above (± 0.14 meV) and conclude that the value of this separation energy is (1.52 ± 0.14) meV, or (12.3 ± 1.1) cm^{-1}. A similar analysis of the $^{16,16}O_2^+$ data lead to the conclusion that the $(N' = 9, F_4')$ level lies (1.76 ± 0.21) meV, or (14.2 ± 1.7) cm^{-1}, above the $O(^3P_2) + O^+(^4S^0)$ dissociation limit.

III. THEORETICAL CALCULATION OF THE ANGULAR DISTRIBUTIONS

Angular distributions in the photofragmentation of diatomic molecules have been studied theoretically by many authors.[3-6] Following the pioneering work of Zare on direct (fast) photodissociation and (slow) predissociation, Jonah[5(b)] considered the effects of rotation and finite dissociation velocity, providing a semiclassical picture for delayed photofragmentation. Recently, Mukamel and Jortner[6] have developed a general unified formalism for the quantum-mechanical treatment of the anisotropic distribution of the fragments in the case of predissociation,[6(a)] as well as in the case of interference between direct photodissociation and predissociation[6(b)] (Fano's interference).[25] However, all these treatments have in common the fact that they considered electronic states described by Hund's coupling case (a) or (c). This is clearly inappropriate to the O_2^+ ($a\,^4\Pi_u - b\,^4\Sigma_g^- - {}^4\Sigma_g^+$, $f\,^4\Pi_g$) predissociation process studied in this paper, since the intermediate state and at least one of the final states correspond to Hund's coupling case (b) while the initial state is intermediate between case (a) and case (b).

We shall present here the derivation for the general coupling case. Consider three sets of rovibronic states of the diatomic molecule: (i) the initial bound states $|gJ''M''\rangle$, characterized by a total angular momentum quantum number J'', magnetic quantum number M'' with respect to the laboratory z axis, and other electronic and vibrational-rotational quantum numbers denoted collectively by g; (ii) a set of intermediate bound states $|eJ'M'\rangle$, with e, J', M' having the same definition as above, optically connected to the $|gJ''M''\rangle$ states; and (iii) a set of final unbound continuum states $|dJM\rangle$ corresponding to dissociation of the diatomic molecule with total angular momentum J and projection M on the laboratory z axis, taken here to be the direction of the laser polarization, and always perpendicular to the direction of propagation of the ion beam, the x axis (see Fig. 3).

These levels are in the same energy region as the intermediate $|eJ'M'\rangle$ levels, and directly or indirectly coupled to them by intramolecular couplings such as spin-orbit interaction or rotational coupling. We assume that the continuum $|dJM\rangle$ is not optically connected to the initial $|gJ''M''\rangle$ levels, so that interference between predissociation and direct photodissociation (Fano's interference) is not considered. For the study of directional predissociation, we are not interested in the $|dJM\rangle$ states, which correspond to spherical waves with well-defined angular momentum J, but rather in plane waves $|d\hat{k}\rangle$ moving in the direction $\hat{k}$ with polar angles θ and Φ with respect to the laboratory system of reference. It can be shown[3-6] that, for electronic states for which the projection of the total angular momentum on the internuclear axis [the quantum number Ω in Hund's case (a) or (c)] is a good quantum number,

$$|d\Omega\hat{k}\rangle = \sum_{JM} (2J+1)(i)^J \exp(-i\delta_J)\,|d\Omega JM\rangle\, D^{J*}_{M\Omega}(\Phi, \theta, 0)\,, \tag{5}$$

where $D^{J*}_{M\Omega}(\Phi, \theta, 0)$ is a Wigner rotation matrix and δ_J is a phase shift appearing in the asymptotic form of the nuclear wave function for large internuclear distances.

The differential cross section for predissociation from a given initial state $|gJ''M''\rangle$ to a final state $|d\Omega\hat{k}\rangle$ characterized by an electronic angular momentum Ω along the internuclear axis and a relative motion of the fragments in the direction $\hat{k} = (\theta, \Phi)$ with respect to the laboratory z axis, when the molecule is excited with monochromatic light of angular frequency ω, is given by[6(a)]

$$\sigma(gJ''M'' \to d\Omega\hat{k}) = \frac{(2\pi)^2}{\hbar c} \left| \sum_{eJ'M'} \times \frac{\langle gJ''M''|H_{\rm int}|eJ'M'\rangle \langle eJ'M'|H_v|d\Omega\hat{k}\rangle}{E_{gJ''} + \hbar\omega - E_{eJ'} + i\Gamma_{eJ'}} \right|^2, \tag{6}$$

where $H_{\rm int}$ is the light-matter interaction operator and H_v is the intramolecular coupling. In Eq. (6), the photon states are wave number normalized while the dissociative continuum states are energy normalized. $E_{gJ''}$ and $E_{eJ'}$ are the energies of the initial and intermediate states, respectively, including the level shift for $E_{eJ'}$ induced by the intramolecular coupling. We consider here the molecule in the absence of any external field so that all the magnetic sublevels are degenerate. The particularly interesting case of angular distributions in the presence of an applied magnetic field is being studied experimentally[26] as well as theoretically.[27]

Finally, $\Gamma_{eJ'}$ is the total width of the intermediate

state $|eJ'M'\rangle$, which is given by the Fermi "golden-rule" expression

$$\Gamma_{eJ'} = \pi |\langle eJ'M'|H_v|dJ''M''\rangle|^2 , \tag{7}$$

where we have neglected the radiative width. In writing Eq. (7), we have used the fact that intramolecular coupling conserves J' and M'. Also, the matrix elements of H_v do not depend on M' since the direction of the laboratory z axis is irrelevant for intramolecular dynamics in the absence of external fields. Using these selection rules and Eq. (5), we get from Eq. (6)

$$\sigma(gJ''M'' - d\Omega\hat{K}) = \frac{(2\pi)^2}{\hbar c} \times \left| \sum_{eJ'M'} \langle gJ''M''|H_{int}|eJ'M'\rangle \times \frac{R^{J'}_{e,d\Omega} D^{J''*}_{M''\Omega}(\Phi,\theta,0)}{E_{gJ''} + \hbar\omega - E_{eJ'} + i\Gamma_{eJ'}} \right|^2 , \tag{8}$$

where

$$R^{J'}_{e,d\Omega} = (2J'+1)\langle eJ'M'|H_v|d\Omega J'M'\rangle . \tag{9}$$

Moreover, it can be shown that the matrix elements of the field–matter interaction operator are given in the dipole approximation by[28]

$$\langle iJ''M''|H_{int}|eJ'M'\rangle = C(J''1J';M''0M')\zeta(gJ'', eJ';\mu\cdot\epsilon) , \tag{10}$$

where $C(J''1J';M''0M')$ is a Clebsch–Gordan coefficient, and ζ is a function depending only on the quantum numbers $(i, J'';e, J')$ and the projection of the dipole moment operator μ on the direction of the polarization of the light ϵ. Here we have fixed the laboratory z axis in the direction of polarization of the light and this results in the appearance of the Clebsch–Gordan coefficient in Eq. (10) with the corresponding selection rules $\Delta M = 0$, $\Delta J = 0, \pm 1$. Introducing Eq. (10) into (8), we get finally[6]

$$\sigma(iJ''M'' - d\Omega\hat{k}) = \frac{(2\pi)^2}{\hbar c} \left| \sum_{e,J'\,eJ''=0,\pm1} \zeta(gJ'', eJ';\mu\cdot\epsilon) \times \frac{C(J''1J';M''0M') R^{J'}_{e,d\Omega} D^{J''*}_{M''\Omega}(\Phi,\theta,0)}{E_{gJ''} + \hbar\omega - E_{eJ'} + i\Gamma_{eJ'}} \right|^2 . \tag{11}$$

The initial state is randomly oriented in the absence of external fields, so that the differential cross section for predissociation from an initial state $|g\rangle$ with definite angular momentum J'' is given by an average over magnetic sublevels

$$\sigma(gJ'' - d\Omega\hat{k}) = \frac{1}{2J''+1} \sum_{M''} \sigma(gJ''M'' - d\Omega\hat{k}) . \tag{12}$$

Equations (11) and (12) give the angular distribution of the fragments in the predissociation to a final state corresponding to Hund's coupling case (a) or (c), with electronic angular momentum projection Ω along the internuclear axis. In the general situation, where the final state corresponds to other limiting or intermediate coupling cases, it is convenient to express the wave function of the final state as a linear combination of Hund's coupling case (c) wave functions

$$|dJM\rangle = \sum_{\Omega} C_d(\Omega)|d\Omega JM\rangle . \tag{13}$$

The differential cross section will then be given by

$$\sigma(gJ'' - \hat{k}) = \frac{(2\pi)^2}{\hbar c} (2J''+1)^{-1} \sum_{M''} \sum_{\Omega} \left| \sum_{e,J'\,eJ''=0,\pm1} C(J''1J';M''0M') \times \zeta(gJ'', eJ';\mu\cdot\epsilon) \sum_{d} R^{J'}_{e,d} C^*_d(\Omega) D^{J''*}_{M''\Omega}(\Phi,\theta,0)/(E_{gJ''} + \hbar\omega - E_{eJ'} + i\Gamma_{eJ'}) \right|^2 , \tag{14}$$

with

$$R^{J'}_{e,d} = \langle eJ'M'|H_v|dJM\rangle . \tag{15}$$

Equation (14) provides a general quantum-mechanical expression for the angular distribution of the predissociation fragments for any angular momentum coupling case. It also incorporates the effect of finite dissociation lifetime giving the correct limits for slow and fast predissociation. In the case studied here, we are in the limit of slow predissociation, i.e., the widths $\Gamma_{eJ'}$ are very small compared to the spacings between neighboring levels, and the different P, Q, R lines ($J' - J'' = -1, 0, +1$) are well resolved. Under these circumstances Eq. (14) takes the form (for $\hbar\omega \sim E_{gJ''} - E_{iJ''}$)

$$\sigma(iJ'' - eJ' - \hat{k}) \sim \sum_{\Omega} A_{eJ'}(\Omega) I_{J'J''\Omega}(\theta) , \tag{16}$$

where

$$A_{eJ'}(\Omega) = \left| \sum_{d} R^{J'}_{ed} C^*_d(\Omega) \right|^2 \tag{17}$$

and

$$I_{J'J''\Omega}(\theta) = \sum_{M''} |C(J''1J';M''0M') D^{J''}_{M''\Omega}(\Phi,\theta,0)|^2 . \tag{18}$$

From Eqs. (16)–(18), we notice that the angular distribution for slow predissociation is not affected by the $\zeta(iJ'', eJ';\mu\cdot\epsilon)$ factor defined in Eq. (10), which governs only the total intensity. The consequence is that for slow predissociation the angular distribution does not depend on the parallel or perpendicular nature of the transition but only on the P, Q, R character of the transition. On the other hand, for fast predissociation, it is not longer possible to resolve the P, Q, R lines and we must consider the general expression given by Eq. (14). In that case, the angular distribution will depend on whether the dipole moment is parallel or perpendicular to the internuclear axis. We note also from Eqs. (16)–(18) that the angular distribution for slow predissociation is not affected by any quantum number of the initial state $|iJ''\rangle$, except for J'', whereas it depends upon the intermediate state through the matrix

elements $R_{ed}^{J'J''}$ only in the case where several final states d can be reached from the same intermediate e level.

The angular distribution factors $I_{J'J''\Omega}(\theta)$ have been tabulated by Zare.[3] We reproduce in the Appendix a method used to calculate them in a simple way. Zare's final result is

$$I_{J'\Omega}(\theta)=\frac{3}{4\pi}\,\frac{(1/2)[(J'-1)J'+\Omega^2]\sin^2\theta+(J'^2-\Omega^2)\cos^2\theta}{(2J'-1)J'} \tag{19}$$

for R lines ($J'=J''+1$),

$$I_{J'\Omega}(\theta)=\frac{3}{4\pi}\,\frac{(1/2)[J'(J'+1)-\Omega^2]\sin^2\theta+\Omega^2\cos^2\theta}{J'(J'+1)} \tag{20}$$

for Q lines ($J'=J''$), and

$$I_{J'\Omega}(\theta)=\frac{3}{4\pi}\,\frac{(1/2)[(J'+1)(J'+2)+\Omega^2]\sin^2\theta+[(J'+1)^2-\Omega^2]\cos^2\theta}{(J'+1)(2J'+3)} \tag{21}$$

for P lines ($J'=J''-1$). Each of these equations is of the form

$$I(\theta)=\frac{3}{4\pi}\,(a_{\Delta J}\sin^2\theta+b_{\Delta J}\cos^2\theta)\,, \tag{22}$$

and can be put in the form of Eq. (2) with $\beta_{\Delta J}=2(b_{\Delta J}-a_{\Delta J})$. Thus, from Eq. (16), the angular distributions in the limit of slow predissociation can be put in the form of Eq. (2) with the anisotropy parameter given by

$$\beta_{\Delta J}=2\sum_{\Omega}A_{eJ'}(\Omega)[b_{\Delta J}(\Omega)-a_{\Delta J}(\Omega)]\,. \tag{23}$$

In the limit of large J' ($J'\gg\Omega$, $J'\gg1$), one obtains the simplified expressions

$$I(\theta)=\frac{3}{16\pi}\,(1+\cos^2\theta) \tag{24}$$

for R and P branches, corresponding to $\beta=\frac{1}{2}$, and

$$I(\theta)=\frac{3}{8\pi}\sin^2\theta \tag{25}$$

for the Q branches, corresponding to $\beta=-1$. In this limiting situation, the angular distributions will be independent of the nature of the electronic states implied in the predissociation process and they will be simply given by Eqs. (24) and (25).

We anticipate that, for the O_2^+ photodissociation process studied here, the angular distributions will be similar to those given by Eqs. (24) and (25), since the angular momentum for the observed transitions is rather large. We will show, however, that significant deviations can be observed for $J'\lesssim10$. We consider the predissociation process ($a\,^4\Pi_u-b\,^4\Sigma_g^-\!-\!^4\Sigma_g^-$), neglecting the contribution of the predissociation through the $f\,^4\Pi_g$ state.[9] *The intermediate and final states will be described in Hund's coupling case (b). The predissociation is induced by spin–orbit coupling.*[9] *The different intermediate and final states are characterized by the quantum number N of the nuclear rotational angular momentum. The coefficients of the linear combination* [Eq. (13)] *of the final state $|dNJM\rangle$ in terms of Hund's coupling case (c) wave functions are then given by*

$$C_{dN}(\Omega)=\left(\frac{2N+1}{2J+1}\right)^{1/2}C(SNJ;\Omega-\Lambda,\Lambda,\Omega)\,, \tag{26}$$

with $S=3/2$ and $\Lambda=0$ in our case. Denoting by N' the rotational angular momentum quantum number for the intermediate states $|eN'J'M'\rangle$, one obtains for the intramolecular matrix elements $R_{eN',dN}^{J'J''}$ defined in Eq. (15) the final expression[29]

$$R_{eN',dN}^{J'J''}=\frac{\eta[(J'+\tilde N+1)(J'+\tilde N+2)-S(S+1)]^{1/2}[S(S+1)-(J'-\tilde N)(J'-\tilde N-1)]^{1/2}}{[(2\tilde N+1)(2\tilde N+3)]^{1/2}} \tag{27}$$

for $\Delta N=\pm1$, $\tilde N=\min(N,N')$. All other matrix elements vanish. The coefficient η is a reduced matrix element of the spin–orbit operator and we will assume it to be independent of N. It is now an easy matter to compute the angular distributions using Eqs. (16), (17), (19)–(21), (26), and (27).

Actually, the $b\,^4\Sigma_g^-$ state of O_2^+ is not rigorously a pure Hund's case (b), since spin–orbit coupling is not strictly zero. Therefore, the Clebsch–Gordan coefficients in Eq. (26) should in principle be replaced by the exact coefficients derived from the diagonalization of the Hamiltonian matrix. These coefficients have been computed in the case of the $^{16,16}O_2^+$ isotope by Tadjeddine[30] using the program developed by Albritton.[31] They differ very little (less than 2%) from the Clebsch–Gordan coefficients. We therefore used the latter coefficients as indicated in Eq. (26). The final results for the different lines are given in Table I. For the predissociation to the $f\,^4\Pi_g$ state, only Eqs. (26) and (27) need to be modified. It has been estimated[9] that this predissociation can account for ≈22% of the dissociation observed. Assuming the $f\,^4\Pi_g$ state to be represented by a case (b) basis set, and the spin–orbit coupling to be the major factor inducing predissociation, we find angular distributions very similar to those given in Table I.

It can be seen from Table I that the experimental and theoretical results for β are in agreement within the uncertainty of the experimental measurements. It can also be seen that β varies significantly for $N'\approx9$, but that this variation is not large enough to be observed in the present experimental measurements. The data do, however, clearly demonstrate for the first time the dependence of the angular distribution for a slow predissociation on the P, Q, or R nature of the transition rather than on the orientation of the dipole moment.

IV. DISSOCIATION ENERGIES

The dissociation energies of the $O_2^+(X\,^2\Pi_g)$, $O_2^+(a\,^4\Pi_u)$, and $O_2^+(b\,^4\Sigma_g^-)$ states can now be determined as we have

previously done,[8,14] but with higher accuracy. For example, the bond energy $D(O_2, X\,^3\Sigma_g^-)$ is part of a spectroscopic cycle that includes the $b\,^4\Sigma_g^-$ state of O_2^+ and the separation energy $W(N'=9, F_4', {}^3P_2)$ determined in Sec. II to be 14.2 ± 1.7 cm^{-1}. This cycle can be written[14]

$$E(O_2^+, b) + T(v'=4, N'=9, F_4') = D(O_2, X) + E(O^+, {}^4S^0) + W(N'=9, F_4', {}^3P_2)\,. \quad (28)$$

The ionization potential $E(O_2^+, b)$ was determined by Yoshino and Tanaka[32] from Rydberg series limits to be $146\,556 \pm 2$ cm^{-1}; the ionization potential $E(O^+, {}^4S^0)$ is, from atomic spectroscopy,[33] $109\,837.02 \pm 0.06$ cm^{-1}. The energy T of the $(v'=4, N'=9, F_4')$ level with respect to the $(v'=0, N'=0, F_1')$ level is 4551.80 ± 0.05 cm^{-1}, as determined from the molecular constants of Cosby *et al.*[16] Substituting these values into Eq. (28) yields $D_0(O_2, X) = 41\,256.6 \pm 3.8$ cm^{-1}, where the uncertainty is conservatively determined by the sum of the individual uncertainties. The square root of the sum of the squares of the uncertainties yields ± 2.6 cm^{-1}. The value for $D_0(O_2, X)$ compares with the determination of Brix and Herzberg[34] of $41\,260 \pm 15$ cm^{-1}, obtained using an entirely different spectroscopic cycle involving only neutral O_2, and our previous determination of 41 262 ± 10 cm^{-1}, made in the way described above using a less precise value for W.

Spectroscopic cycles can also be used to allow determination of the bond energies for the O_2^+ a and b states. For the a state,

$$E(O_2^+, b) - E(O_2^+, a) + T(v'=4, N'=9, F_4') = D(O_2^+, a) + W(N'=9, F_4', {}^3P_2)\,, \quad (29)$$

where the ionization potential E and bond energy D of the a state are both referred to the lowest existing level of this state $v''=0$, $J''=5/2$, $\Omega''=5/2$. The energy difference $E(O_2^+, b) - E(O_2^+, a)$ is determined from the molecular constants[16] to be $21\,284.9 \pm 0.1$ cm^{-1}, leading to $D(O_2^+, a) = 21\,270.7 \pm 1.8$ cm^{-1}. For the b state,

$$D(O_2^+, b, v'=0, N'=0) = \Delta E(O^1, D_2\text{–}O, {}^3P_2) - W(N'=9, F_4', {}^3P_2) + T(v'=4, N'=9, F_4')\,. \quad (30)$$

The value of ΔE from atomic spectroscopy of $15\,867.862 \pm 0.005$ cm^{-1} is essentially "exact" on the scale of the present study, and $D(O_2^+, b) = 20\,405.5 \pm 1.8$ cm^{-1}.

The bond energies given above for these oxygen states are among the most accurate bond energies now known. Among neutral diatomic molecules, only the bond energies of the halogen molecules, H_2 and LiH appear to be known to a similar or better accuracy.[35] Among ions, only H_2^+ appears to be as well determined.[35]

It is also of interest to compare the difference in the experimental values for the level $W(v'=4, N'=9, F_4')$ for $^{16,16}O_2^+$ and that for $W(v'=4, N'=14, F_1')$ for $^{16,18}O_2^+$ with values calculated using the best available molecular constants. The calculated energy difference[24] $W(9) - W(14) = 3.9 \pm 0.4$ cm^{-1}; the experimentally determined difference (see Sec. II) is 1.9 ± 2.8 cm^{-1}. However, the data definitely show that $W(9) > W(14)$, since all $N'=9$ kinetic energy spectra are broader than all $N'=14$ spectra.

V. BRANCHING RATIO TO ATOMIC STATES

The discussion above in this paper has only considered the possibility of dissociation from the $b\,^4\Sigma_g^-$, $v'=4$ state to the limit $O^+(^4S^0) + O(^3P_2)$. In fact, levels with $N' \geq 15$ in normal O_2^+ and $N' \geq 18$ in $^{16,18}O_2^+$ are energetically allowed to dissociate to the $^3P_1$ level as well, and levels with $N' \geq 17$ in normal O_2^+ and $N' \geq 20$ in $^{16,18}O_2^+$ can dissociate to all three $^3P_{2,1,0}$ levels. However, the kinetic energy spectra show absolutely no structure giving any evidence of dissociation to the higher levels $^3P_{1,0}$. A careful comparison of the experimental spectra with spectra calculated with varying proportions of $^3P_1$ or $^3P_0$ added to $^3P_2$ allows the determination of upper limits to the branching ratios $^3P_1/^3P_2$ and $^3P_0/^3P_2$. These upper limits are all less than a few percent, and are consistent with all dissociation occurring to the $^3P_2$ limit. Figure 6 shows spectra calculated with different branching ratios $^3P_1/^3P_2$ for the line 18 Q_{11} of $^{16,18}O_2^+$. Clearly, less than 1% of the dissociation goes to $^3P_1$. Earlier data treated in an entirely different manner by Tadjeddine[36] led her to the value

$$^3P_1/^3P_2 \leq 0.007$$

for level $b\,^4\Sigma_g^-$, $v'=4$, $N'=15$ of normal O_2^+.

A quantitative theoretical prediction of the branching ratio in any particular case would require first the computation up to very large internuclear distances of the potential energy and of the couplings for the whole manifold of *gerade* states leading to $O^+(^4S^0) + O(^3P)$, i.e., (in order of increasing energy at small internuclear distances according to Beebe *et al.*[19]), $X\,^2\Pi_g$, $^4\Sigma_g^-$, $f\,^4\Pi_g$, $^2\Sigma_g^-$, $^6\Pi_g$, $^6\Sigma_g^-$, *and second, for each value of* J', *the solution of two systems of 18 coupled equations each.*

However, several limiting cases may be treated without *ab initio* calculations. They are the cases of (i) purely diabatic behavior of the system, (ii) purely adiabatic behavior of the system, (iii) strong radial coupling between all adiabatic states with the same Ω, (iv) strong radial and angular coupling between all states with the same e or f character,[37] and (v) the occurrence of centrifugal barriers.

We shall inspect in turn these five limiting model cases.

A. Purely diabatic behavior

In this model case, the dissociating state, either $^4\Sigma_g^-$ or $f\,^4\Pi_g$, is assumed to preserve its Λ and S quantum numbers and its initial expansion over the Ω's up to separation. From the determination of the (unique) combinations of products of atomic wave functions of O^+ and O for each of these states leading to species with each Ω, one gets the branching ratios shown in Table II. One may see that they slightly differ from one another, and that the average over Ω for each state yields the statistical branching ratio 5 : 3 : 1.

B. Purely adiabatic behavior

Here the system is assumed to preserve at all internuclear distances only the quantum numbers Ω and J and to avoid any crossing of states with this same pair of

TABLE II. Predicted branching ratios according to model case (i), where the system behaves in a purely diabatic way.

State	Ω	$^3P_2$	$^3P_1$	$^3P_0$
$^4\Sigma_g^-$	3/2	3/5	1/5	1/5
	1/2	23/45	21/45	1/45
	Average	5/9	3/9	1/9
$f\,^4\Pi_g$	5/2	7/10	3/10	0
	3/2	19/30	7/30	4/30
	1/2	47/90	27/90	16/90
	−1/2	11/30	15/30	4/30
	Average	5/9	3/9	1/9

quantum numbers. Under these assumptions, as first pointed out by Roche and Lefebvre-Brion,[38] according to the above-recalled ordering of the molecular states, both the $^4\Sigma_g^-$ and the $f\,^4\Pi_g$ states will correlate only with the $O^+(^4S^0)+O(^3P_2)$ limit, for all Ω's. Thus, the branching ratios will be $^3P_2:{}^3P_1:{}^3P_0=1:0:0$.

C. Strong radial coupling between adiabatic states with the same Ω

Here the dissociating system is still assumed to preserve Ω and J, but with numerous transitions between states with this same pair of quantum numbers induced by radial coupling. The probabilities for the system to dissociate into each of the $O^+(^4S^0)+O(^3P_i)$, $i=2,\ 1,\ 0$ limits will be proportional to cross sections σ_i, which according to scattering theory are proportional to $k_i|f_i|^2$, where k_i is the wave number associated with each outgoing channel and f_i is a scattering amplitude. In the limit of strong coupling between various states with a given Ω, the $|f_i|^2$ will be proportional to the statistical weights of the Ω components in each channel; this model yields the branching ratios given in Table III. These branching ratios strongly depend on the excess energy above the various thresholds. Each channel opens with a probability zero at threshold. Far from threshold, the branching ratios are 4 : 3 : 1 for Ω = 1/2, 3 : 2 : 1 for Ω = 3/2, and 24 : 17 : 7 in average. Of course, the component Ω = 5/2 should be included for the treatment of direct photodissociation $a\,^4\Pi_u-f\,^4\Pi_g$.

D. Strong radial and angular couplings between all states with the same *e* or *f* character

The restriction of the coupling to the same e or f character[37] arises from the fact that no part of the Hamiltonian couples states of different parity. This restriction has to be considered in the case of $^{16,18}O_2^+$ isotope only, whereas it is automatically fulfilled for the normal isotope.

In case (iv), the $|f_i|^2$ will simply be proportional to the statistical weight of each channel. Thus, the branching ratio will be $5k_2:3k_1:k_0$; far from threshold, it will tend towards the statistical ratio 5 : 3 : 1.

E. Dissociation process controlled by centrifugal barriers

The observation of the predissociation of the $v'=4$, $N'=9$ level of $^{16,16}O_2^+$, $b\,^4\Sigma_g^-$ (1.76 meV above threshold) and of the $v'=4$, $N'=14$ level of $^{16,18}O_2^+$, $b\,^4\Sigma_g^-$ (1.53 meV above threshold), both with nanosecond lifetimes, precludes the presence of any barriers higher than a few meV in the potential curve of the predissociating state(s). In effect, if any of these states did have such a barrier, that state would play no part in the predissociation except for some quasibound levels in accidental coincidence with particular levels of $b\,^4\Sigma_g^-$.

A centrifugal barrier might appear at higher values of N', precisely those where the levels ($b\,^4\Sigma_g^-$, $v'=4$, N') lie above the limits $O^+(^4S^0)+O(^3P_{1,0})$. If the centrifugal barrier was at large enough internuclear distance for the molecular states to already be split according to the three exit channels, then it would be possible for the predissociated level to lie above the barrier associated with the $^3P_2$ channels, but below the barriers associated with the two other channels.

However, this assumption would be in contradiction with the observation[9] of the predissociation of $^{16,16}O_2^+$, $b\,^4\Sigma_g^-$, $v'=3$, $N'=31$ (<7 meV above the $^3P_2$ threshold). A rotational barrier cannot be more than 11.7 meV high [difference between the $^{16,18}O_2^+$, $v'=4$, $N'=20$ level and the $O^+(^4S^0)+O(^3P_1)$ limit] at $N'=20$, and simultaneously less than 7 meV at $N'=31$, even for two different isotopic species!

Thus, we are left with model cases (i) to (iv). The branching ratios expected in each case are summarized in Table IV along with the experimental data. Only model (ii) agrees with the predissociation data.

However, it is difficult to reconcile the purely adiabatic behavior observed in the predissociation with the behavior observed for direct photodissociation to the $f\,^4\Pi_g$ state by Pernot *et al.*[22] They found a branching ratio $^3P_2:{}^3P_1:{}^3P_0$ close to the statistical ratio of 5 : 3 : 1. This was observed at energies of 91, 71, and 33 meV above the three thresholds, which is comparable to the energies of the $v'=5$, $N'=7$ level of $^{16,16}O_2^+$ of 116, 96, and 88 meV above the three thresholds. If, as proposed in Ref. 9, the $f\,^4\Pi_g$ state is responsible for (22 ± 10)% of the predissociation of the b state, then it appears that the $^3P_1:{}^3P_2$ branching ratio in the predissociation should be (8 ± 4)%, significantly different from the present results.

We have at present no good answer to this question. One possibility would be that the $f\,^4\Pi_g$ state plays no part in the predissociation and that the observed linewidths[9] should be explained by a contribution of the $^2\Sigma_g^+$ rather than the $f\,^4\Pi_g$ state. However, this explanation is hard to reconcile with the location of the potential

TABLE III. Predicted branching ratios according to model case (iii), where strong radial coupling is assumed between adiabatic states with same Ω. If only channels $^3P_2$ and $^3P_1$ are energetically allowed, the branching ratio is obtained from the same formula where k_0 is set equal to zero.

Ω	$^3P_2$	$^3P_1$	$^3P_0$
1/2	$4k_2$	$3k_1$	k_0
3/2	$3k_2$	$2k_1$	k_0
Average	$k_2\times(72k_2+17k_1+24k_0)$	$k_1\times(50k_2+12k_1+17k_0)$	$k_0\times(20k_2+5k_1+7k_0)$

TABLE IV. Comparison of expected and observed branching ratios, considering predissociation only through the $^4\Sigma_g^-$ state.

State and line	Photofragment energy W in various channels (meV)			Ratio	Model				Experiment
	$^3P_2$	$^3P_1$	$^3P_0$		(i)	(ii)	(iii)	(iv)	
$^{16}O^{18}O^+$, $v'=4$									
$18\,Q_{11}$	20.86	1.21	···	$^3P_1:{}^3P_2$	0.72	0	0.18	0.14	≤0.005
$19\,Q_{11}$	24.98	5.33	···	$^3P_1:{}^3P_2$	0.72	0	0.34	0.28	≤0.01
$20\,Q_{11}$	31.32	11.67	3.24	$^3P_1:{}^3P_2$	0.76	0	0.45	0.37	≤0.02
				$^3P_0:{}^3P_2$	0.12	0	0.09	0.06	≤0.02
$^{16,16}O_2^+$, $v'=5$ / $7Q_{43}$	115.8	96.2	87.7	$^3P_1:{}^3P_2$	0.79	0	0.67	0.55	≤0.04
				$^3P_0:{}^3P_2$	0.11	0	0.23	0.17	≤0.03

curve of the $^2\Sigma_g^+$ state as calculated *ab initio* by Beebe *et al.*[19] On the other hand, we can give no clear reason why the $^4\Sigma_g^-$ (and possibly the $^2\Sigma_g^+$) state(s) would dissociate in a purely adiabatic way, whereas the $f\,^4\Pi_g$ state would dissociate in a purely diabatic way.

VI. CONCLUSIONS

It has been demonstrated that kinetic energy spectra of photopredissociation fragments from individual transitions can yield the values of the anisotropy parameter β of their angular distributions in the c. m. reference frame, with an accuracy of ±0.05 or better. The theory developed by Zare[3,4] to predict such angular distributions for slow predissociations of molecules in Hund's cases (a) or (c) was generalized to any kind of predissociation of diatomics, to any coupling scheme, and, in particular, to Hund's case (b), which is relevant for the present experiments. For a large set of lines with various quantum numbers J'', Ω'', J', and N', the β values derived from experiment and from theory were found to be in agreement.

From the same experimental data, photofragment kinetic energies in the c. m. frame W were determined with an accuracy (near threshold) as good as ±1.1 cm^{-1}. This high accuracy was used to improve the accepted values of bond dissociation energies of O_2 and O_2^+ to within a few cm^{-1}. The ensemble of W values directly obtained from experiment was in fair agreement with those predicted by D. L. Albritton using molecular constants derived from earlier experimental data.

It was also shown that, whatever the energy of the predissociated level above threshold was, even as high as 100 meV, the atomic oxygen fragment was only formed in the $^3P_2$ fine-structure level. Upper limits to the relative yields of the two other levels ($^3P_1$ and $^3P_0$) were found to be of the order of 10^{-2}. This selection rule was shown to mean that the $^4\Sigma_g^-$ predissociating state was dissociating in a purely adiabatic way, in contrast with the $f\,^4\Sigma_g^-$ state previously studied in direct photodissociation experiments.

It is interesting to notice that the absence of any predissociation of $b\,^4\Sigma_g^-$ into the two higher fine-structure channels $O^+(^4S^0)+O(^3P_{1,0})$ is perfectly consistent with the absence of any difference in the predissociation linewidths[9] of the $b\,^4\Sigma_g^-$ levels lying higher or lower than these channels. Clearly, if the predissociating $^4\Sigma_g^-$ state would have dissociated without any long-distance coupling with other states, it would have fed the three dissociation channels according to angular momentum algebra [see above, model (i)], and the predissociation rate would have been smaller below each of the upper thresholds than above.

Extensions of this technique to an even more detailed look at the dissociation process can be seen. It seems possible to determine the quantum number Ω of the separating fragments. The term $A_{e,f}(\Omega)$ in Eq. (16) is computed through Eq. (17) with the assumption that the Ω repartition is determined by the predissociation process and does not change during the evolution of the predissociating state. If some coupling with other states occurs by rotational coupling during the separation of the fragments, the final Ω repartition may be different from tne one considered in our calculations. From Eqs. (19)–(21), it is clear that, since in our case Ω is much smaller than J', any disagreement between expected and actual Ω repartitions will be noticeable only in the $\cos^2\theta$ part of the angular distribution for the Q branches. However, in the present experimental setup, fragments ejected in the direction of polarization of the laser (where $\cos^2\theta$ is maximum and equal to 1) are indistinguishable from those ejected in any other direction perpendicular to the ion beam direction. This can be overcome if the circular apertures used for beam collimation are replaced by thin slits either parallel or perpendicular to the laser polarization. In this way, a significant variation of Ω during the final separation of the fragments may be detected.

Another possible extension is the separation of the M_J components involved in each line of the spectrum. From preliminary work by Gaillard *et al.*,[10] the lines are strongly broadened by introducing a magnetic field along the ion beam, and therefore their M_J components could probably be resolved in favorable cases. This arises from the fact that the spin vector S is much more aligned with respect to J in a given F' level of the Hund's case (b) $b\,^4\Sigma_g^-$ state than in a given Ω'' level of the Hund's

case (a) $a\,^4\Sigma_u$ state. Theoretical angular distributions have been worked out by Beswick.[27]

VII. ACKNOWLEDGMENTS

The authors are pleased to acknowledge fruitful discussions with Drs. D. L. Albritton, M. Tadjeddine, A. -L. Roche, and H. Lefebvre-Brion, and the communcation of their results prior to publication. The research at SRI was supported by the National Science Foundation under Grant No. CHE 77-00428, and by the U. S. Army Research Office.

APPENDIX

The angular distribution is governed by the factors[3] [see Eq. (18)]

$$I_{J'',J''\Omega}(\theta)=\sum_{M''}\left|C(J''1J';M''0M')D^{J''}_{M''\Omega}\right|^2, \qquad \text{(A1)}$$

where $C(J''1J';M''0M')$ is a Clebsch–Gordan coefficient[28] and $D^{J''}_{M''\Omega}$ is a Wigner rotation matrix element.[28] Using the Clebsch–Gordan series for the product of two Wigner matrices,[28] we obtain that

$$C(J''1J';M''0M')D^{J''}_{M''\Omega}$$

$$=\sum_{\mu}C(J''1J';\mu,\Omega-\mu,\Omega)D^{J''}_{M''\mu}D^{1}_{0,\Omega-\mu}\,. \qquad \text{(A2)}$$

Squaring both sides and summing over M'', we find

$$I_{J',J''\Omega}(\theta)=\sum_{\mu}\sum_{\mu'}C(J''1J';\mu,\Omega-\mu,\Omega)C(J''1J';\mu',$$

$$\times\Omega-\mu',\Omega)\,D^{1}_{0,\Omega-\mu}D^{1*}_{0,\Omega-\mu'}\sum_{M''}D^{J''}_{M''\mu}D^{J''*}_{M''\mu'}\,, \qquad \text{(A3)}$$

and using the unitarity of the rotation matrices, we obtain

$$I_{J',J''}(\theta)=\sum_{\mu}\left|C(J''1J';\mu,\Omega-\mu,\Omega)\right|^2\left|D^{1}_{0,\Omega-\mu}\right|^2, \qquad \text{(A4)}$$

which gives the final expressions (19)–(21).[3]

[1]G. E. Busch and K. R. Wilson, J. Chem. Phys. **56**, 3626 (1972); **56**, 3639 (1972); **56**, 3655 (1972); M. Dzvonik, S. Yang, and R. Bersohn, J. Chem. Phys. **61**, 4408 (1974); J. H. Ling and K. R. Wilson, J. Chem. Phys. **63**, 101 (1975).
[2]C. Pernot, J.-B. Ozenne, M. Pánczél, and J. Durup, X ICPEAC Abstracts of Papers, p. 94 (Paris, 1977).
[3]R. N. Zare, Ph.D. Thesis, Harvard University (1964).
[4]R. N. Zare, Mol. Photochem. **4**, 1 (1972).
[5](a) R. Bersohn and S. H. Lin, Adv. Chem. Phys. **16**, 67 (1969); (b) C. Jonah, J. Chem. Phys. **55**, 1915 (1971); S. Yang and R. Bersohn, J. Chem. Phys. **61**, 4400 (1974).
[6]S. Mukamel and J. Jortner, (a) J. Chem. Phys. **61**, 5348 (1974); (b) Chem. Phys. Lett. **29**, 169 (1974).
[7]A. Carrington, P. G. Roberts, and P. J. Sarre, Mol. Phys. **34**, 291 (1977); **35**, 1523 (1978).
[8]M. Tadjeddine, R. Abouaf, P. C. Cosby, B. A. Huber, and J. T. Moseley, J. Chem. Phys. **69**, 710 (1978).
[9]J. T. Moseley, P. C. Cosby, J.-B. Ozenne, and J. Durup, J. Chem. Phys. **70**, 1474 (1979).
[10]M. Horani, H. Bukow, M. Carré, M. Druetta, and M. L. Gaillard, J. Phys. (Paris) **40**, C1-57 (1979); M. L. Gaillard (private communication).
[11]J. Schopman, A. K. Barua, and J. Los, Phys. Lett. A **29**, 112 (1969).
[12]B. A. Huber, T. M. Miller, P. C. Cosby, H. D. Zeman, R. L. Leon, J. T. Moseley, and J. R. Peterson, Rev. Sci. Instrum. **48**, 1306 (1977).
[13]J. T. Moseley, M. Tadjeddine, J. Durup, J.-B. Ozenne, C. Pernot, and A. Tabché-Fouhaillé, Phys. Rev. Lett. **37**, 891 (1976).
[14]D. L. Albritton, J. T. Moseley, P. C. Cosby, and M. Tadjeddine, J. Mol. Spectrosc. **70**, 326 (1978).
[15]A. Tabché-Fouhaillé, J. Durup, J. T. Moseley, J.-B. Ozenne, C. Pernot, and M. Tadjeddine, Chem. Phys. **17**, 81 (1976).
[16]P. C. Cosby, J.-B. Ozenne, J. T. Moseley, and D. L. Albritton, J. Mol. Spectrosc. (in press).
[17]M. Tadjeddine, Thèse de Doctorat d'Etat, Orsay (1978).
[18]P. Erman and M. Larsson, Phys. Scr. **15**, 335 (1977); all observed transitions arise from $b\,^1\Sigma_g^+$, $v'=0$–3 [P. Erman (private communication, 1978)].
[19]N. H. F. Beebe, E. W. Thulstrup, and A. Andersen, J. Chem. Phys. **64**, 2080 (1976).
[20]D. L. Albritton, A. L. Schmeltkopf, W. J. Harrop, R. N. Zare, and J. Czarny, J. Mol. Spectrosc. **67**, 157 (1977).
[21]J. Durup, Colloq. Int. C.N.R.S. **273**, 107 (1977).
[22]C. Pernot, J.-B. Ozenne, M. Pánczél, and J. Durup, X ICPEAC Abstracts of Papers, Vol. 1, p. 94 (Paris, 1977).
[23]An earlier computer program for this kind of use was developed by G. Comtet and is described in detail in her Thèse de Doctorat de Spécialité, Orsay (1977).
[24]D. L. Albritton (private communication).
[25]U. Fano, Phys. Rev. **124**, 1866 (1961).
[26]M. L. Gaillard (private communication).
[27]J. A. Beswick, Chem. Phys. (in press).
[28](a) M. E. Rose, *Elementary Theory of Angular Momentum* (Wiley, New York, 1957); (b) D. M. Brink and G. R. Satchler, *Angular Momentum* (Oxford University, Oxford, 1962).
[29]I. Kovács, *Rotational Structure in the Spectra of Diatomic Molecules* (Hilzer, London, 1969).
[30]M. Tadjeddine (private communication, 1978).
[31]D. L. Albritton (private communication, 1978).
[32]K. Yoshino and Y. Tanaka, J. Chem. Phys. **48**, 4859 (1968).
[33]C. E. Moore, "Selected Tables of Atomic Spectra, Atomic Energy Levels and Multiplet Tables," Natl. Stand. Ref. Data Ser. Natl. Bur. Stand. **3** (1976).
[34]P. Brix and G. Herzberg, Can. J. Phys. **32**, 110 (1954).
[35]K.-P. Huber and G. Herzberg, *Molecular Spectra and Molecular Structure IV. Constants of Diatomic Molecules* (Van Nostrand Reinhold, New York, 1979).
[36]M. Tadjeddine, J. Chem. Phys. (submitted for publication).
[37]J. M. Brown, J. T. Hougen, K.-P. Huber, J. W. C. Johns, I. Kopp, H. Lefebvre-Brion, A. J. Merer, D. A. Ramsey, J. Rostas, and R. N. Zare, J. Mol. Spectrosc. **55**, 500 (1975).
[38]A. L. Roche and H. Lefebvre-Brion (private communication, 1978).

APPENDIX D

Laser predissociation spectroscopy of the $f^4\Pi_g$ state of O_2^+[a)]

H. Helm,[b)] P. C. Cosby, and D. L. Huestis

Molecular Physics Laboratory, SRI International, Menlo Park, California 94025
(Received 19 May 1980; accepted 2 June 1980)

Two quasibound vibrational levels of the $f^4\Pi_g$ state of O_2 have been observed by monitoring O^+ photofragments resulting from absorption of laser radiation by the $a^4\Pi_u$ state. The first spectroscopic constants for the f state have been derived from rotational and isotopic analyses. Measurements of the predissociation linewidths and photofragment kinetic energies have been used to refine estimates of the barrier in the f state potential curve and to identify likely predissociation mechanisms.

I. INTRODUCTION

The O_2^+ ion has been the subject of numerous experimental and theoretical investigations to determine the many electronic states of this important species that describe its physical and chemical properties. To date, eight electronic states of this ion have been located by photoelectron spectroscopy[1,2] and emission spectroscopy.[3-6] Five of these states have been observed at sufficiently high resolution to allow accurate representation of portions of their potential energy curves.[6] This makes O_2^+ one of the better understood diatomic molecular ions. Nevertheless, twelve electronic states[2,4,6] $^{2,4}\Sigma^+$, $^{2,4}\Pi_{g,u}$ are expected to arise from the combination of $O^+(^4S^o)+O(^3P)$, the lowest energy separated atom limit of the ion.[7] Of these states, only the $X\,^2\Pi_g$, $A\,^2\Pi_u$, and $a\,^4\Pi_u$ states are known from the above experimental techniques. Figure 1 shows several O_2^+ electronic states lying in the region of the lowest separated atom limit that are relevant to the present study.

Evidence for two additional states correlating to the $O^+(^4S^o)+O(^3P)$ limit has been obtained from the photodissociation of O_2^+. Measurements of the kinetic energy and angular distributions of the O^+ photofragments produced at several visible wavelengths have identified a direct dissociation process (involving transitions from the $a\,^4\Pi_u$ state to the repulsive wall of the $f\,^4\Pi_g$ state) that correlates to this limit.[8] In addition, a predissociation of the O_2^+ ions was also observed. Although initially believed to be predissociation of quasibound levels of the $f\,^4\Pi_g$ state,[9] which is predicted by *ab initio* calculations[10,11] to have a barrier in its potential curve at large internuclear distances, these observations were later conclusively identified as transitions in the $b\,^4\Sigma_g^- - a\,^4\Pi_u$ system in which those levels of the b state lying above the $O^+(^4S^o)+O(^3P_2)$ limit are predissociated.[12-14] Detailed measurements of the predissociation lifetimes as a function of b state vibrational, rotational, and fine-structure level led to the conclusion that the predissociation occurred predominately through spin–orbit coupling to the $d\,^4\Sigma_g^+$ state.[15,16] Unfortunately, only the general locations of the $d\,^4\Sigma_g^+$ and $f\,^4\Pi_g$ states were established by these measurements.

We report here the first experimental observation of quasibound levels in the $f\,^4\Pi_g$ state. Our observation confirms theoretical predictions of a barrier in the potential curve of this state at large internuclear distances. The presence of this barrier is found to support at least two predissociated, quasibound vibrational levels in this state at energies above the $O^+(^4S^o)+O(^3P_2)$ separated atom limit. These levels are observed by pumping transitions to them from $v''=5$, 6 of the $a\,^4\Pi_u$ state and monitoring the production of O^+ photofragment ions. Lifetime measurements suggest that the quasibound levels are predissociated by tunneling through the potential barrier and by coupling to other electronic states.

II. EXPERIMENTAL METHOD

The apparatus used in this study has been described in detail elsewhere,[17] as has its application to the high-resolution spectroscopy of ions.[18] Briefly, the beam of

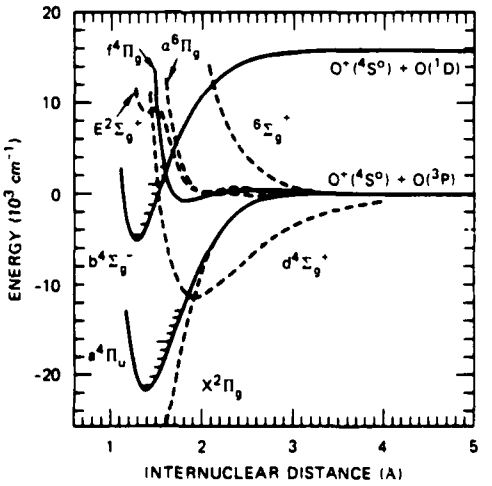

FIG. 1. $a\,^4\Pi_u$ and $b\,^4\Sigma_g^-$ states of O_2^+ are shown together with all gerade states from the $O^+(^4S^o)+O(^3P)$ limit. The potentials of the a and the b states are the RKR potentials from Ref. 18. The f state shown is the Morse potential generated using the spectroscopic constants for the $\Omega'=\frac{3}{2}$ component obtained in this work. The potential curve of the d state is the theoretical curve from Ref. 11. The remaining curves are the theoretical curves from Ref. 10.

a)Research supported by Army Research Office and Air Force Office of Scientific Research.
b)Max Kade Foundation Fellow at SRI International 1979–1980.

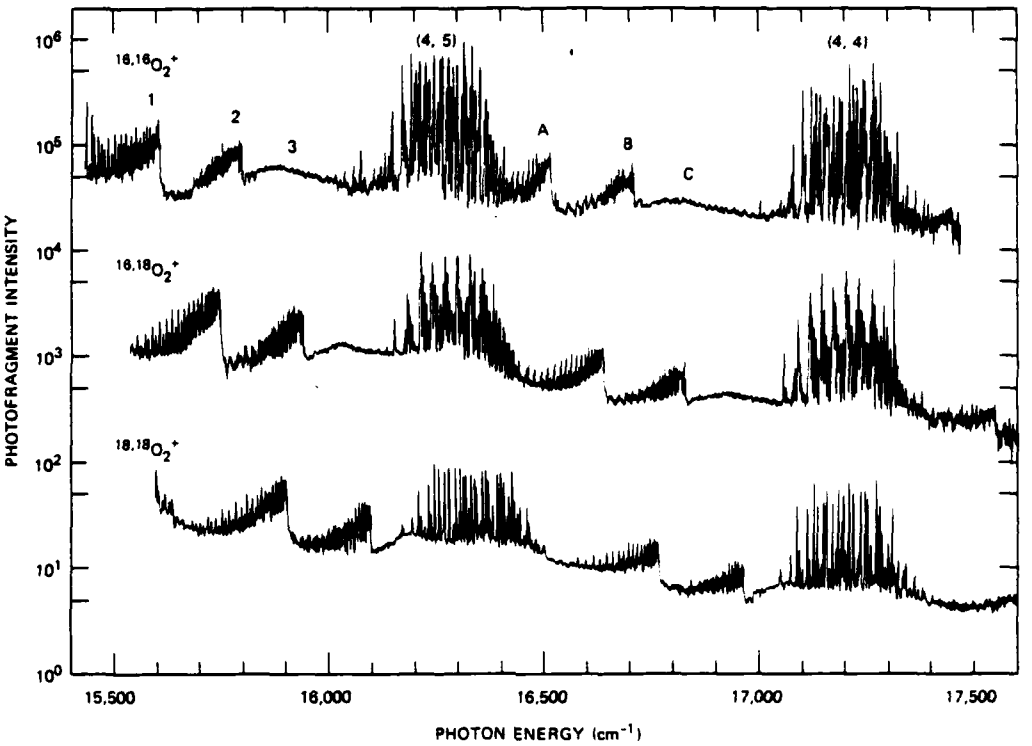

FIG. 2. Wavelength dependence for the production of O^+ photofragments having center-of-mass kinetic energies in the range 0–70 meV from O_2^+ observed at low (1 cm^{-1}) resolution. The bands labeled (4, 4) and (4, 5) refer to the $b\,^4\Sigma_g^- - a\,^4\Pi_u$ system. The six features produced from the photodissociation of the $f\,^4\Pi_g$ state are labeled 1, 2, 3 and A, B, C. The intensities for $^{16,18}O_2^+$ and $^{16,16}O_2^+$ have been multiplied by 10^2 and 10^4, respectively.

a tunable dye laser is made coaxial with a fast ion beam of O_2^+ over an interaction length of about 60 cm. The O_2^+ ions, produced by electron impact (100 eV) on O_2, are accelerated to typically 4000 eV, mass selected, collimated, and merged with the laser beam. If an absorption of photons occurs that results in photodissociation, the O^+ photofragments produced are detected after kinetic energy analysis.

The initial search for the new spectra was made with the dye laser operating multimode and scanning the wavelength of the laser with a birefringent filter. This method results in spectra that are limited in resolution by the 1 cm^{-1} laser bandwidth. Portions of these spectra were then recorded at high resolution using a single-mode ring dye laser having a bandwidth of approximately ±25 MHz (0.0003 Å). In this mode of operation, kinematic compression of the velocity spread in the ion beam produces a total instrumental bandwidth of less than 100 MHz (0.003 cm^{-1}). The actual resolution achieved in these spectra is limited by the natural linewidths of the observed transitions. The wavelength variation of the single-mode laser was accomplished by piezoelectrically scanning a 75 GHz free-spectral-range (FSR) air-spaced intracavity étalon. This technique allowed continuous scans over a range of about 2 cm^{-1} for a fixed setting of the birefringent filter. At the beginning and end of each scan the wavelength of the laser was measured using a digital wavemeter. The linearity of the scan between these end points was monitored by observing the transmission of the laser through a 1.5 GHz FSR confocal interferometer. The overall accuracy of the measurements reported here was limited by the determination of the linecenters of the lifetime broadened transitions to approximately ±0.05 cm^{-1}.

III. RESULTS

The wavelength dependence for the production of O^+ photofragments was measured over the wavelength range of 6450–5750 Å at low (1 cm^{-1}) resolution for $^{16,16}O_2^+$, $^{16,18}O_2^+$, and $^{18,18}O_2^+$. Figure 2 shows the spectra obtained for photofragments produced with center-of-mass kinetic energies (W) between approximately 0–70 meV. The $(v', v'') = (4, 5)$ and (4, 4) bands of the $b\,^4\Sigma_g^- - a\,^4\Pi_u$ First Negative System appear as the most prominent features in the spectra. These bands have been extensively studied and are well understood.[13,18] In addition, a continuum due to direct dissociation from the repulsive wall of the $f\,^4\Pi_g$ state[8] appears as a background in these spectra.

Six new features labeled 1, 2, 3 and A, B, C are observed in the spectra shown in Fig. 2. The difference in

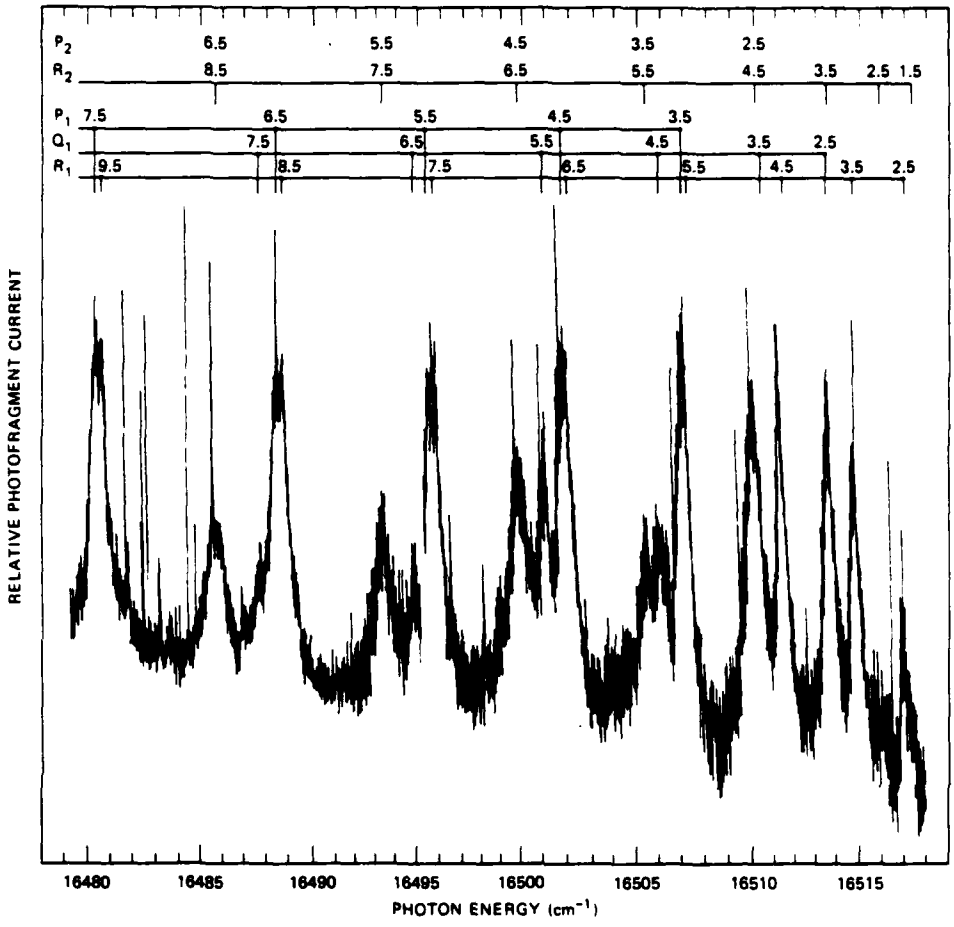

FIG. 3. High-resolution spectrum of the bandhead region of the (2,5) band (band A) of the $f \rightarrow a$ system. For photon energies greater 16 495 cm^{-1} the photofragment signal has been multiplied by a factor of 2.

the bandhead positions of $1-A$ and $2-B$, and the difference in the position of the envelopes of features $3-C$ coincide with the known separations[18] of $v''=5$ and 6 of the $a\,^4\Pi_u$ state in each of the three isotopic molecules. This establishes that the lower (absorbing) level is $a\,^4\Pi_u$ ($v''=5$) for A, B, C and $a\,^4\Pi_u$ ($v''=6$) for 1, 2, 3. In addition, the maximum center-of-mass kinetic energies of the photofragments produced in the bandhead regions of these systems is found to be $W\sim 24$ meV in bands 1, A and $W\sim 40$ meV in bands 2, B. Features 3, C, which do not exhibit a bandhead, produced photofragments with $W\sim 57$ meV in the regions of their maxima. The differences in W among the two pairs of bands 1, A and 2, B roughly reflects the photon energy separation of their bandheads, as expected for a progression in the vibrational levels of the upper electronic state. In addition, W was found to progressively increase from the bandhead values with decreasing photon energy within each structured feature. Such behavior is consistent with the red-shaded appearance of the bands, where decreasing transition energy is expected to access increasingly higher rotational levels of the dissociating state. In contrast, W was found to increase with increasing photon energy within the unresolved features 3, C, as expected for a direct photodissociation process or for predissociation in a violet-shaded band.

Given the known dissociation energy of the a state,[19,20] these observations suggest the four structured bands 1, 2, A, B arise in transitions from $a\,^4\Pi_u$ ($v''=5$, 6) to two predissociated levels of an electronic state lying just above the $O^+(^4S^\circ)+O(^3P)$ dissociation limit.

A. Band identification

In order to understand the rotational structure of these bands and thus identify the predissociated electronic state, the features A, B, and C of $^{16,18}O_2^+$ were investigated at high resolution. Portions of the high-resolution scans in bands A and B are shown in Figs. 3 and 4. Each figure is composed of a number of individual étalon

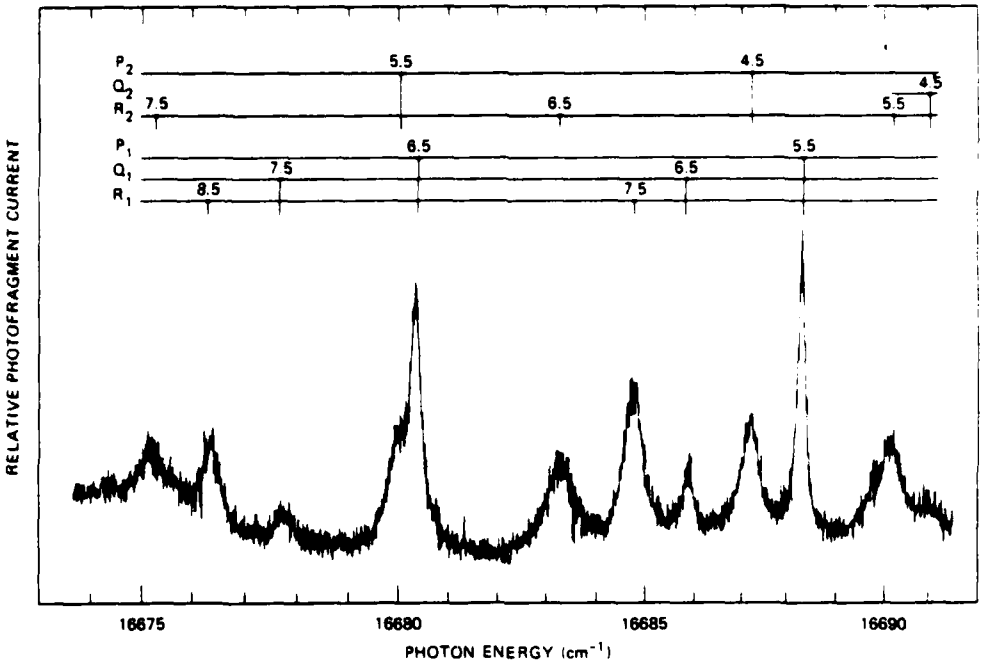

FIG. 4. Portion of the high-resolution spectrum of the (3, 5) band of the $f \leftarrow a$ system (band B).

scans. Feature C was found to be structureless even at high resolution and is not shown.

A first analysis of the high-resolution spectra was made using the conventional method of second differences.[7] In both bands A and B, two subbands could be identified. In band B, the individual transitions are well separated and the rotational analysis was straightforward. The lower state rotational constants obtained from the analysis were in agreement with the known constants[18] for $a\,^4\Pi_u$ ($v'' = 5$), thus confirming the assignment of this state from the low-resolution isotope shifts.

The lowest lines appearing in the two subbands of B were $R(2.5)$, $Q(2.5)$, $P(3.5)$ and $R(1.5)$, $P(2.5)$, respectively. In addition, the intensity of the transitions in the Q branch of each subband was found to decrease strongly with increasing J. The presence of consecutive rotational levels in each subband of this homonuclear molecule with zero nuclear spin, together with the intensity distribution of the rotational lines,[21] suggests $\Delta\Lambda = 0$ for this band, i.e., a $\Pi - \Pi$ transition. In addition, the clear termination of the one subband at $J' = 5/2$ requires that the multiplicity of the upper state be quartet or higher. The intensities of the observed bands relative to those of the $b - a$ system are consistent with an allowed electronic transition. Thus, the upper state is expected to be $^4\Pi_g$. The only $^4\Pi_g$ state lying in the region of the observed bands[10] is the $f\,^4\Pi_g$ state.

For a $\Pi - \Pi$ transition in which both states are well described by Hund's case (a), the strongest features are expected to be the P, Q, and R branches of the major subbands characterized by $\Delta\Omega = 0$.[7] Based on the J' numbering of the lowest lines observed, we identify the two subbands $f\,^4\Pi_{5/2} - a\,^4\Pi_{5/2}$ and $f\,^4\Pi_{3/2} - a\,^4\Pi_{3/2}$. To our knowledge, this is the first time that a $^4\Pi - {}^4\Pi$ transition has been reported. It is also only the second $\Pi - \Pi$ transition with a multiplicity greater than three for which a rotational analysis has been performed.[22]

The lines in band A are substantially less well resolved than those of system B. Consequently, only the $\Omega = \frac{5}{2}$ subband could be identified with certainty. In the second subband the respective lines $R(J+2)$ and $P(J)$ appear persistently blended. However, the lowest line observed could be assigned to $R(1.5)$ and we attribute this second subband to $\Omega = \frac{3}{2}$. Further support for these assignments as well as those in system B comes from measurement of the photofragment kinetic energies, which will be discussed in a subsequent section.

On the basis of the rotational analysis, it appears that two vibrational levels in the $^4\Pi_{5/2}$ and $^4\Pi_{3/2}$ substates of $f\,^4\Pi_g$ are predissociated. Term values for the observed levels of the f state were constructed using the known term values for the $a\,^4\Pi_u$ state and the measured transition energies. These values are given in Table I relative to the $O^+(^4S^\circ) + O(^3P_2)$ separated atom limit. The absolute accuracy of these values is limited by the uncertainty in the dissociation energy[20] of the a state to ± 1.8 cm^{-1}. However, the relative accuracy of the levels reflects the optical precision of the present measurements that is determined by the predissociation linewidths. Whenever more than one observed transition terminated in a particular upper level, as was the case for two thirds of the levels, the term value quoted is the

TABLE I. Rotational term values for the $\Omega' = \frac{1}{2}$ and $\Omega' = \frac{3}{2}$ substates of $v' = 2$ and 3 of the $f\,^4\Pi_g$ state. The energies, given in cm^{-1}, are relative to the $O^+(^4S^o) + O(^3P_2)$ limit. The energy scale is based on the dissociation energy D (O_2^+, $a\,^4\Pi_u$, $v'' = 0$, $J'' = \frac{3}{2}$, $\Omega'' = \frac{3}{2}$) = 21 270.70 cm^{-1}.

	Band A $v' = 2$		Band B $v' = 3$	
J'	$\Omega' = \frac{3}{2}$	$\frac{1}{2}$	$\frac{3}{2}$	$\frac{1}{2}$
1.5		...		344.22[a]
2.5	109.85	158.32	303.59	346.33
3.5	113.28	161.85	306.53	349.27
4.5	117.61	166.60	310.33	353.10
5.5	122.98	172.08	314.93	357.70
6.5	129.32	178.48[a]	320.36	363.09
7.5	136.54	185.78[a]	326.62	369.36
8.5	148.77	194.48[a]	333.68	376.35[a]
9.5	154.03[a]	...	341.50[b]	384.27[a]
10.5	164.13[a]	...	350.13[a]	392.98[b]
11.5	...[c]	...	359.60[b]	...
T_v^Ω	105.64	154.01	300.05	342.74
B_v^Ω	0.484 75	0.500 53	0.415 13	0.416 53

[a]Term value obtained from a single transition only.
[b]Obtained from completely blended lines.
[c]Indicates an unobserved, but allowed, level.

arithmetic mean of the individual values obtained from the different branches. These mean values deviated from the individual values by less than 0.05 cm^{-1} except for the $\Omega = \frac{3}{2}$ component of band A, where the maximum deviation was 0.15 cm^{-1}. Such a large deviation may not be surprising, since all lines in this subband are blended and the width of the blended lines is typically 0.5 cm^{-1}.

As may be seen from Table I, the $\Omega' = \frac{3}{2}$ components lie lower in energy than the $\Omega' = \frac{1}{2}$ in both vibrational levels; that is, the f is inverted. Since the a state is also inverted, we denote transitions in the $\Omega = \frac{1}{2}$ subbands with index 1 and those in the $\Omega = \frac{3}{2}$ subbands with index 2. Figures 3 and 4 show the assignment of the lines in the high-resolution spectra using this notation.

The rotational term values for the individual substates of the $f\,^4\Pi_g$ state were found to be represented within the measurement precision by the simple formula

$$F_v^\Omega = J'(J'+1)B_v^\Omega + T_v^\Omega , \tag{1}$$

where B_v^Ω denotes the effective rotational constant for the substate Ω of vibrational level v and T_v^Ω represents the apparent term origin for this substate with respect to $O^+(^4S^o) + O(^3P_2)$. The two constants are given in Table I for the respective substates.

The fine structure coupling constant A_v' is, to a first approximation, equal to the separation of the respective term origins $T_v^{3/2} - T_v^{1/2}$. This separation is found to be 48.4 and 42.7 cm^{-1}, respectively, for the lower and higher vibrational level observed here (see Table I).

B. Vibrational analysis

Variations in the transition frequencies to the observed predissociated vibrational levels of the $f\,^4\Pi_g$ state with isotopic substitution of the O_2^+ ion can be used to establish the vibrational numbering of the levels and determine the dissociation energy of this state.[7] However, an isotope analysis of a multiplet band system would normally be made using true band origins; that is, the band origins would be obtained by subtracting the magnetic contributions from the observed term values. Several difficulties preclude the direct use of this procedure in the present experiment: (a) discrete structure attributable to the $\Omega = \pm\frac{1}{2}$ components does not appear in the predissociation spectra; (b) only low-resolution spectra are available for the $^{16,18}O_2^+$ and $^{18,18}O_2^+$ isotopic combinations; and (c) persistent blending of the lines in the low-resolution spectra restricted an unambiguous assignment to the $\Omega = \frac{3}{2}$ components of bands 1 and A. Consequently, we were forced to perform the isotope analysis using the $\Omega = \frac{3}{2}$ components alone.

The known vibrational spacings of the $a\,^4\Pi_u$ state were used in the analysis together with the measured separations of the term origins, $T_v^{3/2}$, of bands 2 – 1 and $B - A$ of $^{16,16}O_2^+$ and the separation of the respective term origins of $1 - A$ in the three isotopic combinations. Assuming a vibrational energy expression of the form

$$G'(\xi) = \omega_e'\,\xi - \omega_e' x_e'\,\xi^2 , \tag{2}$$

where

$$\xi = (v' + \tfrac{1}{2})\left(\frac{\mu^{16,16}}{\mu^{i,j}}\right)^{1/2} , \tag{3}$$

μ is the reduced mass, and i and j represent 16 or 18, the vibrational numbering obtained is $v' = 2$ for bands 1, A and $v' = 3$ for bands 2, B. The vibrational constants obtained are given in Table II. In subsequent discussion we will refer to the structured bands 1, 2, A, and B as $(v', v'') = (3, 6)$, $(2, 6)$, $(3, 5)$, and $(2, 5)$, respectively.

C. Transition linewidths

The individual lines in the (3, 5) vibrational band (Fig. 3) are separated well enough to determine the variation of the linewidth Γ as a function of the quantum number J'. Since the instrumental linewidth is small compared to the transition linewidths observed here, we have taken Γ as the full width at half-maximum (FWHM) of the line profiles. Figure 5 shows the variation of Γ with J' for the $\Omega = \frac{3}{2}$ and $\frac{1}{2}$ components of the (3, 5) vibrational band. The lines in the $\Omega = \frac{1}{2}$ subband are consistently about 6 GHz wider than those in the

TABLE II. Effective spectroscopic constants for the $\Omega = \frac{3}{2}$ substate of $f\,^4\Pi_g$.

ω_e	470.7 cm^{-1}
$\omega_e x_e$	46.0 cm^{-1}
B_e	0.6588 cm^{-1}[a]
α_e	0.0696 cm^{-1}[a]
R_e	1.79 Å[b]

[a]Obtained from the relation $B_v = B_e - \alpha_e(v + \frac{1}{2})$ and the $B_v^{3/2}$ values from Table I.
[b]Derived from B_e.

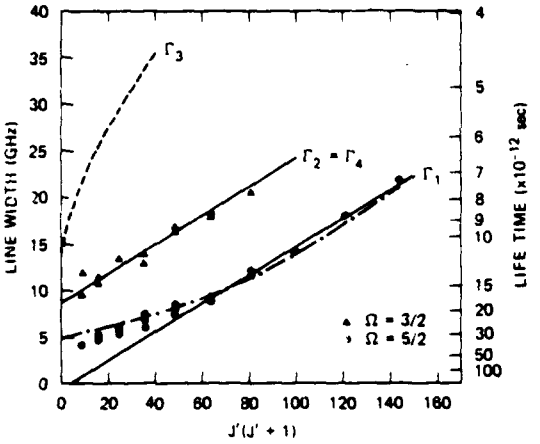

FIG. 5. Transition linewidths Γ and predissociation lifetimes τ for the (3, 5) band of the $f-a$ system as a function of $J'(J'+1)$. The dots and triangles are the experimental values obtained from the $\Omega=\frac{3}{2}$ and $\frac{1}{2}$ subbands, respectively. The full lines represent the best fit of Eqs. (8a) and (8b) to these data. The dotted line is the prediction of Eq. (8c) using the constants obtained from the fit of Γ_1 and Γ_2. The dot-dash curve represents the tunneling lifetime of the $\Omega'=\frac{3}{2}$ substate predicted by the model potential barrier shown in Fig. 8.

$\Omega=\frac{5}{2}$ subband. In addition, both fine-structure components show linewidths which increase approximately with $J'(J'+1)$. Since the lifetime of the levels in the $a\,^4\Pi_u$ state is extremely long, the linewidths observed here directly reflect the predissociation lifetimes of the upper state. Figure 5 shows that the predissociation lifetime τ decreases from 3×10^{-11} s for $\Omega'=\frac{3}{2}$ and 1.5×10^{-12} s for $\Omega'=\frac{1}{2}$ as the rotation of the molecules increases.

Persistent blending of the lines in the (2, 5) vibrational band did not allow a systematic study of linewidth variations in $v'=2$. However, the single unblended line $R_1(4.5)$ in this band was found to have a linewidth of ~13 GHz (i.e., a predissociation lifetime of ~12 ps) as compared to ~7 GHz for the corresponding transition in the (3, 5) band. The spectra indicate that the other lines in the (2, 5) band have comparable or even larger linewidths.

D. Photofragment kinetic energies

An independent confirmation of the consistency of the rotational assignments comes from the measurement of the kinetic energies of the photofragments. The term values listed in Table I predict directly the photofragment energies with respect to the lowest dissociation limit $O(^3P_2)+O^+(^4S^\circ)$. This prediction is possible since both the term values and the dissociation energy of the $a\,^4\Pi_u$ state are known.

The $O(^3P)$ dissociation product has three closely spaced fine-structure components. The energies of the predissociated levels of the f state relative to each of these three dissociation limits is shown in Fig. 6. It can be seen that all levels of $v'=3$ lie energetically above all three fine-structure states. In addition, the higher rotational levels of $v'=2$ lie above the $O(^3P_1)$ limit. Figure 7 shows two examples of photofragment kinetic energy spectra observed in the (3, 5) band. It can be seen that predissociation of the $\Omega=\frac{5}{2}$ component clearly populates both the $O(^3P_2)$ and $O(^3P_1)$ limits. The branching ratio between these two fine-structure states is estimated to be in the range of 1 : 1 to 4 : 1, depending on the functional form assumed for the kinetic energy distribution for the individual asymptotes. In contrast, the $\Omega=\frac{1}{2}$ component favors the two higher dissociation limits $O(^3P_0)$ and $O(^3P_1)$. Small contributions to the third dissociation channel, however, cannot be excluded in either of these spectra.

The predissociated levels in the $\Omega=\frac{5}{2}$ component of the (2, 5) band lie considerably lower in energy and are found to dissociate to $O(^3P_2)$. Analysis of the kinetic energy spectra of the $\Omega=\frac{1}{2}$ component of this band is complicated by the fact that its R and P lines overlap. However, the spectra clearly show that levels of this component up to $J'=9.5$ primarily populate the $O(^3P_2)$ limit, even though dissociation to the $O(^3P_1)$ limit was energetically allowed.

The dominant predissociation channels observed for the $f\,^4\Pi_g$ state are indicated in Fig. 6.

E. Bound-free transitions

The locations of features 3 and C in the low resolution spectrum of Fig. 2 would suggest assigning these to a third vibrational level of the f state lying near the top of the potential barrier. Such a level could have such a short predissociation lifetime that development of the band structure observed for lower vibrational levels is prevented. However, the dependence of photofragment kinetic energies (W) on wavelength observed in features 3 and C is markedly different from that observed for the

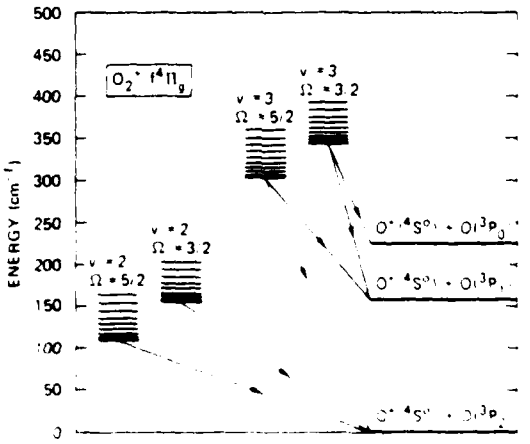

FIG. 6. Rotational levels of the f state observed at high resolution are shown relative to the location of the three dissociation limits. Full lines with arrows indicate the dominant predissociation channels.

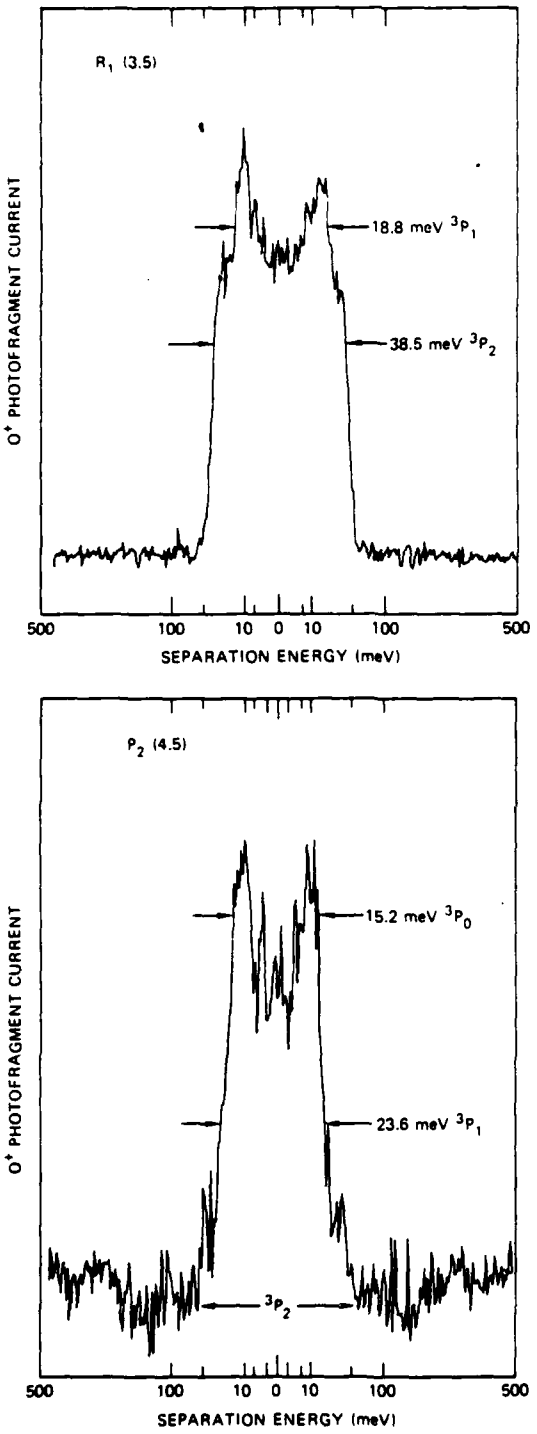

FIG. 7. Photofragment kinetic energy spectra for the predissociation $O_2^+ f\,^4\Pi_g\,(v', \Omega', J') \rightarrow O^+(^4S^\circ) + O(^3P_J)$. Upper figure $v'=3$, $\Omega'=5/2$, $J'=4.5$, $J=2,1$; lower figure: $v'=3$, $\Omega'=\frac{3}{2}$, $J'=3.5$, $J=1,0$.

other bands. In the structured bands, W' is found to *increase* with decreasing photon energy from the bandhead, as transitions to the upper state rotational levels lying at increasing energy above the dissociation limit are accessed. However, in feature 3, for example, W' linearly *decreases* from a value of 76 ± 2 meV near the approximate onset of the feature at 16 000 cm^{-1} to a minimum value of 57 ± 1 meV near the intensity maximum in the feature at 15 875 cm^{-1}. Further decrease in photon energy between this wave number and the onset of band 2 produces no further decrease in W', which remains essentially constant at 57 ± 1 meV. This behavior strongly suggests that features 3 and *C* are due solely to bound-free transitions from $v''=6$ and 5, respectively, of the $a\,^4\Pi_u$ state to the repulsive wall of the $f\,^4\Pi_g$ state. The wavelength dependence of this bound-free transition should exhibit a long wavelength cutoff corresponding to the termination of this process by the potential barrier. A quantitative description of this wavelength dependence will not be undertaken here.

F. Additional features in the spectra

The high-resolution spectrum of system *A* (Fig. 3) shows, apart from the peaks assigned to the (2, 5) band of $f\,^4\Pi_g - a\,^4\Pi_u$ transition, at least 40 other lines that appear as narrow spikes on the broad (2, 5) lines. Nine of these transitions could be identified as lines from the (4, 5) band of $b\,^4\Sigma_g^- - a\,^4\Pi_u$, which extends into the region of system *A* for $^{16,16}O_2^+$. Three transitions could be assigned to the (5, 6) band of the same system. Two other lines that result in photofragments with kinetic energies of 0.5 and 1.0 meV were identified as originating from the $\Omega''=\frac{5}{2}$ and $\frac{3}{2}$ substates, respectively, of $a\,^4\Pi_u(v''=4,\ N''=27)$. We tentatively attribute the upper levels involved to rotationally quasibound levels of the $d\,^4\Sigma_g^+$ state. The remaining 27 transitions could not be assigned on the basis of their transition frequencies alone. Interpretation of these lines will require a detailed study of their linewidths, photofragment kinetic energies, and isotope shifts.

IV. POTENTIAL ENERGY CURVES FOR THE $f\,^4\Pi_g$ STATE OF O_2

The $f\,^4\Pi_g$ state is known from theoretical calculations to correlate adiabatically with $O^+(^4S^\circ) + O(^3P)$ separated atom limit. All of the levels observed in the present study lie substantially above the lowest $O(^3P_2)$ dissociation limit, and the $v'=3$ levels lie above the $O(^3P_1)$ and $O(^3P_0)$ limits as well. Thus the observed quasibound levels must be supported by a maximum in the potential energy curve at large internuclear distance. Since predissociation over a wide range of rotational levels from two vibrational levels is observed, such a barrier cannot arise solely from centrifugal contributions to the potential. Rather, an appreciable barrier must arise from an avoided crossing of an essentially repulsive potential curve arising from $O^+(^4S^\circ) + O(^3P)$ with a bound $^4\Pi_g$ state arising from $O^+(^4S^\circ) + O(^1D)$. Such a barrier has indeed been predicted at internuclear distances ranging from 2.7 to 3 Å in three separate *ab initio* calculations of the $f\,^4\Pi_g$ potential curve.[10,11]

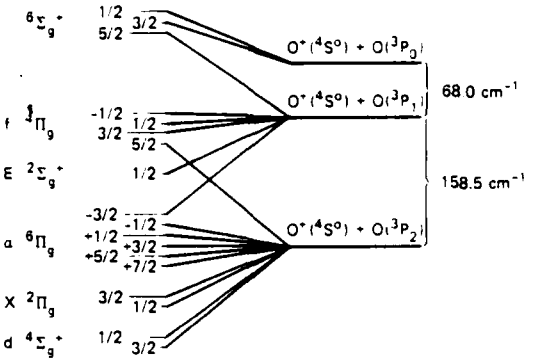

FIG. 8. Rotationless adiabatic correlation diagram for the gerade states of O_2^+ arising from the $O^+(^4S^o) + O(^3P_J)$ separated atom limits.

A. Asymptotic correlations

Before we continue our discussion of the form expected for the $f\,^4\Pi_g$ potential curve, it is useful to consider the complications introduced by spin–orbit coupling. As we have discussed above, a $^4\Pi$ state is expected to have four spin–orbit sublevels, described in case (a) as $\Omega = \frac{5}{2}, \frac{3}{2}, \frac{1}{2}$, and $-\frac{1}{2}$. While the spin–orbit interaction in oxygen is not large, neither are the energy differences under consideration. In the situation of relatively low total angular momentum (J') of interest here, we may describe the sublevels of the $f\,^4\Pi_g$ state in terms of four potential curves, one for each value of Ω. Such a description remains reasonable even in the limit of very large internuclear separation, except that as the electrostatic interactions become smaller compared to spin–orbit, the states are transformed from the case (a) appropriate to the molecule to the case (c) appropriate to the separated atoms.

The understanding of this asymptotic spin recoupling requires that we include all of the gerade states that correlate to $O^+(^4S^o) + O(^3P)$. These various states are shown schematically in Fig. 8. The correlations of the spin–orbit sublevels are based on the calculations of Beebe *et al.*,[10] which suggest that for $R > 3$ Å the ordering of the gerade states is

$$d\,^4\Sigma_g^+ < X^2\Pi_g < a\,^6\Pi_g \leq E\,^2\Sigma_g^+ < f\,^4\Pi_g < {}^6\Sigma_g^+ . \tag{4}$$

B. Potential barrier

An experimental lower limit on the height of the potential barrier in the f state may be obtained from the energy of the highest observed quasibound rotational level relative to the dissociation limit. As seen from Table I, the highest level observed in the high-resolution spectrum is $J' = 10.5$ in the $\Omega' = \frac{1}{2}$ component of band B. However, using the rotational constants and Eq. (1), the assignments in this component can be extended to $J' = 15.5$ in the low-resolution spectrum (Fig. 2). To obtain the barrier height for the rotationless potential, the centrifugal contribution[7] $J'(J'+1)\hbar^2/(2\mu R_b^2)$ must be subtracted from $F_{\frac{1}{2}}^{3/2}(15.5)$. Taking $R_b = 2.7$ Å, the smallest value of the internuclear distance at which theory predicts the barrier to occur, the lower limit on the barrier height is found to be $U_b^{\frac{1}{2}/2} > 376$ cm^{-1} (46.6 meV). A similar calculation for $\Omega' = \frac{3}{2}$, for which $J' = 15.5$ is also the highest level observed at low resolution, yields $U_b^{\frac{3}{2}/2} > 332$ cm^{-1} (41.2 meV). As we shall see (Sec. V A), such low barriers would lead to rapid dissociation by tunneling; to obtain predissociation lifetimes as long as those observed experimentally (see Fig. 4) with a barrier of reasonable thickness, these estimate of the barrier heights must be increased by 20 to 30 cm^{-1}, giving "best estimates" of $U_b^{\frac{1}{2}/2} \sim 395$ cm^{-1} (49 meV) and $U_b^{\frac{3}{2}/2} \sim 360$ cm^{-1} (44.6 meV). (See Sec. V A). We note that these barriers are in remarkably good agreement with the 47 meV calculated by Beebe *et al.*[10]

Crude upper-limit estimates for the barrier heights are available from the photofragment energy distribution of the bound-free bands 3 and C. The lowest photofragment energy (W) observed for these bands is 57 ± 1 meV (460 cm^{-1}). This could be taken as an estimate of the barrier height, but this interpretation is limited by the *contribution of rotation to the barrier maximum* (~4 meV for the most probable $J'' = 10.5$ assuming $R_b = 2.7$ Å) and by the superposition of photofragments from the four spin–orbit sublevels of the f state. At this stage we can conclude only that the bound-free spectra are consistent with the barrier heights derived from the quasibound levels.

C. Dissociation energy

Assuming the lower vibrational levels of the f state can be described by the vibrational constants in Table II, these constants can be used to give the location of the observed levels with respect to the bottom of the potential well. In addition, the location of these levels with respect to the $O^+(^4S^o) + O(^3P_2)$ separated atom limit is given directly from the measured photofragment separation energies (W) or, equivalently, from the observed transition energies and the known potential energy of the relevant levels in the a state. Thus, the dissociation energy of the $f\,^4\Pi_{f5/2}$ substate can be estimated from these values to be 784 cm^{-1} (97 meV).

The full valence configuration interaction calculation (FVCI) of Beebe *et al.*,[10] which used a minimum, Slater-type-orbital basis set, predicts a value $D_e \sim 710$ meV. A more extensive FVCI calculation by Roche[11] using a double-zeta Slater basis set gives $D_e \sim 580$ meV. Roche[11] has also carried out a much larger first-order configuration interaction (FOCI) calculation which, in addition to the configurations used in the FVCI calculation, incorporated both single and double excitations from the dominant electronic configuration of this state at large internuclear distance. This calculation predicts the bottom of the well of the f state to lie above the $O^+(^4S^o) + O(^3P_2)$ dissociation limit by approximately 47 meV.

Since the $f\,^4\Pi_g$ state has a maximum in its potential curve at large internuclear distances, it is interesting to compare the experimental and theoretical values of the "local" well depth of this state, i.e., the difference in energy (D) between the potential barrier and the potential minimum:

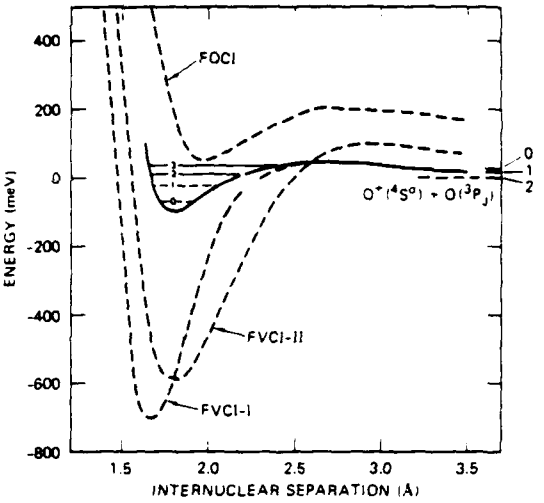

FIG. 9. Theoretical predictions for the location of the well of the $f\,^4\Pi_g$ state [FVCI-I: Beebe *et al.* (Ref. 10), FVCI-II: Roche (Ref. 11), FOCI: Roche (Ref. 11)]. The solid curve is the Morse potential curve generated using the spectroscopic constants given in Table II for the $^4\Pi_{5/2}$ substate. At $R = 2.42$ Å, the Morse curve joins to the model Eckart barrier discussed in Sec. V A.

$$D = D_e + U_b ,$$

where U_b is the height of the barrier with respect to the $O(^3P_2)$ limit. Using the upper and lower limits that we obtained for the barrier height, our estimate for D ranges from 142 to 155 meV, excluding the uncertainty in D_e. The FVCI calculations of Beebe *et al.* and Roche predict $D = 760$ and 673 meV, respectively. The FOCI calculation of Roche, on the other hand, gives $D = 151$ meV, which is in very good agreement with our experimental estimates.

The three theoretical potential energy curves for the $f\,^4\Pi_g$ state are shown in Fig. 9. Also shown in this figure is the Morse potential curve for the $^4\Pi_{5/2}$ substate generated using the experimental constants in Table II. The value of $D = \omega_e'^2/(4\omega_e' x_e')$ for the Morse potential is 149 meV.

V. PREDISSOCIATION OF THE $f\,^4\Pi_g$ STATE

The present observations show that the $f\,^4\Pi_g$ potential curve supports two quasibound vibrational levels behind a potential barrier. To explain the observed spectral linewidths and predissociation rates, two mechanisms of predissociation are available: (1) tunneling through the barrier and (2) predissociation by other electronic states through spin–orbit and/or rotational coupling. As we will see in the following, either mechanism may be invoked to explain the linewidths observed for both Ω' components of the higher $v' = 3$ vibrational level, while for $v' = 2$ the barrier is too high for tunneling and predissociation by other gerade electronic states is required.

A. Barrier penetration

To estimate the characteristics of the potential energy curve that would be required to explain the observed predissociation lifetimes by tunneling, we have examined a series of model potentials obtained by connecting the Morse potential derived from the level positions with an Eckart[23] barrier. Two of the four parameters in the Eckart potential were specified by requiring that the value and slope agree with that of the Morse potential at the right-hand classical turning point. The predissociation linewidths were then calculated from the expression

$$\Gamma = (\hbar\omega/2\pi)T \qquad (5)$$

(see Ref. 24) using the known penetration probability (T) for the Eckart potential combined with the effective vibrational frequency $\omega/2\pi$ derived from the spectroscopic constants given for $\Omega' = \frac{5}{2}$ in Table II. The remaining free parameters in the Eckart potential (essentially the barrier height and thickness) were varied over reasonable limits and the calculated lifetimes compared with those observed. For the extrapolated linewidth ($J' = 0$) for $\Omega' = \frac{5}{2}$ of 4 GHz, agreement was obtained for barriers from 360 to 375 cm^{-1} high and 0.6 to 0.5 Å wide. Unfortunately, the potential resulting from adding the centrifugal barrier contribution, $\hbar^2 J'(J'+1)/2\mu R^2$, is no longer analytically solvable; therefore, effective Eckart barriers were constructed for each J', completely constrained by the potential for $J' = 0$, through the requirements that correct barrier height and outer barrier turning point be reproduced. The observed increasing dissociation rate with increasing J' is easily obtained, as shown by the dot-dash curve in Fig. 5. The corresponding potential barrier is shown in Fig. 9. In the notation of Morse and Feshbach[25] for the Eckart potential, the parameters for $J' = 0$ are $\mu = 0.84$, $\tau = 12802$, $d = 1.18$ Å, with a barrier height of 360 cm^{-1} and a barrier position of 2.68 Å. The width of the barrier at the energy of $J' = 0$, $\Omega' = \frac{5}{2}$, and $v' = 3$ is 0.602 Å. For small variations (of a few cm^{-1}) in the barrier height similar agreement can be obtained with suitable variation of the barrier width. One expects that equally good agreement could be obtained for $\Omega' = \frac{3}{2}$, but we have not yet performed these calculations; we have been awaiting a better determination of the vibrational constants for that substate. Based on the observed lifetimes we estimate that the $\Omega' = \frac{3}{2}$ rotational levels are approximately 7 cm^{-1} closer to the top of the $\Omega' = \frac{1}{2}$ barrier than the corresponding values in the $\Omega' = \frac{5}{2}$ substate. If this trend persists in the $\Omega' = \frac{1}{2}$ and $\Omega' = -\frac{1}{2}$ components, their linewidths would be so large as to prevent their observation in the present experiments.

Levels lying any substantial distance below the barrier are much less likely to dissociate by tunneling. Indeed, for the potential curve shown in Fig. 9, the lifetimes, with respect to tunneling, for $v' = 2$ are predicted to be more than eight orders of magnitude longer than for $v' = 3$. The experiments reported here show that $v' = 2$ has the shorter lifetime; thus it requires an additional predissociation mechanism.

B. Spin-orbit and rotational coupling

Several gerade states of O_2^+ are known to correlate with the lowest $O^+(^4S^0) + O(^3P)$ asymptote (see Fig. 1). In addition to the $f\,^4\Pi_g$ there are the well known $X\,^2\Pi_g$, and the less well known $d\,^4\Sigma_g^+$, along with the poorly characterized $E\,^2\Sigma_g^+$, $\alpha\,^6\Pi_g$, and $^6\Sigma_g^+$ states. In principle all these states can contribute to the predissociation of the $f\,^4\Pi_g$ state. However, the $X\,^2\Pi_g$ state is too strongly bound and the $^6\Sigma_g^+$ state too strongly repulsive to interact effectively with the quasibound levels of the $f\,^4\Pi_g$ state. The $d\,^4\Sigma_g^+$ state has been found in previous experimental studies[9, 11, 15] to explain the predissociation of the $b\,^4\Sigma_g^+$ state. In addition theoretical calculations[10, 11] predict that it crosses the $f\,^4\Pi_g$ state on the inner wall of the potential curves. The $E\,^2\Sigma_g^+$ and $\alpha\,^6\Pi_g$ states are known only from theoretical investigations.[10] These calculations by Beebe *et al.* predict that their weakly attractive potential curves intersect that of the $f\,^4\Pi_g$ near the energetic dissociation limit just to the left of the maximum between 2.1 and 2.6 Å, as illustrated in Fig. 1. Thus, there is a sufficient supply of potential predissociating states, and the available experimental information must be used to decide which effects are dominant. As we shall see below, there are suggestions that all three predissociating states ($E\,^2\Sigma_g^+$, $d\,^4\Sigma_g^+$, and $\alpha\,^6\Pi_g$) may play a role and that much interesting work remains to be done.

The major tool for analyzing the perturbations comes from the observed predissociation lifetimes. As we have discussed above, the lifetimes for the $\Omega' = \frac{5}{2}$ and $\Omega' = \frac{1}{2}$ components of the $v' = 3$ level show a strong dependence on rotational quantum number (Fig. 5). The transitions involving $v' = 2$ also appear to increase in width as J' increases, although the transitions are extensively overlapped (see Fig. 3). Such a dependence would result from predissociation induced by rotational coupling. The only one of the candidate predissociating states that can produce this effect is the $d\,^4\Sigma_g^+$, for which both spin-orbit and rotational contributions to the coupling exist.

To investigate the expected rotational dependence we express the predissociation linewidths using the Fermi golden rule[28]:

$$\Gamma_n = 2\pi |\langle \Psi_n(r, R) | V(R) | \Psi_E(r, R) \rangle|^2 . \tag{6}$$

Here $\Psi_n(r, R)$ and $\Psi_E(r, R)$ denote the rovibronic wave functions of the predissociated discrete level n and the dissociative continuum wave function at energy E, respectively. $V(R)$ is the operator that couples the bound and dissociative states. The contribution of the $d\,^4\Sigma_g^+$ state can be approximated by

$$\Gamma_i = 2\pi \sum_j |H(^4\Pi_g^i;\ ^4\Sigma_g^{+j})|^2 , \tag{7}$$

where the summation extends over all components (j) of the Σ state which interact with a particular fine-structure level i of the $f\,^4\Pi_g$ state ($i = 1, 2, 3, 4$ for $\Omega = \frac{5}{2}, \frac{3}{2}, \frac{1}{2}, -\frac{1}{2}$, respectively). The assumption of the additivity of the predissociation rates is equivalent to assuming that only a small phase difference between the components is accumulated from the point of interaction to the dissociation limit. This is expected to be the case for the $d\,^4\Sigma_g^+$ state. Further, the large spin-orbit coupling constant (A') for the f state, together with its small rotational constant (B'), ensures that to a good approximation the f state may be described in Hund's case (a) coupling at low values of J' ($Y' = A'/B' \sim 100$). We have evaluated Γ_i from Eq. (7) using the matrix elements given by Kovacs[21] for the $^4\Pi(a)$-$^4\Sigma^+$ perturbation:

$$\Gamma_1 \propto \eta_1^2 (2J' - 3)(2J' + 5) , \tag{8a}$$

$$\Gamma_2 \propto \tfrac{1}{5}\xi_1^2 + 4\eta_1\xi_1 + \eta_1^2(4J'^2 + 4J' + 9) , \tag{8b}$$

$$\Gamma_3 \propto \tfrac{1}{5}\xi_1^2 + \tfrac{1}{5}\eta_1\xi_1(2J' + 5) + \eta_1^2(2J' + 5)^2 , \tag{8c}$$

$$\Gamma_4 = \Gamma_2 . \tag{8d}$$

The parameters ξ_1 and η_1 are the vibronic matrix elements for spin-orbit coupling

$$\xi_1 = \langle ^4\Sigma_g^+ | \sum_i \tilde{a}_i \tilde{l}_{iz} | ^4\Pi_g \rangle \tag{9}$$

and rotational coupling

$$\eta_1 = \langle ^4\Sigma_g^+ | \tilde{B} L_z | ^4\Pi_g \rangle . \tag{10}$$

Γ_1 and Γ_2 given by Eqs. (8a) and (8b) can be fitted to the measured linewidths. As illustrated in Fig. 5, the formulation outlined above explains reasonably well the observed J dependence for the $\Omega' = \frac{5}{2}$ and $\Omega' = \frac{1}{2}$ sublevels of $v' = 3$. One important difference remains in that the predicted low J' dependence deviates significantly from that observed for $\Omega' = \frac{5}{2}$: Γ_1 does not drop to zero at $J' = \frac{1}{2}$ as predicted, but remains at the finite value of approximately 4 GHz. While determination of Γ in the experiment is difficult due to the presence of a continuum background and the partial overlap of the Lorentzian profiles of neighboring transitions, the difference between the predicted and observed dependence at low J' is well beyond the experimental uncertainty. Substantial linewidths are also observed in the $v' = 2$, $\Omega' = \frac{5}{2}$ spectra at low J'.

We should also consider our failure to observe the two higher fine-structure components $\Omega' = \frac{1}{2}$ in both $v' = 2$ and 3. Based on the spectroscopic assignment derived from the observed bands, we would predict that the $\Omega' = \pm\frac{1}{2}$ subbands should have been discernible in the vicinity of the other subbands if the linewidths of the former were less than about 30 GHz. We can estimate the contribution of the $d\,^4\Sigma_g^+$ state to the apparently larger predissociation rates of these components in the $v' = 3$ level. Using the values ξ_1 and η_1 obtained from the fit above, we can predict Γ_3 and Γ_4 from Eq. (8). This result is shown by the dotted lines in Fig. 5. Clearly the perturbation $^4\Pi$-$^4\Sigma$ should lead to linewidths for $\Omega' = -\frac{1}{2}$ small enough to be determined in our experiment. Similar arguments hold for the $\Omega' = \frac{1}{2}$ component at low J'. Finally, calculations of $^4\Pi$-$^4\Pi$ transition line strengths[27] indicate only insignificant variations among the various fine-structure components for two Π states belonging to the same coupling case.

Thus, coupling to the d state alone cannot explain either the finite linewidths observed at low J' for the $\Omega' = \frac{5}{2}$ components or the apparently rapid predissociation of the $\Omega' = \pm\frac{1}{2}$ components. Both of these discrepancies can be accounted for in the $v' = 3$ level by barrier penetration (Sec. V A). However, tunneling does not offer a

reasonable explanation for these same discrepancies in the $v' = 2$ level. An explanation for the rapid predissociation of the $\Omega' = \pm\frac{1}{2}$ components can be obtained by invoking the participation of the $E\,^2\Sigma_g^+$ state shown in Fig. 1. This state is expected to consist predominantly of the same configurations as the $d\,^4\Sigma_g^+$ state. The interaction of a $^4\Pi$ and $^2\Sigma$ state must proceed through spin-orbit coupling with only small contributions due to rotation. Using Eq. (6) and the matrix elements from Kovacs,[21] we may predict the linewdiths Γ_i' arising from the perturbation $f\,^4\Pi_g - E\,^2\Sigma_g^+$ to be:

$$\Gamma_1' \propto 0\,, \tag{11a}$$

$$\Gamma_2' \propto 0 + \text{small contribution } (\propto J'^2)\,, \tag{11b}$$

$$\Gamma_3' \propto \tfrac{2}{9}\,\xi_2^2 + \text{small contribution } (\propto J'^2)\,, \tag{11c}$$

$$\Gamma_4' \propto \tfrac{2}{3}\,\xi_2^2 + \text{small contribution } (\propto J'^2)\,. \tag{11d}$$

Here ξ_2 is the vibronic matrix element describing spin-orbit coupling

$$\xi_2 = \langle {}^4\Pi_g | \textstyle\sum_i \tilde{a}_i \tilde{l}_{iz} | {}^2\Sigma_g^+ \rangle\,.$$

Thus if ξ_2 is comparable in magnitude to ξ_1, the $\Omega' = \frac{1}{2}$ and $-\frac{1}{2}$ components should have much larger linewidths than predicted by Eq. (8) and would therefore be unobservable as discrete transitions. It should be noted that the additional perturbation of the f state by the E state leads to no additional linewidth contribution for the $\Omega' = \frac{5}{2}$ component.

Finally, we must consider the contribution that the $\alpha\,^6\Pi_g$ state could make to the predissociation of the $f\,^4\Pi_g$. As illustrated in Fig. 8, the $\alpha\,^6\Pi_g$ has six fine-structure sublevels ($\Omega = \frac{7}{2}, \frac{5}{2}, \frac{3}{2}, \frac{1}{2}, -\frac{1}{2}, -\frac{3}{2}$), five of which correlate adiabatically with $O(^3P_2)$ while the highest ($\Omega = -\frac{3}{2}$) correlates with $O(^3P_1)$. To our knowledge, matrix elements describing the interaction of quartet and sextet states have not yet been published. In Hunds case (a) we expect rotational coupling only between states of equal spin. Thus the interaction between the $\alpha\,^6\Pi_g$ and $f\,^4\Pi_g$ states must proceed predominantly through spin-orbit interaction between sublevels of equal Ω. All four components of the f state will therefore be subject to predissociation by the $\alpha\,^6\Pi_g$ state. These contributions should be largely independent of J' in the $\Omega' = \frac{5}{2}$ component.

Thus, both the J' dependence of the transition linewidths and the two missing fine-structure levels can be explained by coupling to the $d\,^4\Sigma_g^+$, $E\,^2\Sigma_g^+$, and $\alpha\,^6\Pi_g$ states, although tunneling through the potential barrier offers an attractive, alternate explanation for these features in $v' = 3$. A comparison of the linewidths in the two vibrational states would allow conclusions on the location of these various electronic states. Unfortunately, the linewidths for the transitions to $v' = 2$ are too wide and the lines too blended to extract quantitative information on their J' dependence. The low-resolution spectra of $^{18,18}O_2^+$ indicate narrower linewidths or at least less blended lines. We anticipate a detailed study on the linewidths of this isotopic combination in the future.

C. Branching ratios

As Pernot *et al.*[20] have noted, quantitative prediction of photofragment distributions depends on the details of rotational and spin-orbit recoupling among the relevant electronic states at large internuclear distance. This requires a better understanding of the long-range potentials and configuration mixing than is presently available. However, if we assume that the long-range interactions are predominantly adiabatic, we can compare distributions predicted by the previously discussed predissociation mechanisms with the experimental observations summarized in Fig. 6.

The (rotationless) adiabatic correlations shown in Fig. 8 suggest that most of the fine-structure levels that predissociate the $\Omega' = \frac{5}{2}$ and $\frac{3}{2}$ components of the $f\,^4\Pi_g$ state should lead to $O(^3P_2)$ photofragments. The only exceptions are the $E\,^2\Sigma_g^+$ ($\Omega = \frac{1}{2}$) and $\alpha\,^6\Pi_g$ ($\Omega = \frac{3}{2}$) levels, which correlate adiabatically with $O(^3P_1)$, but are only weakly coupled to the $\Omega' = \frac{5}{2}$ and $\frac{3}{2}$ levels of the f state. These arguments are consistent with the observations that $O(^3P_2)$ is the predominant product produced in the predissociation of $v' = 2$.

In contrast, the $\Omega' = \frac{5}{2}$ levels of $v' = 3$ are observed to dissociate to $O(^3P_1)$ and $O(^3P_2)$ while the $\Omega' = \frac{3}{2}$ levels dissociate to $O(^3P_0)$ and $O(^3P_1)$. This production of $O(^3P_0)$ photofragments is clearly inconsistent with the adiabatic correlations given above. However, if the major predissociation mechanism for this vibrational level were barrier penetration, the $\Omega' = \frac{5}{2}$ levels would go to $O(^3P_2)$ and the $\Omega' = \frac{3}{2}$ levels to $O(^3P_1)$. Long-range interactions with the $^6\Sigma_g^+$ state shown in Fig. 8 could then channel some of the dissociation to the $O(^3P_1)$ and $O(^3P_0)$ limits, respectively, and thus explain the observed branching (see Fig. 7).

VI. CONCLUSIONS

Two quasibound vibrational levels have been observed in the $f\,^4\Pi_g$ state of O_2^+ via the absorptions $f\,^4\Pi_g$ ($v' = 2, 3$) $- \alpha\,^4\Pi_u$ ($v' = 5, 6$). Vibrational and rotational constants are determined for these levels. This is the first $^4\Pi - {}^4\Pi$ system for which a rotational analysis has been possible. In confirmation of theoretical predictions, the quasibound levels are found to be supported by a substantial barrier in the rotationless potential curve of the f state, with an estimated height of $> 360\ \text{cm}^{-1}$ (45 meV) for the $\Omega' = \frac{5}{2}$ component. The observed lifetimes, product branching ratios, and the energies of the levels strongly suggest that predissociation of the $v' = 3$ level involves tunneling through the potential barrier. In contrast, these observations suggest that predissociation of $v' = 2$ involves perturbations from the $d\,^4\Sigma_g^+$, $E\,^2\Sigma_g^+$, and $\alpha\,^6\Pi_g$ states.

Note added in proof. Photofragment kinetic energy spectra measured over a wide photon energy range have been used to experimentally determine the repulsive region of the $f\,^4\Pi_g$ potential curve between 0.05–0.8 eV above the $O^+(^4S^0) + O(^3P_2)$ separated atom limit [F. J. Grieman, J. T. Mosely, R. P. Saxon, and P. C. Cosby, Chem. Phys. (in press)]. These measurements, which average over contributions from all four fine-structure components, are consistent with the approximate potential curve for the $^4\Pi_{5/2}$ substate shown in Fig. 9.

ACKNOWLEDGMENTS

The authors would like to thank Dr. R. P. Saxon, Dr. J. Durup, and Dr. J. R. Peterson for useful discussions and suggestions.

[1]O. Edquist, E. Lindholm, L. E. Selin, and L. Åsbrink, Phys. Scr. 1, 25 (1970).
[2]N. Jonathan, A. Morris, M. Okuda, K. J. Ross, and D. J. Smith, J. Chem. Soc. Faraday Trans. II 70, 1810 (1974).
[3]D. S. Stevens, Phys. Rev. 38, 1292 (1931).
[4]F. J. LeBlanc, J. Chem. Phys. 38, 487 (1963).
[5]D. L. Albritton, A. L. Schmeltekopf, W. J. Harrop, R. N. Zare, and J. Czarny, J. Mol. Spectrosc. 67, 157 (1977).
[7]P. H. Krupenie, J. Phys. Chem. Ref. Data 1, 423 (1972).
[7]G. Herzberg, *Molecular Spectra and Molecular Structure I. Spectra of Diatomic Molecules* (Van Nostrand Reinhold, New York, 1950),
[8]A. Tabche-Fouhaille, J. Durup, J. T. Moseley, J. B. Ozenne, C. Pernot, and M. Tadjeddine, Chem. Phys. 17, 81 (1976).
[9]J. T. Moseley, M. Tadjeddine, J. Durup, J. B. Ozenne, C. Pernot, and A. Tabche-Fouhaille, Phys. Rev. Lett. 37, 891 (1976).
[10]N. H. Beebe, E. W. Thulstrup, and A. Anderson, J. Chem. Phys. 64, 2080 (1976).
[11]M. Carre, M. Druetta, M. L. Gaillard, H. H. Bukow, M. Horani, A. L. Roche, and M. Velghe, Mol. Phys. (in press).
[12]A. Carrington, P. G. Roberts, and P. J. Sarre, Mol. Phys. 34, 291 (1977).
[13]M. Tadjeddine, R. Abouaf, P. C. Cosby, B. A. Huber, and J. T. Moseley, J. Chem. Phys. 69, 710 (1978).
[14]P. M. Guyon, T. Baer, L. F. Ferreira, I. Nenner, A. Tabche-Fouhaille, R. Botter, and T. R. Govers, J. Phys. B 11, L141 (1978).
[15]A. Carrington, P. G. Roberts, and P. J. Sarre, Mol. Phys. 35, 1523 (1978).
[16]J. T. Moseley, P. C. Cosby, J. B. Ozenne, and J. Durup, J. Chem. Phys. 70, 1474 (1979).
[17]B. A. Huber, T. M. Miller, P. C. Cosby, H. D. Zeman, R. L. Leon, J. T. Moseley, and J. R. Peterson, Rev. Sci. Instrum. 48, 1306 (1977).
[18]P. C. Cosby, J. B. Ozenne, J. T. Moseley and D. L. Albritton, J. Mol. Spectrosc. 79, 203 (1980).
[19]D. L. Albritton, J. T. Moseley, P. C. Cosby, and M. Tadjeddine, J. Mol. Spectrosc. 70, 326 (1978).
[20]C. Pernot, J. Durup, J. B. Ozenne, J. A. Beswick, P. C. Cosby, and J. T. Moseley 71, 2387 (1979).
[21]I. Kovacs, *Rotational Structure in the Spectra of Diatomic Molecules* (American Elsevier, New York, 1969).
[22]K. P. Huber and G. Herzberg, *Molecular Spectra and Molecular Structure IV. Constants of Diatomic Molecules* (Van Nostrand Reinhold, New York, 1979).
[23]C. Eckart, Phys. Rev. 35, 1303 (1930).
[24]R. J. LeRoy and W. K. Liu, J. Chem. Phys. 69, 3622 (1978), Eqs. (4.1) and (4.4).
[25]P. M. Morse and H. Feshbach, *Methods of Theoretical Physics* (McGraw-Hill, New York, 1953), Vol. II, p. 1659.
[26]L. I. Schiff, *Quantum Mechanics* (McGraw-Hill, New York, 1968), p. 285.
[27]D. Premaswarup, Ind. J. Phys. 27, 578 (1953).

APPENDIX E

LASER PHOTOFRAGMENT SPECTROSCOPY OF NO^+ I. PREDISSOCIATION OF THE $2^3\Pi$ STATE[a]

P. C. Cosby and H. Helm

Molecular Physics Laboratory
SRI International
Menlo Park, California 94025

ABSTRACT

NO^+ ions, produced by electron impact on NO, are observed to predissociate into $O^+(^4S^0) + N(^4S^0)$ when irradiated by a dye laser at wavelengths between 6600-5650 Å. The highly structured wavelength dependence of the photofragments reflects absorptions from three vibrational levels in a long-lived NO^+ electronic state to 20 vibrational levels of a predissociated electronic state. The transitions are tentatively identified as $2^3\Pi(v'=0\text{-}19) \leftarrow \underline{b}'^3\Sigma(v''=8\text{-}10)$. The weakly-bound $2^3\Pi$ state is found to lie 0.698 - 0.925 eV above the lowest separated atom limit of NO^+ and to adiabatically correlate to the $N^+(^3P) + O(^3P)$ limit. This state is also found to be homogeneously perturbed, most likely by the $^3\Pi$ state arising from the $O^+(^4S^0) + N(^2D^o)$ limit and to be predissociated by the $\underline{a}^5\Sigma^+$ state. The predissociation lifetimes for all rotational levels in v'=0-8 are > 1.6 ns. Perturbations in $\underline{b}'^3\Sigma^-(v=9)$ and $\underline{W}^1\Delta(v=5,6)$ are discussed.

---

[a]Research supported by the Air Force Office of Scientific Research and the Army Research Office.

MP 81-32
03/05/81

I. INTRODUCTION

Because of its exceptionally low heat of formation, NO^+ is the most abundant chemical species in the thermosphere and is a key reactant at lower altitudes.[1,2,3] Yet, in contrast to its isoelectronic neutral analogue N_2, very little spectroscopic information has been obtained on the electronic structure of NO^+. Only the $\underline{A}^1\Pi \rightarrow \underline{X}^1\Sigma^+$ Miescher-Baer bands[4] have been identified in a nitric oxide gas discharge. They are also the only emission bands that have been rotationally analyzed.[5,6,7] Two additional band systems attributed to $\underline{b}'^3\Sigma^- \rightarrow \underline{X}^1\Sigma^+$ and $\underline{b}^3\Pi \rightarrow \underline{X}^1\Sigma^+$ have been observed at low resolution in the fluorescence from an NO^+ ion beam.[7,8] Nevertheless, a relatively complete description of eight low-lying electronic states of NO^+ has emerged from the combination of these measurements with electronic structure calculations[9,10,11] and the photoelectron spectroscopy of NO.[12] Current knowledge of these states has recently been reviewed by Albritton, Schmeltekopf, and Zare[13] who derived the NO^+ potential energy curves shown in Figure 1.

Experimental information on electronic states above the lowest dissociation limit $O^+(^4S^o) + N(^4S^o)$ is only fragmentary. Theoretical calculations by Michels[11] predict twelve additional bound states to lie within 24 eV of the NO $\underline{X}^2\Pi$ ground state. Only two prominent features are observed by photoelectron spectroscopy above the lowest dissociation limit.[12] They refer to bound states at 21.72 and 22.7 eV. Photoabsorption,[14,15] photodissociative ionization,[15,16] and photoelectron-photoion coincidence[17] spectroscopy of NO, together with studies of the spontaneous[18-20] and collisional dissociation[20-22] of NO^+, have also probed the NO^+ electronic states in this region, but none of these techniques has achieved sufficient resolution to permit state identifications.

We report here the initial application of predissociation photofragment spectroscopy to the investigation of NO^+ excited states. This technique allows the first observation of bound-bound absorption transitions in NO^+. The transitions are pumped by a laser and are detected by observing the subsequent predissociation of the upper electronic state to $O^+(^4S^o) + N(^4S^o)$ products. Measurement of the kinetic energies of these photofragments establishes the absolute energy locations of both the (lower) absorbing and (upper) predissociating states with respect to this lowest separated atom limit of NO^+. The transitions are attributed to $2^3\Pi(v'=0, 19) \leftarrow b'^3\Sigma^-(v''=8, 9, 10)$. Vibrational analysis of the absorption bands indicates the $2^3\Pi$ state correlates to the $N^+(^3P) + O(^3P)$ separated atom limit and exhibits a shallow well ($D_o > 0.21$ eV) at an internuclear distance near 1.7 Å. Abrupt changes observed in the vibrational spacings suggest this state is homogeneously perturbed. Portions of the spectra are observed with sub-Doppler resolution allowing complete resolution of a complex rotational structure which could not yet be assigned. The absorption linewidths yield a predissociation lifetime of $> 1.6 \times 10^{-9}$ s for the lower vibrational levels of the $2^3\Pi$ state.

II. EXPERIMENTAL METHOD

The apparatus used in the present study has been described in detail elsewhere,[23] as has its application to the high resolution spectroscopy of molecular ions.[24] Briefly, the beam from a tunable CW dye laser is made coaxial with a fast ion beam of NO^+ over an interaction length of about 60 cm. The NO^+ ions are produced by electron impact ionization of NO in a high pressure ion source (0.5 torr, ~ 100 eV electron energy). The ions are accelerated to typically 4000 eV, mass selected, collimated, and merged with the laser beam. If an absorption of photons occurs which results in photodissociation, the photofragments, N^+ or O^+, which are ejected perpendicular to the direction of laser polarization are detected after kinetic energy analysis. The time interval between formation of the NO^+ ions in the source and their irradiation by the laser is estimated to be between 12-30 μs, the principal uncertainty in this estimate being the residence time of the ions in the source.

Most of the spectra reported here were obtained with the dye laser operating multimode at a bandwidth of approximately 1 cm^{-1} and irradiating the NO^+ ion beam within the cavity of the laser. The advantage of high photon flux obtained using this technique is partially offset by the doubling of each absorption transition by the opposite Doppler shifts produced by photons propagating parallel and antiparallel to the ion beam velocity. Scans of the dye laser wavelength were made over the range of 6600-5650 Å for various settings of the energy analyzer to detect either N^+ or O^+ photofragments produced with center-of-mass separation energies (W) between 0 and 1 eV. More limited scans were made using the extracavity beam of the laser to irradiate the ion beam. In this case only a single Doppler component is observed, but at a substantially reduced signal to noise ratio.

Portions of the spectra were obtained using the extracavity beam of a single-mode ring dye laser having a bandwidth of ± 25 MHz (0.0008 cm^{-1}). The laser was scanned over wavenumber ranges of ~ 1.5 cm^{-1} by piezoelectrically tuning an intracavity etalon while modulating the laser cavity length to obtain a homogeneous distribution of laser frequencies between its 100 MHz cavity mode spacing. The procedure increased the effective bandwidth of the laser to between 50-100 MHz. A substantially smaller bandwidth could be achieved by fixing the laser frequency and velocity tuning the ion beam. However, this necessitated a more limited wavelength coverage than was required in the present study. The total apparatus produced linewidth of an absorption is the convolution of the laser bandwidth with the Doppler width of the transition due to the finite velocity spread in the NO^+ ion beam. The coaxial arrangement of the laser and ion beams together with the use of relatively high ion beam kinetic energies reduces this Doppler contribution to < 100 MHz.

During the course of these measurements, the previously reported[18-20] metastable decomposition (spontaneous predissociation) of NO^+ was observed to produce O^+ fragments with W = 50, 140, 220, 300, and 370 meV. This fragmentation is not influenced by laser irradiation at wavelengths between 6600-5650 Å. No higher energy O^+ fragments and no N^+ fragments arising from metastable decomposition were detected. It should be noted that the weak features observed at W = 95 and 181 meV in the kinetic energy spectra of Govers and Schopman[19] did not appear in the present measurements, probably reflecting the difference in ion sources and flight times between the two experiments.

In addition, no direct photodissociation processes (bound-free transitions), which would arise from perpendicular transitions to repulsive NO^+ states, were observed between 6600-5650 Å. The direct dissocitation of NO^+

to N^+, which has been observed[25] in a parallel transition at an unspecified argon ion laser wavelength, was not investigated here.

III OBSERVED SPECTRA

More than forty NO^+ absorption bands are observed between 6600-5650 Å which produce O^+ photofragments with W in the range of 0-900 meV and N^+ photofragments with W in the range of 0-600 meV. The most prominent band system produced O^+ photofragments with W between 698-925 meV. Only this predissociation band system will be discussed in the present paper.

The wavelength dependence for the production of O^+ photofragments between 6500-5750 Å with various center-of-mass separation energies (W) is shown in Figure 2. The data were obtained intracavity; the Doppler doublets are separated by ~ 5 Å at 6000 Å. Two prominent vibrational progressions appear in this wavelength range. For the purpose of discussion, the members of these progressions are labelled $\alpha_0 - \alpha_6$ and $\beta_1 - \beta_5$. The reason for this choice of subscripts will become apparent.

The variation of photofragment separation energy with wavelength is an important factor for the identification of the spectra. If we follow any given band in Fig. 2, we observe a maximum intensity at a particular setting of the energy analyzer. For example, bands α_1 and β_1 are observed with maximum intensity in the W ~ 711 meV spectrum. A composite spectrum of the two band progressions which reflects the absorption strengths of the transitions rather than the kinetic energy distributions of the resulting photofragments may be constructed by piecing together wavelength scans at the optimum energy analyzer setting of each band. Such a spectrum is shown in Fig. 3 for the wavelength range of 6600-5650 Å.

More detailed information on the photofragment separation energies is obtained by setting the laser to a fixed wavelength within each band and scanning the energy analyzer. The value of W observed in each of the bands is

given in Table I together with the photon energy of the transitions ($G_{v',v''}$). It can be seen that within each of the progressions α and β, the variation in W from one band to the next corresponds directly to the photon energy difference of the bands $\Delta G_{v'}$. We may therefore conclude that progression α involves transitions from one vibrational level of the absorbing state to 11 closely-spaced vibrational levels in the upper electronic state which predissociate. In addition, bands $\beta_0 - \beta_5$ have the same values of W and $\Delta G_{v'}$ as bands $\alpha_0 - \alpha_5$ in the progression at higher photon energy. This demonstrates that both progressions share the same upper state vibrational levels. The relative numbering of these levels is given by the subscripts in the band designations.

The energies of the absorbing levels in the lower electronic state, relative to the $O^+ + N$ limit produced by the photodissociation, are obtained by subtracting the transition energy $G_{v',v''}$ for each band from the photofragment kinetic energy W observed in the band. These values are listed in the last column of Table I. It can be seen that the α bands arise from a vibrational level of 1.323 eV below the separated atom limit whereas the β bands originate in a higher vibrational level located 1.187 eV below this limit. The similarity in the rotational structure of the α and β bands suggests that each progression originates from the same lower electronic state.

In addition to these two strong progressions, two weaker progressions produce O^+ photofragments with center-of-mass kinetic energies between 830-925 meV. These transitions, labeled γ and δ, in Fig. 4 appear at wavelengths between 6134-5914 Å and 6379-6268 Å, respectively. It is clear from the $W - G_{v',v''}$ values in Table I that the γ bands originate from the same lower vibrational level as the β bands, but access higher vibrational levels in the predissociated upper state. The δ bands, on the other hand,

originate from a third, higher vibrational level in the absorbing electronic state. The values of W, together with the upper state vibrational spacings, show that the pairs of bands α_8 and γ_8, α_9 and γ_9, as well as α_{10} and γ_{10} each share the same upper state vibrational levels. Similarly, the four pairs of bands γ_{13}-δ_{13} through γ_{16}-δ_{16} also share common upper state vibrational levels. Thus, three absorbing vibrational levels in an upper electronic state are observed in the 6600-5650 Å wavelength region.

Band α_2 and portions of bands α_0-α_8 were investigated at high resolution. A 0.5 Å segment of band α_4 is shown in Fig. 5. The transition linewidths observed here, as well as in the other bands, are $\sim$ 100 MHz, corresponding to the apparatus-induced linewidth. This places a lower limit on the predissociation lifetime of the upper electronic state of $\tau_d > 1.6 \times 10^{-9}$ s. The high resolution spectrum of band α_2 was found to consist of more than 280 resolved transitions having no discernible pattern other than an apparent clustering of rotational lines into three groups separated by approximately 10-12 cm^{-1}. It should be noted that detection of transitions in only the P and R branches of the band is expected here. Photofragments arising from Q-branch ($\Delta J = 0$) transitions, which are expected to be preferentially ejected in the center-of-mass frame along the direction of laser polarization,[26] will be greatly attenuated by the angular discrimination of the apparatus. Rotational analysis of this spectrum has not yet been possible, but even without it we are able to identify the observed transitions primarily on the basis of the measured photofragment separation energies, as discussed in the following sections.

IV DISCUSSION

A. Identification of the lower electronic state.

The locations of the three absorbing vibrational levels in the lower electronic state below the $O^+ + N$ separated atom limit are directly given by the $W - G_{v',v''}$ values listed in Table I. The energies of these levels averaged over the α, β, γ, and δ bands are -1.323 ± 0.002, -1.187 ± 0.005, and -1.055 ± 0.005 eV. The error limits here refer only to the relative uncertainties in the measurement of W. An absolute uncertainty of $^{+\ 0.005}_{-\ 0.010}$ eV in the W measurement is the actual accuracy with which the abolute energy of this group of three levels can be established.[27]

The separation of the lower state vibrational levels can be more precisely determined from the photon energy difference of bands terminating in the same upper state vibrational levels. These separations are given as $\Delta G_{v''}$ in Table I. Average values of $\Delta G_{v''} = 1098 \pm 6\ cm^{-1}$ and $\Delta G_{v''+1} = 1036 \pm 6\ cm^{-1}$ from the four progressions each contain an unknown error due to our use of band centers rather than band origins, in the absence of a rotational analysis. This error is manifested by the small, but statistically significant, decrease in $\Delta G_{v''}$ with increasing upper state vibrational level. The magnitude of the error introduced by the use of band centers, however, is not likely to exceed $6\ cm^{-1}$; measurements of these band separations from other locations within the rotational envelopes of the bands give values for the lower state vibrational spacings which agree with the band-center values to within the stated precisions.

Although the measurement of photofragment kinetic energies establishes the location of the lower state vibrational levels with respect to $O^+ + N$, the electronic states of the photofragments must be deduced indirectly. If the predissociation leads to the lowest separated atom limit $O^+(^4S^o) + N(^4S^o)$,

the lowest of the three vibrational levels would lie 18.80 eV above NO $\underline{X}^2\Pi$ (v=0). Dissociation to the next higher O^+ limits: $O^+(^4S^o) + N(^2D^o)$, $O^+(^2D^o) + N(^4S^o)$, or $O^+(^4S^o) + N(^2P^o)$ would place this vibrational level at 21.17, 22.12, or 22.37 eV, respectively. However, it is unlikely that bound states at the energies required for the production of electronically excited photofragments would be present in the ion beam. No features appear in the NO photoelectron spectrum[12] at these energies, which indicates such levels would not be populated by direct ionization of NO in the ion source. Nevertheless, electronic states not observed in the photoelectron spectrum are predicted by theory[10,11] to lie in this general energy range. These states are bound at internuclear distances too large to permit their production in a direct ionization process or involve multiple electron excitations but could conceivably be produced by radiative cascade from higher states. Such higher states would, however, be metastable with respect to predissociation by the manifold of states arising from the two lowest separated atom limits. Indeed, production of O^+ and N^+ is observed in the photodissociative ionization spectrum[15,16] of NO at all photon energies above these respective thresholds. In addition, no production of N^+ or O^+ from the unimolecular decomposition of NO^+ in a beam is observed from states above 20.5 eV, indicating the predissociation lifetimes of such states, if formed, is much shorter than the $\sim 10^{-5}$ s transit time between the ion source and the photon interaction region in the present experiment. We therefore conclude that the observed photon-induced predissociations produce photofragments in their ground electronic states. Further support for this conclusion is presented in Section IV B.

Eight of the 22 electronic states which arise from the two lowest dissociation limits have been defined experimentally. Using the molecular constants[13] for these eight states, we may calculate the locations of their

vibrational levels in the energy region of our observed lower state levels. Only three of these states, the $\underline{A}'^1\Sigma^-$, $\underline{b}'^3\Sigma^-$, and $\underline{W}^1\Delta$, have vibrational spacings in the vicinity of the measured values of 1098 and 1036 cm^{-1}. The calculated positions of their vibrational levels with respect to the $O^+(^4S^o) + N(^4S^o)$ separated atom limit are given in Table II. It can be seen from this table that the $\underline{A}'$ state must be excluded from the list of candidate lower states because the locations of its relevant vibrational levels are 0.05 eV away from the observed levels, which is well beyond the combined uncertainties in these locations.

In addition to these well characterized states of NO^+, theory predicts two additional bound states, the $2^1\Sigma^+$ and perhaps the $2^3\Delta$, to lie in the energy range of interest here. Neither of these states has been previously observed and several considerations speak against either of these states being the lower state observed in the present experiment. The Franck-Condon overlap between the relevant vibrational levels of these states with $NO(\underline{X}^2\Pi)$ is very poor. In addition, the $2^3\Delta$ state cannot be formed from $NO(\underline{X}^2\Pi)$ in a single electron removal process. Neither state appears in the photoelectron spectrum of NO. Hence, it is unlikely that either of these states would be populated by direct ionization of NO. Formation by radiative cascade is also unlikely, for the reasons discussed earlier in this section.

We are therefore left with the choice of two possible lower state candidates: $\underline{b}'^3\Sigma^-$ (v"=8, 9, 10) and $\underline{W}^1\Delta$ (v"=5, 6, 7). The consideration of candidate upper states for the photodissociation will narrow this choice to the $\underline{b}'$ state alone.

B. Vibrational Structure in the Upper Electronic State.

The lowest vibrational level of the upper electronic state which predissociates in the wavelength region of 6600-5650 Å lies $0.698 \begin{smallmatrix} + 0.005 \\ - 0.010 \end{smallmatrix}$ eV above the $O^+(^4S^o) + N(^4S^o)$ separated atom limit. This level is accessed by bands α_o and β_o in Fig. 3. A detailed search of this spectral region gave no indication of lower energy vibrational levels in this electronic state (see, e.g., the W = 628 meV spectrum in Fig. 2). The relative intensities of transitions to the upper state levels from each of the three vibrational levels in the b' state are given in Fig. 6. It can be seen that the intensities from v"=8 and 9, which otherwise exhibit a periodic variation with upper state level, abruptly terminate at our lowest observed level. This suggests assignment of the W = 0.698 eV level to v'=0. We note that the long predissociation lifetimes of these levels, as evidenced by their narrow absorption linewidths, demonstrates a predissociation caused by a weak interaction. It is unlikely that the onset of this interaction would begin abruptly at other than the lowest upper state vibrational level. However, the intensities of the observed bands reflect not only the vibrational overlap between the lower and upper states in the electronic transition, but also the overlap between the upper electronic state and the state inducing the predissociation. Since the predissociating state is presumably unbound in the region of the interaction, the overlap between it and the upper state should also vary smoothly. The combination of these two variations, on the other hand, could result in several upper state vibrational levels having unobservably small predissociation rates. If these levels were the first several vibrational levels of the upper electronic state, this could also be consistent with the present observations. Nevertheless, it is convenient to adopt, for the sake of discussion, the assignment of the lowest observed level to

v'=0 while awaiting future work on the isotopically substituted ion to confirm the assignment. Thus, bands $\alpha_0 - \alpha_{10}$ correspond to (v',v") = (0,8) - (10,8), bands $\beta_0 - \beta_5$ correspond to (0,9) - (5,9), bands $\gamma_8 - \gamma_{16}$ correspond to (8,9) - (16,9), and bands $\delta_{13} - \delta_{19}$ correspond to (13,10) - (19,10).

The upper state vibrational spacing may be accurately determined from the spacing of the band origins in the observed progressions. However, as mentioned in the preceeding section, the absence of a rotational assignment requires that the band origins be approximated by other features of the band rotational envelopes. The envelopes of transitions to $v' \leq 6$ exhibit a well-defined bandhead on the high photon energy side of the bands and isolated rotational lines on the low photon energy side. In the bands for transitions to $v' > 6$, however, the bandhead becomes increasingly diffuse and the isolated rotational lines blend with lower energy bands as the spacing of the bands decreases. In order to minimize the influence of these changes in the bandshape, we have chosen to measure the vibrational intervals as the difference in photon energy between band centers, defined as the mean pnoton energy of a band at the intensity half-maximum of its rotational envelope.

The upper state vibrational spacings, $\Delta G_{v'}$, determined from the centers of the observed bands, are shown as a function of mean upper state vibrational quantum number, (v' + 1/2), in Fig. 7a. The squares, circles, open triangles, and closed triangles are the values determined from bands α, β, γ, and δ, respectively. The error bars for (v' + 1/2) = 0.5 - 6.5 reflect the variation in $\Delta G_{v'}$ values obtained using the separations of bandheads, isolated rotational lines, and band centers. Thus, the magnitude of this variation gives some measure of the influence of changes in the upper state rotational constants with vibrational level on the apparent upper state vibrational sepa-

rations determined from the band centers alone. The error bars for points at $(v' + 1/2) > 7.5$ reflect only the uncertainty in locating the band centers.

The slope of $\Delta G_{v'}$ in Fig. 7a exhibits a strong discontinuity at $v' \sim 4$. The magnitude of this discontinuity far exceeds any possible uncertainty in the upper state vibrational spacing arising from the use of band center separations rather than band origins. Its presence suggests[28,29] that a homogeneous perturbation occurs in the upper electronic state. This will be discussed in Section IV D.

The observed values of $\Delta G_{v'}$ are replotted in Fig. 7b as a function of the energy of the upper state vibrational levels with respect to the $O^+(^4S^o) + N(^4S^o)$ separated atom limit ($W_{v'+1}$). The functional dependence of the energy eigenvalue separations of a Morse oscillator on such a plot is that of a parabola with its apex near the dissociation energy of the oscillator.[29] Also shown in Fig. 7b are the corresponding energies of the nine fine-structure combinations possible for the $N^+(^3P) + O(^3P)$ separated atom limit. Taking into account the $^{+\ 5}_{-\ 10}$ meV uncertainty in the absolute energies of the observed levels, it is clear from this figure that the upper electronic state adiabatically correlates to $N^+(^3P) + O(^3P)$. Since the energy difference between $N^+(^3P) + O(^3P)$ and $O^+(^4S^o) + N(^4S^o)$ is unique, this observation lends additional support to the argument made in Section IV A that only ground state photofragments are produced in the predissociation of the observed NO^+ levels.

C. Identification of the Upper Electronic State.

The selection of candidate upper states can be restricted to those correlating to the $N^+(^3P) + O(^3P)$ limit which can reasonably be expected to exhibit the vibrational frequencies and homogeneous perturbation discussed in

the preceeding section. In addition, we require an upper state that is optically connected to either the $\underline{W}^1\Delta$ or $\underline{b}'^3\Sigma^-$ lower state by a dipole-allowed transition. A further consideration which could be introduced is that the candidate upper state must be predissociated by a state arising from the $O^+(^4S^o) + N(^4S^o)$ limit. In practice, however, the long predissociation lifetimes and the absence of observable changes in this lifetime with upper state vibrational level do not make this latter consideration sufficiently restrictive to aid in the upper state identification. Discussion of the predissociation mechanism will be given in Section IV F.

The $\underline{W}^1\Delta$ state would be optically connected in allowed transitions only to the $\underline{A}^1\Pi$ and the $2^1\Pi$ states. The molecular constants of the $\underline{A}$ state are known[13] up to v = 10. If we extrapolate these constants five vibrational levels into the energy region of the observed predissociation, the vibrational spacing of the $\underline{A}$ state is found to be three times larger than the observed values. In addition, the vibrational overlap between these $\underline{A}$ state levels and $\underline{W}^1\Delta$ (v"=5,6,7) is very poor.

The properties of the $2^1\Pi$ state are known only from molecular structure calculations. The potential curve calculated by Thulstrup, et al.[10] for this state is drawn as the upper dashed curve in Fig. 1. The curve of Michels[11] is qualitatively similar, but with the bottom of the inner well at 23.2 eV and 1.4 Å. It can be seen from this figure that in order to pump vertical transitions from the relevant vibrational levels of the $\underline{W}$ state into bound levels of the $2^1\Pi$ state in the region of 20.9 eV, the potential curves of Thulstrup et al. and Michels would have to be lowered by ~ 1 eV and ~ 3 eV, respectively.

The large number of rotational lines observed at high resolution in band α_2 effectively eliminates these singlet states from consideration. A

$^1\Pi - {}^1\Delta$ band, which has the highest complexity of known singlet systems,[28] would consist of only six rotational branches. In order to produce the observed 280 rotational lines that differ by less than a factor of 10 in intensity, the rotational temperature of the ion beam would have to be > 800 K. In contrast, we have found[30] the rotational temperature of O_2^+ ions formed by electron impact on O_2 to be 400 ± 50 K and fully expect a similar temperature for NO^+. It is therefore very unlikely that the upper electronic state in the observed bands is a singlet.

If the $\underline{b}'{}^3\Sigma^-(v=8, 9, 10)$ is the lower electronic state, there are also two states optically connected to it in allowed transitions: the $\underline{b}^3\Pi$ and the $2^3\Pi$. The same difficulties occur for the $\underline{b} \leftarrow \underline{b}'$ transition as were discussed for the $\underline{A}^1\Pi \leftarrow \underline{W}^1\Delta$; namely, the (extrapolated) vibrational spacing of the $\underline{b}$ state is much larger than observed for the predissociated upper state and the vibrational overlap between these states is poor. On the other hand, the properties of the $2^3\Pi$ state are qualitatively in agreement with those expected from the observed transitions, which makes it the most likely candidate for the predissociated upper state.

The potential curve of the $2^3\Pi$ state calculated by Thulstrup et al.[10] is shown as the lower dashed curve in Fig. 1. The curve calculated by Michels[11] for this state has an outer minimum of ~ 0.5 eV at ~ 1.95 Å and no inner minimum. Each of these calculations yields a $2^3\Pi$ potential curve which allows vertical transitions to this state from the $\underline{b}'{}^3\Sigma^-(v''=8-10)$ and has the shallow potential well necessary to explain the small upper state vibrational spacings observed in the predissociation spectra. In addition, both calculations predict one or more avoided crossings between the $2^3\Pi$ state and other curves arising from higher NO^+ dissociation limits. In the calculations of Thulstrup et al., one of these perturbations occurs within the

bound region of the potential, leading to the formation of a second minimum at shorter internuclear distances. Such a feature would qualitatively account for the abrupt change in vibrational spacings observed in the predissociation spectra. However, it should be emphasized here that neither the calculations of Thulstrup et al. nor Michaels, which employ limited basis sets, purport to quantitatively describe the NO^+ electronic states in this energy region.

In summary, the following arguments have led us to identify the main features of the observed band systems as $2^3\Pi \leftarrow \underline{b}'^3\Sigma^-$ transitions: a. The energy locations and vibrational spacing of v = 8, 9, and 10 of the $\underline{b}'$ state agree with the lower state vibrational levels measured in this experiment; b. The complexity of the band structure, coupled with the apparent clustering of rotational lines into three groups, is consistent with a $^3\Pi \leftarrow {}^3\Sigma^-$ combination; c. The predicted position of the $2^3\Pi$ state allows good vibrational overlap with the relevant $\underline{b}'$ levels; and d. The homogeneous perturbation predicted for the $2^3\Pi$ state is consistent with the perturbed vibrational spacings observed in the upper state. Additional confirmation for this identification comes from the observation of a rotational perturbation in the v = 9 level of the $\underline{b}'^3\Sigma^-$ state, which is discussed in Section IV E.

D. Location of the Upper State

As we have discussed in the preceeding sections, the uniform intensity distributions within the predissociation bands, coupled with the gradual variation of rotational features within each v" progression, suggests treating the observed upper state levels as consecutive vibrational levels in a single electronic state, the $2^3\Pi$. The upper state vibrational spacings arising from this single-state interpretation (Fig. 7) show a change in slope between v' = 4 and 8. We have modeled a single potential energy curve such that its

vibrational eigenenergies correspond to the observed $2^3\Pi$ levels and positioned it at various internuclear distances until the vibrational overlap between its levels and $\underline{b}'^3\Sigma^-(v''=8, 9, 10)$ reflected the intensity distributions observed in the predissociation spectra. The resulting potential energy curve is shown by the dashed curve in Fig. 8. Because rotational constants for the upper state vibrational levels are not available to fix both the internuclear distance scale and the relative slopes of the curve at its inner and outer turning points, the curve shown in this figure is not a unique description of the $2^3\Pi$ potential curve and should be regarded only as a schematic. However, the wide potential well shown by this curve, which is necessary to support the narrow spacing of the observed vibrational levels, and the general region of internuclear distance at which it is drawn are features of the $2^3\Pi$ potential energy curve which should be substantially accurate if the observed predissociated levels are attributed to a single upper state potential.

Both of these features present somewhat of a dilemma when trying to emplain the breadth of the rotational band structures observed here for the $2^3\Pi \leftarrow \underline{b}'^2\Sigma^-$ system: The main band features spread over a range of 30 to 50 cm^{-1}. Such a narrow distribution in a $^3\Pi \leftarrow {}^3\Sigma$ transition can only be achieved if the rotational constants in both states are similar and the fine-structure constant of the $^3\Pi$ state is relatively small.[31]

We have attempted to model the rotational envelopes of the $2^3\Pi \leftarrow \underline{b}'^3\Sigma^-$ transitions using the known rotational constants for the b' state (see next section), the rotational constants calculated for the $2^3\Pi$ potential curve shown in Fig. 8, and a rotational temperature of 400 K. The resulting band structures were red degraded and extended over several hundred cm^{-1}. Band structures approximating the predissociation spectra could only be achieved by

incorporating one of the following devices: (a) Assuming rotational levels $J \gtrsim 10$ were either not populated in the $\underline{b}'$ state or were not predissociated in the upper state; or (b) Assuming a rotational constant for the upper state which was nearly equal to that for the b' state, i.e., by moving the potential curve drawn in Fig. 8 to substantially shorter internuclear distance.

As will be shown in the next section, there is evidence that high rotational levels are indeed observed in the bands. Hence, we rule out (a) as being responsible for their narrow appearance. In addition, we could not account for the vibrational intensity distributions when the upper state potential curve was moved to the shorter internuclear distances required in (b). Of course, when comparing the intensity of the predissociated levels to Franck-Condon factors for the $2^3\Pi \leftarrow \underline{b}'^3\Sigma^-$ transitions, we neglect contributions to these intensities from the vibrational overlap between the $2^3\Pi$ state and the predissociating state. This neglect may be partially justified on the basis that we observe (at high resolution) no linewidth variations among the various vibrational levels. We also note that no features are observed in the NO photoelectron spectrum at energies near our observed upper state levels. This suggests that the $2^3\Pi$ state must lie at sufficiently large internuclear distances to prevent its being reached in vertical transitions from NO $\underline{X}^2\Pi(v = 0)$. Consequently, moving the $2^3\Pi$ potential curve to shorter distances does not seem justified.

We must therefore consider the possibility that the observed vibrational structure of the upper state arises from the interplay of two separate electronic states of $^3\Pi$ character that perturb each other only slightly. For the purpose of discussion, we will name these two states $\underline{x}^3\Pi$ and $\underline{x}'^3\Pi$, where $\underline{x}$ refers to the state at shorter internuclear distance. If the $\underline{x}$ state is bound more strongly than the $\underline{x}'$, then vibrational levels at energies above

the well of the $\underline{x}'$ state will exhibit effective rotational constants which are intermediate between those of the unperturbed states and vibrational spacings for the unperturbed states that are bigger than those appearing in Fig. 7. The actual relationship between those two states could be similar to the interaction between the $\underline{C}^3\Pi_u$ and $\underline{C}'^3\Pi_u$ states in N_2. There the $\underline{C}$ state, with the deeper well and lying at shorter internuclear distance, intersects the inner wall of the potential well of the more weakly bound $\underline{C}'$ state. Carroll and Mulliken[32] have proposed that the intersection of these states is not avoided, but produces an overlapping of the vibrational manifolds in each state. The rotational constants within each level then vary in $\underline{C}$ and $\underline{C}'$ character as the degree of perturbation between the two manifolds changes.

This mechanism is also known to produce violent perturbations in the spacing of vibrational levels within the manifold of each state. In the present case of NO^+, strong, regular displacements could be realized if, say, every third upper state vibrational level were assigned to $\underline{x}^3\Pi$ (e.g., $v' = 0, 3, 6, \ldots$) and the remaining levels to $\underline{x}'^3\Pi$. This would allow a symmetric perturbation of the levels in each state and may account for the contiguous nature of the band shapes and intensities. However, even approximate treatment of this problem will require information on the properties of at least one of these states outside the perturbed region.

Some additional, although negative, information on the $2^3\Pi$ state is obtained from photoelectron spectroscopy. No significant structure appears in the NO photoelectron spectrum[12] which could be associated with the predissociated levels of this state. However, an intense peak is observed in the spectrum at 21.722 eV. Four Rydberg series involving excitation of the NO σ^*2s orbital have been identified which converge to this same energy.[14] These observations have suggested that the origin of an NO^+ state lies at this

energy with an equilibrium internuclear distance close to that of $NO(\underline{X}^2\Pi)$ and an electron configuration of

$$\sigma 1s^2\ \sigma^* 1s^2\ \sigma 2s^2\ \sigma^* 2s^1\ \sigma 2p^2\ \pi 2p^4\ \pi^* 2p^1. \qquad (1)$$

Lefebvre-Brion[33] has calculated the properties of the NO^+ states arising from this configuration and found that assignment of this feature to a $^3\Pi$ state is in best agreement with the experimental observations. This state has been named[12,33] $\underline{c}^3\Pi$ by analogy with the N_2 state having the same configuration,[11] $\underline{C}^3\Pi_u$, which adiabatically correlates to very highly excited atomic products.[34] The approximate location[13] of this state is shown in Fig. 8.

The configuration of the $2^3\Pi$ state has not been reported; however, we know that it must correlate to the $N^+(^3P) + O(^3P)$ separated atom limit. Only three $^3\Pi$ configurations are possible from this limit. One of these is known[11] to describe the $\underline{b}^3\Pi$ state. We therefore attribute either of the remaining configurations:

$$\sigma 1s^2\ \sigma^* 1s^2\ \sigma 2s^2\ \sigma^* 2s^2\ \sigma 2p^2\ \pi 2p^1\ \sigma^* 2p^1 \qquad (2)$$

or

$$\sigma 1s^2\ \sigma^* 1s^2\ \sigma 2s^2\ \sigma^* 2s^2\ \sigma 2p^1\ \pi 2p^3\ \pi^* 2p^2 \qquad (3)$$

to the $2^3\Pi$ state. Configuration (3) is equivalent to the major configuration[11] of the $\underline{C}'^3\Pi_u$ state in N_2. Thus this state is likely tne isoelectronic analog of the $2^3\Pi$ in NO^+. However, it is clear from Fig. 8 that, despite the analogy with N_2, the $\underline{c}^3\Pi$ state is too far removed in energy to

be the $x^3\Pi$ component of the $2^3\Pi$ state which was discussed above. Rather, a third $^3\Pi$ state will most likely be responsible for the homogeneous perturbation of the $2^3\Pi$. Figure 8 does suggest that the repulsive wall of the $2^3\Pi$ state will pass close to the potential well of the $\underline{c}^3\Pi$ state. Even the weak coupling expected between (1)-(2) or (1)-(3) would predissociate the $\underline{c}$ state. Indeed photoelectron-photoion coincidence studies[17] have found that the $\underline{c}$ state is completely predissociated to $N^+(^3P) + O(^3P)$.

The theoretical calculations which are presently available do not accurately describe the NO^+ potential curves above the first separated atom limit. This is particularly unfortunate in the present investigation since the states in this region are expected to have strongly mixed configurations, particularly at the larger internuclear separations observed here. Thus existing calculations are of little assistance in identifying the true form of the $2^3\Pi$ potential curve. We are currently analyzing the numerous other predissociation bands, apparently unrelated to the present band systems, which terminate in levels above and below those discussed here. Hopefully, some of these bands will provide additional information on the location of the perturbing $^3\Pi$ state.

E. Rotational Features in the Bands

Detailed comparison of the low resolution spectra of the α and β band systems shown in Fig. 3 reveals marked differences in their rotational envelopes. These differences are shown more clearly in Fig. 9 where the (3,8) and (3,9) bands are given on an expanded wavelength scale. Although both bands have the same general shape, the rotational structure in the (3,9) band is decidedly less congested. This suggests that $v'' = 9$ of the $b'^3\Sigma^-$ state has fewer rotational levels populated among the NO^+ ions in the beam than does $v'' = 8$.

The $\underline{b}'^3\Sigma^-$ state is not the lowest triplet state in the NO^+ manifold (see Fig. 1). It may radiate in allowed transitions to the $\underline{b}^3\Pi$ [the (9,0) band origin would be at 5272 Å]. However, transitions in the $\underline{b}' \rightarrow \underline{b}$ system have never been observed despite intensive searches in spectra emitted from discharge lamps. Field[7] suggests that the triplet states of NO^+ are quenched in the discharge faster than they can radiate. Evidence for a long radiative lifetime for the $\underline{b}'$ state comes from the ion beam emission studies of Maier and Holland.[8] Several features in their spectra have been attributed to transitions in the $\underline{b}'^3\Sigma^- \rightarrow \underline{X}^1\Sigma^+$ system, induced by spin-orbit interaction between the $\underline{A}^1\Pi$ and $\underline{b}'^3\Sigma^-$ states.[7] Their measurements indicate lifetimes of order 10 μs for several vibrational levels in the $\underline{b}'$ state. The corresponding system $\underline{e}^3\Sigma^- \rightarrow \underline{X}^1\Sigma^+$ in the isoelectronic CO molecule is also known[35] to be long-lived (τ = 3 μs).

The time required for NO^+ ions in our experiment to reach the laser from the ion source is about 20 μs. Therefore, an appreciable fraction of the $\underline{b}'$ state levels that are populated during the ionization process will be lost due to radiation. This direct radiative loss should be essentially uniform among the rotational levels, hence the Boltzmann distribution of rotational levels in the ion source will be retained during the transit time of the beam and will be similar within each of the vibrational levels in the $\underline{b}'$ state. However, v" = 9 of the $\underline{b}'$ state is locally perturbed by the v = 3 level of the $\underline{A}^1\Pi$ state, whereas the v" = 8 and 10 levels are not. This perturbation was first predicted by Field[7] and has more recently been observed by Alberti and Douglas[6] in the $\underline{A}^1\Pi \rightarrow \underline{X}^1\Sigma^+$ emission spectrum. Figure 10a shows the deviation of the rotational term positions measured by Alberti and Douglas for the $\underline{e}$ levels in v = 3 of the $\underline{A}$ state from the term values that are expected in the absence of the perturbation. The discontinuities in this figure arise from

the near-degeneracy of several rotational levels in $\underline{A}^1\Pi(v=3)$ with the corresponding levels in the F_1 ($N = J-1$) and F_3 ($N = J + 1$) components ($\underline{e}$ levels) of $\underline{b}'^3\Sigma^-(v''=9)$. Perturbation of the $\underline{f}$ levels by the F_2 ($N = J$) component is also observed.

The $\underline{A}$ state is short-lived (56 ns);[36] hence, the radiative lifetime of the perturbed rotational levels in the $\underline{b}'$ state will decrease to a degree dependent on the strength of the perturbation. In order to assess this effect on the rotational distribution of NO^+ ion arriving at the laser, we have analyzed[37] these perturbations using a nonlinear least-squares fitting procedure employing the rotational energy expressions given by Herzberg[38] and Kovacs[39] for the $^3\Sigma^-$ and $^1\Pi$ states, respectively. The resulting deperturbed molecular constants obtained for $\underline{A}^1\Pi(v=3)$ and $b'^3\Sigma^-(v=9)$ are given in Table III. Also given in this table is the value obtained for the spin-orbit matrix element (H_{so}) that couples these states. We note that it differs by less than 10% from the estimate given by Field.[7] Using these constants, together with the measured lifetimes of 56 ns for the $\underline{A}$ state and 10 μs for the $\underline{b}'$ state, we have calculated the lifetime of individual rotational levels in $\underline{b}'^3\Sigma^-(v=9)$. The predicted lifetimes of the F_1 and F_3 components of this state together with those of the $\underline{e}$ levels of $\underline{A}^1\Pi(v=3)$ are shown in Fig. 10b. A similar dependence is found for the F_2 component and the $\underline{f}$ levels with their respective lifetime extrema occurring at $J = 22$. The resulting effect of this perturbation on the rotational distribution in $\underline{b}'^3\Sigma^-(v=9)$ after a 20 μs beam transit time is shown by the solid curve in Fig. 10c. In comparison with the 400 K Boltzmann distribution that should characterize the $\underline{b}'^3\Sigma^-(v=9)$ levels, which is shown by the dashed curve in this figure, an appreciable fraction of the higher rotational levels of $v = 9$ will not be present in the beam at the time of photoabsorption. The loss of these levels

likely accounts for the different rotational envelopes in the v" = 8 and v" = 9 progressions.

A second prominent feature in the band structure of the $2^3\Pi \leftarrow \underline{b}'^3\Sigma^-$ transitions is the two isolated lines which appear in the low resolution spectra, Fig. 3 and 9, on the long-wavelength side of each band terminating in $v' < 7$. Above v' = 7, the lines appear to be blended with adjacent band structures due to the decreasing vibrational spacing in the $2^3\Pi$ state. The spacing within each pair of lines is weakly dependent on upper state vibrational quantum number, varying from 22 cm^{-1} at v' = 0 to 15 cm^{-1} at v' = 7, and is comparable in both the v" = 8 and 9 progressions. The isolated line which appears in Fig. 9 with Doppler components at 16654 and 16669 cm^{-1} was examined at high resolution. It was found to consist predominately of two strong transitions separated by 3.00 cm^{-1}, each having linewidths < 100 Mhz. A number of other, weaker features also appear in this wavelength region as well as in the interval between this "line" and the main band.

The sudden onset of the isolated lines at v" = 0 in both the v" = 8 and 9 progressions, their intensity pattern, their photofragment kinetic energies, as well as the upper state vibrational spacings derived from their spacings are all consistent with the bands which we have attributed to the $2^3\Pi \leftarrow \underline{b}'^3\Sigma^-$ transitions. This strongly suggests that these lines also terminate in the $2^3\Pi$ state. However, the substantial separation of the lines from the main body of each band makes it difficult to associate them with the same rotational envelopes. In addition, the lower state separation derived from the isolated lines (1110.1 cm^{-1} at v' = 0 increasing to 1114.4 at v' = 4) is significantly different from that derived from the main band features (1101.7 cm^{-1} at v' = 0 decreasing to 1098.9 at v' = 4). These difficulties might be explained if the population of a high rotational level in the

$\underline{b}'^3\Sigma^-$ state were substantially increased due to perturbations in both v" = 8 and 9 by near-degenerate levels in a longer-lived state, e.g., the $\underline{a}^3\Sigma^+$. However, the photofragment kinetic energies produced at these lines are less than 80 cm^{-1} higher than the lowest kinetic energy photofragments produced in the main body of the bands. This precludes the rotational levels corresponding to the isolated lines from being more than ~ 5 quanta larger than the average rotational level within the main body of the bands. Such a small difference in rotational quantum number is insufficient to explain the large separation of the isolated lines from the main band structure.

A more likely explanation would be to attribute the isolated lines to transitions into the $2^3\Pi$ from a lower state other than the $\underline{b}'^3\Sigma^-$. The lower-state spacing of the lines restricts the choice for this state to both the $\underline{A}'^1\Sigma^-$ and the $\underline{W}^1\Delta$ (see Table II), but only the $\underline{W}$ state could be sufficiently long-lived to persist in the NO^+ ion beam for the required transit time. In order for the $2^3\Pi \leftarrow \underline{W}^1\Delta$ transitions to occur with reasonable intensity, the $\underline{W}$ state would have to be perturbed by near-degenerate levels of a triplet state to lend it sufficient triplet character. Intersection of $\underline{W}^1\Delta(v=5,6)$ at $J < 30$ with all candidate perturbing states can be ruled out on the basis of their known molecular constants[13] with the exception of the $\underline{b}^3\Pi(v=11,12)$, where the molecular constants are known only for $v < 2$. The ($\underline{W}$, $\underline{b}$) perturbation would occur only in the $^3\Pi_2$ substate; hence, the $2^3\Pi \leftarrow \underline{W}^1\Delta$ transition from a single perturbed rotational level could give rise to a maximum of three Λ-doubled lines for each of the upper state vibrational levels. If the intensity of the Q branch were weak, or if the photofragments arising from this branch were attenuated by their angular distributions, then only two pairs of lines would appear in the spectrum. These $2^3\Pi \leftarrow \underline{W}^1\Delta$ transitions could account for the isolated rotational lines.

F. Predissociation Mechanism

The high resolution spectra of the bands terminating in v" = 0-8 show no measurable variation in transition linewidths. Rather, the observed linewidths are apparatus limited demonstrating that predissociation of the $2^3\Pi$ state occurs only slowly (predissociation lifetimes $\gtrsim$ 1.6 ns). Because only O^+ photofragments are produced, the state responsible for the predissociation must be one of the four states ($^{1,3,5,7}\Sigma^+$) arising from the $N(^4S^o) + O^+(^4S^o)$ limit. The $\underline{X}^1\Sigma^+$ and $\underline{a}^3\Sigma^+$ states are too strongly bound to interact effectively with bound levels of the $2^3\Pi$ state and the $^7\Sigma^+$ state is not directly coupled to the $2^3\Pi$ state ($\Delta S = 2$). This leaves the $\underline{\alpha}^5\Sigma^+$ as the best candidate for the predissociating state.

The $\underline{\alpha}^5\Sigma^+$ state is coupled to the $2^3\Pi$ state through the spin-orbit operator. The general effects of this interaction on the linewidths (Γ_n) of the predissociating transitions may be investigated using the Fermi golden rule:[40]

$$\Gamma_n = 2\pi|\langle\Psi_n(r,R)|V(R)|\Psi_E(r,R)|^2 \quad . \qquad (4)$$

Here $\Psi_n(r,R)$ and $\Psi_E(r,R)$ denote the rovibronic wavefunction of the predissociated level n and the continuum wavefunction at energy E above the dissociation limit, respectively, and V(R) is the operator that couples the bound and continuum states. The use of equation (4) to predict the linewidths of the transitions neglects any linewidth contributions from the properties of the lower state involved in the transitions, $\underline{b}'^3\Sigma^-$. This neglect is justified on the basis of the long lifetimes[7,8] of the $\underline{b}'$ levels.

For the ($2^3\Pi$, $\underline{\alpha}^5\Sigma^+$) interaction, Eqn. (4) reduces to

$$\Gamma_\Omega = 2\pi \sum_j |H(2^3\Pi_\Omega; \underline{\alpha}^5\Sigma_j^+)|^2 \quad . \qquad (5)$$

The summation over the components j of the Σ^+ state which interact with a particular fine-structure level Ω of the $^3\Pi$ state is based on the assumption that only insignificant phase differences among the j components are accumulated from the point of interaction to the dissociation limit. This is expected to be valid for a Σ state because its fine-structure levels lie close in energy. We have evaluated the matrix elements for the $H(2^3\Pi_\Omega; \underline{\alpha}^5\Sigma_j^+)$ using the $^5\Sigma^+$ transformation matrix elements given by Kovacs[41] and Hund's case (a) elements for spin-orbit coupling given by Freed:[42]

$$\langle J\Omega S'\ \Lambda'\ \Sigma' | H_{so} | J\Omega S\Lambda\Sigma \rangle = (-1)^{\Sigma} \begin{pmatrix} 1 & 1 & 2 \\ \Sigma-1 & 1 & -\Sigma \end{pmatrix} A_{10} \quad , \qquad (6)$$

where A_{10} is the intercombination analog of the spin-orbit parameter. The resulting linewidths for the three substates of $2^3\Pi$ are:

$$\Gamma_0 \propto A_{10} \qquad (7a)$$

$$\Gamma_1 \propto 3A_{10} \qquad (7b)$$

$$\Gamma_2 \propto 6A_{10}. \qquad (7c)$$

On the other hand, the (unlikely) event where both states are described by case (b) coupling reduces the ratio of expected linewidths among the three components to only 0.67 : 0.77 : 1.

Neither case would be distinguishable if A_{10} were so small ($< 10^{-3} cm^{-1}$) that the expected linewidth variations fall below the limit of our experimental resolution. We should therefore consider the possible magnitude of this matrix element. The dominant electron configuration for the $\underline{\alpha}^5\Sigma^+$ state is:[11]

$$\sigma 1s^2\ \sigma^* 1s^2\ \sigma 2s^2\ \sigma^* 2s^2\ \sigma 2p^2\ \sigma 2p^2\ \pi 2p^2\ \pi^* 2p^2 \quad . \qquad (8)$$

The probable configurations of the $2^3\Pi$ state were given by (2) and (3) in Section IV D. Both of these configurations transform into (8) via single electron excitations. This suggests approximating A_{10} by single electron spin-orbit integrals. Thus

$$A_{10} \sim \langle v|\chi\rangle \langle \pi^* 2p|a\ell_+|\sigma^* 2p\rangle \qquad (9)$$

if $2^3\Pi$ is described by configuration (2), or

$$A_{10} \sim \langle v|\chi\rangle \langle \pi 2p|a\ell_+|\sigma 2p\rangle \qquad (10)$$

for configuration (3), where $|v\rangle$ and $|\chi\rangle$ are the vibrational and continuum wavefunctions of the $2^3\Pi$ and $\underline{\alpha}^5\Sigma^+$ states, respectively. The one-electron spin-orbit matrix element in (10) has been reported[7] to be 76.6 cm^{-1}. The value for the corresponding matrix element in (9) has not been measured, but is likely to be the same order of magnitude. Consequently, at this level of approximation, only a uniformly small ($\sim 10^{-4} - 10^{-5}$) vibrational overlap between the $2^3\Pi$ and $\underline{\alpha}^5\Sigma^+$ states would lead to the observed linewidths.

As can be seen in Fig. 8, the calculated potential energy curve for the $\underline{\alpha}$ state passes directly through the potential well of the $2^3\Pi$ state. While this may certainly lead to the requisite small overlaps for specific vibrational levels of the $2^3\Pi$, it is unreasonable to expect accidentally small vibrational overlaps to account for the narrow linewidths observed in each of the first nine vibrational levels of the $2^3\Pi$ state.[43] This could indicate that the relative locations shown for these two curves in Fig. 8 are not accurate. However, we also note that the $(2^3\Pi, \underline{\alpha}^5\Sigma^+)$ crossing occurs in the perturbed region of the $2^3\Pi$ state. Since the perturbing $^3\Pi$ state undoubtedly has a configuration different from either (2) or (3), the use of a single configuration description for the $2^3\Pi$ state is clearly inappropriate. Proper treatment of the $(2^3\Pi, \underline{\alpha}^5\Sigma^+)$ interaction will therefore require explicit calculation of the complete spin-orbit matrix element taking full account of the configuration mixing when improved theoretical potential curves become available.

V CONCLUSIONS

Twenty vibrational levels of a weakly bound NO^+ electronic state correlating to $N^+(^3P) + O(^3P)$ are observed to predissociate to $O^+(^4S^o) + N(^4S^o)$. The levels are accessed by electronic transitions from three vibrational levels in a lower energy electronic state of NO^+ which are sufficiently long-lived to be significantly populated 20 μs after their formation. The energies of the predissociated levels, together with the rotational and vibrational structure in the transitions, are most consistent with assignment of the upper and lower electronic states to $2^3\Pi$ and $\underline{b}'^3\Sigma^-$, respectively. The predissociated vibrational levels in the $2^3\Pi$ state are tentatively identified as $v' = 0\text{-}19$.

A number of perturbations are observed in the predissociation spectra. The rotational population of the $\underline{b}'^3\Sigma^-(v''=9)$ levels appears to be selectively depleted due to interaction with $\underline{A}^1\Pi(v=3)$. Isolated rotational structure which accompanies the $2^3\Pi \leftarrow \underline{b}'^3\Sigma^-$ bands suggests that perturbation of $\underline{W}^1\Delta(v=5,6)$ by $\underline{b}^3\Pi(v=11,12)$ also occurs. The $2^3\Pi$ state is believed to be predissociated by the $\underline{a}^5\Sigma^+$ state, but the long predissociation lifetime of > 1.6 ns has not allowed confirmation of this assignment. In addition, the $2^3\Pi$ state is found to be homogeneously perturbed. The perturbing state is likely not the $\underline{c}^3\Pi$ state observed by photoelectron spectroscopy, but the $^3\Pi$ state arising from the $O^+(^4S^o) + N(^2D^o)$ limit. On the other hand, the location of the $2^3\Pi$ state makes it the likely candidate for causing the reported predissociation of the $\underline{c}^3\Pi$ state.

Molecular constants are not given for the highly perturbed vibrational structure of the $2^3\Pi$ state nor has rotational assignment of the spectra been possible. However, this study has suggested a number of experimental investigations which may lead to a unique description of the $2^3\Pi$ state. Zeeman

splitting of the rotational lines in the $2^3\Pi \leftarrow \underline{b}'^3\Sigma^-$ transitions would greatly assist in their assignment. Extension of the wavelength region covered in the predissociation spectra to include transitions originating in lower vibrational levels of the $\underline{b}'$ state would also more precisely establish the $2^3\Pi$ state location. Isotope shifts in the vibrational structure would confirm the vibrational numbering in the bands and identify those bands which may arise from the perturbing $^3\Pi$ state. Finally, assignment of the other band systems in the NO^+ predissociation spectra may locate the perturbing $^3\Pi$ state. These will be the subject of future investigations on NO^+.

ACLKNOWLEDGMENTS

The authors would especially like to thank Dr. D. L. Huestis and Dr. R. P. Saxon for many helpful discussions during the course of this work. The authors also thank Dr. D. L. Albritton for his encouragement and for providing unpublished Franck-Condon factors for some of the NO^+ states. The use of a laboratory computer system furnished by an equipment grant (PHY-14436) from the National Science Foundation is gratefully acknowledged.

REFERENCES

1. M. Oppenheimer, A. Dalgarno, E. P. Trebino, L. H. Brace, H. C. Brinton, and J. H. Hoffman, J. Geophys. Res. 82, 191 (1977).

2. D. G. Torr and M. R. Torr, J. Atmos. Terr. Phys. 41, 797 (1979).

3. E. E. Ferguson, in Kinetics of Ion-Molecule Reactions, edited by P. Ausloos (Plenum Press, New York, 1979), p. 377.

4. P. Baer and E. Miescher, Helv. Phys. Acta 26, 91 (1953).

5. E. Miescher, Helv. Phys. Acta 29, 135 (1956).

6. F. Alberti and A. E. Douglas, Can. J. Phys. 53, 1179 (1975).

7. R. W. Field, J. Mol. Spectrosc. 47, 194 (1973).

8. W. B. Maier and R. F. Holland, J. Chem. Phys. 54, 2693 (1971).

9. H. Lefebvre-Brion and C. M. Moser, J. Chem. Phys. 44, 2951 (1966).

10. P. W. Thulstrup, E. W. Thulstrup, A. Anderson, and Y. Ohrn, J. Chem. Phys. 60, 3975 (1974).

11. H. H. Michels, in The Excited State in Chemical Physics, edited by J. W. McGowan (Wiley, New York, 1980), Vol. II.

12. O. Edqvist, L. Asbrink, and E. Lindholm, Z. Naturforsch. 26a, 1407 (1971).

13. D. L. Albritton, A. L. Schmeltekopf, and R. N. Zare, J. Chem. Phys. 71, 3271 (1979).

14. M. Sasanuma, Y. Morioka, E. Ishiguro, and M. Nakamura, J. Chem. Phys. 60, 327 (1974).

15. H. Hertz, H. W. Jochims, H. Schenk, and W. Sroka, Chem. Phys. Lett. 29, 572 (1974).

16. P. L. Kronebusch and J. Berkowitz, Int. J. Mass Spectrom. Ion Phys. 22, 283 (1976).

17. J. H. Eland, J. Chem. Phys. 70, 2926 (1979).

18. A. S. Newton and A. F. Sciamanna, J. Chem. Phys. 50, 4868 (1969).

19. T. R. Govers and J. Schopman, Chem. Phys. Lett. 12, 414 (1971).

20. Pham D. and M. Bizot, Int. J. Mass Spectrom. Ion Phys. 10, 227 (1972/73).

21. T. F. Moran, F. C. Petty, and A. F. Hedrick, J. Chem. Phys. 51, 2112 (1969).

22. T. O. Tiernan and R. E. Marcotte, J. Chem. Phys. 53, 2107 (1970).

23. B. A. Huber, T. M. Miller, P. C. Cosby, H. D. Zeman, R. L. Leon, J. T. Moseley, and J. R. Peterson, Rev. Sci. Instrum. 48, 1306 (1977).

24. P. C. Cosby, J. B. Ozenne, J. T. Moseley, and D. L. Albritton, J. Mol. Spectrosc. 79, 203 (1980).

25. A. Carrington, D. R. Milverton, and P. J. Sarre, Mol. Phys. 32, 297 (1976).

26. C. Pernot, J. Durup, J. B. Ozenne, J. A. Berwick, P. C. Cosby, and J. T. Moseley, J. Chem. Phys. 71, 2387 (1979).

27. The angular distribution of the photofragments, which establishes the exact shape of the kinetic energy spectrum in the laboratory frame for a given W value, is dependent on rotational quantum number. See Ref. 26.

28. G. Herzberg, Molecular Spectra and Molecular Structure I. Spectra of Diatomic Molecules (Van Nostrand Reinhold, New York, 1950) p. 295.

29. A. G. Gaydon, Dissociation Energies and Spectra of Diatomic Molecules, 3rd Ed. (Chapman and Hall, London, 1968) p. 96.

30. F. J. Grieman, J. T. Moseley, R. P. Saxon, and P. C. Cosby, Chem. Phys. 51, 169 (1980).

31. The clustering of rotational lines into three groups separated by approximately 10 cm^{-1} suggests the spin-orbit parameter for the $2^3\Pi$ state is of this magnitude.

32. P. K. Carroll and R. S. Mulliken, J. Chem. Phys. 43, 2170 (1965).

33. H. Lefebvre-Brion, Chem. Phys. Lett. 9, 463 (1971).

34. R. S. Mulliken, in The Threshold of Space, edited by M. Zelikoff (Pergamon, New York, 1957) p. 169.

35. W. C. Paske, A. W. Garrett, and D. E. Golden, Bull. Am. Phys. Soc. 25, 1119 (1980).

36. J. H. Hesser, J. Chem. Phys. 48, 2518 (1968).

37. H. Helm, to be published.

38. Ref. 28, p. 223. A constant term of $+ 5.05 \times 10^{-6} [N(N + 1)]^2$ was included in equations (V, 17) to correct for centrifugal distortion.

39. I. Kovacs, Rotational Structure in the Spectra of Diatomic Molecules, (American Elsevier, New York, 1968) p. 58.

40. L. I. Schiff, Quantum Mechanics, (McGraw-Hill, New York, 1968) p. 285.

41. Ref. 39, p. 150.

42. K. F. Freed, J. Chem. Phys. 45, 4214 (1966).

43. J. N. Murrell and J. M. Taylor, Mol. Phys. 16, 609 (1969).

Table I. Observed Transitions and Photofragment Kinetic Energies

Band	v"	v'	$G_{v',v"}(cm^{-1})^a$	$\Delta G_{v'}(cm^{-1})^b$	$\Delta G_{v"}(cm^{-1})^c$	W(eV)[d]	$W-G_{v',v"}(eV)^e$
α_o	8	0	16306	203	1103	0.698	-1.324
α_1	8	1	16509	182	1100	0.724	-1.323
α_2	8	2	16691	155	1099	0.748	-1.321
α_3	8	3	16846	120	1102	0.765	-1.324
α_4	8	4	16966	118	1097	0.781	-1.323
α_5	8	5	17084	107	----	0.793	-1.325
α_6	8	6	17191	100	----	0.808	-1.323
α_7	8	7	17291	106	----	0.823	-1.321
α_8	8	8	17396	97	1095	0.832	-1.325
α_9	8	9	17493	88	1097	-----	------
α_{10}	8	10	17581	---	1094	-----	------
	9	0	15203	206	----	-----	------

AD-A098 265 SRI INTERNATIONAL MENLO PARK CA MOLECULAR PHYSICS LAB F/G 20/9
PROPERTIES OF THE EXCITED STATES OF MOLECULAR IONS.(U)
APR 81 P C COSBY, J T MOSELEY, J R PETERSON DAAG29-77-C-0037
UNCLASSIFIED SRI-MP-81-72 ARO-15069.8-P NL

2 OF 2
AD A
098265

END
DATE FILMED
5-81
DTIC

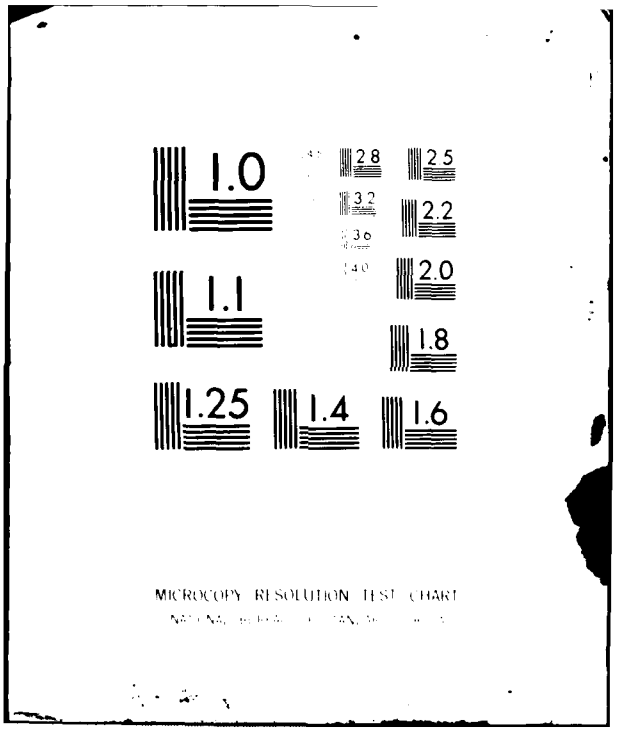
1.0
2.8
2.5
3.2
2.2
3.6
4.0
2.0
1.1
1.8
1.25
1.4
1.6
MICROCOPY RESOLUTION TEST CHART

β_1	9	1	15409	183	----	0.723	-1.188
β_2	9	2	15592	152	----	0.745	-1.188
β_3	9	3	15744	125	----	0.771	-1.181
β_4	9	4	15869	124	----	0.780	-1.188
β_5	9	5	(15993)[f]	---	----	0.794	-1.189
γ_8	9	8	16301	95	----	0.828	-1.193
γ_9	9	9	16396	91	----	0.847	-1.186
γ_{10}	9	10	16487	90	----	-----	-----
γ_{11}	9	11	16577	78	----	0.869	-1.186
γ_{12}	9	12	16655	68	----	0.882	-1.183
γ_{13}	9	13	16723	67	1035	0.893	-1.180
γ_{14}	9	14	(16790)	59	1036	0.899	-1.183
γ_{15}	9	15	(16849)	54	1039	-----	------
γ_{16}	9	16	(16903)	---	1035	-----	------
δ_{13}	10	13	15688	66	----	-----	------
δ_{14}	10	14	15754	56	----	0.900	-1.053
δ_{15}	10	15	15810	58	----	-----	------
δ_{16}	10	16	15868	52	----	0.915	-1.052
δ_{17}	10	17	15920	43	----	-----	------

δ_{18}	10	18	15963	(36)	----	-----	------
δ_{19}	10	19	(15999)	---	----	0.925	-1.059

[a]Photon energy measured at band center.

[b]$G_{v'+1,v''} - G_{v',v''}$

[c]$G_{v',v''} - G_{v',v''+1}$

[d]Translational energy released in the photodissociation. The absolute uncertainties in these values are $^{+\ 0.005}_{-\ 0.010}$ eV. The relative uncertainty between measurements is about a factor of two smaller.

[e]1 eV ≡ 8065.479 cm^{-1}.

[f]Parentheses denote values especially uncertain because spectral features were weak or poorly defined.

Table II. Lower State Vibrational Levels[a]

State	v"	$\Delta G_{v"}(cm^{-1})$[b]	$\Delta G_{v"+1}(cm^{-1})$[c]	$D_{v"}(eV)$[d]
$\underline{b}'^3\Sigma^-$	8	1089 ± 13	1068 ± 14	-1.338 ± 0.015
$\underline{A}'^1\Sigma^-$	7	1069 ± 6	1042 ± 6	-1.277 ± 0.010
$\underline{W}^1\Delta$	5	1079 ± 18	1056 ± 20	-1.326 ± 0.058
This Work	v"	1098 ± 3	1036 ± 10	$-1.323 \begin{smallmatrix}+0.005\\-0.010\end{smallmatrix}$

[a]Values for the $\underline{b}'$, $\underline{A}'$, and $\underline{W}$ states are calculated from the molecular constants in Table I of Ref. 13.

[b]$G_{v"} - G_{v"+1}$

[c]$G_{v"+1} - G_{v"+2}$

[d]Energy of v" with respect to the $O^+(^4S^o) + N(^4S^o)$ separated atom limit. The $\underline{b}'$, $\underline{A}'$, and $\underline{W}$ states actually correlate to the $N^+(^3P) + O(^3P)$ limit, which is higher in energy by 0.916 eV.

Table III. Molecular Constants from the $\underline{A}'\Pi(v=3)$, $b'^3\Sigma^-(v=9)$ Perturbation[a]

$\underline{A}'\Pi(v=3)$	$\underline{b}'^3\Sigma^-(v=9)$[b]
$T_v = 77638.399$	$T_v = 77806.8$
$B_e = 1.50095$	$B = 1.15997$
$B_f = 1.50109$	$\gamma = -0.141$
$D = 6.7931 \times 10^{-6}$	$\lambda = 1.01$
$H_{so} = 4.649$	

[a]Units are cm^{-1}.

[b]See Ref. 38.

FIGURE CAPTIONS

Figure 1. Potential energy curves for the experimentally observed electronic states of NO^+ given by Ref. 13. The accuracy of the individual curves varies - see Ref. 13. Unobserved states are listed at their expected separated atom limits. The potential curves for the $2^1\Pi$ and $2^3\Pi$ states are the adiabatic curves calculated by Ref. 10.

Figure 2. Low resolution (~ 1 Å) wavelength dependence for the production of O^+ photofragments with various center-of-mass kinetic energies (W). The NO^+ ions were irradiated in the laser cavity; each absorption appears as a Doppler doublet separated by ~ 5 Å.

Figure 3. Moderate resolution (~ 1 cm^{-1}), composite spectrum for the production of O^+ photofragments. The center-of-mass kinetic energy of the collected photofragments linearly increases with photon energy from 0.68 eV at 15100 cm^{-1} to 0.81 eV at 16150 cm^{-1} and from 0.67 eV at 16250 cm^{-1} to 0.85 eV at 17670 cm^{-1}. The NO^+ ions were irradiated in the laser cavity; each absorption appears as a Doppler doublet separated by ~ 14 cm^{-1}.

Figure 4. High resolution (~ 0.003 cm^{-1}) spectrum of a portion of the α_2 band.

Figure 5. Moderate resolution ($\sim 1\ cm^{-1}$), intracavity spectra of the γ and δ bands. The center-of-mass kinetic energies of the collected O^+ photofragments increases linearly with photon energy from 0.85 eV to 0.94 eV in the upper spectrum and from 0.81 eV to 0.92 eV in the lower spectrum.

Figure 6. Relative intensities of transitions to the predissociated vibrational levels (v') of the upper electronic state from $\underline{b}'^3\Sigma^-$(v"=8,9,10). The intensities (points) are connected by arbitrary, smooth curves.

Figure 7. Vibrational spacing in the predissociated upper electronic state as a function of (a) mean upper state vibrational quantum number $(v' + 1/2)$ and (b) upper state energy with respect to $O^+(^4S^o) + N(^4S^o)$. The energies of the nine fine-structure combinations of $N^+(^3P) + O(^3P)$ are also shown in (b). The squares, circles, open triangles, and closed triangles are the spacings derived from the α, β, γ, and δ bands, respectively. The dashed curves are least-squares fits of $\Delta G_{v'}$ to a linear functional dependence on (v' + 1/2) in (a) and a quadratic functional dependence on $W_{v'+1}$ in (b). The horizontal error bar in (b) shows the absolute uncertainty in the energy scale.

Figure 8. Selected NO^+ potential energy curves in the region of the lowest energy separated atom limit.. The RKR potential curve of the $\underline{b}'^3\Sigma^-$ state and the estimated potential curve of the $\underline{c}^3\Pi$ state are taken from Ref. 13. The $\underline{\alpha}^5\Sigma^+$ potential energy curve is that

calculated in Ref. 11. The $2^3\Pi$ state is represented by the schematic potential energy curve suggested by the predissociation bands (see text). The vibrational levels observed in the $2^3\Pi \rightarrow \underline{b}'^3\Sigma^-$ transitions are indicated by horizontal lines.

Figure 9. Moderate resolution ($\sim 1\ cm^{-1}$), intracavity spectra of predissociations in $2^3\Pi(v'=3)$ when accessed by absorptions from $v'' = 9$ (upper spectrum) and $v'' = 8$ (lower spectrum) of the $\underline{b}'^3\Sigma^-$ state. Each absorption appears as a Doppler doublet separated by $\sim 14.6\ cm^{-1}$ in the upper spectrum and $\sim 13.8\ cm^{-1}$ in the lower spectrum. The Doppler doublets corresponding to the isolated rotational features discussed in the text are indicated in each spectrum.

Figure 10. Effects of the $\underline{A}^1\Pi(v=3)$, $\underline{b}'^3\Sigma^-(v=9)$ perturbation as a function of rotational quantum number. The upper figure (a) shows the deviation of the term energies of $\underline{e}$ levels in $\underline{A}^1\Pi(v=3)$ reported by Ref. 6 from the energies expected in the absence of perturbation by $\underline{b}'^3\Sigma^-(v=9,F=1,3)$. The center figure (b) gives the expected radiative lifetimes of these levels as a result of the perturbation and the lifetimes of the perturbing $\underline{b}'^3\Sigma^-(v=9)$ levels. The bottom figure (c) shows the expected 400 K Boltzmann population distribution in the rotational levels of the $\underline{b}'^3\Sigma^-$ state produced by electron impact in the ion source (dashed curve) and the population distribution in $\underline{b}'^3\Sigma^-(v=9)$ upon arrival at the laser 20 μs later (solid curve).

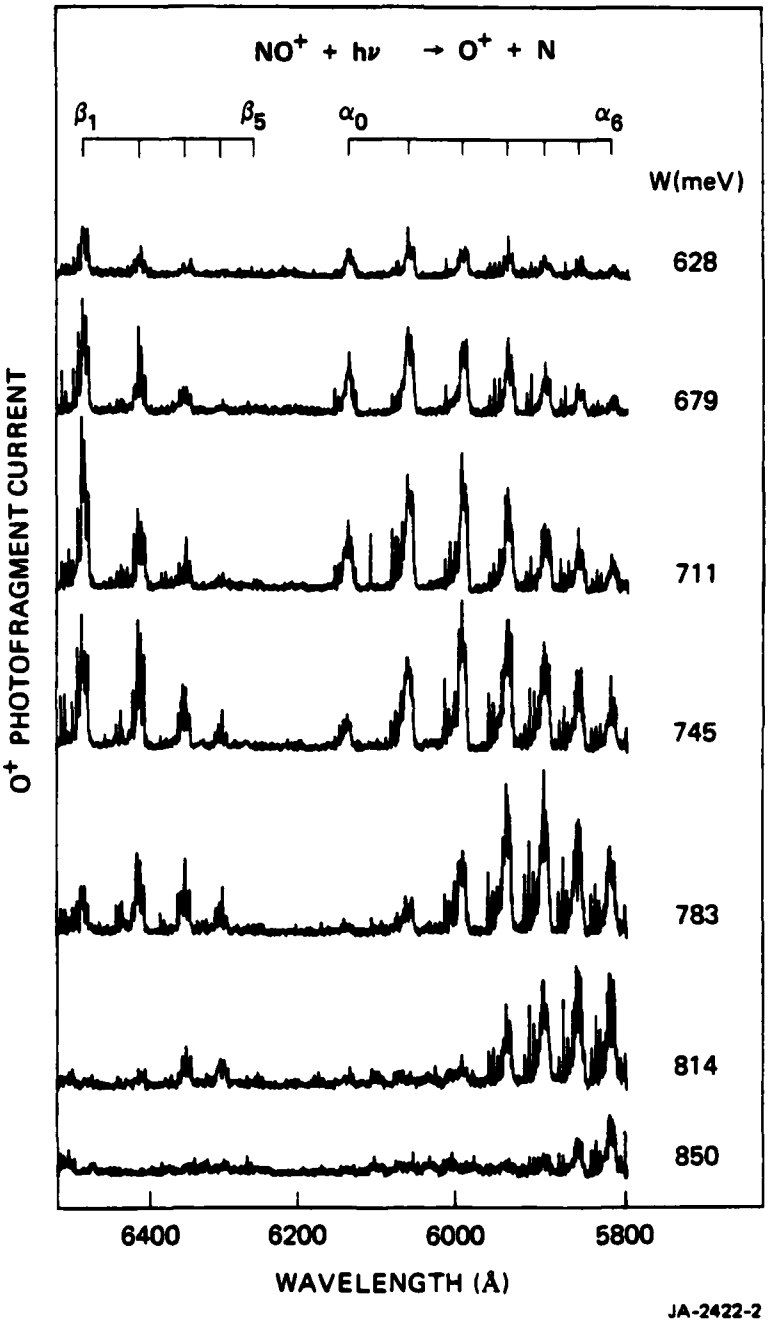
NO+ + hν → O+ + N
β1
β5
α0
α6
W(meV)
628
679
711
745
783
814
850
O+ PHOTOFRAGMENT CURRENT
6400
6200
6000
5800
WAVELENGTH (Å)
JA-2422-2

Figure 1

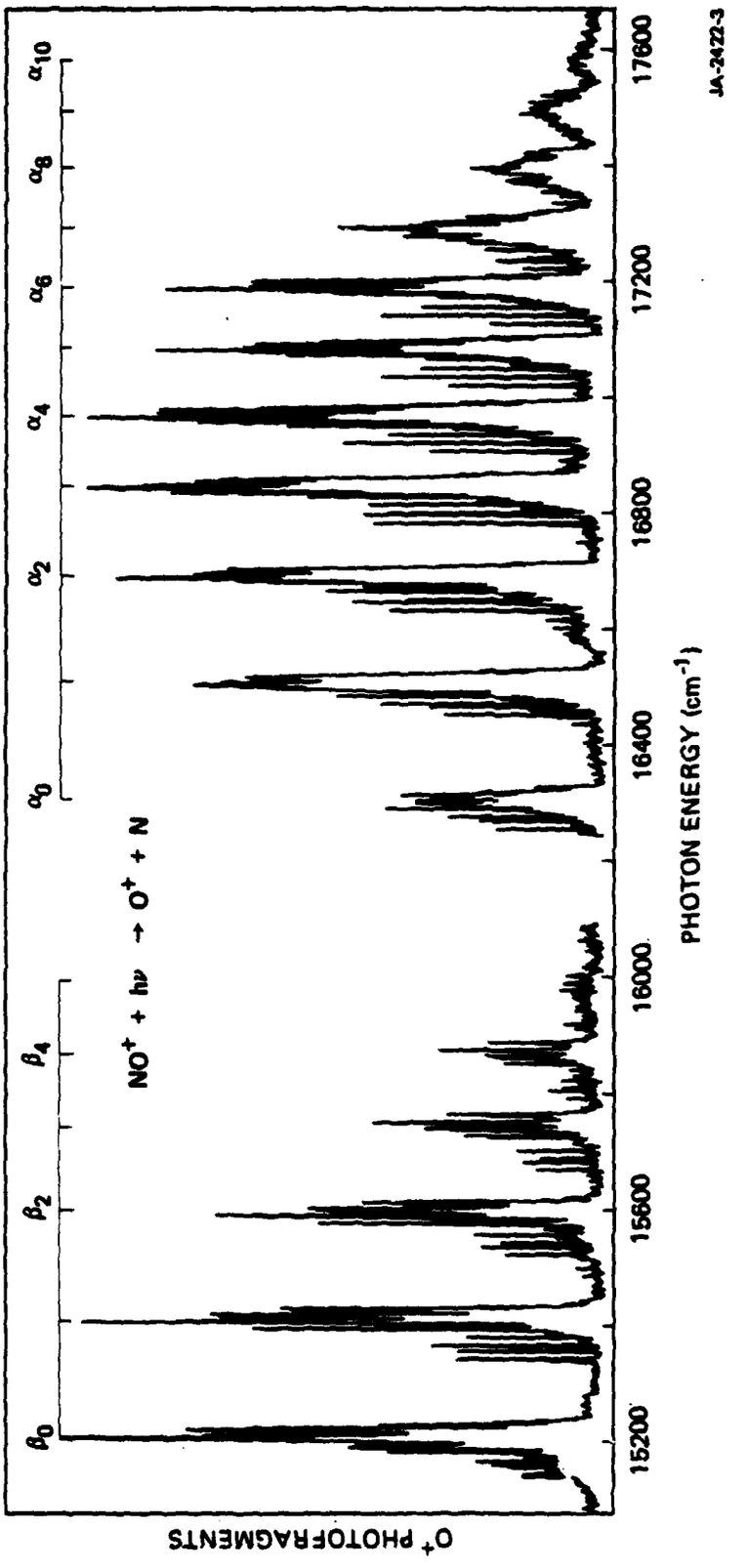
α_0
α_2
α_4
α_6
α_8
α_{10}
β_0
β_2
β_4
$NO^+ + h\nu \rightarrow O^+ + N$
15200
15600
16000
16400
16800
17200
17600
PHOTON ENERGY (cm^{-1})
O^+ PHOTOFRAGMENTS
AA-2422-3

Figure 2

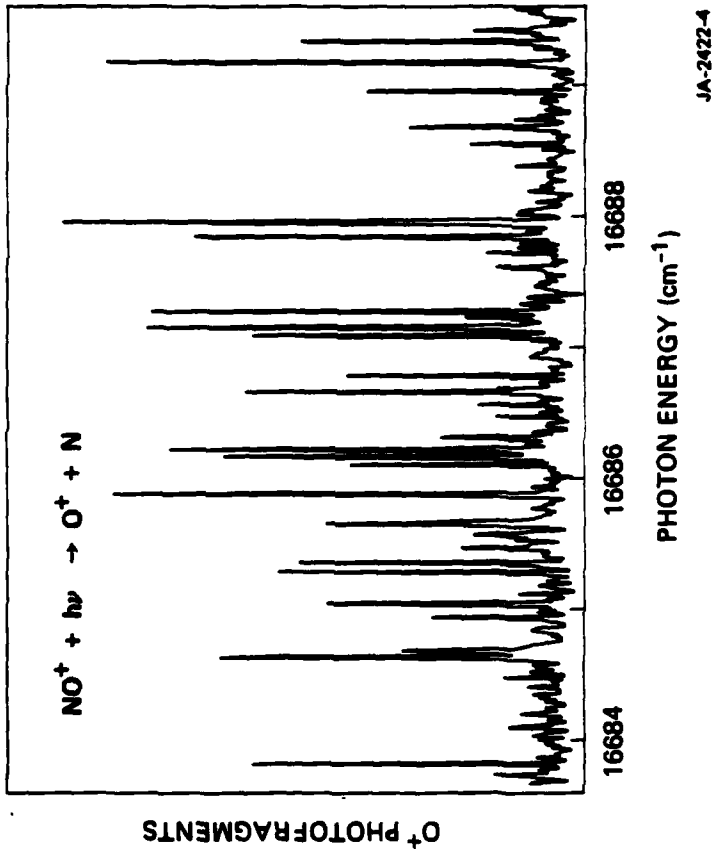
$NO^+ + h\nu \rightarrow O^+ + N$
16684
16686
16688
PHOTON ENERGY (cm^{-1})
O^+ PHOTOFRAGMENTS
JA-2422-4

Figure 3

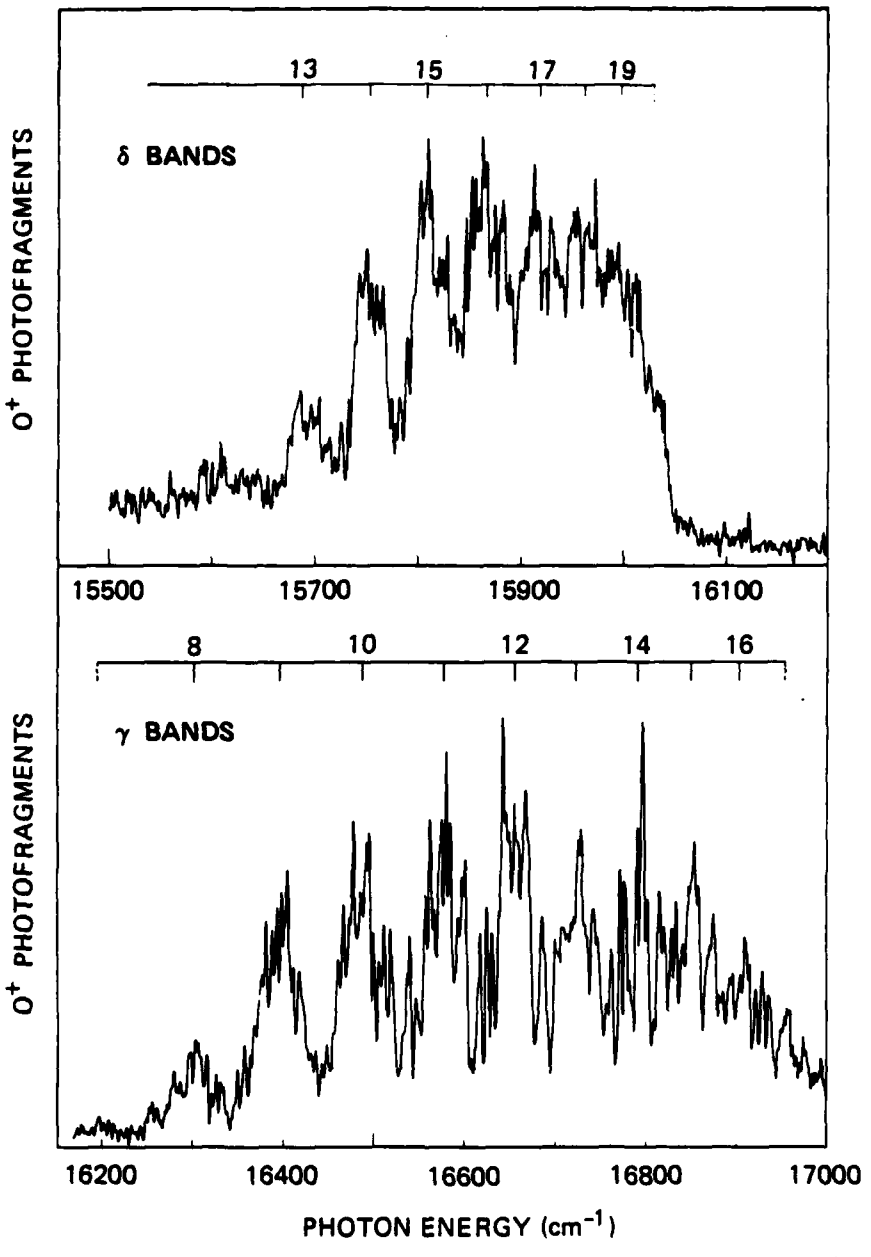
13
15
17
19
δ BANDS
O+ PHOTOFRAGMENTS
15500
15700
15900
16100
8
10
12
14
16
γ BANDS
O+ PHOTOFRAGMENTS
16200
16400
16600
16800
17000
PHOTON ENERGY (cm-1)
JA-2422-5

Figure 4

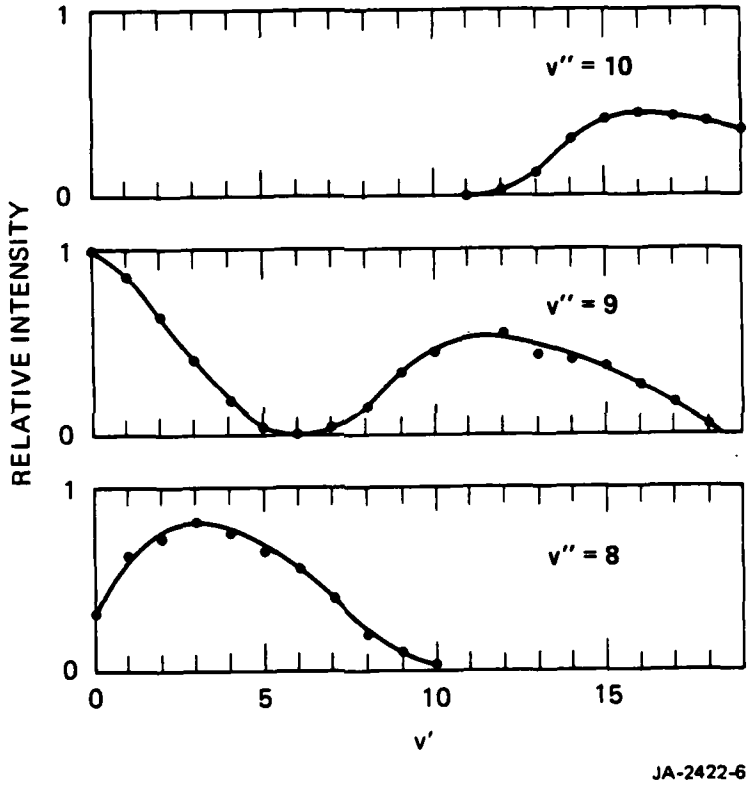

Figure 5

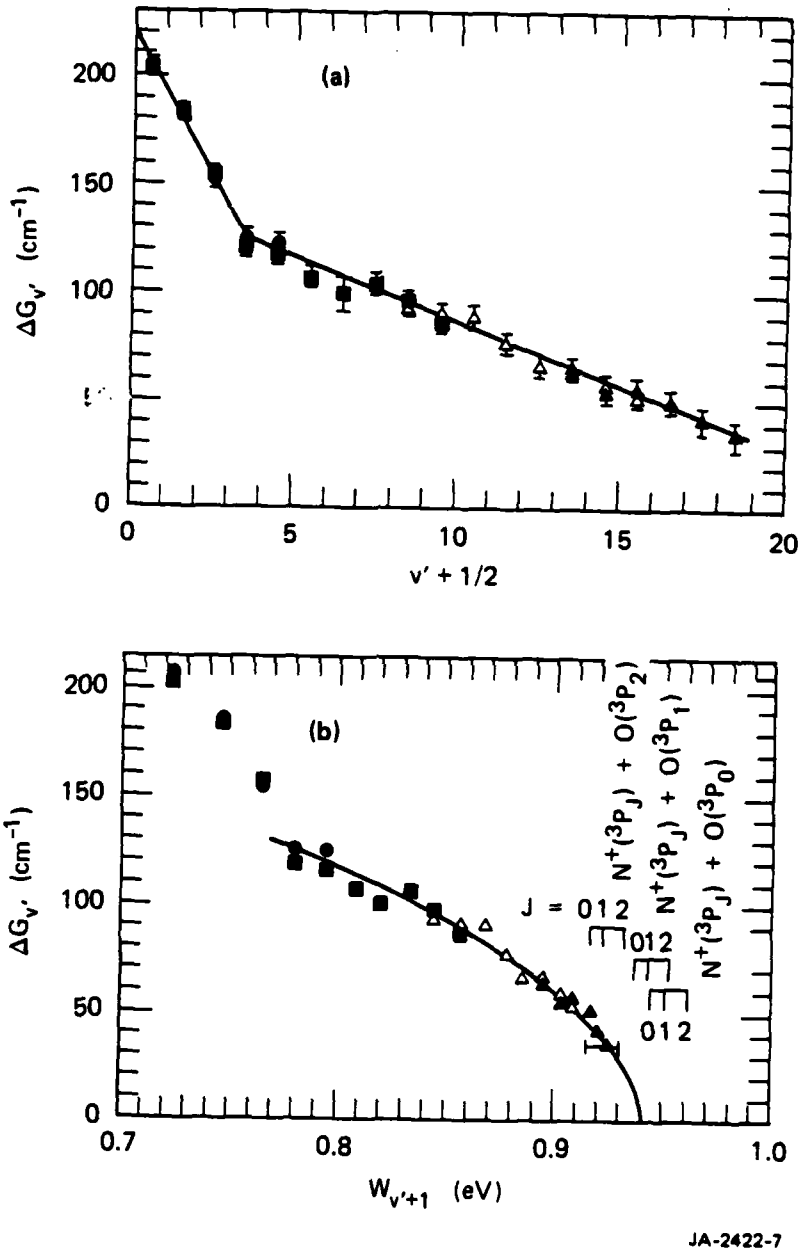
(a)
200
150
100
0
$\Delta G_{v'}$ (cm^{-1})
0
5
10
15
20
v' + 1/2
(b)
200
150
100
50
0
$\Delta G_{v'}$ (cm^{-1})
0.7
0.8
0.9
1.0
$W_{v'+1}$ (eV)
J = 012
012
012
$N^+(^3P_J) + O(^3P_2)$
$N^+(^3P_J) + O(^3P_1)$
$N^+(^3P_J) + O(^3P_0)$
JA-2422-7

Figure 6

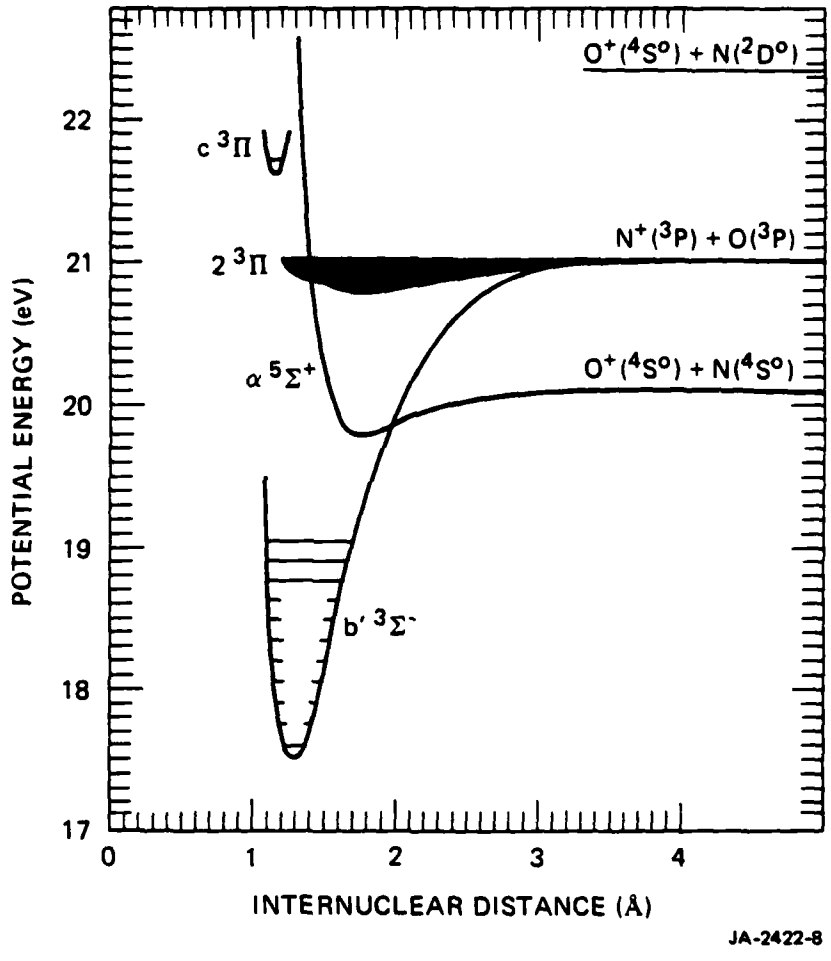
$O^+(^4S^o) + N(^2D^o)$
$c\,^3\Pi$
$N^+(^3P) + O(^3P)$
$2\,^3\Pi$
$\alpha\,^5\Sigma^+$
$O^+(^4S^o) + N(^4S^o)$
$b'\,^3\Sigma^-$
POTENTIAL ENERGY (eV)
22
21
20
19
18
17
0
1
2
3
4
INTERNUCLEAR DISTANCE (Å)
JA-2422-8

Figure 7

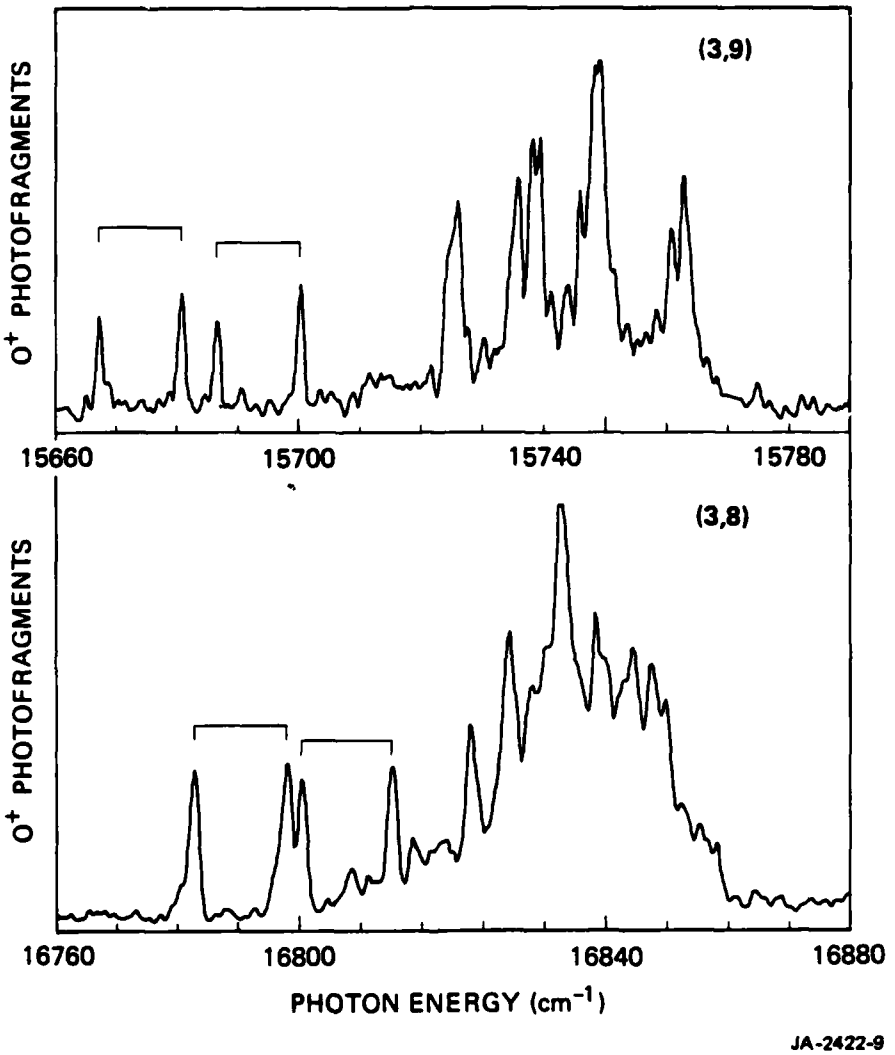
(3,9)
O+ PHOTOFRAGMENTS
15660
15700
15740
15780
(3,8)
O+ PHOTOFRAGMENTS
16760
16800
16840
16880
PHOTON ENERGY (cm-1)
JA-2422-9

Figure 8

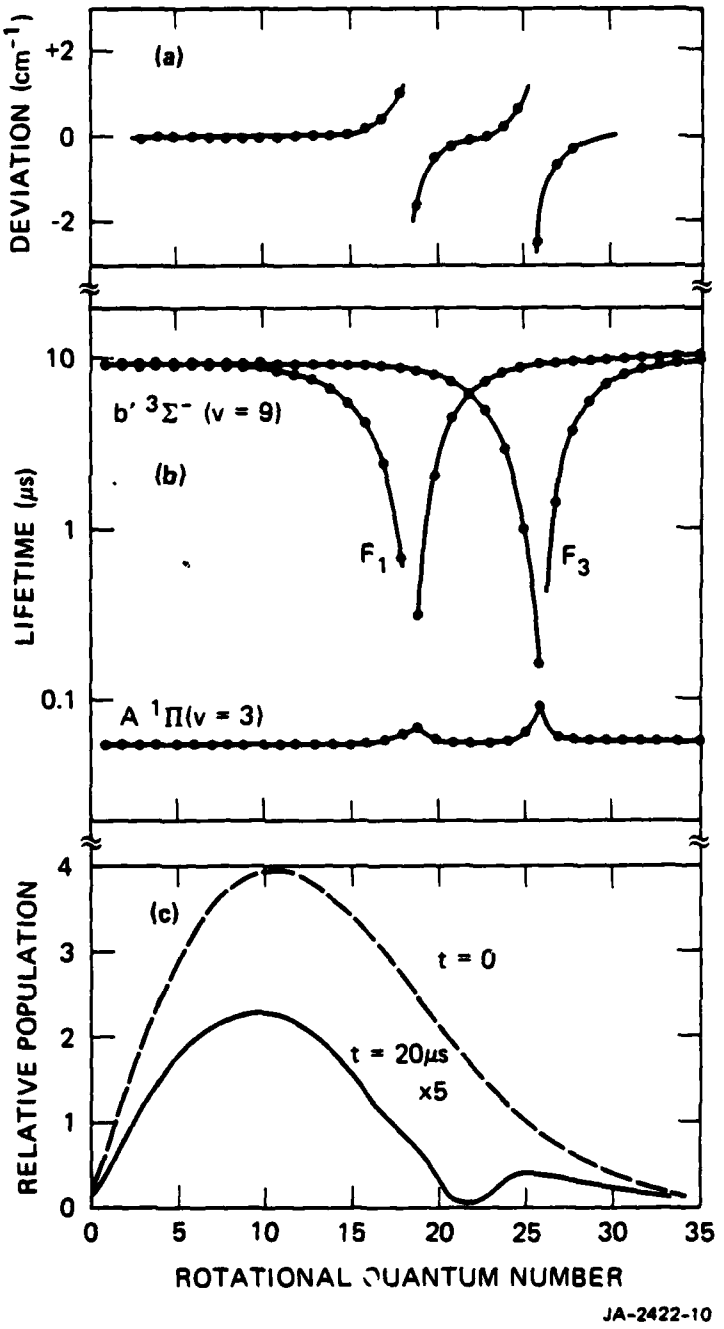
DEVIATION (cm^{-1})
+2
0
-2
(a)
10
1
0.1
LIFETIME (μs)
b' $^3\Sigma^-$ (v = 9)
(b)
F_1
F_3
A $^1\Pi$(v = 3)
4
3
2
1
0
RELATIVE POPULATION
(c)
t = 0
t = 20μs
x5
0
5
10
15
20
25
30
35
ROTATIONAL QUANTUM NUMBER
JA-2422-10

Figure 9

APPENDIX F

Photodissociation and photodetachment of molecular negative ions. VIII. Nitrogen oxides and hydrates, 3500–8250 Å

G. P. Smith, L. C. Lee, and P. C. Cosby

Molecular Physics Laboratory, SRI International, Menlo Park, California 94025
(Received 20 June 1979; accepted 14 August 1979)

Total photodestruction cross sections for the ions, NO_3^-, $NO_2^-\cdot H_2O$, NO_3^-, $NO_3^-\cdot H_2O$, and the peroxy isomers, $O_2^-\cdot NO$ and $O_2^-\cdot NO\cdot H_2O$ have been measured at wavelengths between 3500 and 8250, Å, using Ar^+, Kr^+, and dye lasers and a drift tube mass spectrometer. A threshold of ~2.5 eV was observed for the photodetachment of thermalized NO_3^-. Upper limits were set for the photodestruction cross sections of $NO_3^-\cdot H_2O$, NO_2^-, and $NO_3^-\cdot H_2O$ over this wavelength range. The NO_3^- isomer $O_2^-\cdot NO$ and its hydrate, formed in N_2O, have large photodissociation cross sections at wavelengths shorter than 5500 Å. Observations of collisional dissociation of cluster ions such as $NO_3^-\cdot H_2O$ by laser-excited NO_2 in the drift tube are also discussed.

I. INTRODUCTION

The ion NO_3^- is a key constituent of the *D* region of the earth's ionosphere,[1] due to its stability. With a bond energy[2] of nearly 4 eV, NO_3^- will react with neutrals only to form cluster ions such as $NO_3^-\cdot H_2O$. Once formed, these ions are only slowly removed by neutralization with positive ions or by photodetachment. Efforts to model the *D* region require knowledge of the photodestruction processes for the important NO_3^- ion and its hydrates, and for the precursor NO_2^- ion.

During the course of reaction rate measurements relevant to *D* region ion chemistry, a second isomer of NO_3^- was discovered.[3,4] Since this second form is produced via switching reactions such as $O_2^- + NO \rightarrow O_2^-\cdot NO + O_2$, the isomeric state is believed to have a peroxide (OONO) rather than nitrate (NO_3) structure. Investigations[3–6] into the reactions producing and destroying $O_2^-\cdot NO$ have fixed this ion's place in the *D* region reaction scheme which converts O_2^- and CO_3^- ions to NO_3^- ions, but photodestruction measurements are also needed. In addition, comparison of the photophysics of the two forms of NO_3^-, and their hydrates, can provide important structural information on the isomers. Finally, different photophysical behavior of the two forms allows their differentiation and should be useful in clarifying the chemistry of the production and subsequent reactions of the ions.

In this paper we report total photodestruction cross sections at wavelengths from 3500–8250 Å for the ions NO_2^-, NO_3^-, $O_2^-\cdot NO$, and their first hydrates. Photochemical destruction of weakly bound cluster ions such as $NO_3^-\cdot H_2O$ by laser-excited NO_2 was also observed in the drift tube, and was briefly investigated.

II. EXPERIMENTAL DETAILS

The apparatus is a drift tube–mass spectrometer coupled with an ion or dye laser, and has been described in detail previously.[6] Negative ions formed by gas phase electron attachment and subsequent ion–molecule reactions drift slowly through the ~0.50 Torr gas mixture under the influence of a weak applied electric field (E/N = 10 Td) toward an exit aperture. Before passing through the aperture into the high vacuum quadrupole mass spectrometer region at the end of the drift tube, the ions intersect an intracavity laser beam, which is chopped at 100 Hz. By counting mass-specific ion intensities, laser on and off, laser photodestruction rates for various ions can be measured. The relative cross sections thus determined are placed on an absolute scale by normalization to the known[7] O_2^- photodetachment cross section measured in O_2. The ratio of the relative laser powers is measured for this determination. The ratio of ion drift velocities through the laser beam is also needed, and is calculated from the ion mobilities. Mobilities used[8] in this work were 1.3 $cm^2 V^{-1} s^{-1}$ for $O_2^-\cdot NO$, 1.25 for $O_2^-\cdot NO\cdot H_2O$ in N_2O, and 1.3 for $NO_3^-\cdot H_2O$ in CO_2, all scaled from the measured mobilities of positive and negative ions in CO_2; and 2.5 $cm^2 V^{-1} s^{-1}$ for NO_2^- in O_2 scaled from the measured mobility of O_2^- in O_2.

A variety of laser sources was used. Prism tuned Ar^+ laser lines at 5145, 5017, 4965, 4880, 4765, 4658, and 4579 Å, and Kr^+ laser lines at 5309, 5208, 4825, 4762, 4680, 4131, and 4067 were used, with the drift tube interaction region within the laser cavity. The unseparated Kr^+ laser ultraviolet output, consisting of 25% 3564 Å and 75% 3507 Å, was also used. Intracavity dye laser measurements were made from 4200 to 4650 Å using stilbene 3 dye, pumped by the 4 W UV Ar^+ laser output; from 7150 to 7700 Å using oxazine dye; and at 8350 Å using DEOTC dye pumped by the Kr^+ laser red lines.

III. NO_2^- AND $NO_3^-\cdot H_2O$

Photodestruction cross section measurements for NO_2^- are shown in Fig. 1. Photodetachment is responsible for the photodestruction, since the photodissociation threshold is above 4.0 eV.[9] The measurements were made in 0.40 Torr O_2 with ~1% NO and a trace of NO_2 present, at E/N = 10 Td and a drift distance of 20 cm from the ion source to the laser. The ions are formed in the source region by the rapid charge transfer reactions[4,10]

$$O^- + NO_2 \rightarrow NO_2^- + O \quad , \tag{1a}$$

$$O_2^- + NO_2 \rightarrow NO_2^- + O_2 \quad , \tag{1b}$$

and by the three-body association reaction

$$O^- + NO + O_2 \rightarrow NO_2^- + O_2 \quad , \tag{2}$$

where $k_1 \sim 1.2 \times 10^{-10}$ cm^3/s. Extrapolation of the NO_2^- cross section measurements to wavelengths longer than

 0021-9606/79/234484-07$01.00

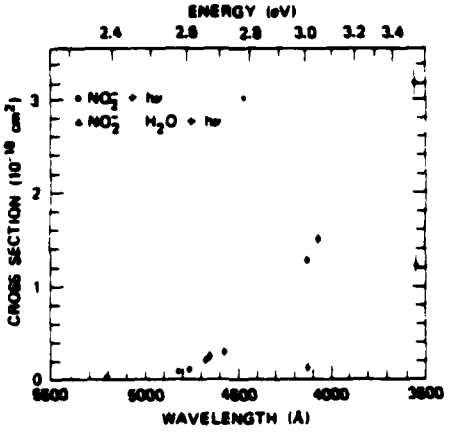

FIG. 1. Photodetachment cross section of thermal NO_3^- (circles) and $NO_3^- \cdot H_2O$ (triangles), as a function of laser wavelength.

4600 Å indicates an approximate threshold of 2.5 eV, in accord with the photodetachment value[11] of 2.36 ± 0.10 eV for the NO_3 electron affinity.

Other studies[12,13] have reported larger cross sections between 4000 and 5000 Å than the current measurements. As Huber *et al.*[9] have demonstrated, these can be attributed to vibrationally excited NO_3^-. Since vibrationally excited NO_3^- is formed[9] in reaction (1), drift tube conditions were chosen to permit relaxation of the nascent NO_3^- to 300 K prior to their arrival at the laser. Huber *et al.*[9] have measured an effective relaxation rate of 8.5×10^{-10} cm^3/s in O_2, for excited NO_3^- which can be photodissociated at 5400 Å. Then for the drift tube conditions stated above, only 3% of the nascent NO_3^- ions will remain excited after drifting 2 cm from their point of formation. Measurements of ion composition as a function of drift distance show that less than 7% of the NO_3^- ions arriving at the laser are formed within 2 cm of the laser. Given the photodetachment cross section for nascent, unrelaxed NO_3^- of 0.75×10^{-18} cm^2 at 5400 Å,[9] the contribution of excited NO_3^- to the cross section measurements presented in Fig. 1 is thus estimated to be less than 1×10^{-20} cm^2.

At 4880 Å, a constant cross section was observed for drift distances between 20 and 30 cm, indicating complete relaxation of any initially excited NO_3^- ions to a 300 K internal energy distribution. Larger cross sections were measured at shorter drift distances. An analysis similar to that of Ref. 9 gives an effective relaxation rate constant of 3×10^{-10} cm^3/s. This is slower than the relaxation rates observed previously[9] at 5400 and 6300 Å, because pin photodetachment at the longer wavelengths samples only the more highly excited vibrational levels, which are more quickly depopulated as the ions approach thermal equilibrium via collisions.

A small positive cross section of $2.3 \pm 0.9 \times 10^{-20}$ cm^2 is observed at 5208 Å (2.38 eV). This cross section is larger than that calculated for the contribution from excited NO_3^- ions. Given the current value[11] of 2.36 ± 0.10 eV for the electron affinity of NO_3, this observation is consistent with threshold photodetachment of relaxed NO_3^-.

Warneck[13] has observed a similar threshold for NO_3^- photodetachment, but his cross section measurement at 3500 Å is only 30% of our value. The reason for this discrepancy is unclear, particularly since his experiments utilized a discharge source-beam apparatus and should reflect a larger fraction of vibrationally excited ions.

Measurements on $NO_3^- \cdot H_2O$ were made in a mixture of 0.1%–2.0% NO in 0.4 Torr CO_2, with traces of impurity NO_2 and added H_2O. Under these conditions no O_2^- contaminates mass 64. Nevertheless, D_2O was also used to produce $NO_3^- \cdot D_2O$ for some experiments, to verify the absence of O_2^-. The amount of NO_2 present is sufficiently low to prevent significant collisional dissociation by excited NO_2 (see Sec. VI). The $NO_3^- \cdot H_2O$ ions are created from NO_3^- by the fast three-body reaction[4]

$$NO_3^- + H_2O + CO_2 \rightarrow NO_3^- \cdot H_2O + CO_2, \quad k_3 \sim 1.6 \times 10^{-28} \text{ cm}^6/\text{s}. \tag{3}$$

The measured $NO_3^- \cdot H_2O$ photodestruction cross sections are given in Table I and Fig. 1. A threshold near 4131 Å is evident, and the cross section is nearly one-half that of the parent NO_3^- at 3500 Å. The products of the $NO_3^- \cdot H_2O$ photodestruction could not be experimentally established because of the presence of a large excess of NO_3^- ions in the drift tube. It is likely, however, that dissociative photodetachment is the observed process. This would be consistent with the observed blue-shift in the hydrate threshold with respect to that of NO_3^-. One might expect the same electronic transition to be responsible for the photon absorption in each species, but the hydrate requires additional energy to break the NO_3^-–H_2O bond. Given the electron affinity[11] of NO_3 of 2.36 eV and the $NO_3^- \cdot H_2O$ bond energy[14] of 0.62 eV, the thermodynamic threshold for dissociative photodetachment of the hydrate is 2.98 eV, a value essentially identical to the observed photodestruction threshold.

IV. NO_3^- AND $NO_3^- \cdot H_2O$

The ground state (nitrate) isomer of NO_3^- was created in a mixture of 2% NO_2 in CO_2 at 0.40 Torr by the reaction[4]

$$CO_3^- + NO_2 \rightarrow NO_3^- + CO_2, \quad k_4 = 2.0 \times 10^{-10} \text{ cm}^3/\text{s}, \tag{4}$$

and, to a minor degree,

$$NO_2^- + NO_2 \rightarrow NO_3^- + NO, \quad k_5 = 4.0 \times 10^{-12} \text{ cm}^3/\text{s}. \tag{5}$$

Reaction (4) is exothermic by 2.8 ± 0.3 eV, as calculated from the dissociation energies of CO_3^- (1.8 eV)[15] and NO_3^- (see next paragraph), and the NO_2 and O electron affinities.[2,11] Only the ground state NO_3^- isomer should be formed. Since the excited isomer is known to react quickly with CO_2 via reaction (–4), its production via (4) must be endothermic and slow.

Table I gives upper limits on the NO_3^- photodestruction

TABLE I. Photodestruction cross section upper limits (10^{-18} cm^2).

E (eV)	λ (Å)	NO_3^-	$NO_3^- \cdot H_2O$	NO_3^-	$NO_3^- \cdot H_2O$	$O_2^- \cdot NO$	$O_2^- \cdot NO \cdot H_2O$
1.503	8250					<0.067	<0.072
1.653	7500		<0.041				<0.036
1.746	7100					<0.054	
2.335	5309	<0.029	<0.014	<0.011	<0.10		
2.381	5208	0.023±0.009	<0.026	<0.054	<0.10		
2.569	4825		<0.046	<0.075	<0.22		
2.603	4762		<0.095	<0.092	<0.12		
2.649	4680		<0.071	<0.106	<0.16		
2.708	4579		<0.045				
3.001	4131		0.16±0.03	<0.074	<0.10		
3.479	3564		1.23±0.16	0.10±0.03	0.41±0.08		
3.535	3507						

cross sections from 4131 to 5309 Å. These values represent one standard deviation of statistical uncertainty, and all measurements were consistent with zero cross sections in this region. However, a small positive cross section was measured at the Kr^+ laser UV lines (3.5 eV). This energy is at or near the thermodynamic threshold for either photodetachment or photodissociation. The NO_3^- photodetachment threshold, from the electron affinity[9] of NO_3, is 3.9±0.2 eV. Given an NO_3 dissociation energy[10] of 2.15±0.2 eV and an NO_3 electron affinity[11] of 2.36 eV, the photodissociation threshold for NO_3^- $\rightarrow NO_3^- + O$ is 3.7±0.4 eV. Although the thermodynamic threshold for the photodissociation channel $NO_3^- \rightarrow O_2^- + NO$ is only 3.6 eV, an energy barrier may be expected for the rearrangement from the NO_3^- nitrate structure. An alternate explanation to NO_3^- photodissociation at 3500 Å is also possible. The isomer $O_2^- \cdot NO$ has a large cross section at 3500 Å of 7×10^{-18} cm^2 (see Sec. V). The presence of only 1.5% peroxy form at mass 62, produced by reactions other than (4), could account for the observed cross section. A similar effect should have been observed at 4131 Å, but the error limit set there is higher, and the fraction of excited isomer may easily vary for different drift tube experiments. Future experiments at shorter wavelengths using excimer lasers should resolve this question.

The hydrate of ground state NO_3^- was formed in the same mixture with added traces of H_2O via the three-body reaction[14]

$$NO_3^- + H_2O + CO_2 \rightarrow NO_3^- \cdot H_2O + CO_2, \quad k_6 \sim 7.5\times10^{-30} \text{ cm}^6/\text{s}. \tag{6}$$

For a 2% NO_2 fraction, collisional dissociation of $NO_3^- \cdot H_2O$ by laser excited NO_2 should not affect the measurements (see Sec. VI). The observations given in Table I are consistent with a cross section below 1.0×10^{-19} cm^2 and probably zero, at wavelengths longer than 4100 Å. A positive cross section larger than that of the parent NO_3^- was measured at ~3500 Å. The observed photodestruction cannot be attributed to the presence of the hydrate of the peroxy form, $O_2^- \cdot NO \cdot H_2O$. A sizeable excited isomer fraction of 12% would be required for this explanation, and would produce a larger cross section than is observed at 4131 Å. This case may be similar to CO_3^- and its hydrate,[15] in that an electronic transition centered on the parent ion can result in photodissociation of the hydrate at energies below the thermodynamic threshold for the parent. Photodissociation of $NO_3^- \cdot H_2O$ to NO_3^- and H_2O is the thermodynamically likely process at 3500 Å.

V. $O_2^- \cdot NO$, $O_2^- \cdot NO \cdot H_2O$ AND $O_2^- \cdot N_2O$

A second form of NO_3^- can be produced by reaction of NO with O_4^-, CO_4^-, or $O_2^- \cdot H_2O$ via the exchange reactions[3,4]

$$O_2^- \cdot X + NO \rightarrow O_2^- \cdot NO + X, \quad X = O_2,\ CO_2,\ H_2O, \tag{7}$$

with $k_7 = 0.5 - 3.0\times10^{-10}$ cm^3/s. This isomeric form is distinguishable from NO_3^- in that it reacts[3,4] with NO and CO_2 by donating an O^- to form NO_2^- and CO_3^-. These reactions are endothermic by 0.5 and 2.7 eV, respectively, for ground state NO_3^-. The formation reactions (7), and the lack of conversion by collisions to form ground state NO_3^-, suggest an oxygen–oxygen bond for the excited isomer, with the negative charge residing on the more electronegative O_2 portion of the molecule.

Since the reverse of reaction (4) occurs[5] for $O_2^- \cdot NO$, it is at least 2.7 eV more energetic than NO_3^-, and has these thermodynamic thresholds for various photoprocesses:

$$\begin{aligned} O_2^- \cdot NO + h\nu &\rightarrow NO_3^- + O \quad \Delta H \leq 1.0 \text{ eV} \\ &\rightarrow O^- + NO_2 \quad 1.9 \text{ eV} \\ &\rightarrow O_2^- + NO \quad 0.9 \text{ eV} \\ &\rightarrow OONO + e^- \quad 1.0 \text{ eV} \\ &\rightarrow O_2 + NO + e^- \quad 1.3 \text{ eV} \end{aligned} \tag{8}$$

These values are based on a dissociation energy of 3.7 eV for normal NO_3^-, the known electron affinities[7,11] of O, O_2, and NO_2, and an estimate[17] of 0.3 eV for the OO–NO bond energy. Given these low energy photodestruction channels, photodissociation or photodetachment of

$O_2^- \cdot NO$ should be observed at visible wavelengths. We attempted to produce $O_2^- \cdot NO$ in the drift tube from other O_2^- cluster ions. Unfortunately, these cluster ions could not be made in large quantities, and the amount of NO required for efficient switching reactions to form $O_2^- \cdot NO$ also produced large amounts of NO_2^- and normal NO_3^-.

In our search for NO_2-free sources of nitrogen oxide ions, we examined negative ions in ~0.5 Torr N_2O with a trace of O_2 in the drift tube, although previous work[10] indicated no NO_3^- would be formed. However, the major ions we observed were O_2^-, $O_2^- \cdot N_2O$, NO_3^-, and NO_2^-. The $O_2^- \cdot N_2O$ is formed by the reaction[9]

$$O_2^- + 2N_2O \rightarrow O_2^- \cdot N_2O + N_2O, \quad k_9 = 5 \times 10^{-38}\ \text{cm}^6/\text{s}\ , \qquad (9)$$

and has a slowly increasing photodestruction cross section of $0.8-1.0 \times 10^{-18}$ cm^2 from 6400 to 5300 Å. The NO_3^- produced in N_2O is observed to photodissociate into O_2^- and NO at wavelengths shorter than 6000 Å, and therefore is probably the peroxy form $O_2^- \cdot NO$.

The amount of $O_2^- \cdot NO$ in the drift tube appears to build up with time and then stabilize after ~15 min, indicating it may be formed by reactions of the other ions with impurities. A reaction $O_2^- \cdot N_2O + NO \rightarrow O_2^- \cdot NO + N_2O$ is one possibility, but in the excess of N_2O equilibria should favor $O_2^- \cdot N_2O$, which is contrary to observations.

The photodestruction cross section measurements for $O_2^- \cdot NO$ are shown in Fig. 2. The data were taken at 10 Td in 0.4 Torr N_2O and a drift distance of 20 cm, and show a gradually increasing cross section with little detailed structure. Sizeable O_2^- photofragment signals were observed at 5300 and 4400 Å, indicating photodissociation to O_2^- and NO is the major process throughout this wavelength range, and suggesting that a single electronic transition may be responsible. This is further strong evidence for the peroxy structure of this isomer. The large cross section also suggests using photodissociation as a detection method in differentiating the chemistry of $O_2^- \cdot NO$ and NO_2^-.

There is some discrepancy between ion and dye laser measurements near 5200 Å and between Ar^+ and Kr^+ laser measurements near 4750 Å. Given the uncertainty concerning the production mechanism, we believe these differences are attributable to different fractions of $O_2^- \cdot NO$ and NO_2^- at mass 62 in the drift tube. Since we cannot be certain that all the NO_2^- is the peroxy form, the measured cross sections should be considered lower limits to the true values. Nevertheless, the measurements are generally repeatable, and we believe the cross section magnitudes are accurate. The probable absence of large amounts of normal NO_2^- is supported by the high cross section values observed near 4100 and 3500 Å and by the lack of a position (5–30 cm) or pressure (0.40–1.00 Torr) dependence at 5300–5400 Å. In addition, measurements in mixtures up to 50% O_2 gave identical results. In mixtures free of NO, NO_2, and CO_2, and to a degree in the ionosphere, $O_2^- \cdot NO$ appears to be a stable ion. The relevant destruction and interconversion reactions are

$$O_2^- \cdot NO + NO \rightarrow NO_2^- + NO_2\ , \qquad (10)$$

$$NO_2^- + NO_2 \rightarrow NO_3^- + NO\ , \qquad (11)$$

and

$$O_2^- \cdot NO + CO_2 \rightarrow CO_3^- + NO_2 \qquad (12)$$

with rate constants[2,5] of $k_{10} = 1.5 \times 10^{-11}$ and $k_{11} = 4.0 \times 10^{-12}$ cm^3/s.

By adding trace amounts of water, the hydrate ion $O_2^- \cdot NO \cdot H_2O$ can be produced by the reaction

$$O_2^- \cdot NO + H_2O + N_2O \rightarrow O_2^- \cdot NO \cdot H_2O + N_2O\ . \qquad (13)$$

The photodestruction cross section of this ion, shown in Fig. 3, is different from that of $NO_3^- \cdot H_2O$ and indicates

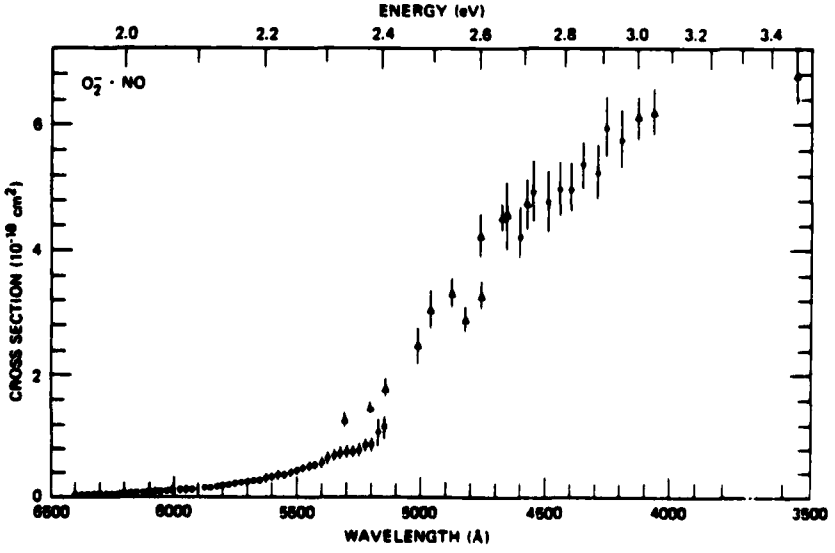

FIG. 2. Photodestruction cross section for $O_2^- \cdot NO$ vs wavelength. Solid circles are dye laser measurements and the triangles are ion laser measurements.

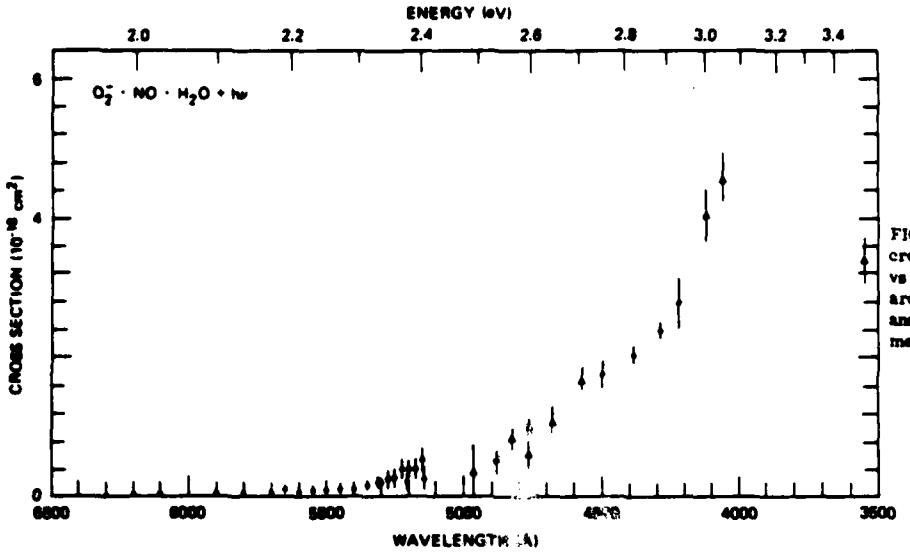

FIG. 3. Photodestruction cross section for $O_2^- \cdot NO \cdot H_2O$ vs wavelength. Solid circles are dye laser measurements and the triangles are ion laser measurements.

that the peroxy structure is preserved upon hydration. The cross section has a shape similar to that of the parent $O_2^- \cdot NO$, but is smaller in magnitude. Thus, the electrostatic bonding of H_2O to the parent anion does not significantly alter its peroxy identity. Similar behavior has been observed for the O_2^- ion and its first two hydrates.[19] Large amounts of $O_2^- \cdot NO$ were detected as a principal product of $O_2^- \cdot NO \cdot H_2O$ photodestruction.

An attempt was made to produce $O_2^- \cdot NO$ by direct three-body association in a mixture of 5% NO in O_2 in 0.50 Torr. The NO_2^- cross section measured at 5300 Å was less than 3×10^{-20} cm^2, indicating that only ground state NO_2^- was present. However, upon adding D_2O, $NO_2^- \cdot D_2O$ ions were produced which were photodestroyed at the same rate as $O_2^- \cdot NO \cdot H_2O$ ions formed in N_2O. This suggests that the peroxy isomer of $O_2^- \cdot NO$ is initially formed, and that hydration competes effectively with conversion to normal NO_2^- by reactions (10) and (11). The $O_2^- \cdot NO$ isomer apparently is more easily hydrated than NO_2^-, and $O_2^- \cdot NO \cdot H_2O$ is apparently not readily converted to $NO_2^- \cdot H_2O$ or otherwise consumed by reactions with nitrogen oxides. This is in agreement with the observation of Ref. 4 that hydration of O_2^- inhibits the conversion, in CO_2, of O_2^- into CO_3^- ions. These observations suggest the importance of considering the chemistry and photochemistry of the peroxy ion and hydrate in modeling the ionosphere, particularly since the peroxy ion appears easily hydrated with retention of its structural identity.

In 1.0 Torr N_2O, ions of mass 60 were also observed. The ion $N_2O_2^-$ has been reported in earlier studies[16] of negative ions in N_2O, but photodestruction cross section measurements made between 5300 and 5650 Å reproduced the structure previously observed[16] for CO_3^-. The magnitude of the mass 60 cross section was 30% of the CO_3^- value. This suggests that the observed photodestruction is due to CO_3^- formed from CO_2 impurity, and that some $N_2O_2^-$ is present, but has only a small photodestruction cross section ($\leq 10^{-19}$ cm^2) in this wavelength region.

VI. COLLISIONAL DISSOCIATION BY EXCITED NO_2

During the course of these experiments, a highly structured apparent photodestruction cross section was observed for $NO_2^- \cdot D_2O$ between 5800 and 6300 Å, which varied with NO_2 partial pressure. Measurements for 5% NO_2 in 0.5 Torr Ar are shown in Fig. 4. As the solid line indicates, the structure closely resembles that of the NO_2 absorption spectrum,[20] and suggests that the observed $NO_2^- \cdot D_2O$ photodestruction is caused by collisions with electronically or vibrationally excited NO_2. Thus the measurements reported in Table I were made using NO/CO_2 mixtures, and resulted in zero cross sections.

Similar, but much smaller effects were observed at 5800 Å for the ions $NO_2^- \cdot NO_2$, $NO_2^- \cdot D_2O$, and $NO_2^- \cdot NO_2$. The cross sections relative to that of $NO_2^- \cdot D_2O$ were 0.014, 0.067, and 0.025, respectively. We believe the much higher rate for collisional dissociation of $NO_2^- \cdot D_2O$ is not caused by any great disparity in the bond energies of these cluster ions, but is due to enhancement by resonant charge transfer. Since the charge is shared equally between NO_2 molecules in $NO_2^- \cdot NO_2$, only $NO_2^- \cdot D_2O$ has an extra electron centered on NO_2. An approaching NO_2 molecule will share this charge. The D_2O will be attracted to both NO_2 molecules, and should the system have sufficient (~0.5 eV) vibrational energy, the D_2O will not remain bound to it.

The observed $NO_2^- \cdot D_2O$ photodestruction is too large to be attributed to electronically excited NO_2^-. Given an NO_2 absorption cross section[21,22] (Q) of $\sim 3 \times 10^{-20}$ cm^2 at 5800 Å and an intracavity laser power of 60 W ($\rho = 2 \times 10^{20}$ photons/s) over the 0.04 cm^2 cross sectional area of the laser beam, the excitation rate ($Q\rho/A$) is 150 molecule/s. The quenching rate constant[21,22] of $\sim 10^{-19}$ cm^3/s gives a

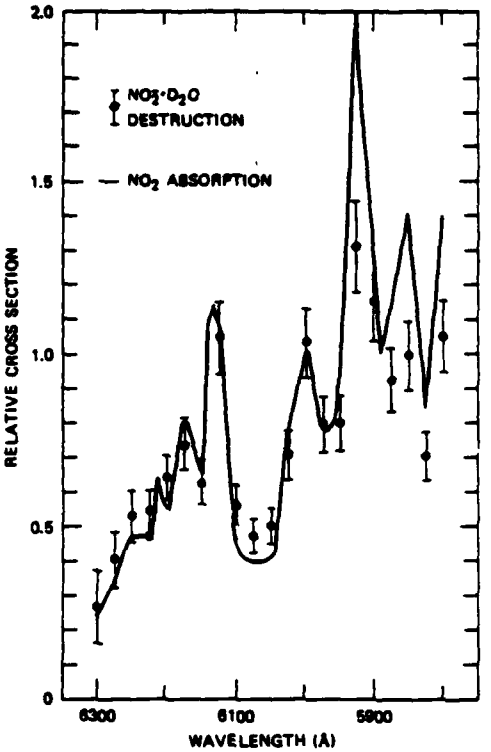

FIG. 4. Relative apparent photodestruction cross section for $NO_3^-\cdot D_2O$ measured at 10 Td in 5% NO_2 in Ar at 0.50 Torr. A relative apparent cross section of 1.0 corresponds to the same destruction rate as would be observed for a true photodestruction cross section of 10^{-18} cm^2. The solid line is the relative NO_2 absorption spectrum from Ref. 20.

quenching rate in 0.025 Torr NO_2 partial pressure (to vibrationally hot ground state NO_3^0) of 9×10^4/s. [Fluorescence[22] ($\sim2\times10^4$/s) and diffusion[23] ($\sim10^3$/s) are slower loss processes, and the Ar buffer gas is a much less efficient quencher than NO_2.] At most only $\frac{150}{9000}=0.002$ of the NO_2 or 1.5×10^{12} cm^{-3} will be electronically excited. For the observed 18% destruction ($I-I_0/I_0$) and a laser beam width $l=0.2$ cm, the expression

$$\ln(I_0/I)=[NO_3^*]\,l\sigma \qquad (14)$$

gives a cross section of 6600 Å^2 for collisional dissociation of $NO_3^-\cdot D_2O$ by NO_3^*. This represents interaction at 45 Å, and is unrealistically large.

It thus seems more likely that vibrationally excited NO_3^0 is responsible for the observed dissociation. We can modify the above treatment for vibrationally excited NO_3^0, but the quenching rate can only be roughly estimated. Several collisions will be required to deactivate the hot NO_3^0 (2.3 eV) to energies below the dissociation energy of $NO_3^-\cdot H_2O$ (~0.5 eV). Unfortunately, this energy range lies between the values for which experimental data are available. We will thus approach the problem by estimating the effective vibrational quenching rate from two limits.

Some quenching rate constants have been measured for low-lying levels. A typical $V-T$ quenching rate constant[24] for O_2^0 in Ar is $\sim10^{-14}$ cm^3/s. In these experiments, 0.09 eV of energy was removed, but NO_3^0 deactivation requires the removal of ~1.6 eV. Thus seventeen relaxing collisions will be required, and the effective quenching rate constant is 6×10^{-16} cm^3/s. Of course, at higher vibrational energies, the density of states is high enough to permit more efficient collisions, which remove smaller amounts of energy. Thus the above rate is a lower limit.

Lower pressure recombination (three-body association) rate constants can provide some information on energy transfer at high energies (near molecular dissociation limits). Typical results[25] for small molecules in Ar show ~0.035 eV vibrational energy is removed in each hard sphere collision. Thus 46 collisions at the rate of $\sim10^{-10}$ cm^3/s are required to deactivate NO_3^0, or $k\sim2\times10^{-12}$ cm^3/s. This is an upper limit since our NO_3^0 is less excited. A wide range of rate constants is obviously possible, but for this calculation a value of 5×10^{-14} cm^3/s was chosen, with an order of magnitude uncertainty likely.

Following the method of the electronic quenching calculation, at 0.5 Torr Ar this rate constant gives a deactivation rate of 875/s. For a 150/s excitation rate, $\frac{150}{875}$ or 1.5×10^{14} cm^{-3} NO_3^0 is excited at steady state. Then Eq. (14) gives a collisional dissociation cross section of 66 Å^2. This is a reasonable value for a process which is enhanced by the resonant exchange of an electron between the two NO_2 groups, but is only accurate to an order of magnitude. Given the uncertainty in the vibrational deactivation rate, the vibrational mechanism for collisional dissociation, while more likely, is not certain.

Finally, we note a previous example of visible laser induced NO_3 reactions,[26] where the slow reaction $NO_3^0+CO\rightarrow NO+CO_2$ was attributed to electronically excited NO_3^*.

ACKNOWLEDGMENTS

We thank Dr. J. T. Moseley and Dr. J. R. Peterson for many useful discussions. This work was supported primarily by the U. S. Army Research Office, and the Atmospheric Sciences Laboratory, U. S. Army Electronics Command, White Sands, New Mexico, and in part by the U. S. Air Force Office of Scientific Research and the U. S. Air Force Geophysics Laboratory. The use of a laboratory computer system obtained under an equipment grant from the National Science Foundation is acknowledged.

[1] F. C. Fehsenfeld and E. E. Ferguson, Planet. Space Sci. 20, 295 (1972).
[2] E. E. Ferguson, D. B. Dunkin, and F. C. Fehsenfeld, J. Chem. Phys. 57, 1459 (1972).
[3] N. G. Adams, D. K. Bohme, D. B. Dunkin, F. C. Fehsenfeld, and E. E. Ferguson, J. Chem. Phys. 52, 3133 (1970).
[4] F. C. Fehsenfeld and E. E. Ferguson, J. Chem. Phys. 61, 3181 (1974).
[5] F. C. Fehsenfeld, E. E. Ferguson, and D. K. Bohme, Planet.

Space Sci. 17, 1759 (1969).
[6]P. C. Cosby, R. A. Bennett, J. R. Peterson, and J. T. Moseley, J. Chem. Phys. 63, 1612 (1975).
[7]L. C. Lee and G. P. Smith, J. Chem. Phys. 70, 1727 (1979); D. S. Burch, S. J. Smith, and L. M. Branscomb, Phys. Rev. 112, 171 (1958).
[8]H. W. Ellis, R. Y. Pai, E. W. McDaniel, E. A. Mason, and L. A. Viehland, At. Data Nucl. Data Tables 17, 177 (1976); E. W. McDaniel and E. H. Mason, *The Mobility and Diffusion of Ions in Gases* (Wiley, New York, 1973).
[9]B. A. Huber, P. C. Cosby, J. R. Peterson, and J. T. Moseley, J. Chem. Phys. 66, 4520 (1976).
[10]E. E. Ferguson, F. C. Fehsenfeld, and A. L. Schmeltekopf, Adv. Chem. 80, 83 (1969).
[11]E. Herbst, T. A. Patterson, and W. C. Lineberger, J. Chem. Phys. 61, 1300 (1974).
[12]J. H. Richardson, L. M. Stephenson, and J. I. Brauman, Chem. Phys. Lett. 25, 318 (1974).
[13]P. Warneck, Chem. Phys. Lett. 3, 532 (1969).
[14]J. D. Payzant, R. Yamdagni, and P. Kebarle, Can. J. Chem. 49, 3308 (1971).
[15]J. T. Moseley, P. C. Cosby, and J. R. Peterson, J. Chem. Phys. 65, 2521 (1976).
[16]JANAF Thermochemical Tables, NBSRDS-NBS 37 (Government Printing Office, Washington, D.C., 1970).
[17]S. W. Benson, *Thermochemical Kinetics* (Wiley, New York, 1976).
[18]D. A. Parkes, J. Chem. Soc. 68, 2103 (1972); J. L. Moruzzi and J. T. Dakin, J. Chem. Phys. 49, 5000 (1968).
[19]P. C. Cosby, G. P. Smith, and J. T. Moseley, J. Chem. Phys. 69, 2779 (1978).
[20]C. G. Stevens and R. N. Zare, J. Mol. Spectrosc. 56, 167 (1975).
[21]S. E. Schwartz and H. S. Johnston, J. Chem. Phys. 51, 1286 (1969).
[22]V. M. Donnelly and F. Kaufman, J. Chem. Phys. 66, 4100 (1977).
[23]R. C. Reid and T. K. Sherwood, *The Properties of Gases and Liquids* (McGraw-Hill, New York, 1968).
[24]D. I. Rosen and T. A. Cool, J. Chem. Phys. 62, 466 (1975).
[25]H. Vandenbergh, N. Benoit-Guyot, and J. Troe, Int. J. Chem. Kin. 9, 223 (1977).
[26]P. Herman, R. P. Mariella, Jr., and A. Javan, J. Chem. Phys. 65, 3792 (1976).

APPENDIX G

Photodissociation and photodetachment of molecular negative ions. VII. Ions formed in $CO_2/O_2/H_2O$ mixtures, 3500–5300 Å

G. P. Smith, L. C. Lee, and J. T. Moseley

Molecular Physics Laboratory, SRI International, Menlo Park, California 94025
(Received 11 June 1979; accepted 2 August 1979)

Photodestruction cross sections have been measured for CO_3^-, $CO_3^- \cdot H_2O$, CO_4^-, $CO_4^- \cdot H_2O$, HCO_3^-, and $HCO_3^- \cdot H_2O$ at various ion laser and dye laser wavelengths between 5300 and 3500 Å using a drift tube mass spectrometer as the source of the ions. CO_3^- shows a structureless peak centered about 4500 Å, which is attributed to photodissociation. The possible excitation of CO_3^- in these studies was investigated in detail and no evidence was found for any excitation. Additional evidence is presented which indicates that the bond energy $D(CO_2\text{–}O^-)$ is less than or equal to 1.9 eV. The $CO_3^- \cdot H_2O$ cross section decreases smoothly with decreasing wavelength over this wavelength range. CO_4^- photodestruction was observed at 3500 Å, but the other ions listed above have cross sections below 10^{-19} cm^2, and possibly zero, throughout this spectral region.

I. INTRODUCTION

The photodissociation and photodetachment of negative ions are important ionospheric processes, affecting both ion composition and the electron density. Thus, cross section measurements for these processes are needed to understand the *D* region ion chemistry.[1] Previous work[2–5] has examined photodestruction processes of atmospheric negative ions at wavelengths between 4579 and 8400 Å. We have recently extended these measurements to 3500 Å, and report here the photodestruction cross sections for the following carbon-containing ions from 3500 to 5300 Å: CO_3^-, $CO_3^- \cdot H_2O$, CO_4^-, $CO_4^- \cdot H_2O$, HCO_3^-, and $HCO_3^- \cdot H_2O$. Results for oxygen and nitrogen containing atmospheric negative ions (O_3^-, NO_3^-, $O_3^- \cdot H_2O$, etc.) at these wavelengths will be reported elsewhere.[6,7]

These measurements also provide information on the electronic structure of the negative ions. Previous work has measured and interpreted the structure in the CO_3^- photodissociation cross section.[8] We have now examined the CO_3^- photodestruction cross section at higher photon energies, where photodetachment is also reported to occur.[9] Possible excitation of the CO_3^- was investigated, and it is concluded that the CO_3^- in this and previous studies in this laboratory is either thermally relaxed or has an unusually stable excited state. The implications of these experiments on the CO_3^- and O_3^- thermochemistry are discussed.

II. EXPERIMENTAL TECHNIQUE

The basic apparatus consists of a drift tube mass spectrometer and an ion or tunable dye laser, and has been described in detail previously.[2,3] Briefly, the negative ions are formed by electron attachment in the source region, and by subsequent ion–molecule reactions. They drift to the end of the tube under the influence of a weak electric field, at a fraction of their thermal velocity. Approximately 0.2 cm in front of the exit aperture in the end plate of the drift tube, the ions intersect the cavity of a chopped tunable dye laser or prism-tuned Ar or Kr ion laser. The ions then pass through the exit aperture into a high vacuum region containing a quadrupole mass spectrometer which selects the ion to be studied. A two-channel counter accumulates the data, laser on (I) and off (I_0).

The present measurements were all made with an intracavity laser beam intersecting the ion swarm. A prism was used to select the 4579, 4658, 4765, 4880, 4965, 5017, and 5145 A Ar laser lines and the 4067, 4131, 4680, 4762, 4825, 5208, 5309 Å Kr laser lines. Ultraviolet measurements were made with a Kr laser using only UV mirrors. The intracavity beam was measured to be 25% 3564 Å and 75% 3507 Å by focusing the reflection off a Brewster window into a monochromator.

Dye laser measurements from 4250 to 4600 Å were made using the dye Stilbene 420 (Exciton Chemical Co.), pumped by the 4 W UV output of an Ar laser. Measurements directed toward the study of excited CO_3^- were made at 6550 Å, using the dye Rhodamine 640 pumped by an Ar laser.

All cross sections were measured relative to the O_3^- photodetachment cross section, and normalized to our previously reported values.[3,4,6] The cross section for an ion A^- is given by

$$\sigma_{A^-}(\lambda) = \sigma_{O_3^-}(\lambda) \frac{\ln(I_0/I)_{A^-} P_{O_3^-} K_{A^-}}{\ln(I_0/I)_{O_3^-} P_{A^-} K_{O_3^-}} , \quad (1)$$

where P is the measured laser output power and K is the reduced ion mobility. Values[6,10] used for K are 2.51 cm^2/V sec for CO_3^- in O_2, 2.4 for CO_4^- and 2.3 for $CO_4^- \cdot H_2O$ in O_2, and 1.34 for HCO_3^- and 1.3 for $HCO_3^- \cdot H_2O$ in CO_2.

Measurements were made at 0.4 torr pressure, with a ratio of the drift field to the gas number density (E/N) of 10 Td (1 Td = 10^{-17} V cm^2), where the ion drift velocity is approximately one tenth its thermal velocity, and a drift distance of 20 cm. The CO_3^- ions were produced in various mixtures of 0.01% to 10% CO_2 in O_2. The CO_4^- ions were made using 2% CO_2 in O_2, and HCO_3^- was made using 4% CH_4 in CO_2. These conditions insure that O^- photofragment recombination with CO_2 to form CO_3^- is negligible.[8] Hydrates were formed by adding a

 0021-9606/79/[illegible]4-0[illegible]01.00

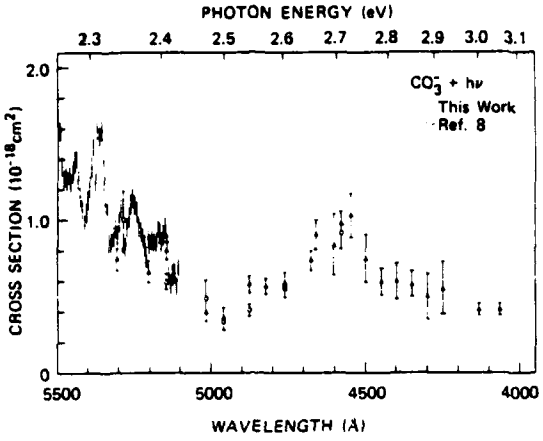

FIG. 1. CO_3^- photodestruction cross section. New data given by Δ. Old data from Ref. 8. The value at 3.4 eV (3500 Å), not shown, is $0.07 \pm 0.02 \times 10^{-18}$ cm^2.

trace of H_2O. Sufficient mass spectrometer resolution was maintained to prevent contamination of the $CO_3^- \cdot H_2O$ signal by $HCO_3^- \cdot H_2O$.

III. CO_3^- PHOTODESTRUCTION FROM 3500 TO 5300 Å

Detailed dye laser measurements of the structured CO_3^- cross section have previously been made between 5200 and 6900 Å, and the spectrum has been analyzed.[8] Argon laser wavelength measurements were also made.[4] We have repeated these Ar laser measurements, determined the cross sections at the Kr laser wavelengths between 3500 and 5309 Å, and made dye laser measurements of the cross section for the 4250 to 4600 Å region. The results are shown in Fig. 1. The Ar laser data disagree slightly beyond statistical uncertainties with the previous results at 4765, 4880, 5145 Å. The slight disagreement between ion and dye laser results may be attributable in part to the much narrower bandwidth of the ion laser. The current measurements also agree well with the Ar laser measurements made by Beyer and Vanderhoff,[11] using a similar apparatus. The previous Ar laser measurements were made in CO_2, while the current measurements were made in O_2 with only trace amounts of CO_2 present.

The new results are consistent with a lack of sharp detailed structure below 5000 Å, but do show a broad peak in the cross section near 4550 Å. No obvious relationship is apparent between this peak and the structure at longer wavelength, suggesting the existence of a dissociative transition to a repulsive electronic state. Increased O^- photofragment detection between 4765 and 4579 Å, observed previously,[2] supports the conclusion that the photodissociation in this wavelength range is due to a different transition than that at longer wavelength. The 4000 to 5000 Å measurements are consistent with the photodissociation cross sections measured by Vestal and Mauclaire[12] using a tandem mass spectrometer ion beam technique.

Hong, Woo, and Helmy[9] report values for the CO_3^- photodetachment cross section, determined by measuring photoelectron currents from CO_3^- relative to O^- using a drift tube and various cutoff filters. They infer a very sharp peak in the photodetachment cross section near 4500 Å, with a magnitude of $\sim 1 \times 10^{-18}$ cm^2, and a second broader peak from 2900 to 3900 Å. The total photodestruction cross section at 3500 Å reported here is only about 25% of their photodetachment cross section alone. In the 4500 Å region, the good agreement between our total photodestruction cross section and the photodissociation measurements of Ref. 12 are not consistent with significant photodetachment here.

To investigate this problem further, the total O^- photofragment current from CO_3^- was measured between 4300 and 4880 Å. The ratios of O^- photofragment appearance to CO_3^- photoloss are given in Table I. No significant change in this ratio is detectable between 4300 and 4579 Å, where the ratio is essentially 1. No evidence is seen for a sharp photodetachment threshold at 4590 Å or rapidly declining photodetachment cross section at 4300 Å.[9] The nearly constant O^- photoproduction ratio throughout this region indicates that no new photodestruction process, such as photodetachment, occurs on a scale comparable to photodissociation to $O^- + CO_2$. The decrease in O^- photofragments between 4579 and 4880 Å is consistent with existing observations and interpretations[2,8] that the photodissociation at wavelengths between 5145 and 4880 Å (2.41 to 2.53 eV) is due primarily to the $2\,^2B_2 - 1\,^2B_2$ transition, which is parallel, while at wavelengths shorter than 4880 Å, the perpendicular $1\,^2A_2 - 1\,^2B_2$ transition dominates. The structured cross section at wavelengths longer than 5145 Å has been assigned to a third transition $1\,^2A_1 - 1\,^2B_2$.

We conclude that the CO_3^- studied here photodissociates, but does not significantly photodetach for wavelengths longer than 4300 Å. If it is assumed that O^- and CO_3^- are detected with equal efficiency, the data are consistent with 100% photodissociation. From the uncertainties in the relative O^- observed, the upper limits shown in Table I can be placed on the photodetachment cross section. Evidence presented below strongly indicates that the CO_3^- studied here is in its ground electronic state, and is essentially thermalized to 300 °K.

TABLE I. Fraction of O^- photofragment observed from the photodestruction of CO_3^-.

Wavelength (Å)	Relative O^- observed[a]	Maximum photodetachment $\sigma(10^{-18}$ cm$^2)$
4300	0.90 ± 0.34	0.24
4400	0.79 ± 0.27	0.35
4500	1.86 ± 0.19	0.30
4550	0.99 ± 0.12	0.25
4579	0.87 ± 0.09	0.25
4600	0.70 ± 0.23	0.58
4765	0.68 ± 0.04	0.26
4880	0.59 ± 0.04	0.29

[a]This is the amount of O^- photofragment observed divided by the observed photodestruction of CO_3^-.

IV. THERMODYNAMICS AND EXCITED STATES OF CO_3^-

The picture of CO_3^- that results from this and our previous work[2,6] is consistent and reasonable. These conclusions are, in summary, as follows: (i) The ground state $1\,^2B_2$ has a bond dissociation energy of 1.8 ± 0.1 eV; (ii) the first observed excited state is $1\,^2A_1$, which has its origin 1.520 eV above the ground vibrational level of the ground state, has three stretching vibrational modes with energies of 880, 990, and 1470 cm^{-1}, and is predissociated above 1.8 eV; (iii) the second observed excited state is $2\,^2B_2$ and leads to direct dissociation between 2.41 eV (5145 Å) and 2.53 eV (4880 Å); (iv) the third observed excited state $1\,^2A_2$ is mainly responsible for dissociation above 2.53 eV; and (v) the electron affinity of CO_3 is 2.9 ± 0.3 eV. However, our conclusion that the 1.8 eV dissociation energy refers to the ground state has been called into question by results from other laboratories.

The measurements made by Vestal and Mauclaire[12] on the photodissociation of CO_3^-, while they agree quite well with the measurements presented here between 4000 and 5000 Å, show significant differences at longer wavelengths. Near 6000 Å, their measurements depended strongly on the ion source pressure. The cross section magnitude increased with decreasing source pressure, and agreed with the drift tube results only at low pressure. This pressure dependence was attributed to an excited state of CO_3^-, which is slowly relaxed by collisions with CO_2. It was determined that a relaxation rate of 5×10^{-14} cm^3/sec would explain their results.

Wu and Tiernan[13] have studied the collisional dissociation of CO_3^- by measuring the translational energy threshold for the dissociation. They observed that when CO_3^- was formed from the reaction[14]

$$O_3^- + CO_2 - CO_3^- + O_2 , \tag{2}$$

it exhibited a collisional dissociation threshold of 2.5 eV, while a fraction of the CO_3^- formed from the reaction

$$O^- + CO_2 + M - CO_3^- + M \tag{3}$$

exhibited a threshold at 1.8 eV, with a second threshold at 2.5 eV. This lower energy threshold was interpreted as being indicative of an excited state of CO_3^-, which is not effectively collisionally deactivated, even at relatively high source pressures. It was thus suggested that the photodissociation threshold observed near 1.8 eV refers to this excited state.

Dotan *et al.*[15] have pointed out that there is a significant discrepancy in the reported dissociation energies and electron affinities of O_3^-, O_3, CO_3^-, and CO_3. They determined that $D(CO_2\text{–}O^-) - D(O_2\text{–}O^-) \geq 0.58$ eV. The O_3^- dissociation energy can be determined from the recently measured O_3 electron affinity[16] of 2.1028 ± 0.0025 eV. These two numbers are related by

$$\text{E. A. } (O_3) = D(O_2\text{–}O^-) + \text{E. A. } (O) - D(O_2\text{–}O) , \tag{4}$$

where the oxygen atom electron affinity[17] is 1.462 ± 0.003 eV and the ozone dissociation energy[18] is 1.05 ± 0.02 eV. This results in $D(O_2\text{–}O^-) = 1.69$ eV, and thus implies $D(CO_2\text{–}O^-) \geq 2.27$ eV.

A value near 2.5 eV for the bond energy of CO_3^- would be consistent with the observations from these three laboratories.[12,13,15] We therefore investigated the photodissociation of CO_3^- in the region of 1.9 eV in more detail.

First, in the drift tube apparatus, it is possible to form CO_3^- either primarily by Reaction (2), or primarily by Reaction (3). Measurement of the photodissociation cross section near 1.9 eV as a function of the formation mechanism will then test for the presence of excited CO_3^- if it is formed, as reported, from Reaction (3), and if it survives de-excitation to cross the laser cavity. The ion production mechanisms can be accurately modeled since the reaction rates and mobilities involved are reasonably well known. The rate for Reaction (2) is 5.5×10^{-10} cm^3/sec,[14] and for Reaction (3) is 1×10^{-27} cm^6/sec[19] when CO_2 is the third body and 3.1×10^{-28} cm^6/sec[14] when O_2 is the third body. The third needed reaction, the formation of O_3^-, i.e.,

$$O^- + O_2 + M - O_3^- + M , \tag{5}$$

has a rate of 1×10^{-30} cm^6/sec[20] when O_2 is the third body. The drift velocities for O^-, O_3^-, and CO_3^- in O_2 are[10] 0.860, 0.691, and 0.677×10^4 cm/sec, respectively, at the E/N of 10 Td used here.

Figure 2 shows the results of integrating the rate equations (2), (3), and (5) to predict ion intensities, as compared with experimental measurements. The effect of diffusion was removed from the measurements by comparison with Cl^-, an ion formed on the filament which does not react with O_2 or CO_2. Figure 2(a) shows the relative ion intensity and the model calculation for 0.003% CO_2 in O_2, Fig. 2(b) for 0.1% CO_2 in O_2, and Fig. 2(c) for 1.0% CO_2 in O_2. The difference between these situations is clear. In Fig. 2(a), CO_3^- is being produced primarily from O_3^- [Reaction (2)], while in Fig. 2(c) most of it is being produced primarily from O^- [Reaction (3)]. The model predicts that, for a drift distance of 30 cm, 96% of the CO_3^- is produced by Reaction (2) for 0.003% CO_2 in O_2, 62% for 0.1%, and only 15% for 1%. The model consistently accounts for the observed chemistry for CO_2 percentages ranging from 0.001% to 100%, and predicts that over this range the percentage of CO_3^- produced by Reaction (2) varies from zero to 98%.

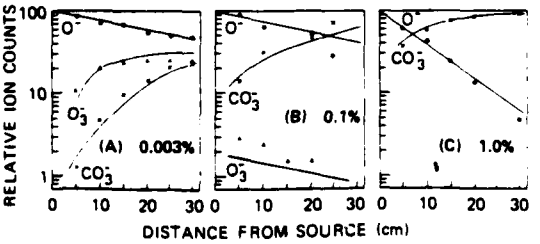

FIG. 2. Ion currents vs drift distance, with predictions of the kinetic model discussed in the text, for (a) 0.003%, (b) 0.1%, and (c) 1.0% CO_2 in O_2 at 0.4 torr.

TABLE II. CO_3^- photodissociation cross section at 6550 Å, 10 Td, 0.4 torr, 30.5 cm.

Mixture % CO_2 in O_2	% Reaction (2) production	$\sigma(10^{-18}$ cm$^2)$
0.0014	98	3.76 ± 0.60
0.003	96	4.08 ± 0.80
0.006	90.	4.16 ± 0.48
0.1	62	4.28 ± 0.40
1	15	3.20 ± 0.32
2	8	4.36 ± 0.52
100[a]	0	4.0 ± 0.30

[a]See Ref. 8, 0.05 torr.

Since the reaction rates are not precisely known, these percentages are subject to some uncertainty. However, the conclusion that CO_3^- can be produced primarily by Reaction (2), or by Reaction (3), is inescapable. For example, to model the data of Fig. 2(a) under the assumption that the CO_3^- was produced primarily by Reaction (3) would require increasing the rate of this reaction by an order of magnitude while decreasing the rate for Reaction (2) by a similar amount. The uncertainties in these reaction rates are no more than a factor of 2, and further, the data at higher CO_2 concentrations could not be fit using such rates.

It is therefore clear that the production mechanism for CO_3^- can be varied from primarily Reaction (2) to primarily Reaction (3). If either of these reactions produces a substantial amount of excited CO_3^-, and if the excitation survives to reach the interaction region, then the photodissociation cross section near 1.9 eV should reflect this excitation. Table II lists the CO_3^- photodissociation cross section at 6550 Å (1.89 eV), measured at 10 Td, 0.40 torr total pressure, and 30.5 cm drift distance, for various percentages of CO_2 in oxygen. Also listed is the percentage of CO_3^- produced by Reaction (2), as predicted by the kinetic model. This wavelength corresponds to the lowest photon energy where there is a large peak in the photodissociation cross section.

Although these experiments clearly span the range of CO_2 partial pressures over which the CO_3^- production mechanism changes, no significant variation of the cross section is observed. Thus, we conclude that the CO_3^- studied here, and consequently in previous research in this laboratory, has a dissociation energy $D(CO_2\text{–}O^-) \leq 1.9$ eV. If, as suggested by Wu and Tiernan,[13] Reaction (3) produces some excited CO_3^-, this excitation is apparently substantially relaxed by the time the ions encounter the laser photons. The question of whether or not both reactions produce *equally* excited CO_3^-, which is subsequently not easily relaxed, is unresolved. However, this seems unlikely due to the very different exothermicities of the two reactions.

As a further test for possible excitation common to both Reactions (2) and (3), the CO_3^- photodissociation cross section was measured at 6550 Å (1.89 eV) as a function of drift distance, both in pure CO_2 and in O_2 with 1% CO_2. In both cases, the primary formation mechanism for CO_3^- is Reaction (3).

The results for 0.2 torr pure CO_2 are shown in Fig. 3(a). At this pressure, virtually all O^- is converted to CO_3^- within 2 cm of the ion source. The error bars represent one standard deviation statistical uncertainty in the count rate. The solid line gives the most rapidly decreasing cross section consistent with these error limits, and yields a maximum de-excitation rate constant of 1×10^{-15} cm^3/sec. The data are certainly consistent with a constant cross section, i.e., no de-excitation. If an excited state of CO_3^- is responsible for the dissociative photoabsorption, its relaxation rate is very slow. This rate is a factor of 50 smaller than that assumed by Vestal and Mauclaire[12] to explain their results. The rate assumed by Vestal and Mauclaire would lead to relaxation of any excited CO_3^- within about 10 cm from the ion source, and thus would have led to a decrease of the photodissociation cross section to zero over the range of drift distance in Fig. 3(a), if absorption from an excited state were responsible.

Figure 3(b) shows similar data obtained for 1% CO_2 in 0.4 torr of O_2 at an E/N of 10 Td. The main differences between these data and those of Fig. 3(a) is that, for the conditions of Fig. 3(b), the production of the CO_3^- is spread out over a much greater drift distance, and the de-excitation is by O_2 rather than CO_2. The photodissociation cross section is larger at drift distances shorter than 5 cm, indicating that the CO_3^- may be initially formed with significant excitation from Reaction (3). Wu and Tiernan[13] also observe excited CO_3^- from Reaction (3), although the interpretations of these two studies disagree. The excitation we observe is substantially relaxed after 15 cm of drift, and only a slight decrease in the cross section is observed for longer drift distances. From the data between 15 and 46 cm, an upper limit of 6.1×10^{-15} cm^3/sec can be

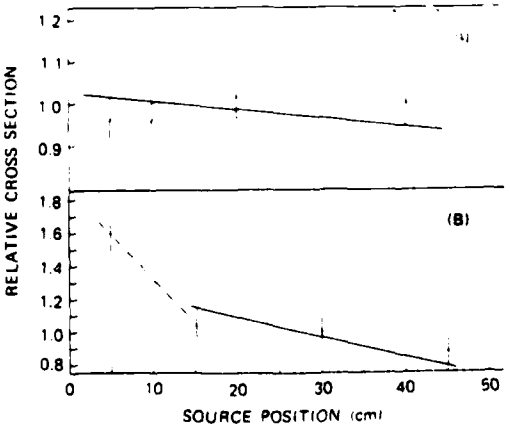

FIG. 3. Position dependence of the relative CO_3^- photodestruction cross section at (a) 6580 Å in 0.2 torr CO_2 and (b) 6550 Å in 0.4 torr O_2 with 1% CO_2. Solid lines give the maximum relaxation rates if excited CO_3^- only is responsible for the dissociation. The dashed line in (b) represents relaxation of nascent CO_3^- (see text).

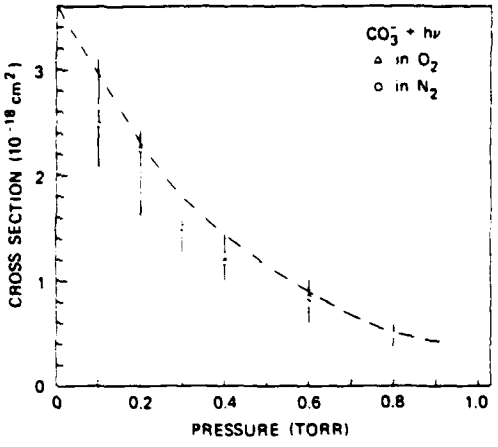

FIG. 4. Pressure dependence of the CO_3^- photodestruction cross section at 6550 Å, measured at a drift distance of 10 cm, in N_2 and O_2. The dashed line represents the quenching mechanism described in the text.

placed on the de-excitation rate constant for CO_3^- in O_2. However, the data at shorter drift distances shows that the de-excitation rate for nascent CO_3^- formed from Reaction (3) is faster. A de-excitation rate for drift distances between 5 and 15 cm is somewhat greater than 1.3×10^{-14} cm^3/sec. This faster de-excitation observed at shorter drift distances where there is significant CO_3^- formation may be that observed by Vestal and Mauclaire.[12]

V. CONCLUSIONS ON CO_3^-

A number of conclusions can thus be drawn from this study of the photodissociation of CO_3^- at 6550 Å. First, CO_3^- produced by either Reaction (2) or (3) photodissociates at 6550 Å, and the cross section for photodissociation does not vary significantly with the production mechanism if the ions are allowed to undergo on the order of 5000 collisions after formation. Further, the cross section at this wavelength is substantial, and is the largest value observed from the threshold near 7000 to 3500 Å. Thus, the dissociation here cannot reasonably be attributed to a small fraction of excited ions. It seems necessary to conclude that the CO_3^- studied here is reasonably well relaxed, and that the bond energy of the ground state of CO_3^- is less than or equal to 1.9 eV.

An alternate possibility is that both Reactions (2) and (3) produce equally excited CO_3^-, and that this excited CO_3^- is very stable, with a relaxation rate in CO_2 of less than 10^{-15} cm^3/sec. This possibility seems very unlikely, and would not resolve the previously described thermodynamic dilemma. The flow-drift tube measurements of Dotan *et al.*[15] were made over similar time and pressure regimes as the measurements reported here, and the CO_3^- was formed primarily by Reaction (2). Thus, the bond energy difference determined between O_3^- and CO_3^- would refer to the presumed excited state of CO_3^-.

It does appear [see Fig. 3(b)] that CO_3^- produced from Reaction (3) is excited, and that this excitation is relaxed by O_2 at a rate exceeding 1.3×10^{-14} cm^3/sec. All CO_3^- photodissociation cross sections reported from our laboratory have been obtained under conditions such that this initial excitation is substantially relaxed.

VI. OTHER OBSERVATIONS ON CO_3^-

In a further search for evidence of excitation of CO_3^-, the dependences of the photodissociation cross section at 6550 Å on total pressure and on E/N were investigated. These experiments were done at low CO_2 partial pressures, so the previously observed effects[2] of the fast three-body recombination Reaction (3) of the photofragment O^- to reform CO_3^- are negligible for these measurements.

The pressure dependence of the CO_3^- photodestruction cross section at 6550 Å, measured at 10 Td and a drift distance of 10 cm, is shown in Fig. 4. The observed decline with increased pressure is indepenent of the method of CO_3^- production. The measured values are the same for a 0.025% CO_2 in O_2 gas mixture, in which most of the CO_3^- is formed via Reaction (2), and for a 1% CO_2 in N_2 mixture in which CO_3^- is produced entirely by Reaction (3). Furthermore, the position dependence measurements discussed in the previous section rule out relaxation of vibrationally excited CO_3^- at higher pressures as a possible explanation. The fact that increasing the number of collisions by increasing the drift distance does not cause a decrease in the cross section, while increasing collisions by increasing the pressure does cause such a decrease, indicates the pressure dependence is due to a variation in the number of collisions following laser irradiation, just in front of the drift tube exit aperture. It is thus that a likely mechanism for the observed pressure dependence involves collisional quenching of laser excited CO_3^{-*}. The predictions of such a model are given by the dashed line in Fig. 4, and are developed in the following discussion.

The proposed mechanism for CO_3^- photodissociation is fully discussed in Ref. 2. The CO_3^- photodestruction cross section is smaller and more structured than that of the hydrate $CO_3^-\cdot H_2O$. Since the hydrate electronic transition should basically be the same one, centered on CO_3^-, the CO_3^- absorption cross section is substantially larger than the photodissociation cross section. For the purposes of this discussion, we will assume that the total CO_3^- absorption cross section equals the observed $CO_3^-\cdot H_2O$ photodissociation cross section of 7×10^{-18} cm^2 at 6550 Å (see Sec. VII). The electronic state of CO_3^- excited by the laser decays by the competitive process of fluorescence and predissociation. At 0.1 torr and 6550 Å, the photodissociation cross section of 3.6×10^{-18} cm^2 is therefore roughly one half the photoabsorption cross section of CO_3^-. The radiative decay rate k_R thus approximately equals the CO_3^- photodissociation rate, since the processes compete equally for CO_3^{-*} at 6550 Å.

The radiative lifetime, which is the reciprocal of this rate, can be estimated from the formula of Strickler and

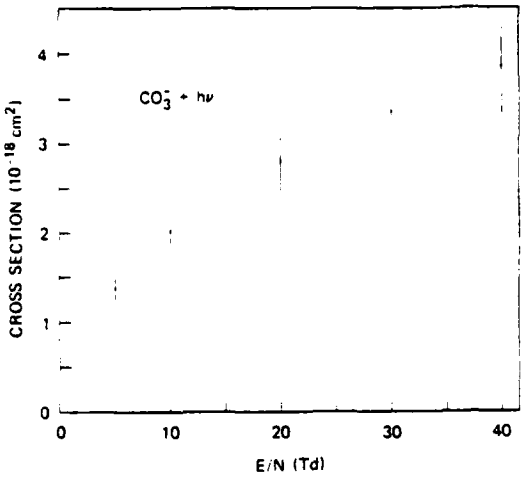

FIG. 5. The dependence of the CO_3^- photodestruction cross section at 6550 Å on E/N.

Berg[22]:

$$\tau_R^{-1} = 2.88\times10^{-9}\langle\nu_f^{-3}\rangle^{-1}\int \epsilon d(\ln\nu_a)\,, \qquad (6)$$

where ν_f is the fluorescence frequency in cm^{-1}, ν_a is the absorption frequency, the brackets indicate an average over the emission spectrum, and ϵ is the decadic molar extinction coefficient in mole/liter cm ($\epsilon = 2.6\times10^{20}\,\sigma$). To approximate the unknown $\langle\nu_f^{-3}\rangle$ term, we assume that the fluorescence spectrum is a reflection of the absorption spectrum through the origin of the transition at 7000 Å, as is typically the case.[23] Then, Eq. (6) predicts $\tau_R = 500$ nsec, i.e., a radiative decay rate of 2×10^6 sec^{-1} at 6550 Å. The predissociation rate thus is approximately equal to this value.

As shown in Fig. 4, the CO_3^- photodissociation cross section at 6550 Å declines to half its value upon the addition of each 0.20 torr of gas. This can be attributed to collisional quenching of the predissociating electronically excited state. Since the origin of the electronic state lies at a lower energy than the thermodynamic limit for CO_3^- dissociation, only vibrational quenching within the excited state is necessary to prevent dissociation. At 6550 Å, only 0.10 eV need be removed. At 0.20 torr, the quenching rate equals the dissociation rate of 2×10^6 sec^{-1}, giving a quenching rate constant of 3×10^{-10} cm^3/sec. Efficient removal of such small amounts of vibrational energy, at rates approaching gas kinetic, is certainly reasonable.

This model is also consistent with previous observations[24] of no significant pressure dependence from 0.04 to 0.10 torr in the CO_3^- cross section at 5980 Å. At this wavelength, 0.27 eV of excess energy must be removed to prevent dissociation, so more collisions—higher pressures—are required.

Figure 5 shows the variation of the CO_3^- cross section with the drift field E/N at 6550 Å, in 0.20 torr N_2 with 1% CO_2. The effect of increasing E/N to 40 Td is to raise the ion translational, rotational, and probably vibrational temperatures to 600 °K. As Fig. 3(b) illustrates, hot nascent CO_3^- has an enhanced photodissociation cross section. Large effects on cross sections near the thresholds have been seen previously,[25] and attributed to vibrational excitation. For CO_3^-, however, we are observing the predissociation of a particular vibronic transition. Since rotation is known to enhance some predissociation rates,[26] this suggests one possible explanation of the E/N dependence. As the drift field and rotational temperature increase, the faster predissociation competes more effectively with collisional quenching and the observed cross section rises.

In conclusion, both the E/N and pressure effects may be attributed to subtle mechanistic details of the predissociation process. Future experiments should provide additional information. The lack of a position or gas mixture dependence of the CO_3^- photodissociation cross section clearly indicates that the pressure dependence of the cross section cannot be explained by the relaxation of excited CO_3^-.

VII. $CO_3^- \cdot H_2O$

Photodestruction cross sections for $CO_3^- \cdot H_2O$ are shown in Fig. 6. The new measurements agree, within statistical uncertainty, with the previous results,[2,4,5] A declining, generally featureless cross section is indicated below 5300 A. The cross section for the hydrate continues to exceed that of the parent CO_3^- ion at all wavelengths, but to a lesser degree at wavelengths shorter than 4500 Å. The hydrate cross section has the appearance of a single band, while CO_3^- photodissociation has a second peak near 4500 A.

Previous work has suggested[6] that the electronic states of the hydrate are those of the parent CO_3^-, only slightly perturbed. This type of behavior is more clearly illustrated by the ozonide ion O_3^- and its hydrates.[21] The CO_3^- photodissociation cross section is lower than that of $CO_3^- \cdot H_2O$ because of competition from fluorescence. Dissociation of the hydrate to $CO_3^- + H_2O$

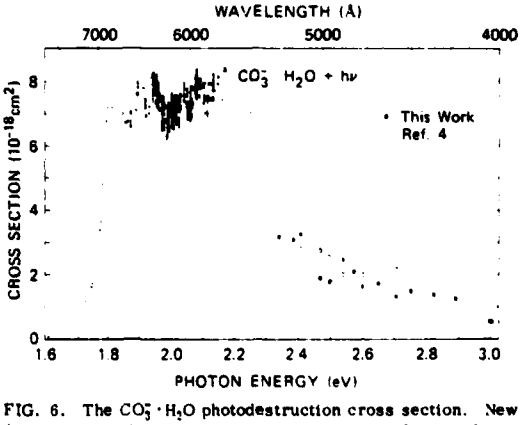

FIG. 6. The $CO_3^- \cdot H_2O$ photodestruction cross section. New data are given by solid squares. Old data are from Ref. 4. The value of $0.12\pm0.05\times10^{-18}$ cm^2 at 3.5 eV is not shown.

TABLE III. Photodestruction cross sections (10^{-18} cm^2).

λ(Å)	5309	5208	4825	4762	4680	4131	3507 + 3564
E(eV)	2.34	2.38	2.57	2.60	2.65	3.00	3.5
CO_4^-	< 0.06	< 0.12	< 0.32	< 0.16	< 0.36	< 0.06	0.45 ± 0.06
$CO_4^- \cdot H_2O$	< 0.07	< 0.12	< 0.13	< 0.17	< 0.13	< 0.12	< 0.17
HCO_3^-	< 0.017	< 0.085	< 0.035	< 0.031	< 0 051	< 0.082	< 0.077
$HCO_3^- \cdot H_2O$	< 0.013	< 0.040	< 0.038	< 0.029	< 0.034	< 0.063	< 0.066

requires less energy and is faster. When CO_3^- photodissociation is closer to its thermodynamic threshold, the predissociation is slower. At the 4500 Å peak, however, the CO_3^- cross section is nearly equal to that of the $CO_3^- \cdot H_2O$. This indicates that the fluorescence yield has probably decreased at higher excitation energies. The lack of CO_3^- structure at these wavelengths also offers evidence for a faster dissociation rate.

VIII. CO_4^- AND $CO_4^- \cdot H_2O$

Table III presents the Kr laser wavelength results for these ions. The upper limits shown for most cross sections are based on one standard deviation statistical counting error. With one exception, all such measurements are consistent with zero cross sections, and limits $\leq 1 \times 10^{-19}$ cm^2 can generally be set. Note that CO_4^- has begun to photodetach or photodissociate in the ultraviolet. The onset of photodestruction appears well above the thermodynamic threshold for either process. We were unable to detect photoproducts due to the large amounts of O^-, O_2^-, and CO_3^- ions also present in the drift tube. The hydrate $CO_4^- \cdot H_2O$ has a cross section less than half the parent's value, and possibly zero, at 3500 Å. Similar behavior[7] has been observed for $NO_3^- \cdot H_2O$. A very small nonzero CO_4^- photodestruction cross section of $(3.7 \pm 2.0) \times 10^{-20}$ cm^2 was previously measured[4] at 5145 Å. The cross section at this wavelength, if it is in fact nonzero, fails to rise significantly at shorter wavelengths.

Vestal and Mauclaire[12] have reported positive cross sections for CO_4^- photodissociation at wavelengths shorter than 5300 Å. Their results show a flat cross section of $(1.0 \pm 0.7) \times 10^{-18}$ cm^2, rather than a sharp rise, between 4000 and 3500 Å. Photoproduction of both O_2^- and a small amount of CO_3^- was observed at 3650 Å. Excited ions from the source of the beam experiments of Ref. 12 are the probable explanation for these results.

IX. HCO_3^- AND $HCO_3^- \cdot H_2O$

No photodestruction was observed for these ions at all wavelengths above 3500 Å, as shown by the limits given in Table III. Previous studies have established similar results[4,6] for wavelengths longer than 5145 Å. Initial reports[2] of a small positive cross section have since been attributed to operation at excessively high total ion densities.[4]

ACKNOWLEDGMENTS

The authors wish to acknowledge useful discussions with Dr. P. C. Cosby and to thank Dr. R. Hodges for his participation in some of the measurements during the conclusion of this research. This work was primarily supported by the Atmospheric Sciences Laboratory, U. S. Army Electronics Command, White Sands, NM, and in part by the U. S. Air Force Office of Scientific Research, the U.S. Air Force Geophysics Laboratory, and the U.S. Army Research Office. The use of a laboratory computer system through an equipment grant (PHY76-14436) from the National Science Foundation is acknowledged.

[1] L. Thomas, Radio Sci. 9, 121 (1974); J. R. Peterson, J. Geophys. Res. 81, 1433 (1976).
[2] J. T. Moseley, P. C. Cosby, R. A. Bennett, and J. R. Peterson, J. Chem. Phys. 62, 4826 (1975).
[3] P. C. Cosby, R. A. Bennett, J. R. Peterson, and J. T. Moseley, J. Chem. Phys. 63, 1612 (1975).
[4] P. C. Cosby, J. H. Ling, J. R. Peterson, and J. T. Moseley, J. Chem. Phys. 65, 5267 (1976).
[5] G. P. Smith, L. C. Lee, P. C. Cosby, J. R. Peterson, and J. T. Moseley, J. Chem. Phys. 68, 3818 (1978).
[6] L. C. Lee and G. P. Smith, J. Chem. Phys. 70, 1727 (1979).
[7] G. P. Smith, L. C. Lee, and P. C. Cosby, J. Chem. Phys. (to be published).
[8] J. T. Moseley, P. C. Cosby, and J. R. Peterson, J. Chem. Phys. 65, 2512 (1976).
[9] S. P. Hong, S. B. Woo, and E. M. Helmy, Phys. Rev. A 15, 1563 (1977).
[10] H. W. Ellis, R. Y. Pai, E. W. McDaniel, E. A. Mason, and L. A. Viehland, At. Data Nucl. Data Tables 17, 177 (1976).
[11] R. A. Beyer and J. A. Vanderhoff, J. Chem. Phys. 65, 2313 (1976).
[12] M. L. Vestal and G. H. Mauclaire, J. Chem. Phys. 67, 3758 (1977).
[13] R. L. C. Wu and T. O. Tiernan, 31st Gaseous Electronics Conference, Abstract HA-7, Buffalo, NY, 1978.
[14] F. C. Fehsenfeld and E. E. Ferguson, J. Chem. Phys. 61, 318 (1974).
[15] I. Dotan, J. A. Davidson, G. E. Streit, D. L. Albritton, and F. C. Fehsenfeld, J. Chem. Phys. 67, 2874 (1977).
[16] S. E. Novick, P. C. Engelking, P. L. Jones, J. H. Futrell, and W. C. Lineberger, J. Chem. Phys. 70, 2652 (1979).
[17] H. Hotop and W. C. Lineberger, J. Phys. Chem. Ref. Data 4, 539 (1975).
[18] JANAF Thermochemical Tables, Natl. Stand. Ref. Data Ser. Natl. Bur. Stand. 37 (1970).
[19] D. A. Parkes, J. Chem. Soc. Faraday Trans. 1 68, 627 (1972).
[20] J. L. Pack and A. V. Phelps, Bull. Am. Phys. Soc. 16, 214 (1971).

[21]P. C. Cosby, J. T. Moseley, and G. P. Smith, J. Chem. Phys. 69, 2779 (1978).
[22]S. J. Strickler and R. A. Berg, J. Chem. Phys. 37, 814(1962).
[23]N. J. Turro, *Modern Molecular Photochemistry* (Benjamin/Cummings, Menlo Park, 1978).
[24]P. C. Cosby and J. T. Moseley, Phys. Rev. Lett. 34, 1603 (1975).
[25]L. C. Lee and G. P. Smith, Phys. Rev. A 9, 2329 (1979).
[26]G. Herzberg, *Spectra of Diatomic Molecules* (Van Nostrand, New York, 1950), p. 418.

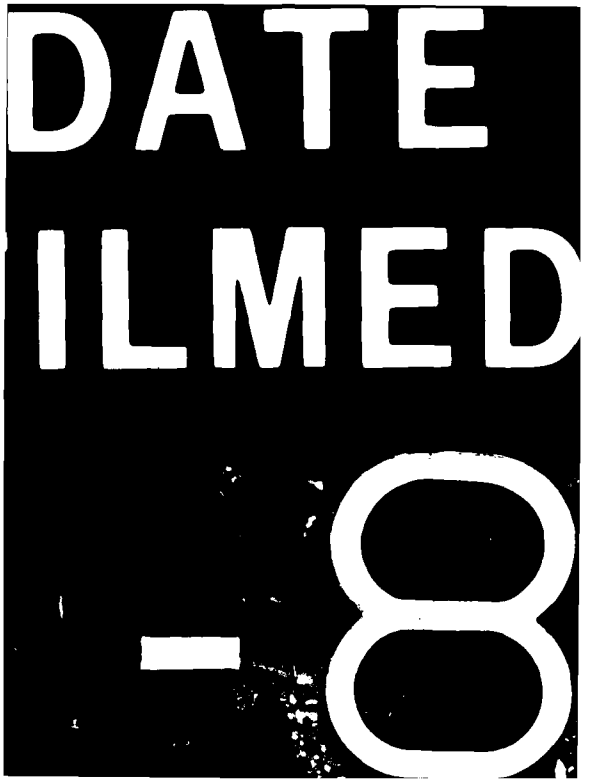
DATE
ILMED
-8